A superconducting microcalorimeter for low-flux detection of near-infrared single photons

Dissertation

zur Erlangung des Doktorgrades

des Department Physik

der Universität Hamburg

vorgelegt von

JAN DREYLING-ESCHWEILER

aus Tübingen

Hamburg

2014

Abstract

This thesis covers the development and the characterization of a single photon detector based on a superconducting microcalorimeter. The detector development is motivated by the Any Light Particle Search II (ALPS II) experiment at DESY in Hamburg, which searches for weakly interacting sub-eV particles (WISPs). Therefore, a detection of low-fluxes of 1064 nm light is required. The work is divided in three analyses: the characterization of a milli-kelvin (mK) cryostat, the characterization of superconducting sensors for single photon detection, and the determination of dark count rates concerning 1064 nm signals.

Firstly, an adiabatic demagnetization refrigerator (ADR) is characterized, which allows to reach mK-temperatures. During commissioning, the ADR cryostat is optimized and prepared to stably cool superconducting sensors at 80 mK $\pm$ 25 μK. It is found that sensors can be continuously operated for ~20 h before recharging the system in <2 h. Furthermore, the adiabatic system reaches a chance of success of ~80 % for a recharge without technical problems.

Secondly, superconducting sensors are analyzed. The focus is on microcalorimetric transition-edge sensors (TESs) based on 20 nm Tungsten (W) films fabricated by the U.S. National Institute of Standards and Technology (NIST). NIST TESs have a near unity detection efficiency for 1064 nm light (literature value). The energy resolution for 1064 nm signals is measured to be <8 %. The exponential falling time of a photon pulse is 1.5 μs. Furthermore, by determining TES parameters, it is found that the linear TES theory describes measured photon pulses well. The TES response is read out by a superconducting quantum interference device (SQUID) fabricated by Physikalisch-Technische Bundesanstalt (PTB). The system bandwidth is measured to be 0.9 MHz. Finally, the operation in the ADR cryostat as well as the ALPS II laboratory is optimized. This setup forms the ALPS TES detector.

Thirdly, the background is measured to obtain a dark count rate for 1064 nm signals. The ALPS TES detector is calibrated by a 1064 nm single photon source and methods are developed to analyze signals. In long-term measurements, background events are measured by using different optical setups. By operating the TES without an optical link outside mK-environment, intrinsic background components are observed and classified. This results in an intrinsic dark count rate for 1064 nm signals of $1.0 \cdot 10^{-4}$ s^{-1}. By operating a fiber-coupled TES, it is found that the dark count rate for 1064 nm signals is dominated by pile-up events of near-infrared thermal photons coming through the fiber from the warm environment. Considering a detection efficiency of ~18 %, a dark count rate of $8.6 \cdot 10^{-3}$ s^{-1} is determined for 1064 nm ALPS photons.

Concerning ALPS II, this results in a sensitivity gain compared to the ALPS I detector. Furthermore, this thesis is the starting point of TES detector development in Hamburg, Germany.

Zusammenfassung

Diese Arbeit beschreibt den Aufbau und die Charakterisierung eines supraleitenden Mikrokalorimeters zum Messen einzelner Lichtteilchen. Die Entwicklung geschah im Rahmen des "Any Light Particle Search II" (ALPS II) Experiments bei DESY, welches die Existenz von schwach wechelwirkenden, leichten Teilchen (WISP) erforscht. ALPS II benötigt dafür ein Messgerät für Lichtteilchen der Wellenlänge 1064 nm, welche bei niedrigen Ereignisraten als Signal erwartet werden. Dieses Messgerät wird in drei Analysen beschrieben.

Zunächst wird ein adiabtischer Demagnetisierungskühler (ADR) behandelt, welcher Millikelvintemperaturen erreicht. Während der Inbetriebnahme wurde der Kryostat optimiert, um supraleitende Sensoren bei 80 mK ± 25 μK stabil zu betreiben. Dieser Betrieb kann etwa 20 Stunden durchgängig erfolgen, bevor der Kühler in weniger als 2 Stunden aufgeladen werden muss. Solche Aufladevorgänge bei 4-10 Kelvin lassen sich mit einer 80 prozentigen Erfolgsquote durchführen.

Im zweiten Teil werden supraleitende Sensoren behandelt. Als Lichtsensoren werden supraleitende Übergangs-Mikrokalorimeter (TES) aus 20 nm dicken Wolframfilmen benutzt, die vom amerikanischen Metrologieinsitut (NIST) hergestellt wurden und eine hohe Nachweiseffizienz für 1064 nm Licht erreichen sollen. Die Untersuchung an 1064 nm Signalen zeigt, dass einzelne Lichtteilchen als kalorimetrische Pulse mit einer Abfallzeit von 1.5 μ gemessen werden. Die Energieauflösung wurde zu <8 % bestimmt. Zudem wurden wichtige Kenngrößen des TES-Sensors bestimmt. Anhand dieser Parameter und der linearen TES Theorie können gemessene Pulse beschrieben werden. Der TES wird mit supraleitenden Quanteninterferenzdetektoren (SQUID) ausgelesen. Desweiteren wurde der Betrieb des TES/SQUID-Detektormoduls im ADR Kryostaten und im ALPS II Labor optimiert. Dieser Aufbau stellt den *ALPS TES Detektor* dar.

Zuletzt wurden Hintergrundereignisse untersucht, um eine Dunkelrate für den ALPS TES Detektor zu bestimmen. Mit einer 1064 nm Einzelphotonenquelle wurde der Detektor kalibriert und Analysemethoden wurden entwickelt. Anhand von Langzeitmessungen mit verschiedenen optischen Aufbauten wurden Hintergrundereignisse gemessen und unterschieden. Intrinsische Hintergrundereignisse wurden untersucht, indem der TES dunkel in seiner Millikelvinumgebung betrieben wurde. Bezogen auf 1064 nm Signale wurde eine intrinsische Dunkelrate von $1.0 \cdot 10^{-4}$ s^{-1} bestimmt. Mit einem fasergekoppelten TES wurde herausgefunden, dass die Dunkelrate durch Vielfachereignisse einzelner nahinfraroter Lichtteilchen des Raumtemperaturspektrums dominiert ist, die durch die optische Faser zum TES gelangen. Betrachtet man eine Gesamteffizienz von etwa 18 % für 1064 nm ALPS Signale, beträgt die Dunkelrate $8.6 \cdot 10^{-3}$ s^{-1}.

Verglichen mit dem ALPS I Detektor verbessert der ALPS TES Detektor damit die experimentelle Empfindlichkeit von ALPS II. Zudem stellt diese Arbeit den Beginn der TES-Detektorentwicklung in Hamburg, Deutschland, dar.

Contents

Contents

1. Introduction

Modern particle research utilizes extremely high-developed machines to obtain new results. Considering high energy physics, the success of many particle discoveries in the last decades is due to kilometer long colliders with complex house-high detectors. Reaching TeV energies at the LHC has been recently indicated a Higgs particle, which is the last missing brick of the Standard Model (SM) of Particle Physics.

Considering astronomy, cosmology, and astroparticle physics, extreme observation tools are also developing: Neutrino experiments like ICECUBE incorporate giant volumes to obtain higher sensitivity; gamma ray telescopes like CTA will be built having large effective detection areas; and satellites like SPICA/SAFARI are planned using newest detector technologies. As a current status of such observations, the present picture of the universe claims dark matter and moreover dark energy – which cannot be explained by the SM.

By embedding the SM in theories like supersymmetry and other SM extensions, heavy particles are predicted which could explain dark matter phenomena. Such particles are summarized as weakly interacting massive particles (WIMPs) having higher masses than SM particles. Thus, collider experiments can probe WIMPs. However, up to now, there is no detection of WIMPs leaving aside some disputed results.

Complementary to high energy searches for physics beyond the SM, in the last decade a new field has emerged. Motivated by many SM extensions, this field searches for light particles, which are additionally linked to the high-energy scale due to their weakly interacting dynamics with the SM. It has been shown that such particles could explain, for example, cold dark matter or anomalous astroparticle phenomenons like white dwarf cooling or the intergalactic propagation of very-high-energy gamma-rays. Such particles are summarized as weakly interacting sub-eV particles (WISPs) having lower masses than SM particles. Since the weakness of the interaction with SM particles, WISPs searches require extreme precision experiments.

One WISP laboratory experiment is the Any Light Particle Search (ALPS) at DESY. ALPS incorporates an intense laser, long-distance resonant cavities, and strong magnetic fields in order to reach a high sensitivity. Furthermore, for the second experimental phase a sensitive single photon detector has been developed within the scope of this thesis. This detector setup incorporates extreme conditions like:

- pressures from 10^{-7} mbar to 10^4 mbar (11 orders of magnitude),
- temperatures from 30 mK to 300 K (4 orders of magnitude),
- magnetic fields from 1 μT to 6 T (7 orders of magnitude), or
- currents from 70 nA to 40 A (9 orders of magnitude).

The understanding, the development, and the application of this extreme machine are the topics of this thesis.

$$\star \quad \star \quad \star$$

To complete the introduction, in the following subsections, axions and WISPs (sect. 1.1) and the ALPS II experiment (sect. 1.2) are briefly described. Furthermore, it is motivated to use a single photon detector based on a superconducting microcalorimeter for the ALPS II experiment (sect. 1.3).

This thesis covers the understanding, the development, and the characterization of a single photon detector based on a superconducting microcalorimeter. Furthermore, the completed detector is used to characterize signals and backgrounds. Thus, this thesis is divided in three analyses:

- In chapter 2, milli-kelvin (mK) environments for cryogenic photon detection are discussed. The focus is on adiabatic demagnetization refrigerators (ADR), since with this thesis an ADR cryostat was set up. The cooling principle is explained. Then, components of the ADR cryostat and the working principle are explained. The ADR cryostat is characterized using it as a mK-environment for superconducting photon sensors.

- In chapter 3, superconducting sensors for photon detection and their environments are investigated. The focus is on fiber-coupled transition-edge sensors (TES) and a read-out with a superconducting quantum interference device (SQUID). The working principle of these sensors are described. Furthermore, a mathematical framework is given to describe TES signals and noise. Sensors for the ALPS TES detector are extensively characterized and compared to theory. Furthermore, the environment is tested. Components and the setup of the ALPS TES detector are summarized in section 3.4.

- In chapter 4, the ALPS TES detector is used to study 1064 nm photon signals and background events. The experimental setup is explained and methods to analyze signals are developed. Results of long-term measurements are analyzed to classify background events. Finally, a dark count rate of the detector setup is determined.

In chapter 5, the findings of this thesis are summarized and a prospect for the ALPS II experiment is given.

1.1. The axion and weakly interacting sub-eV particles

One drawback of the SM is the so-called strong CP problem: In quantum chromodynamics (QCD), a violation of charge conjugation (C) and parity (P) is not excluded. However, a violation is experimentally not indicated. This evident fine-tuning can be explained by extending the SM by the so-called Peccei-Quinn symmetry (Peccei and Quinn, 1977). The breaking of this chiral symmetry gives rise to a spin-0 particle, a so-called pseudo-Nambu-Goldstone boson (Wilczek, 1978; Weinberg, 1978). Since this particle would wash out the strong CP problem, it had been named after a detergent: the axion. Because it is motivated by the QCD, it is also called QCD axion.

Since a QCD axion necessarily couples to gluons, the axion gets an effective light mass m_a. This can be expressed by the mass and the decay constant of the pion, m_π and f_π:

$$m_a \approx \frac{m_\pi f_\pi}{f_a} \approx 1\,\text{meV} \times \left(\frac{10^{10}\,\text{GeV}}{f_a}\right) \tag{1.1}$$

where f_a is the axion decay constant, which sets a high energy scale at which the Peccei-Quinn symmetry is broken. Furthermore, the effective coupling to other SM particles is small if f_a is large (Srednicki, 1985). For example, the coupling strength to photons is:

$$g_{a\gamma} \propto \frac{1}{f_a} \tag{1.2}$$

Due to the smallness of mass and the weakness of coupling, an axion is the prime example of weakly interacting sub-eV particles (WISPs). Equations 1.1 and 1.2 results in a mass-coupling relation which constrains the parameter space of QCD axion models (yellow band in figure 1.2).

In the following, most important is the coupling to photons. An axion effectively couples to two photons via a pion (fig. 1.1a). This corresponds to the so-called Primakoff process (fig. 1.1b): A photon converts in an axion and vice versa in the presence of an external electro-magnetic field. This results in a photon-axion oscillation in the presence of an external magnetic field, which is most relevant for experiments (see below). Assuming the external magnetic field B is perpendicular to the photon propagation, the probability $\mathcal{P}$ for a photon-axion conversion or vice versa is given by (Arias et al., 2010):

$$\mathcal{P}_{a\leftarrow\gamma} = \mathcal{P}_{a\rightarrow\gamma} = \frac{1}{4}\frac{\omega}{k_a}\left(g_{a\gamma}BL\right)^2|F|^2 \tag{1.3}$$

1. Introduction

(a) effective photon vertex   **(b)** Primakoff effect   **(c)** light shining through a wall
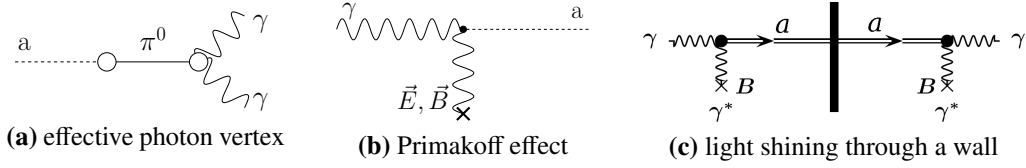
Figure 1.1.: Axion-photons vertices: (a) illustrates the effective coupling of an axion via a pion to two photons. (b) illustrates a photon-axion conversion in the presence of an external electric or magnetic field. This is the so-called Primakoff effect which is most important for experiments and observations. (c) illustrates the light-shining-through-a-wall scheme utilizing the Primakoff effect twice so that the axion state can pass the wall. [(c) taken from Ehret et al. (2010)]

where ω is the photon energy[1], $k_a^2 = \omega^2 - m_a^2$, L the travel distance through the magnetic field, and F a form factor. For homogeneous fields with length L, it is $|F| = \frac{2}{qL} \sin\left(\frac{qL}{2}\right) \leq 1$. q is the momentum transfer for the magnetic field which is given by $q = n\omega - \sqrt{\omega^2 - m_a^2}$ where n is the refractive index of the medium. This explains the exclusion shape of experiments like ALPS or CAST in the parameter space (fig. 1.2): For small m_a, there is a constant bound on the coupling, before the steep rise including the oscillating behaviour for higher masses occurs.

The axion mechanism can be generalized to axion-like particles (ALPs) whose existence is well motivated from considering compactifications in string theory (Goodsell et al., 2009, e.g.). Analogously, ALPs have photon-conversion properties like the axion and are candidates for WISPs. However, ALPs are not constrained by the mass-coupling relation of the QCD axion. Thus, an ALP can be realized in a wide parameter space which can be tested by observations and experiments (fig. 1.2).

Further WISP candidates are hidden photons. A hidden photon is the massive partner of the photon due to a U(1) extension of the SM (Holdom, 1986, e.g). Thus, a kinetic mixing is expected and hidden photons can be analogously probed like axions and ALPs, however, an external electro-magnetic field is not required. For example in the first and second phases of ALPS II, this will be explicitly tested (sect. 1.2). Furthermore, mini-charged particles (Gies et al., 2006, e.g) and chameleons (Khoury, 2013, e.g.) are allocated to the family of WISPs. In the following sections, the focus is on ALPs including axions as most relevant for ALPS II.

Considering the ALP parameter space (fig. 1.2), observations and models can constrain as well as motivate the existence of such particles. In the following, the most prominent examples are given:[2]

- Astrophysical observations:

---

[1] With $\hbar = c = 1$.
[2] See, for example, Hewett et al. (2012) or Arias et al. (2012) for a detailed overview.
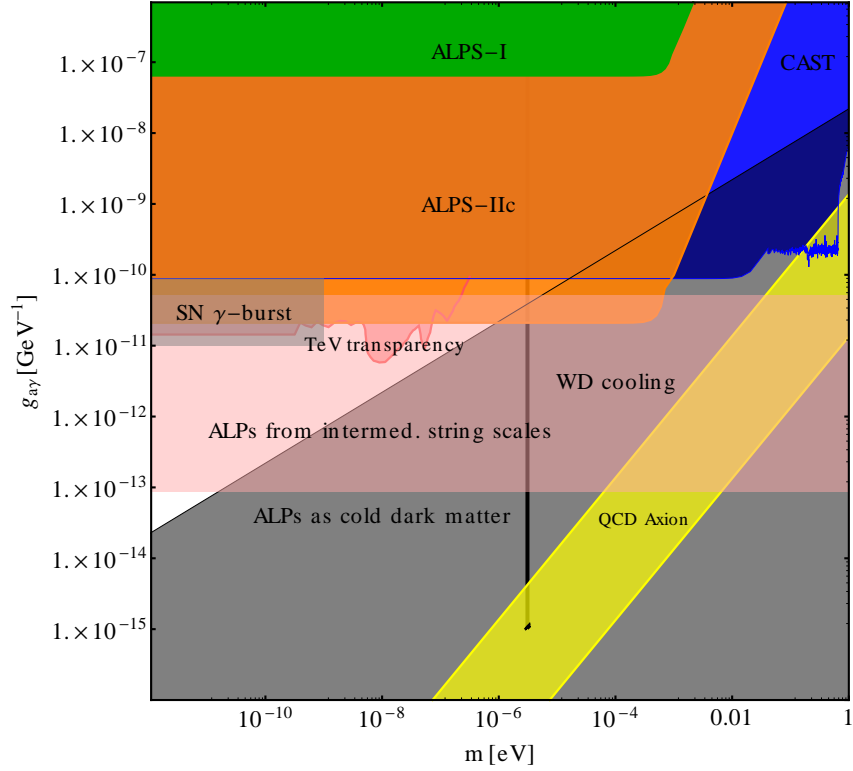
Figure 1.2.: ALP parameter space: The parameter space is spanned by the ALP mass m_a and the photon coupling $g_{a\gamma}$. Exemplary, hints and constraints from observations, models, and experiments are depicted. Astrophysical hints are the WD cooling or the TeV transparency. SN γ-bursts constrain the parameter space. Other motivations are string theories, cold dark matter explanations, and the QCD axion. Experimental constraints are related to CAST, ALPS, and ADMX (black vertical line). For details, see text. [Taken from Bähre et al. (2013)]

- Cooling channels for stellar objects: WISPs could provide an additional energy-loss channel. Assuming WISPs are produced in the stellar core, they could pass the outer stellar region not interacting with SM matter. Lifetimes of HB-stars[3] mainly set a bound on ALPs with masses smaller than ~30 keV (Gondolo and Raffelt, 2009, e.g.). The non-observation of γ-ray bursts during SN[4] 1987A constrains a region for m_a below 10^{-9} eV. Furthermore, a discrepancy is indicated between the luminosity of white dwarfs (WD) and models describing the cooling process (Isern et al., 2012, e.g.). This could be explained by an additional cooling channel through ALPs in a large region of parameter space.

---

[3] horizontal branch stars

[4] supernova

5

- TeV transparency: A higher observed flux of high energetic γ-rays as expected could be explained by photon-ALPs oscillations due to intergalactic and galactic magnetic fields (Meyer et al., 2013). This overlaps with the hint of WD cooling.

- Cold dark matter: ALPs could be produced during the early universe and could explain cold dark matter (Arias et al., 2012, e.g.). Thus, ALPs of a large parameter space are candidates for cold dark matter.

- String theory: As mentioned above, string theories automatically include ALP particles (Goodsell et al., 2009). The motivated parameter space overlaps with other indications.

To test the existence of WISPs, experiments are divided in three categories:

- Haloscopes: Microwave cavities surrounded by a strong magnet could probe ALPs which could form the cold DM halo at the location of the sun. Due to the resonance requirement, the search is restricted to a small mass range but scans several orders of magnitude of the coupling constant. An exclusion region from ADMX[5] is depicted in figure 1.2. Many haloscopes are performed or proposed (Hagmann et al., 1990; Horns et al., 2013, e.g.).

- Helioscopes: The sun could have a cooling channel through ALPs. This is tested by dark telescopes incorporating a strong magnet and guiding to the sun. CAST[6] provides the lowest sensitivity test of a wide range in the parameter space. Next generation helioscopes are developed.[7]

- Light-shining-through-a-wall (LSW): LSW experiments incorporate a light source and a detector separated by a wall. LSW are designed so that SM particles cannot pass the wall, so that the existence of WISPs can be tested (Redondo and Ringwald, 2011). Using strong magnets for photon-ALP oscillations, a photon could convert to an ALP in front of the wall (fig. 1.1c). The ALP could pass the wall. For detection, the ALP has to re-convert to a photon. Thus, the detected photon rate is given by:

$$\dot{n}_{\text{det}} = \eta \; \mathcal{P}_{\gamma \to \text{a}} \, \mathcal{P}_{\text{a} \to \gamma} \, \dot{n}_{\text{prod}} \tag{1.4}$$

where η is a generic efficiency including the detector efficiency, $\mathcal{P}$ the probabilities for photon-ALP-photon oscillation, and $\dot{n}_{\text{prod}}$ the photon rate of the source. If a photon-signal will be detected behind the wall, this would be a strong evidence for physics beyond the SM. Different LSW experiments are realized and planned at different wavelengths.[8] ALPS I has reached the

---

[5]Axion Dark Matter eXperiment (van Bibber and Carosi, 2013, e.g.).
[6]CERN Axion Solar Telescope (Andriamonge et al., 2005, e.g.).
[7]Like IAXO (Armengaud et al., 2014).
[8]For example, LIPSS at Jefferson Lab (Afanasev et al., 2008), OSQAR at CERN (Schott et al., 2011), CROWS in the microwave regime (Betz et al., 2013), REAPR (planned) (Mueller et al., 2010).

strongest bounds until now (Ehret et al., 2010). ALPS II will improve the sensitivity by three orders of magnitude (fig. 1.2 and next sect. 1.2).

The first two types of experiments depend on a model describing the source of WISPs. At LSW experiments as pure laboratory experiments, the source is controlled. However, the sensitivity has to be high, since the detection probability depends on the 4th power of $g_{\text{a}\gamma}$ due to the photon-ALPs-photon conversion (eqn. 1.3).

Until today, there is no indication of WISPs. However, the WISP search is motivated by many hints from observations and explanations by WISP-based models as described above.

1.2. The ALPS II experiment

The Any Light Particle Search (ALPS) experiment is a LSW experiment (see above, sect. 1.1). After ALPS I has set the best laboratory-based bounds in the WISP parameter space (Ehret et al., 2009, 2010), the ALPS collaboration started with the second phase in 2011, ALPS II (Bähre et al., 2013). To reach the full sensitivity of ALPS II, basically, three phases are planned (fig. 1.3). ALPS IIa is mainly a technical proof: A high-power production cavity (PC) with a continuous 1064 nm laser in front of the wall, the locking scheme for the regeneration cavity (RC) behind the wall, as well as the integration of a new detector (next sect. 1.3) will be tested.[9] ALPS IIb would extend this scheme from 2x10 m to 2x100 m in order to prove the stability of such long cavities. Furthermore, ALPS IIa and ALPS IIb can set bounds on the parameter space of hidden photon oscillations. The last stage, ALPS IIc, will probe the ALP parameter space using 2x10 superconducting HERA dipole magnets. Compared to ALPS I, the final stage is expected to lower the overall sensitivity by three orders of magnitude (fig. 1.2): This should confirm limits due to astrophysical observations and helioscope results; but, especially, ALPS IIc will test regions which overlap with astrophysical hints or possible cold dark matter regions.

In the following, the components of ALPS II and their improvement related to ALPS I are briefly described. To compare the improvements, a sensitivity for the ALP-photon coupling can be estimated by combining equations 1.3 and 1.4 (von Seggern, 2014):

$$\mathcal{S}(g_{\text{a}\gamma}) \propto \frac{1}{BL} \left(\frac{DC}{T} \right)^{1/8} \left(\frac{1}{DE \, \beta_{\text{PC}} \, \beta_{\text{RC}} \, \dot{n}_{\text{prod}}} \right)^{1/4} \tag{1.5}$$

Here, T is the duration of measurement, β_{PC} and β_{RC} are the power build-up factors of the cavities, DC is the dark count rate of the detector, and DE is the detector efficiency of the detector. In table 1.1, parameters of ALPS I and ALPS IIc are compared which results in a total sensitivity gain for the ALPS II experiment. The

---

[9]This thesis was written during this phase. At the end of this thesis, ALPS IIa was not finished.
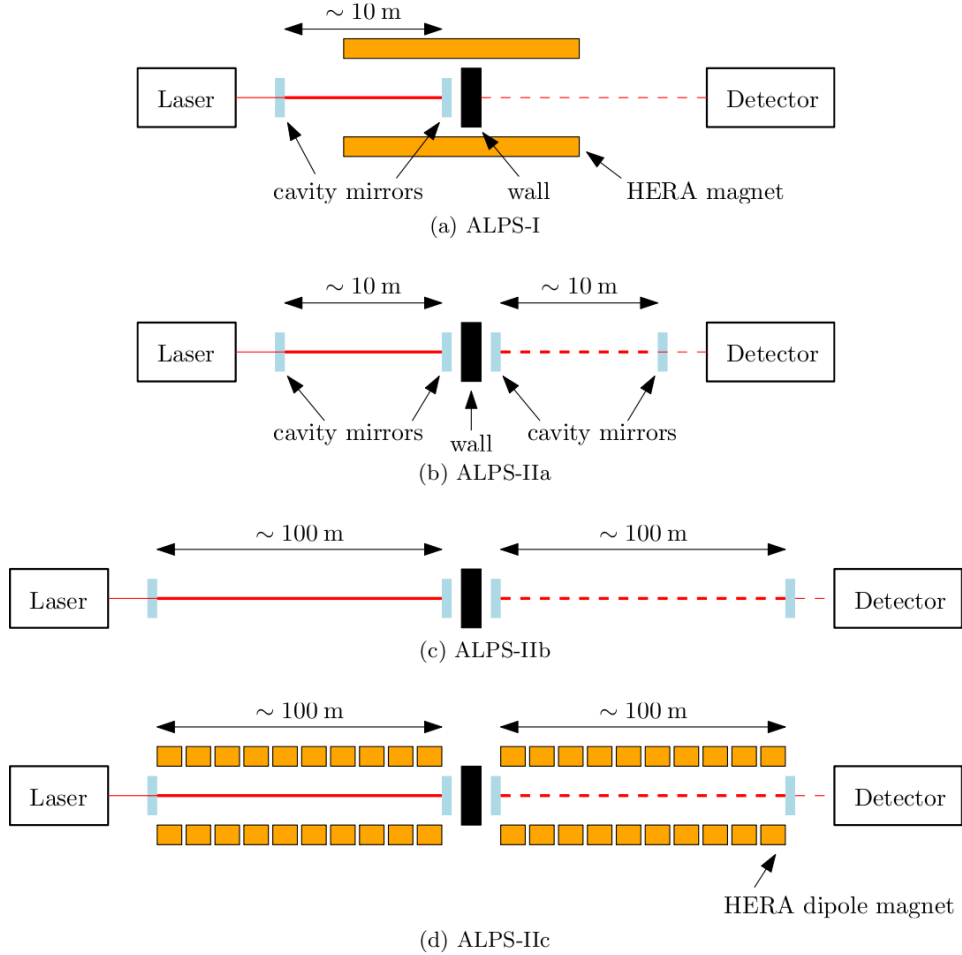
Figure 1.3.: The ALPS experiment: The evolution of the ALPS experiment is illustrated. (a) sketches ALPS I incorporating one HERA dipole as magnetic field and a production cavity in front of the wall. The magnetic length was 2x4 m. ALPS I was stopped in 2010. (b) is the first stage ALPS IIa of the second phase. Two 10 m cavities will be set up, a production cavity and regeneration cavity. First measurements are expected in 2015. (c) sketches ALPS IIb. The optical system is planned to be expanded to 2x100 m. ALPS IIa/b could probe hidden photons. (d) would be the last stage, ALPS IIc. Superconducting HERA dipoles would be installed to probe ALPs. [Taken from Bähre et al. (2013)]

improvements are:

- Magnetic length: Due to the scaling with $g_{a\gamma}$, the best improvement is possible by increasing the magnetic length BL. Thus, 2x10 superconducting HERA dipoles which were used to guide the proton beam in the curve will be straightened. One dipole has been successfully straightened and operated with > 5 T (Trines, 2013).

- Optical system: Resonant cavities enhance the effective power. To improve the PC, the laser wavelength is 1064 nm instead of 532 nm at ALPS I. One crucial technical reason is the stability of the high-efficient end mirrors: At ALPS I, the collaboration struggled with damaged mirrors due to 532 nm light. A 10 m long high power cavity has been established and can be stably locked in the ALPS IIa laboratory (Hodajerdi, 2013). The best sensitivity gain will provide the RC behind the wall. The technical challenge is the tuning of the RC related to the PC. The locking scheme with 532 nm light has been successfully tested in a small test setup (Bähre, 2013).

- Detector system: If WISPs exist, the detected photon rate of the ALPS experiment would be small: The challenge is to detect low rates of single photons – approximately ~1 photon per hour against background. Concerning the sensitivity (eqn. 1.5), detector requirements are a high efficiency and low dark count rate. At ALPS I with 532 nm light, a low-noise Si-CCD camera as detector system has shown a satisfactory performance (Ehret et al., 2009). The detection efficiency is $DE_{\text{CCD, 532 nm}} \approx 90$ % and the detector noise is of the order of 10^{-3} s^{-1} mainly due to the dark current (cf. tab. 1.1). For near-infrared light, the detector efficiency of a Si-CCD would drop down due to the silicon band gap. Concerning ALPS II and an experimental wavelength of 1064 nm, the efficiency was estimated to be below <5 % due to the datasheet values.[10] Thus, the ALPS collaboration had decided to research on a high-efficient superconducting detector for 1064 nm, which is discussed in the next section 1.3.

More details are found in the technical design report of ALPS II (Bähre et al., 2013).

1.3. New detector for ALPS II: transition-edge sensor

As mentioned above, concerning the sensitivity of the ALPS experiment, the main requirements for detecting low-rate of single photons are a high detection efficiency DE and a low dark count rate DC. According to equation 1.5, a new detector type should gain referred to a factor of $(\sqrt{DC}/DE)^{1/4}$. A further requirement to a new detector is a long-term stability due to experimental data taking. In addition,

---

[10]This was recently confirmed: The CCD detection efficiency of 1064 nm light is measured to be ~1.2 % (von Seggern, 2014).

parameter	scaling	ALPS I	ALPS IIc	sens. gain
BL (total)	$g_{a\gamma} \propto (BL)^{-1}$	22 Tm	468 Tm	21
PC built up ($P_{\text{laser,eff.}}$)	$g_{a\gamma} \propto \beta_{\text{PC}}^{-1/4}$	1 (kW)	150 (kW)	3.5
rel. photon flux $\dot{n}_{\text{prod}}$	$g_{a\gamma} \propto \dot{n}_{\text{prod}}^{-1/4}$	1 (532 nm)	2 (1064 nm)	1.2
RC built up β_{RC}	$g_{a\gamma} \propto \beta_{\text{RC}}^{-1/4}$	1	40,000	14
detector eff. DE	$g_{a\gamma} \propto DE^{-1/4}$	0.9	0.75	0.96
detector noise DC	$g_{a\gamma} \propto DC^{1/8}$	$1.8 \cdot 10^{-3}$ s^{-1}	10^{-6} s^{-1}	2.6
combined				3082

Table 1.1.: Sensitivity gain of ALPS II: Setup parameters which are related to the photon-axion coupling constant are compared between ALPS I and ALPS II. Thus, the improvement of the different components can be expressed as a sensitivity gain (see text). The combined improvement lowers the parameter space which is probed by more than three orders of magnitude (fig. 1.2). The latter two parameters are important concerning the detector development (sect. 1.3).

a detector having an energy and a time resolution can be used for advanced data analysis, for example, in order to discriminate background.

A promising field of sensitive detectors is the field of cryogenic particle detectors. During the last years, this field has been developed and applications were the driving force (Previtali, 2006). In general, sensors operated at low temperatures naturally show a low thermal noise. In addition, cryogenic particle detectors take advantage of material properties occurring at low temperature. Cryogenic detection techniques are based on, for example, superconducting tunnel junctions, kinetic inductance detectors, superconducting transition-edge sensors, metallic magnetic calorimeters, or novel techniques like nanowires. Furthermore, low-noise read-out techniques have been developed based on superconducting quantum interference devices (SQUIDs). For example, SQUIDs are realized as current sensors or are used to read-out sensor arrays for imaging by using multiplexing.

Mostly, the basic sensor scheme is a calorimeter[11] in which the energy deposition of a particle causes a heat change of the absorber material. The heat change is measured by a thermistor. One well developed thermistor technique is the transition-edge sensor (TES). A TES is operated on its superconducting phase transition. Here, small changes in temperature result in measurable changes of the TES resistance. Thus, a high detector sensitivity and accuracy can be realized. A prominent example are TES-based X-ray detectors which have reached an energy resolution which is or-

---

[11] Analogously for bolometers which are defined to measure power.

ders of magnitude better than semiconductor-based detectors (McCammon, 2005). During the last years, many detector applications have been realized, for example:

- high resolution X-ray astronomy

- microwave bolometers in astronomy

- ultraviolet/optical/infrared single photon detection in quantum information

- material analysis and nuclear and mass spectroscopy

- neutrino mass experiments

- direct dark matter searches[12]

This indicates how broad the spectrum of development and applications is. The book "Cryogenic particle detection" (Enss, 2005) as well as the agenda of the "Low Temperature Detectors" workshop[13] provide a state-of-art overview.

To detect single near-infrared 1064 nm photons at the ALPS II experiment, there is an overlap with the field of quantum information, which uses TES detectors as single-photon counter at telecommunication wavelengths 1330 and 1550 nm (Dreyling-Eschweiler et al., 2013). The research and development of fiber-coupled high-efficient TES for near-infrared photon detection is actively carried out at NIST (National Institute of Standards and Technology) in the U.S. and AIST (National Institute of Advanced Industrial Science and Technology) in Japan. These TES sensors are realized having a small sensitive volume working as absorber and thermistor simultaneously (see sect. 3.2). Both metrology institutes have reached a near unity quantum efficiency of fiber-coupled TES (Lita et al., 2010; Fukuda et al., 2011), which fits to ALPS detection requirements.[14]

Furthermore, TES detectors intrinsically have no dark current like a CCD and are expected to show a low dark count rate (Miller et al., 2007). However, different groups observed that infrared photons of the black body spectrum of room temperature surfaces can result in a considerable dark count contribution concerning near-infrared signals (see sect. 4.3.1). But a realization with a narrow bandwidth around 1064 nm is estimated to result in a promising low dark count rate of $\sim 10^{-6}$ s^{-1} (Bähre et al., 2013). Considering these numbers, the ALPS II sensitivity would also gain concerning the detector part (tab. 1.1). Thus, the ALPS collaboration had decided to research on a TES-based single photon detector.[15]

However, there were open questions at the beginning of establishing a TES detector system. Firstly, the dark count rate for 1064 nm signal had not been explicitly

---

[12]WIMP searches like CMDS (Agnese et al., 2013), CRESST (Angloher et al., 2012), or EDEL-WEISS (Armengaud et al., 2011).

[13]The recent LTD workshop was held in 2013 (see http://conference.ipac.caltech.edu/ltd-15/).

[14]The Turin group of INRIM (Istituto Nazionale di Fisica Nucleare) in Italy also researches and develops optical-infrared TES devices for single photon detection (Lolli et al., 2012). However, the detection efficiency is below ~10 %.

[15]Within the ALPS collaboration, other single photon detectors were considered (von Seggern, 2013). However, a TES-based detector has shown to be the best alternative to CCDs concerning the low signal flux and the signal wavelength.

	Si-CCD		TES	
$DE_{1064\ nm}$ [%]	- (?)	<5 %	+ (?)	>90 %
energy resolution	-	none	+ (?)	~0.2 eV
$DC_{1064\ nm}$ [s^{-1}]	+	~10^{-3}	?	<10^{-3} (estimated)
time resolution	-	1 h frames	+ (?)	~1 μs
technical status	+	proven to use	?	mK cryogenics
			?	sensor availability

Table 1.2.: Detector parameters and technical status of possible ALPS II detectors in 2011: Advantages (+), disadvantages (-), and open questions (?) of the Si-CCD detector and the TES detector system at the beginning of the ALPS II phase are given. Since the Si-CCD detector was operated in ALPS I, the main advantage of a use at ALPS II is that it is proven to work in an experiment (Ehret et al., 2009). The main disadvantage is the low detection efficiency for the ALPS II wavelength 1064 nm. A TES detector system would have many advantages: high detector efficiency for near-infrared photons and a certain energy and time resolution. However, a dark count rate for 1064 nm signals was not known and technical uncertainties were given.

measured up to this work. Secondly, the ALPS collaboration had no experience with cryogenic mK-environments. Thirdly, the availability of high-efficient TES devices was unclear due to the fabrication by NIST or AIST. As a summary, in table 1.2, this status of a possible TES detector for ALPS is compared to Si-CCD camera system if it would be used at ALPS II. Finally, this leads to the goals and the contents of this thesis:

- Setting up and optimizing a stable mK-environment for cryogenic photon detection (chapter 2).
- Obtaining and characterizing TES sensors and stably operating as a single photon detector (chapter 3).
- Investigating the background and determining a dark count rate related to 1064 nm signals (chapter 4).

2. Milli-kelvin environment for cryogenic photon detection

The goal of this chapter is a comprehensive understanding on how to establish a milli-kelvin (mK) environment. This is the basis to operate highly sensitive superconducting sensors (chap. 3). Within this thesis, an adiabatic demagnetization refrigerator (ADR) has been set up. Furthermore, the ADR cryostat system[1] was characterized and optimized to operate superconducting sensors in the mK-regime. The ADR is one of the essential components of the ALPS TES detector which is used to measure single photons (chap. 4).

Firstly, the working principle of adiabatic demagnetization cooling is briefly described in section 2.1, according to White and Meeson (2002) and Pobell (2007). Secondly, the realization of the ADR cryostat and its individual components are presented in section 2.2. Finally, the ADR cryostat is characterized in section 2.3. The focus is on a stable and reliable operation to use the ADR as the mK-environment for cryogenic photon detection. This forms the first of two technical analyses of this thesis, which is summarized in section 2.4.

---

[1] Simply called ADR cryostat or ADR.

2.1. Theory on adiabatic demagnetization cooling

In 1926/27, Giauque and Debye independently considered an assembly of magnetic dipoles as a thermodynamic system, representing a certain temperature by the order of the dipoles. Furthermore, the energy scale of typical magnetic dipole interactions is in the order of the liquid helium temperature. This allows to establish cooling stages below 4.2 K by utilizing magnetic dipoles. A first thermodynamic cycle by magnetic cooling was realized by groups in Berkeley, Leiden and Oxford in 1933/34.

In section 2.1.1, the working principle including the thermodynamic cycle is explained. In section 2.1.2, a quantitative description is derived to quantify the entropy S and heat capacity C of a spin system: The focus is on electron spin systems of paramagnetic salts. However, this description can be adopted to nuclear spin systems, as shown in standard literature (White and Meeson, 2002; Pobell, 2007, e.g.).

2.1.1. Thermodynamic cycle

To describe the magnetic cooling, an electron spin system of a paramagnetic substance is considered. The electron spin system distributes to energy levels depending on the temperature. By applying an external magnetic field, energy levels can be manipulated and, with them, the electron distribution. This manipulation is the basis of the so-called magnetocaloric effect, which is utilized to establish a cooling cycle.

The thermodynamic cycle of magnetic cooling is illustrated in figure 2.1: (a) in a qualitative way, and (b) in a quantitative way according to equation 2.5. The manipulation of energy levels and the distribution of the electron spin system corresponds to the spin order. Thus, the spin order is sketched by orientated arrows in figure 2.1a, which represent the entropy S of the system. The cycle is split up into the following three steps:

1. **Isothermal magnetization:** The paramagnetic system is coupled to a bath, and is in thermal equilibrium at temperature T. Applying an external magnetic field B, the electron spin system is ordered: Energy levels are spread and electrons occupy lower energy levels. Therefore, the entropy of the system is decreased. At the same time, the magnetization heat is removed by the bath.[2]

2. **Adiabatic demagnetization:** The paramagnetic system is uncoupled from the bath. When ramping the magnetic field to zero, the temperature of the paramagnet decreases. This is caused by the adiabatic process ($S = const.$) due to a maintaining distribution of the electron spins when the energy levels are contracted again. Considering the Boltzmann statistic allows a direct

---

[2]This process can be split up into adiabatic magnetization and isomagnetic enthalpic transfer. Since a system coupled to a bath is considered here, these processes take place simultaneously.

(a) spin and temperature condition

(b) entropy and temperature balance
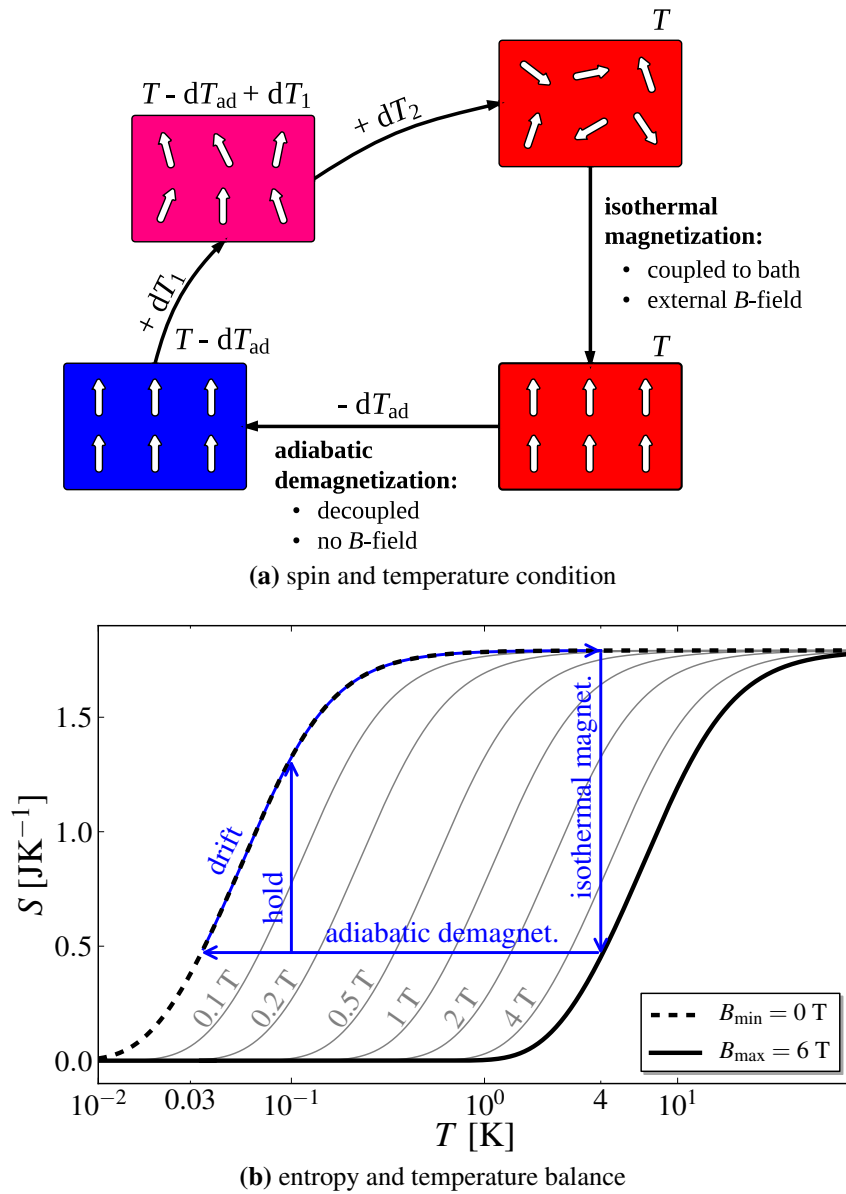
Figure 2.1.: Thermodynamic cycle of magnetic cooling: Both representations illustrate the thermodynamic cycle. Starting in the upper right corner, the cycle splits up into isothermal magnetization, adiabatic demagnetization and entropic transfer (see text for details).
(a) illustrates the cycle by depicting the order of spins (arrows) of a system like a paramagnet. As an important quantity, the temperature of the system is given.
(b) is a plot of the quantitative description of the cycle. Equation 2.5 gives the entropy-temperature dependence of an ideal spin system, here with $nR = 1$ J/K. The total spin is exemplarily chosen by $J = 5/2$. In addition, magnetic field values, B, are matched to the magnet of the ADR system (sect. 2.2.3). Isomagnetic curves are depicted in light-grey.

15

insight into this process: Since the occupation probability, $P \sim \exp(B/T)$, stays constant, B/T stays constant or the temperature is proportional to the magnetic field, $T \propto B$.

3. **(Isomagnetic) entropic transfer:** The cold spin system can now refrigerate other subsystems. Due to a non-perfect isolation, the system begins to heat corresponding to a disorder of the spins. This entropic transfer can take place either isomagnetically as drifting or isothermally by regulating the external field (sect. 2.3.4).

Finally, it should be noted that this cooling cycle corresponds to the Carnot cooling cycle of an ideal gas. The volume change of an ideal gas corresponds to an external magnetic field change of a dipole system. Thus, in both cases, manipulating energy levels and their relative occupation define the entropy and the temperature.

2.1.2. Quantitative description

Considering an ideal spin system allows to derive the entropy which depends on two variables, the external magnetic field B and the temperature T. In addition, the heat capacity of a paramagnetic system is derived in the following. It should be noted that these quantities describe only the spin system influenced by an external magnetic field. However, this allows to quantify the total heat capacity of paramagnetic salts, which were used in the ADR setup (sect. 2.2.3).

The **electron spin energy levels** of a single paramagnetic ion, due to an external magnetic field B, are given by:

$$\epsilon_m = m\,\mu_{\mathrm{B}} g_e\, B \tag{2.1}$$

where μ_{B} is the Bohr magneton, and g_e the electron g-factor.[3] m is the magnetic quantum number, which has a half-integer value between $-J$ to $+J$, where J is the total angular momentum of a paramagnetic ion. Thus, there are $2J+1$ possible energy levels for electrons.

The total electron distribution in a paramagnet is given by the partition function Z. Using equation 2.1 it is:

$$Z = \left[\sum_{m=-J}^{m=J} \exp\left(-\frac{\epsilon_m}{k_{\mathrm{B}}T}\right)\right]^{nN_{\mathrm{A}}} = \left[\sum_{m=-J}^{m=J} \exp\left(-mx\right)\right]^{nN_{\mathrm{A}}} \tag{2.2}$$

where n is the number of moles of paramagnetic ions, N_{A} the Avogadro constant, and k_{B} the Boltzmann constant. Furthermore, it is substituted:

$$x = \frac{\mu_{\mathrm{B}} g_e B}{k_{\mathrm{B}} T} \tag{2.3}$$

---

[3]Constants are given in appendix F.2.

The entropy is derived from the free energy by considering a constant volume and a magnetic field. Thus, it is:

$$S = k_\text{B} \frac{\partial (T \ln Z)}{\partial T} \tag{2.4}$$

Calculating equation 2.4 with equation 2.2 results in the **entropy** S per mole n in units of the gas constant R:

$$\frac{S}{nR} = \frac{x}{2} \left[\coth\left(\frac{x}{2}\right) - (2J + 1) \coth\left(\frac{(2J + 1)\, x}{2}\right) \right] + \ln \left[\frac{\sinh\left((2J + 1)\, x/2\right)}{\sinh\left(x/2\right)} \right] \tag{2.5}$$

This equation describes the entropy of a spin system depending on $x \propto B/T$ (eqn. 2.3). Therefore, the temperature T is proportional to the magnetic field B. To describe a real paramagnetic system, the magnetic field is an effective field, which is given by a constant internal magnetic field B_int and the applied field B_app:

$$B = \sqrt{B_\text{int}^2 + B_\text{app}^2} \tag{2.6}$$

B_int limits the minimal temperature. In figure 2.1b, equation 2.5 is plotted for $J = 5/2$ and $nR = 1$ J/K. The applied magnetic field B_app is varied from 0 to 6 T, and it is assumed $B_\text{int} = 0.05$ T.

The **heat capacity** is derived from the entropy. The heat capacity C_B for a constant magnetic field is given by:

$$C_B = T \frac{\partial S}{\partial T} \tag{2.7}$$

Using equation 2.5, this results in:

$$\frac{C_B}{nR} = \left(\frac{x}{2} \frac{1}{\sinh\left(x/2\right)} \right)^2 - \left(\frac{x}{2} \frac{(2J + 1)}{\sinh\left((2J + 1)x/2\right)} \right)^2 \tag{2.8}$$

It should be noted that the mole number n corresponds to $nR = m/MZ$, where m is the mass, M is the molecular mass of the paramagnetic salt, and Z is the number of atoms having magnetic properties in the chemical compound.

To obtain the total heat capacity of a paramagnetic salt, the phonon contribution C_deb has to be added:[4]

$$C = C_B + C_\text{deb} \tag{2.9}$$

---

[4]Analogously, for the total entropy. This, however, is not needed in the following.

The phonon contribution is given by the Debye model:

$$C_{\text{deb}} = m/M \cdot f_{\text{deb}} \cdot T^3 \tag{2.10}$$

where $f_{\text{deb}} = \frac{12\pi^4 k_{\text{B}}^4}{5\hbar^3 \omega_{\text{deb}}^3}$ is a factor from the Debye model including the Debye frequency ω_{deb}. Equation 2.9 is a quantitative description for paramagnetic salts at low temperatures including the influence of external magnetic fields. Using this formulation, the heat capacity of each salt pill of the ADR system can be estimated (fig. 2.5).

2.2. Realization of an ADR cryostat

To reach experimental environments below 100 mK, today, basically, two types of cryostats are common: dilution refrigerators (DR) and adiabatic demagnetization refrigerators (ADR). DR cryostats utilize the dilution principle of a ^{3}He/^{4}He-mixture (White and Meeson, 2002, e.g.). During this thesis, work has been carried out in DR systems during measurements at PTB-Berlin (sect. 3.2 and 3.2.3.1) and in Camerino, Italy (sect. 3.2.3.3). With the work of this thesis, an ADR cryostat system was set up in cooperation with Entropy GmbH.[5] Therefore, the focus is on this ADR cryostat system to establish mK-environments for photon detection.

The astroparticle group of the University of Hamburg, as ALPS member, purchased the ADR cryostat system in September 2011 (Entropy, 2011).[6] The ALPS collaboration decided on an ADR system due to two arguments:

- An ADR system is a cryogen-free[7], compact, stand-alone mK-refrigerator, only requiring an external cold water and power supply.
- ADR systems are by a factor of two cheaper than DR systems, which need ^{3}He.

The main disadvantage of an ADR is the limited operation time at mK-temperatures due to the thermodynamic cycle (sect. 2.1.1). However, 48 h holding times at mK-temperatures and 2 h recharge times are realized and are suitable for superconducting sensor applications. The specifications of the ADR system without experimental installations are (Entropy, 2011):

- cool-down time from 300 K to 100 mK: < 20 h
- lowest temperature: < 30 mK
- hold time at 100 mK: > 48 h
- temperature stability at 100 mK: < 25 μK (rms)
- experimental space: dia. 230 mm x 300 mm

Before testing these specifications and describing the performance of the ADR system (sect. 2.3), the ADR system including different components is briefly presented in this section:

- Precooling system (sect. 2.2.1)
- Dewar and cooling stages (sect. 2.2.2)
- Adiabatic demagnetization system, including a superconducting magnet, salt-pills unit, and a heat switch (sect. 2.2.3)

---

[5]Status in 2013, two companies only offer ADR systems: the US company HPD, www.hpd-online.com, and the German company Entropy GmbH (Entropy, 2013). Entropy GmbH was founded in 2010 and has experience to run TES/SQUID sensors in mK-environment. Furthermore, Entropy GmbH cooperates with Magnicon GmbH and PTB-Berlin on issues of low-temperature detectors (Phelan, 2012).

[6]The ADR has the product name "PRO-A-0278-00, ADR Kryostat M-Serie, Hamburg".

[7]Cryogen-free means no liquid nitrogen or helium is required for precooling.

- Operating and monitoring infrastructure, including thermometry, pressure measurement, magnet current supply, and heat switch control (sect. 2.2.4)

The operation of the ADR system is explained in the Entropy (2012) manual. Furthermore, the installation and the operation concerning the ALPS TES detector is found in appendix D.1 and D.2.

2.2.1. Precooling system

The ADR system is equipped with a pulse tube based cryocooler from the company SHI Cryogenics Group (2013). Basically, the cryocooler incorporates

- a two stage pulse tube cooler,
- a closed ^{4}He gas cycle, and
- a water cooled compressor unit.

These components set up a continuous cooling cycle (see fig. D.2 in the appendix).

The pulse tube cooler is connected to the compressor unit by helium lines. The compressor unit provides the helium compression of supplied helium gas. The compression heat is cooled by an integrated water chiller. A rotary valve, connected to the compressor and placed next to the pulse tube unit, steers the cooling cycle within the pulse tube cooler. The cycle alternates with 1.3 Hz.

The two stage pulse tube cooler is implemented in the ADR dewar (sect. 2.2.2). The first stage of the pulse tube unit has a cooling power of 25 W at 65 K, the second of 0.4 W at 4.2 K (SHI, 2011). The second stage is the basis for the adiabatic demagnetization cooling (sect. 2.2.3). Vacuum insulation is provided by a vacuum pump, which is active during cooling down (app. D.2.1). The infrastructure and the installation is described in more detail in appendix D.1.1.1.

2.2.2. Dewar and cooling stages

The most important parts of the ADR cryostat system are the cooling stages integrated in a vacuum dewar. The cooling stages are constructed in a top-down principle where mK-temperatures are reached at the innermost stage. Therefore, this construction is sometimes simply called ADR cryostat or ADR (fig. 2.2).

The vacuum dewar incorporates a cylindrical can and a top flange to set up a low pressure environment. The top flange integrates several vacuum feedthroughs: the cold head unit of the pulse tube cooler, electrical feedthroughs for thermometry, magnet current, and heat switch (sect. 2.2.4), an electrical feedthrough for the SQUID cryocable (app. C.3), and a port for an optical fiber feedthrough (app. C.4). Furthermore, an evacuation port to establish the vacuum by connecting a suitable pump is integrated as well as a security valve in case of overpressure during warm-up. The dewar is mounted in a moveable trolley (fig. 2.2). Within the trolley, the

(a) operational closed ADR

(b) opened ADR
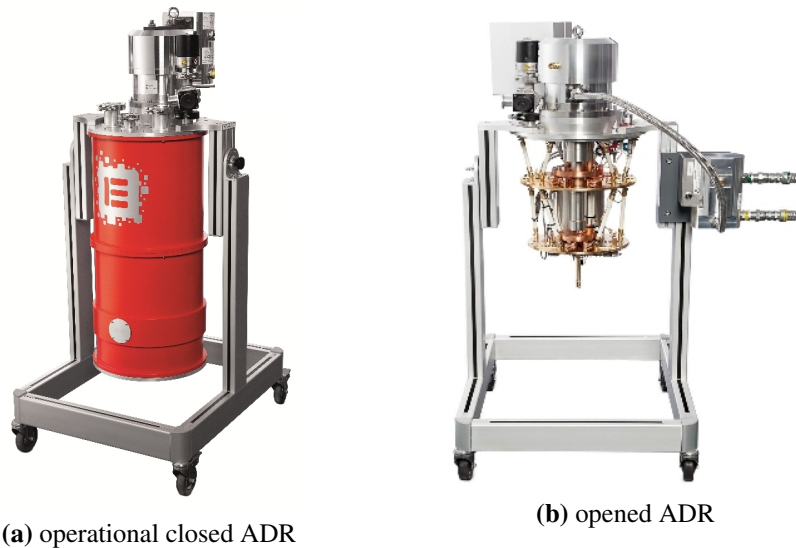
Figure 2.2.: ADR cryostat in a moveable trolley: (a) The ADR cryostat is closed with all shields. (b) The ADR cryostat is depicted without shields. Right, the rotary valve is connected to the pulse tube unit and to the supply and return line of the helium cycle. Both pictures show the ADR in operating position. [Taken from Entropy (2013)]

dewar can be turned by 180°. This allows to set the ADR in a mounting position in order to remove the shields and to modify the experimental setup.

In figure 2.3, the inside of the ADR with temperature stages is depicted. The ADR stages from outside to inside are:

1. The **300K-stage** incorporates the top flange and the red vacuum can/shield in order to set up the vacuum environment. The temperature is assumed to be at ambient temperature.

2. The **70K-stage** incorporates a copper plate and a aluminum shield. This is cooled by the first stage of the pulse tube cooler, which is attached to the copper plate. To this, the aluminum shield is mounted. The 70K-stage is named after the liquid nitrogen temperature. In operation, temperatures below 50 K are reached (sect. 2.3.2).

3. The **4K-stage** incorporates a copper plate and a copper shield. This is cooled by the second stage of the pulse tube cooler, which is attached to the copper plate. To this, the copper shield is mounted. The 4K-stage is named after the liquid helium temperature. In operation, temperatures below 3 K are reached (sect. 2.3.2).

4. The **GGG-stage** is a copper plate, which is connected to the outer pill of the salt pills unit. In operation, temperatures below 500 mK are reached. The name and details are explained in section 2.2.3.

5. The **FAA-stage** is a copper rod, the cold finger, which is connected to the
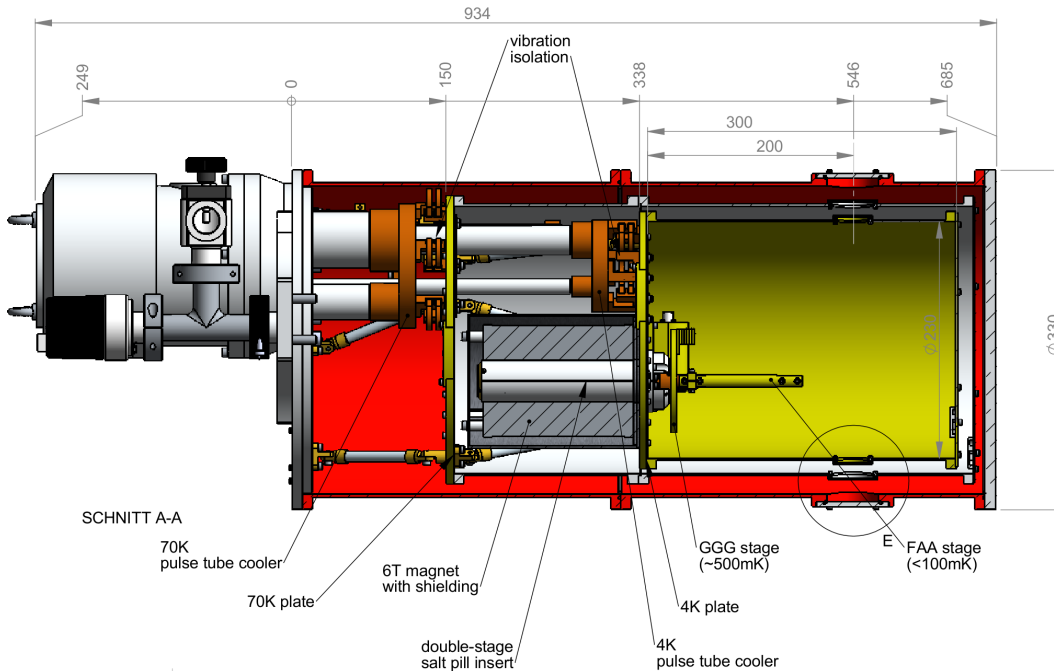
Figure 2.3.: Sketch of cross section of the ADR dewar: The inner structure of the ADR with temperature stages is depicted: The top flange (left) with red shield is called 300K-stage due to room temperature. Inside are the 70K-stage (light grey), the 4K-stage (light green), the GGG stage (~500 mK) and the FAA-stage (<100 mK). [Taken from Entropy GmbH]

> inner pill of the salt pills unit. In operation, temperatures below 30 mK are
> reached. The name and details are explained in section 2.2.3. To the cold
> finger, superconducting sensors are mounted (app. D.1.2.1).

The top flange of the 300K-stage and the copper plates of the 70K- and 4K-stages are connected by suspensions made of glass-fibre reinforced plastic. This provides a sufficient mechanical stability as well as a low thermal flow. Furthermore, the thermal contact between the pulse tube cooler and the corresponding stage is realized by copper wires to reduce mechanical vibrations.

2.2.3. Adiabatic demagnetization system

The 4K-stage is the heat sink (cold bath) for the adiabatic demagnetization cooling. The following components are installed on the 4K-stage (fig. 2.4), which set up the adiabatic demagnetization system:

- **Superconducting magnet:** On the bottom side, a superconducting solenoidal 6 Tesla magnet is mounted. The magnet is surrounded by a passive magnetic shield made of Cryoperm[8] in order to screen the experimental room from the

---

[8]Cryoperm is an alloy consisting mainly of nickel and iron.

22
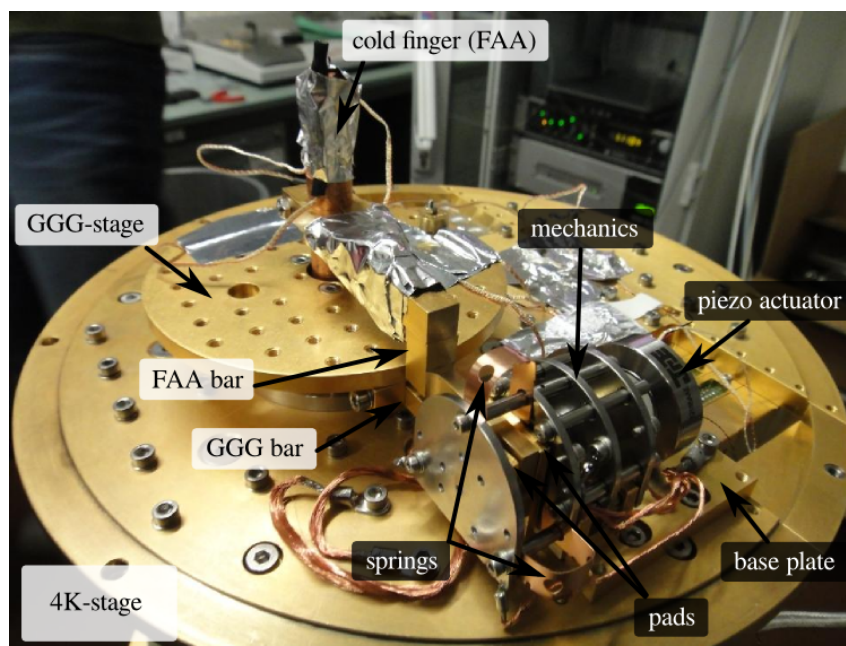
Figure 2.4.: 4K-stage with adiabatic demagnetization system: The experimental side of the 4K-stage is depicted. The heat switch unit with its components (terms in dark boxes) is located in front. The GGG-stage and FAA-stage (cold finger) are connected to the pills unit. The pills unit surrounded by the superconducting magnet is attached below the 4K-stage in this view (see fig. 2.3).

stray field. The solenoid surrounds the pills unit to magnetize the dipoles of the salt pills.

- **Salt pills unit:** The salt pills unit consists of two stages made of containers filled with a salt. Each salt acts as the paramagnetic spin system (sect. 2.1):

    - **GGG-pill:** The salt of the outer pill is ~80 g of Gadolinium Gallium Garnet ($Gd_3Ga_5O_{12}$), or in short GGG. The GGG-pill surrounds the inner pill in order to screen it from thermal radiation of the 4K-stage. To the GGG-pill, a copper plate (GGG-stage) is mounted which provides thermal anchoring of cables guiding to the FAA-stage.

    - **FAA-pill:** The inner pill is filled with ~95±5 g of Ferric Ammonium Alum ($Fe_2(NH_4)_2(SO_4)_4 24H_2O$), or in short FAA. After a successful thermodynamic cycle, this stage reaches temperatures below <100 mK in order to operate superconducting sensors. To the FAA-pill, a cold finger (FAA-stage) is assembled where sensor modules can be attached.

Each salt container is mounted with six pins made of Vespel, three at the top and three at the bottom. Vespel shows a sufficient mechanical stability from 300 K to mK-temperatures and a sufficient thermal isolation at low tempera-

(a) heat capacity of FAA

(b) heat capacity of GGG
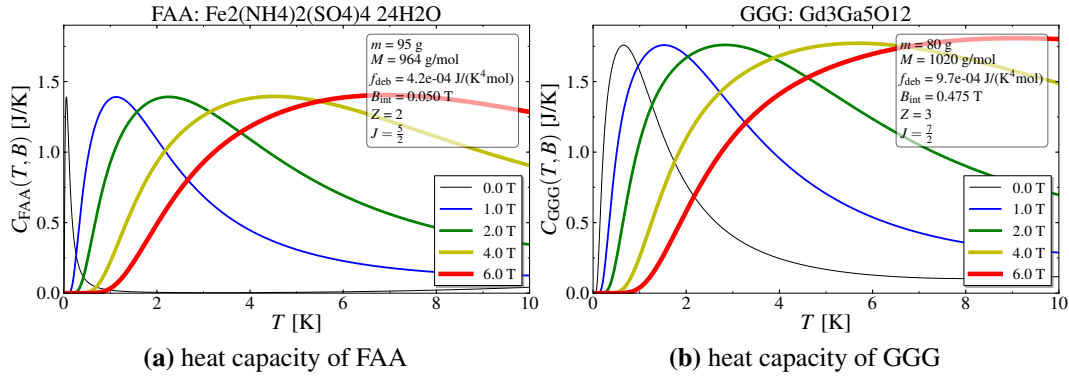
Figure 2.5.: Heat capacity of FAA and GGG: Equation 2.9 allows to calculate the heat capacity of the salt pills. For each pill, corresponding parameters are given in the upper right box in each plot.

tures. The heat capacity of each pill is calculated with formula 2.9. The low temperature dependence for each pill is shown for different external magnetic fields in figure 2.5.

- **Heat switch unit:** Both pills can be thermally coupled to and decoupled from the 4K-stage by a heat switch unit. Therefore, at each pill stage, a copper bar is mounted, which leads to the heat switch unit placed at the 4K-stage (fig. 2.4). The heat switch unit consists of a piezo-ceramic actuator,[9] which moves two copper pads forward and backward.[10] The copper pads surround the copper bars of the pills. Thus, the pads can clamp the bars from both sides symmetrically in order to establish a thermal contact between the pills and the 4K-stage. The actuator and the mechanism of the clamps have play in all directions and are self-aligning (cf. app. D.1.1.3), thus preventing asymmetrical forces on the pill support structures.

2.2.4. Operating and monitoring infrastructure

Apart from the precooling system[11], every component of the ADR system can be operated and monitored by a computer with the "Adiabatic Control" software. Each component inside the ADR[12] is operated by its corresponding electronics, which is

---

[9]The piezo-ceramic actuator is from the Janssen Precision Engineering (2013) company. The model PK3001 is developed for working in vacuum, magnetic and cryogenic environments. It has a maximal axial load capacity of 50 N. The step size differs from 1 to 25 nm depending on temperature. The maximal travel range is 12 mm.

[10]Opening the heat switch by driving backward is supported by springs.

[11]The electronically separated precooling system is switched on or off at the beginning or at the end of a cool-down.

[12]It should be noted that all cables inside the ADR dewar, connecting the components to the electrical feedthroughs at the top flange, are thermally coupled to each cooling stage they pass. This

connected to the computer by a suitable interface. The computer and electronics are integrated in the ADR rack (fig. 3.12).

The performance of each component is briefly explained:

- **Pressure measurement:** The pressure inside the ADR dewar is measured by a vacuum gauge from the Leybold company. The gauge is placed at the top flange. The pressure indicates the quality of the thermal insulation ("leak tightness"). Furthermore, it indicates the starting point of a cool-down at a sufficiently low pressure (app. D.2.1).

- **Thermometry and heat switch control:** On each cooling stage, a resistance thermometer is mounted to monitor temperatures (Entropy, 2012):

    - **70K-thermometer** on the 70K-stage measuring T_{70K}
    - **4K-thermometer** on the 4K-stage measuring T_{4K}
    - **GGG-thermometer** on the GGG-stage measuring T_{GGG}
    - **FAA-thermometer** on the FAA-stage measuring T_{FAA}

  A measuring bridge from the Picowatt company measures the resistance of each thermometer. The measurement principle is the four-terminal sensing; thus, each channel incorporates 4 wires. The measured resistance corresponds to a value in temperature.

  Additionally, two channels of the bridge are used for heat switch control:

    - **GGG touch** measures R_{TGGG} between 4K- and GGG-stage.
    - **FAA touch** measures R_{TFAA} between 4K- and FAA-stage.

  The electrical resistance indicates whether the pads of the heat switch touch the bars connected to the pills or not (sect. 2.2.3). Therefore, these channels are called touch channels. This allows to define conditions of a closed or opened heat switch. A closed heat switch results in a low ohmic resistance, a opened heat switch results in a high ohmic resistance (app. D.2.2).

- **Magnet current supply:** An electronics from the Agilent company provides the current supply for the superconducting magnet. The current, corresponding to a 6 T field, is assumed to be 40 A. The electronics allows to ramp current in and out the magnet coil with a constant rate in order to prohibit quenching. Furthermore, one interface of the electronics is manipulated for a fine regulation of the magnet current. The current digitization step is adjusted to 0.03 mA. This allows to regulate the magnetic field in order to hold a mK-temperature at the FAA-stage. The regulation is established by the software utilizing the FAA temperature as feedback. Results are found in section 2.3.4.4.

---

diminishes the heat flow from the outer warm to the inner cold environment.

- **Heat switch driving:** The heat switch controller from Janssen Precision Engineering (2013) company allows to drive the piezo actuator of the heat switch unit. The actuator can be moved forward (+) in order to close and backward (-) in order to open in different step speeds. In order to move the actuator manually, an additional "Piezo Knob" software is used. Steps between 1,000 (1 k) and 50,000 (50 k) can be moved. Since the step size varies with the temperature and the mechanical condition of the heat switch, the touch measurements provide a feedback (see above), whether the heat switch moves or not.

The "Adiabatic Control" software allows to operate all devices manually. Automation processes are possible (sect. 2.3.3.3) as well as an external access via TCP/IP. Furthermore, values of temperatures, pressure, and magnet current and voltage are logged during operation. An additional program, "Entropy Log File Viewer", allows to display the logfiles, which helps to monitor the system.

A detailed description of the ADR system is found in the ADR manual (Entropy, 2012). Furthermore, the operation concerning the ALPS TES detector is found in the appendix D.2.

2.3. Characterization of the ADR cryostat system

In this section, the ADR cryostat system (sect. 2.2) is characterized. The system is in operation since July 2012. At first, it was operated at PTB-Berlin for first installation and factory tests. In November 2012, the system was moved to DESY, Hamburg, and operated in the ALPS IIa laboratory (sect. 3.3). Since that time, it is optimized to become the mK-environment of the ALPS TES detector (sect. 3.4).

In the following, the most important results from the characterization and the operation during this thesis are described:

- The different operational phases and their corresponding temperature evolutions of a successful ADR run are explained in section 2.3.1. An overview of the ADR working principle is given and important figure of merits are defined. Details are described in the following sections.

- The performance of precooling the ADR is summarized in section 2.3.2.

- The performance of the adiabatic demagnetization system to charge the pills is described in section 2.3.3.

- Finally, the performance of the charged pills is examined which establish the mK-environment in section 2.3.4.

As a result of this technical analysis, the installation and the operation is explained in appendix D.1 and D.2.

2.3.1. Operational phases of an ADR run

In this section, a successful ADR run is described.[13] A complete single run incorporates four main phases of temperature evolution. Main phases are grouped due to different cooling and warming mechanisms. Each phase has a characteristic thermalization time. Subsequently, one phase is considered in more detail: The recharge phase is sub-divided in five sub-phases due to different operations of the adiabatic demagnetization system (sect. 2.2.3). Since the thermalization and operation times depend on installations within the ADR, the setup of the ALPS TES detector is considered.[14]

The four main phases of an ADR run are:

1. **Cool-down: Cooling down from 300 K to base temperature T_{4K}.** A cooldown starts by switching on the precooling system and pumping a vacuum at the same time (sect. 2.2.1). As figure of merit, the cool-down time t_{CD} is defined as the duration from passing 288 K at the 77K-stage to passing 4 K

---

[13]An ADR run is sometimes also called cool-down (CD). Furthermore, a successful run includes a normal performance of the heat switch. Impacts of the heat switch are discussed in section 2.3.2 and 2.3.3.

[14]This setup includes the NIST module and a copper shield attached to the cold finger of the ADR (see sect. 3.4). Influences due to to different setups are compared in section 2.3.4.

(a) Cooling to 4 K

(b) Recharge and cooling to mK-temperature
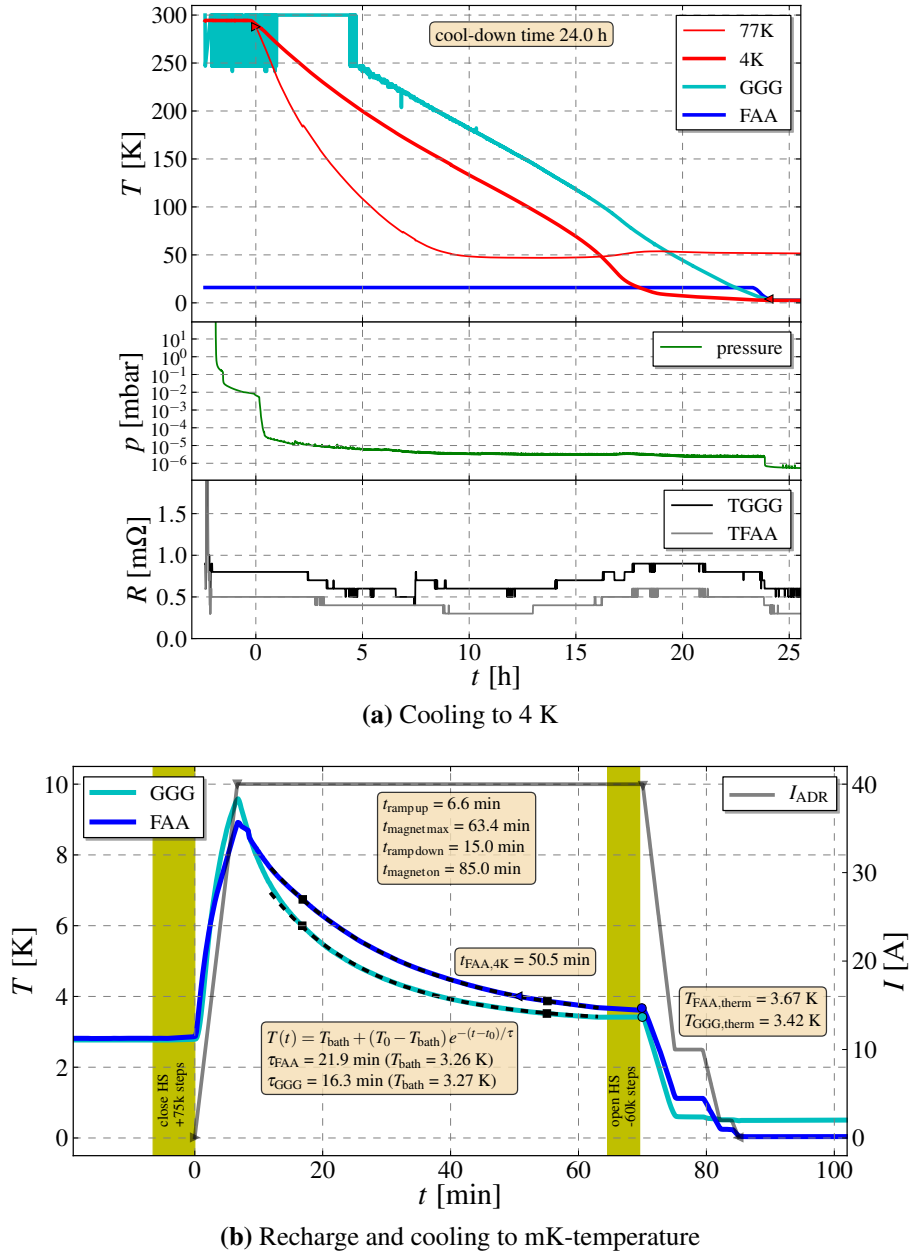
Figure 2.6.: Examples of cooling down: cool-down and recharge.
(a) shows a typical cool-down. The GGG-thermometer starts to work below 250 K, the FAA-thermometer is calibrated only below 16 K. The GGG-pill lags behind the 4K-stage with ~50 K before the 4K-stage reaches its minimal temperature, the bath temperature for adiabatic demagnetization cooling. Furthermore, the pressure evolution (middle plot) and the touch measurements during a cool-down (lower plot) are depicted (sect. 2.3.3.1).
(b) shows a typical and successful recharge: closing the heat switch (yellowish area), ramping up the magnet (gray line), exponential thermalization (GGG-temperature in cyan, FAA-temperature in blue), opening the heat switch (second yellowish area), ramping down the magnet in several steps (gray line). By ramping down, the FAA-stage reaches the operational mK-temperature. Analysis parameters are found in boxes. A detailed description is found in the text.

(a) drift

(b) hold

(c) Warming to 300 K
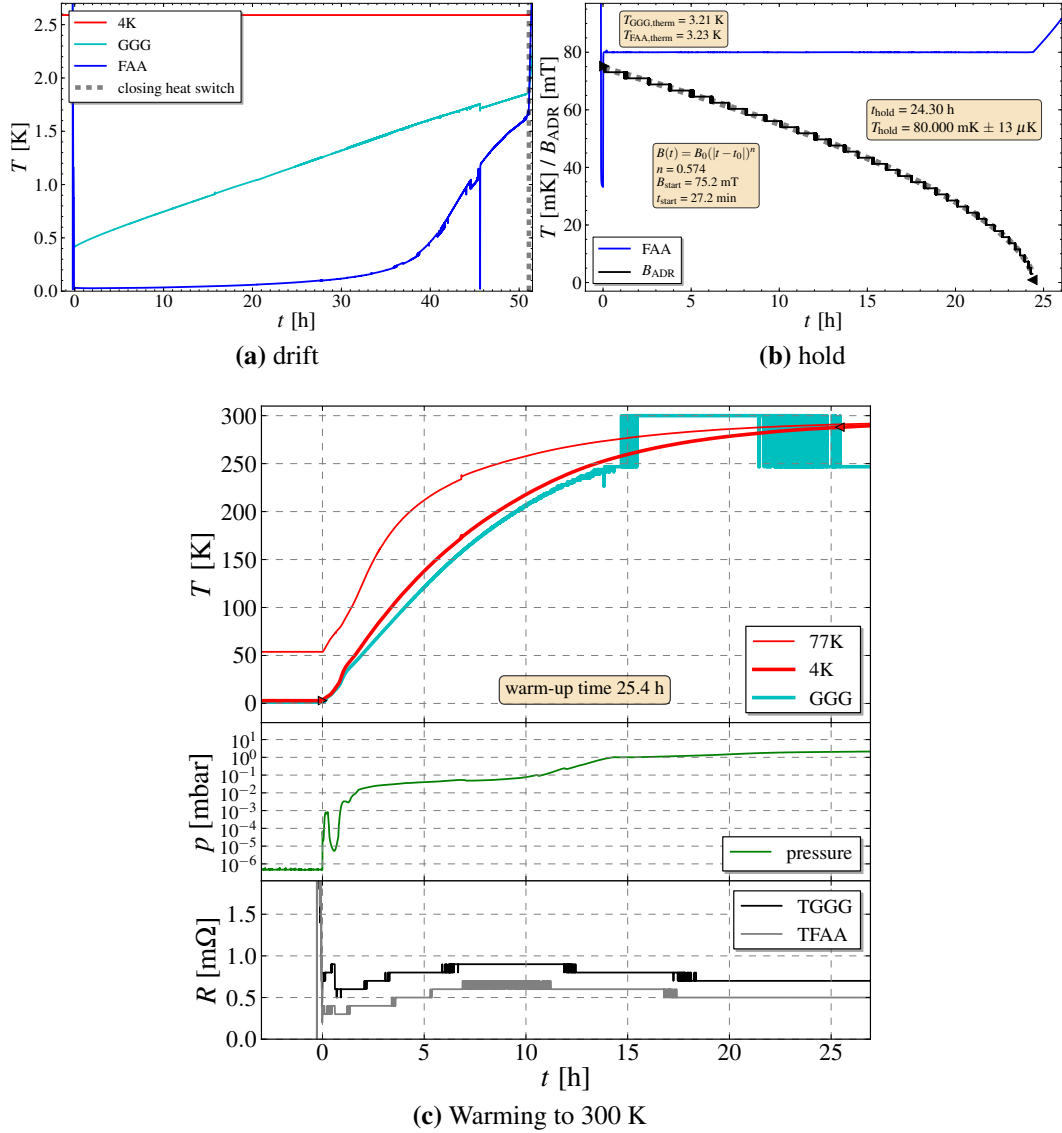
Figure 2.7.: Examples of warming up: drifting pills and warm-up of ADR.
(a) and (b) show two possible temperature evolutions after a recharge. (a) shows a slow temperature drift of uncoupled pills due to external power loads (sect. 2.3.4.1).
(b) shows a 80 mK regulation of the FAA-stage, a hold. Regulating the magnetic field (measured in black and fit in dashed grey) compensates the energy loss due to external power loads (sect. 2.3.4.1). When reaching 0 T, the FAA pill begins to drift.
(c) shows a typical warm-up. The warm-up starts by switching off the precooling system. Additionally, a small amount of exchanging gas is let into the ADR dewar (app. D.2.4).

measured by the FAA thermometer.[15] A sample of successful cool-downs results in

$$t_{\text{CD}} = 24.8 \pm 1.3 \text{ h.}$$

After that time, the ADR system is thermalized and reaches the following status:

- 70K-stage at $T_{70K} \simeq 49.5$ K
- 4K-stage including pills at $T_{4K} \simeq 2.5$ K
- pressure at $p \simeq 3 \cdot 10^{-7}$ mbar

Figure 2.6a illustrates the evolution of an exemplary cool-down. Cool-downs of different runs are compared in section 2.3.2.

2. **Recharge: Cooling down from T_{4K} to experimental temperature T_{FAA}.** After reaching the base temperature T_{4K} and thermalizing the magnet and the pills unit, the adiabatic cooling cycle can be started. This phase includes the first two stages of the thermodynamic cycle (sect. 2.1.1): the isothermal magnetization and the adiabatic demagnetization. Figuratively, the pills are charged with energy to establish low temperatures. This charging process can be repeated. Therefore, this phase is called a recharge.

   A typical recharge is depicted in figure 2.6b. A recharge splits up in five operational phases which are described below in detail in bullets a) to e). Thus, the total recharge time depends on many operational factors. Furthermore, recharge times vary due to the thermalization time which results from the heat switch performance (sect. 2.3.3). Considering a thermalization till 4 K of the FAA-stage, typical recharge times are

   $$t_{\text{recharge, FAA at 4 K}} \simeq 90 \pm 7 \text{ min.} \qquad (2.11)$$

   The standard deviation results from a variation in thermalization due to the heat switch (sect. 2.3.3.2). After a recharge, each pill reaches a minimal temperature. Typical values are:

   - $T_{\text{GGG}} \simeq 480\text{-}540$ mK
   - $T_{\text{FAA}} \simeq 30\text{-}32$ mK

   The minimal temperature depends on different factors which are discussed in section 2.3.4.2.

3. **Drift and hold: Warming up to T_{4K}.** After a recharge, the cooling energy of the pills is dissipated due to external loads (sect. 2.3.4.2 and 2.3.4.3). There-

---

[15]288 K corresponds to 15 °C. The ALPS IIa laboratory is climatized to 22 °C. The 70K-stage passes 288 K in 10-15 minutes after switching on the compressor. This time and the time of about 60-90 min including the vacuum pumping and a tentative leak test have to be added to obtain the real cool-down duration.

fore, the FAA pill temperature drifts to higher temperature. A so-called drift is depicted in figure 2.7a. Applying and readjusting a proper magnetic field by the ADR magnet allows to regulate the FAA-temperature. This temperature can be held as long as the charged energy of the pill is sufficient for cooling. A so-called hold is depicted in figure 2.7b. A drift or a hold are the entropic transfer of the thermodynamic cycle (sect. 2.1.1).

The drift time t_{drift} is defined as the time till the FAA pill exceeds a defined temperature after a recharge. The hold time t_{hold} is defined as the period in which a magnetic field can hold a temperature. Typical values for a temperature of 80 mK are:

$$t_{\text{drift, 80 mK}} \simeq 18 \text{ h}$$
$$t_{\text{hold, 80 mK}} \simeq 25 \text{ h}$$

These times strongly depend on different factors which are discussed in section 2.3.4. A hold or a drift can be finished by closing the heat switch to start a new recharge (see bullet 2.).

4. **Warm-up: Warming up to 300 K.** Stopping the precooling system starts warming up the cryostat to ambient temperature again. The warm-up time of the ADR cryostat t_{WU} is defined as the duration from 4 K to 288 K measured by the 4K-thermometer. Typical times are

$$t_{\text{WU}} \sim 19 - 26 \text{ h},$$

which strongly depends on the amount of exchanging gas introducing into the ADR dewar (app. D.2.4).

In the following, the **operational phases of a recharge** are explained (bullet 2. and fig. 2.6b). Since the recharge time is a dead time for operating sensors in a mK-environment, the focus is on times needed for the different operations. The standard parameters of moving the heat switch and ramping the magnet current are found in the appendix D.2.2. A recharge is sub-divided into five phases:

a) **Closing the heat switch** provides the thermal contact of the pills to the 4K-stage working as bath. The time is given by the needed steps to close $\#_{\text{close HS}}$, divided by the driving frequency f_{HS}:

$$t_{\text{close HS}} = \#_{\text{close HS}}/f_{\text{HS}} \simeq 6.3 \text{ min}$$

The time increases if the heat switch is moved manually or more steps are needed (sect. 2.3.3.1).

b) **Ramping up the magnet** provides the magnetic field to order the dipoles in the salt pills. The time is given by the current difference ΔI_{ADR} divided by the

ramping rate $\dot{I}_{ADR}$:

$$t_{\text{ramp up}} = \Delta I_{ADR}/\dot{I}_{ADR} \simeq 6.7 \text{ min}$$

At $I_{ADR} = 40$ A, the magnetic field inside the solenoid is assumed to correspond to $B_{ADR} = 6$ T. The pills heat up to ~10 K due to the adiabatic magnetization heating and eddy current heating; however, at the same time the pills already thermalize due to the contact to the bath (sect. 2.3.3.2).

c) **Thermalization of the pills:** After reaching 6 T, the pills cool down approximately exponentially toward the bath temperature. The thermalization time is from the moment of a closed heat switch till the moment of an opened heat switch defining the thermalization temperatures $T_{\text{GGG, therm}}$ and $T_{\text{FAA, therm}}$ (sect. 2.3.3.2). As a comparable figure of merit between recharges, the thermalization time is additionally defined as the time from the start of ramping up till $T_{\text{FAA, therm}} = 4$ K $\equiv t_{\text{thermalize, FAA 4 K}}$. This means $t_{\text{thermalize, FAA 4 K}}$ includes $t_{\text{ramp up}}$. A representative sample of recharges results in:

$$t_{\text{thermalize, FAA 4 K}} \simeq 75.0 \pm 7.0 \text{ min}$$

The uncertainty is caused by unsystematic variations in the performance of the heat switch (sect. 2.3.3.2). Furthermore, the thermalization temperatures strongly affect the heat capacity of the pills, and thus, the available energy for cooling (fig. 2.1b and sect. 2.3.4.2).

d) **Opening the heat switch** uncouples the pills from the 4K-stage. As before in a), the time is given by

$$t_{\text{open HS}} = \#_{\text{open HS}}/f_{HS} \simeq 5.0 \text{ min}.$$

The shorter time compared to the closing time is due to mechanical springs of the heat switch design (sect. 2.3.3.1). Furthermore, the time increases if more steps are needed to open due to forces acting on the heat switch (sect. 2.3.3.1).

e) **Ramping down the magnet** provides the adiabatic demagnetization and the cooling effect of the pills (sect. 2.1.1). Approximately, the temperature of each pill decreases linearly till reaching the minimum value. To reduce energy losses due to eddy current heating, the rate of ramping down is fitted to different current ranges. In total, the ramping time is given by

$$t_{\text{ramp down}} = \sum_i \Delta_i I_{ADR}/\dot{I}_{ADR,i} \simeq 8.8 \text{ min}.$$

The ramping sequence with different rates can affect available energy for cooling (sect. 2.3.4.2).

It is summarized that the recharge time according to the definitions above is given

by

$$t_{\text{recharge, FAA 4 K}} = t_{\text{close HS}} + t_{\text{thermalize, FAA 4 K}} + t_{\text{open HS}} + t_{\text{ramp down}}$$

This results in the value in equation 2.11.

2.3.2. Performance of precooling the ADR

A reliable precooling of the ADR system is essential to start the adiabatic demagnetization cooling, in order to reach mK-temperatures. Therefore, the operation of the precooling system is analyzed. The analysis covers >10,000 h of operation including 35 cool-downs.[16] To obtain a **successful precooling**, all installations on the 4K-stage have to thermalize to the base temperature T_{4K} and all installations have to be operated properly in the cold environment. It is observed that the thermalization to temperatures below 3 K depends on the precooling system including

- a sufficient amount of helium in the pulse-tube cycle,
- a sufficient vacuum pumping, and
- a sufficient cooling water flow (see below).

Furthermore, an improperly functioning heat switch can prevent a successful cool-down (see below). Apart from a mostly stable operation, three issues are discussed which can degrade the performance:

1. The precooling fails because of a nonworking heat switch in the cold.
2. The cool-down time depends on the heat switch performance.
3. The base temperature T_{4K} depends on the water cooling.

This is briefly discussed in the following.

Especially, during the ADR commissioning, the **heat switch** did not work, repeatedly jamming during cool downs.[17] This could only be resolved by aborting the precooling. Since the heat switch unit has several degrees of freedom due to its self-adjustability (sect. 2.2.3 and 2.3.3.1), the heat switch unit can reach an inappropriate position; and the actuator does not have enough force to resolve it. During cooling down, an inappropriate position is presumably caused by different expansion coefficients of heat switch and pills components. Thus, the heat switch is opened slightly before a cool-down. This ensures a sufficient movability during passing temperatures from 300 K to 4 K.[18] Opening the heat switch by -2 k steps indicates a satisfactory trade-off between a moveable heat switch after cool-down and a sufficient thermal coupling to the pills.

---

[16]This includes 10 cool-downs at PTB-Berlin and 24 cool-downs at DESY, Hamburg. A brief cool-down history is found in appendix E.2.

[17]The heat switch was opened and closed regularly during a cool-down in order to ensure the mobility. Nevertheless, this procedure resulted in a jammed actuator between 40 to 10 K.

[18]Changing touch resistances indicates a moving of the heat switch unit during a cool-down (lower graph in fig. 2.6).
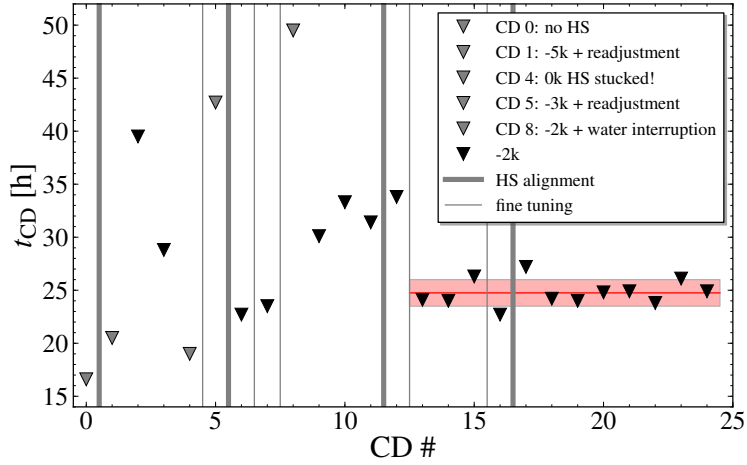
(a) time of cooling below 4 K
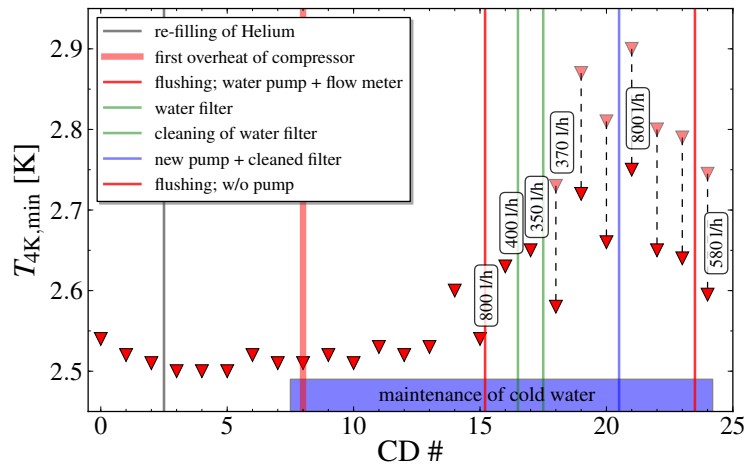
(b) 4K-temperature

Figure 2.8.: Cool-down times and base temperature of ADR:

(a) shows cool-down times t_{CD} of runs in Hamburg. In the first runs, t_{CD} varies a lot due to different setups and heat switch alignments. $t_{CD} = 16.5$ h of CD 0 indicates the intrinsic cool-down without pills unit and heat switch installation. From CD 13 onwards, a quite reproducible performance is observed. The legend contains the steps used to slightly open the heat switch in the warm (see text).

(b) shows the minimal base temperature $T_{4K,min}$ of runs in Hamburg. With the beginning of the cold water maintenance, $T_{4K,min}$ increases due to a unstable water flow. The measured values of CD 18-23 are corrected by -0.15 K, which occurred because of a loose contact of the 4K-thermometer. From CD 15 onwards, the cold water flow is monitored, the water flow is given in units of l/h (white labels).

The **cool-down time** is defined as the time when the FAA-stage reaches the base temperature (sect. 2.3.1). The cool-down time depends on

- the cooling power and stability of the precooling system,
- the installations or mass to thermalize, and
- the thermal coupling to the installations inside the ADR.

This is proven by evaluating cool-down times, t_{CD}, of different runs (fig. 2.8a). The considered runs include different installations at the 4K-stage and different adjustments of the heat switch unit. CD 0 indicates an intrinsic cool-down without pills unit and heat switch installation. CD 4 shows the fastest thermalization with installed pills; however, the heat switch unit was jammed and inoperable after the cool-down. With the setup of the ALPS TES detector (sect. 3.4) and fine tuning of the heat switch (app. D.1.1.3), a reproducible performance is established. Averaging cool-down times from CD 13-24 results in $t_{CD} = 24.8 \pm 1.3$ h.

As mentioned above, the **water cooling performance** of the precooling system affects the success of a cool-down as well as the base temperature, T_{4K}. Due to a degradation of the cold water quality during a maintenance phase at the DESY site, the performance of the precooling system was temporarily affected. Dirt deposited inside the water chiller of the compressor and caused a decrease of the water flow. Thus, the returned helium of the pulse-tube was not sufficiently cooled. This caused several automatic switch-offs of the compressor. Thus, the base temperature, T_{4K}, was higher compared to a normal operation (fig. 2.8b). In addition, an increase of T_{4K} within a single cool-down was indicated during this period: For example, during a ~22 day run, the base temperature increased constantly by ~0.5 K in total. This was presumably caused by a decreased water flow due to dirt deposition. The cleaning of the chiller and the installation of a filter and a water pump ensured that the flow of the cooling water stayed in the admissible range for cooling (SHI, 2008). After the maintenance and cleaning of the chiller, the operation was stable again.

2.3.3. Performance of the adiabatic demagnetization system

In this section, the performance of the adiabatic demagnetization system concerning the (re)charge of the pills is considered. This forms the basis to establish mK-environments, which are analyzed in section 2.3.4. Concerning the thermodynamic cycle, charging the pills includes the isothermal magnetization (fig. 2.1 in sect. 2.1.1). Concerning the technical realization, the following operational phases of a recharge (fig. 2.6b and sect. 2.3.1) and components of the adiabatic demagnetization system (sect. 2.2.3) are analyzed: movability of the heat switch unit (sect. 2.3.3.1) and magnetization and thermalization of the pills (sect. 2.3.3.2). As a summary, the reliability and the chance of success of a recharge cycle is discussed. Furthermore, this results in a recommendation about the alignment and the use of the heat switch (sect. 2.3.3.3).

(a) heat switch in mounting position

(b) heat switch in operational position

(c) heat switch during recharge phases
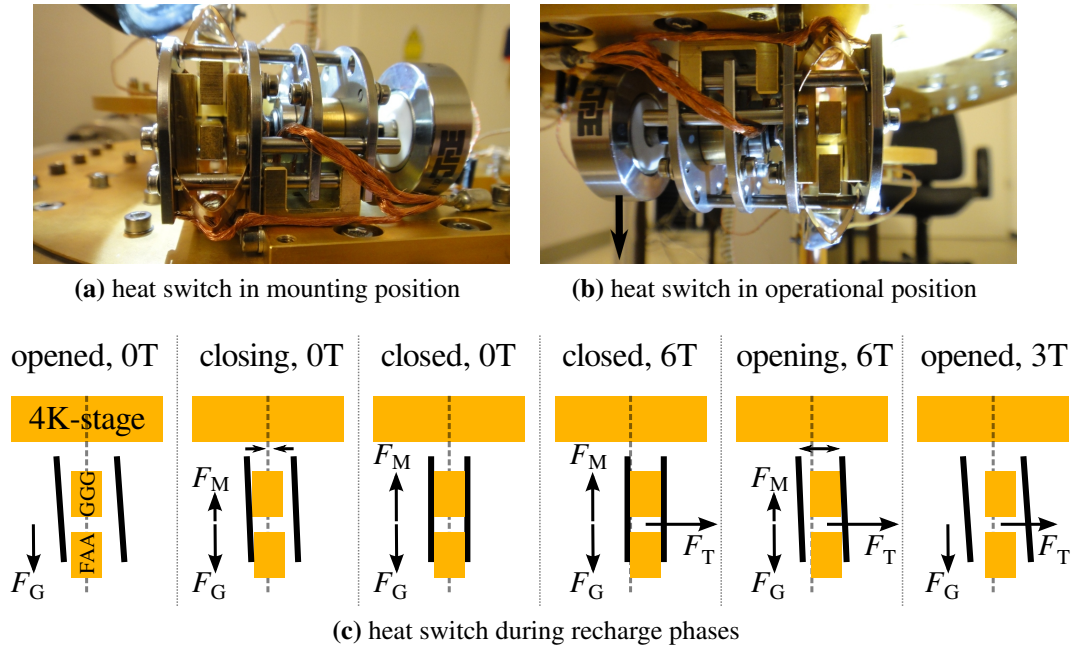
Figure 2.9.: Forces on the heat switch unit: (a) and (b) illustrate the effect of gravity: In operational position (b), the heat switch is inclined because of the mass of the actuator spindle. (c) illustrates the forces acting on the heat switch during recharge phases. The sketch illustrates the pads (black lines) and the copper bars connecting the FAA- and GGG-stage (orange blocks) from a view like in (b). The nominal position is indicated by the dashed line. The inclination is caused by F_G because of the actuator spindle mass. During closing the heat switch, at first, there is a touch between the left pad and the FAA bar. Because of the design, the heat switch self-aligns during closing: F_M compensates F_G at closed condition. During ramping up the magnet, a twisting force is acting on the pills. This results in F_T and a movement of the whole heat switch unit with clamped bars to the right. During opening in full magnetic field, at first the left pad declamps. During ramping down the magnet, the twisting force on the pills decreases and the bars are relaxing to their starting position.

To analyze the performance, ~125 recharges within 24 cool-downs operated in Hamburg (app. E.2) form the recharge sample, which is analyzed in the following. The recharge sample includes various alignments of the heat switch unit (app. E.3). For each recharge, the steps for closing and opening the heat switch are considered as well as the touch channels indicating the condition of the heat switch (sect. 2.2.4). Furthermore, using a self-written Python program allows to analyze ADR logfiles and the temperature evolution of a recharge (for example fig. 2.6b).

2.3.3.1. Movability of the heat switch unit

In this section, the performance of the heat switch is considered concerning its movability at low temperatures. Within a recharge cycle (fig. 2.6b and bullets a)-e) in sect. 2.3.1), **requirements to the heat switch** are:

a) reliable and reproducible closing of the heat switch in 0 T magnetic field after an opened condition,

b) stable closed condition during ramping up the magnet,

c) sufficient thermal coupling of the pills to the 4K-stage during ramping up the magnet and in full magnetic field,

d) reliable and reproducible opening of the heat switch in full magnetic field of 6 T after thermalization of the pills, and

e) stable opened condition during ramping down the magnet.

In this section, bullets a), b), d), and e) are discussed. The resulting thermal coupling between the pills and the 4K-stage due to a closed heat switch, bullet c), is considered in section 2.3.3.2.

During recharges, many **problems** due to the heat switch design are observed.[19] The basic heat switch design is explained in sections 2.2.3 and 2.2.4. It is indicated that the performance strongly depends on the alignment of the heat switch unit: Slight misalignment of the mounting plate, heat switch orientation or the pill-arms (copper bars) change dramatically the performance in the cold. Analyzing the performance due to different alignments (app. E.3) allows to reconstruct the different conditions of the heat switch during a recharge.

By observing the touch channels, which indicate the contact between the copper pads of the heat switch and the copper bars connected to the salt pills, it is indicated that **three different forces** act on the heat switch during a recharge (fig. 2.9):

- **Gravitational force F_G:** In contrast to the mounting ADR position (fig. 2.9a), in operational ADR position, the heat switch is inclined due to the mass of the actuator spindle (black arrow in fig. 2.9b). This inclination results in a deviation of parallelism between the pads and the bars (fig. 2.9c). However, this asymmetry allows to understand the following forces by comparing the touch channels.

- **Force when closing F_M:** Closing the heat switch results in a force that is contrary to the gravitational inclination. If the pads touch the bars, the heat switch self-aligns due to degrees of freedom of its design (sect. 2.2.3). In a closed condition, F_M compensates F_G (fig. 2.9c).

- **Force during magnetic field F_T:** It is indicated that during the full magnetic field of 6 T the heat switch is moved to one side related to the 0 T position.

---

[19]For example, problems were: more steps needed for closing, unstable closed condition during ramping up, no complete opening or no opening at full magnetic field, unstable opened condition, and further technical problems related to the electronics.

> Due to the mounting of the pills, the pills are twisted in the magnetic field.[20]
> This slight twist is transferred to the connected bars between the heat switch
> pads.[21] In a closed heat switch condition, the heat switch is moved due to
> degrees of freedom of its design.

Figure 2.9c illustrates the heat switch conditions during the recharge phases.

Using this interpretation, all occurred problems can be explained. Furthermore, a best alignment and performance in the cold are found:

- **Best alignment in the warm:** The parallelism between the bars and the pads is crucial as well as the symmetrical movability of the pads. The recommended alignment procedure is described in appendix D.1.1.3. A closed heat switch has touch values below ~1.0 mΩ; an opened heat switch has high-ohmic touch values (>2 MΩ and overrange of electronics). To open the heat switch, ~-20 k steps are needed; to close the heat switch, +25 to +30 k steps are needed. In the cold without magnetic field, these steps are reproducible.

- **Best performance in the cold:** The closed and opened condition is the same as in the warm; during ramping up and down the magnet, the touch values stay constant. The heat switch is opened by -60 k steps at full magnetic field. Here, more steps are needed, because of the force F_T due to the twisted pills (see above). To close the heat switch for starting a new recharge, +75 to +80 k steps are needed. A successful operation is described in appendix D.2.2.

The ~25 % imbalance of number of steps to close and open is caused by the three springs in the mechanics of the heat switch (fig. 2.4). They act as a permanent force in the opening direction. A reproducible series of 9 recharges results in (25.7±7.0) % additional steps for closing the heat switch.

2.3.3.2. Magnetization and thermalization

In this section, the ramping up phase and the thermalization phase of a recharge is discussed (fig. 2.6b and sect. 2.3.1). The superconducting magnet and the pills coupling to the 4K-stage due to a closed heat switch (bullet c) in sect. 2.3.3.1) are examined.

The **superconducting ADR magnet** has shown a stable operation: During ramping up a maximal current of 40 A, holding this current up to 24 hours, and ramping down in different speeds, no technical errors occurred. Only during one cool-down a quench occurred, presumably because of an external ground motion[22]. The current of 40 A dropped to 0 A within 2 seconds and flowed off a 1 Ω acting as quench

---

[20]The Vespel pins could be tightened to diminish the twisting of the pills. However, this affects shorter mK-times due to a higher thermal coupling (sect. 2.3.4.3).

[21]The resulting force F_T is to the right in figure 2.9b or 2.9c. In a 4K-stage top view illustrated by sketch D.3, the movement is clockwise.

[22]At this time, a little truck hit overhead lines in front of building 50 at DESY's site where the ALPS IIa laboratory is located.

protection. Because of Joule heating and eddy current heating, this caused a heat-up of the pills unit and the 4K-stage to ~11 K. The next recharge cycle showed a normal performance.

During **ramping up the magnet**, the salt pills heat up (fig. 2.6b) due to adiabatic magnetization and eddy currents because of the magnetic field change. Having a normal pills-4K-stage coupling and using 0.1 A/s for ramping up[23], the pills heat up to ~10 K. This heat-up affects mostly the recharge time because of the thermalization.

After ramping up, the pills **thermalize** due to the coupling to the 4K-stage. The temperature evolution of each pill, $T_{\mathrm{pill}}(t)$, can be described by

$$T_{\mathrm{pill}}(t) = T_{\mathrm{bath}} + (T_0 - T_{\mathrm{bath}})\, e^{-(t-t_0)/\tau_{\mathrm{pill}}} \tag{2.12}$$

where T_0 and t_0 are fit parameters and T_{bath} is the 4K-stage temperature. τ_{pill} is the time constant and is defined by the pill heat capacity C_{pill} and the thermal coupling to the bath, $G_{\mathrm{heat\ switch}}$, which is given by the closed heat switch:

$$\tau_{\mathrm{pill}} = \frac{C_{\mathrm{pill}}}{G_{\mathrm{heat\ switch}}} \tag{2.13}$$

Therefore, τ_{pill} allows to indicate the performance of the coupling defined by the closed heat switch: the smaller τ_{pill} the better the thermal coupling. Apart from the thermal constants τ_{FAA} and τ_{GGG}, the thermalization time $t_{\mathrm{FAA,\ 4K}}$ is additionally considered which is defined as the time till the FAA-pill reaches 4 K after ramping up (sect. 2.3.1).[24]

For the **thermalization analysis**, equation 2.12 is fitted to temperature evolutions of the recharge sample.[25] In figure 2.6b, an exemplary fit is depicted. Figure 2.10a and 2.10b show the thermal constants; figure 2.10c shows the time $t_{\mathrm{FAA,\ 4K}}$ of each recharge (small dots). For each cool-down, the median is calculated. In table 2.10d, the mean values within a same alignment of the heat switch unit are given.

Before the analysis results are discussed, the **quality of the analysis** is considered. Fits deviate slightly (e.g. fig. 2.6b) because two quantities of equation 2.12 are not constant during thermalization:

- **Temperature dependence of the pills' heat capacity at 6 T:** The heat capacity $C(T)$ of the pills at 6 T (red lines in fig. 2.5) is not constant between temperatures of ~4 to 10 K. Due to equation 2.13, this affects the thermal constant.

---

[23]Recommended by Entropy GmbH.

[24]This figure of merit is used as a cross check, which is not taking into account uncertainties from the fit procedure.

[25]To ensure the comparability between each recharge, the fit includes data when GGG passes 6 K till GGG is 0.1 K above the end temperature $T_{\mathrm{GGG,therm}}$ of an individual cycle (see fig. 2.6b).

(a) τ_{FAA}

(b) τ_{GGG}

(c) $t_{FAA,4K}$

CD	τ_{FAA}	τ_{GGG}	$t_{4K,FAA}$
[#]	[min]	[min]	[min]
(all	42±57	20.7±4.7	87±74)
(1-5	100±140	20±10	150±170)
6-11	29.4±6.7	22.2±3.4	69±12
12-16	26.5±5.7	20.4±5.8	57±14
17-24	33.0±2.7	21.7±1.0	75.0±6.9

(d) Values and means
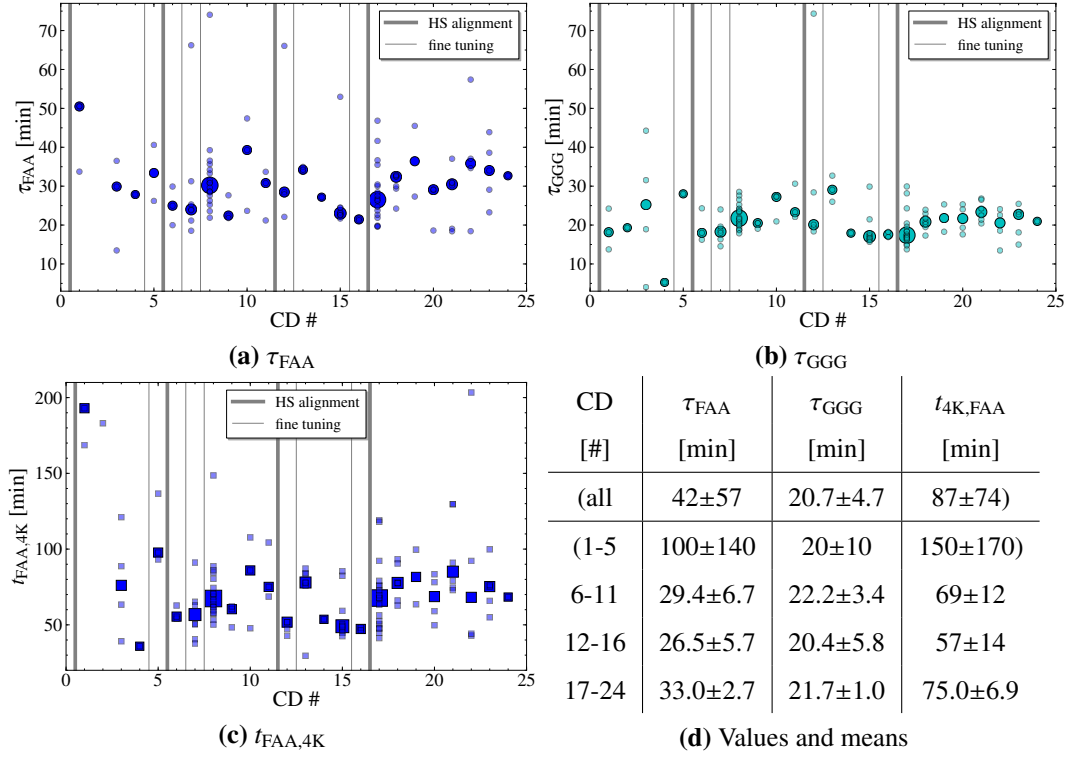
Figure 2.10.: Thermalization of pills after ramping up: (a) shows the time constant τ_{FAA} which is evaluated by fitting equation 2.12 to FAA's temperature evolution. (b) shows the corresponding result for the GGG pill, τ_{GGG}. (c) shows the real time of thermalization by defining the duration till FAA reaches 4 K after ramping up the magnet. (d) lists the means of the medians summarizing values of different heat switch alignments.

- **Heating of 4K-stage due to magnet current:** A heat-up of the 4K-stage is observed while the magnet is operated at 6 T. Despite the magnet being superconducting, it is assumed that a resistive part of the connection causes a Joule heating. The power due to Joule heating and the cooling power result in equilibrium after ~250 min. The temperature is ~0.5 K higher than the 4K-temperature with switched-off magnet. This is uncritical for the thermalization of the pills; however, it affects the thermalization evolution since T_{bath} changes with time.

However, by comparing the results of $t_{FAA,4K}$ and τ_{FAA}, both analysis methods result in the same trend (fig. 2.10a and 2.10c). Therefore, the chosen fit procedure is valid in a first approximation.

Most important results of this analysis are:

- **Unstable thermalization times:** The time constants differ from cool-down to cool-down and from recharge to recharge (fig. 2.10). It is indicated that a proper alignment of the heat switch unit and a fine tuning of the motor

base plate can improve the times (app. D.1.1.3). For a good coupling, the parallelism of the bars to the pads is crucial. Using the measurement of the touch channels as feedback is not sufficient to judge the coupling quality. For example, in CD 17 (fig. 2.10), the touch values for the closed condition varies only from 0.4 to 0.6 mΩ, although $t_{\text{FAA,4K}}$ vary from 40 to 120 min. Closing the heat switch to the tightest position can result in a condition in which the heat switch is not opened before ramping down (sect. 2.3.3.1). Therefore, it is recommended not to close the heat switch too tight, in order to ensure the chance of success (sect. 2.3.3.3).

- **More stable coupling of GGG:** When comparing τ_{FAA} and τ_{GGG} (fig. 2.10), a higher scattering of FAA data is observed. It is indicated that the GGG bar is clamped by the heat switch more tightly than the FAA bar: Before the second alignment (CD 6), a slightly loose FAA bar was found in a closed condition.[26] This explains the quite unstable and long thermalization within CD 1-5.

- **Better coupling of GGG than FAA:** Considering quite reproducible recharges (CD 6-24 in tab. 2.10d), the thermal constants result in τ_{FAA} = 29.9 ± 5.1 min and τ_{GGG} = 21.2 ± 3.2 min. Using equation 2.13 and assuming a heat capacity ratio[27] of $C_{\text{GGG}}/C_{\text{FAA}} \simeq 1.2$, it results in a thermal conductance ratio of $G_{\text{GGG}} \simeq 1.7 \times G_{\text{FAA}}$. This indicates a better coupling of the GGG pill to the 4K-stage than of the FAA pill. This could be caused by:

    - a slightly smaller contact surface between the FAA bar and the clamps of about 90 % (fig. 2.9b),

    - a slightly thinner bar, and thus, a smaller force for coupling in comparison to the GGG bar (see above),

    - thus, a more unstable FAA coupling due to forces during a full magnetic field (fig. 2.9), and

    - the longer thermal path of the FAA to the 4K-stage as cold bath compared to the GGG bar (fig. 2.9).

It is concluded that the thermalization of the pills strongly depends on the geometry of the bars and the closing condition of the heat switch. Having an alignment resulting in a reproducible heat switch performance (CD 17-24 in tab. 2.10d), it results in $t_{\text{4K,min}}$ = 75 ± 7 min as a representative thermalization time. As already pointed out above (sect. 2.3.1), the thermalization forms the main part of the recharge time.
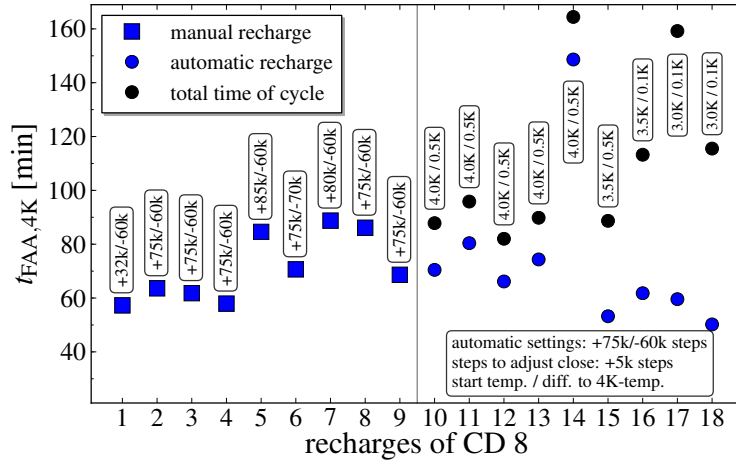
Figure 2.11.: Performance after successful alignment: In cool-down 8, reproducible and stable recharges are observed. No moving problems occur. The first nine recharges are operated manually and thermalization times $t_{\mathrm{FAA},4K}$ are depicted (blue squares). The used steps of closing and opening are found in the white text boxes. The recharges 10-18 are operated automatically (blue circles), all with the same steps of closing and opening and with different settings of starting the ramping down (white boxes). The black circles indicate the total recharge time which is determined by the time while the magnet is on, plus the time of closing the heat switch at the beginning of a recharge.

2.3.3.3. Reliability, automation and chance of success

As shown in the previous sections, the recharge performance mainly depends on the performance of the heat switch. In the following, the automation function of a recharge is discussed as well as the chance of success after a satisfactory alignment. Finally, a recommendation to align and operate the heat switch is given.

The "Adiabatic Control" software allows to operate a **recharge automatically**. The automation is tested with a proper recharge sample, at which no heat switch moving problems occur. It includes 9 manual and 9 automatic recharges after a proper alignment.[28] In figure 2.11, the thermalization times $t_{\mathrm{FAA},4K}$ as well as the needed steps for closing and opening the heat switch are shown. With the manual recharges, the steps for the automation settings are determined. In this series, the heat switch completely closes with +75 k steps and opens with -60 k steps.[29]

---

[26]Together with Entropy GmbH.

[27]This is estimated by comparing the pills' heat capacities in a full magnetic field over the thermalization temperature range (see fig. 2.5).

[28]During cool-down 8 and after the 2nd alignment with a subsequent fine tuning (app. E.3).

[29]Only twice, more steps are necessary in the manual recharges 5 to 7. Therefore, the settings for automatic recharges, 10 to 18, are `steps to close` 75 k, `steps to open` 60 k, `Ramp down when the pill is (K)` 4.0 for recharge 1-14 or 3.5 for recharge 15+16 or 3.0 for recharge 17+18. Furthermore, with `steps to adjust close` 5 k, every half hour the automation closes the heat switch for additional 5 k steps after ramping up.

In this series (fig. 2.11), the manual and automatic recharges work with **100 % chance of success**. The thermalization time till 4 K of recharges 1 to 13 scatters between 50-90 min, and recharge 14 takes even ~140 min. This is caused by the unstable coupling (see sect. 2.3.3.2). In addition, longer recharge times are observed, when choosing a smaller ramp down temperature, due to the exponential cooling. How the ramp down temperature of the pills affects the mK-environment, is considered in section 2.3.4.2.

Within this thesis, the alignment for CD 17-24 indicates the most reproducible performance of the heat switch design. Therefore, this is considered as a **representative sample** of ADR operation. Here, the overall chance of success is approximately 80 % including ~50 recharges. In few cases, it was not possible to open the heat switch before ramping down. In addition, it was observed that the heat switch sometimes did not move during closing. This is presumably caused by a wear and tear of the piezo element of the actuator.

In addition, it is observed that the performance after a satisfactory alignment and fine tuning gets gradually worse. This is caused by an increasing movability of the whole pills and heat switch unit because screws or Vespel pins gradually loosen. A higher movability provides probably inappropriate conditions such as a jammed heat switch unit in the full magnetic field. Therefore, a regular alignment is unavoidable. An **alignment recommendation** is found in appendix D.1.1.3. After a coarse alignment, a fine tuning before the subsequent cool-down should reach a satisfactory performance.

Finally, to obtain a reliable moving, a sufficient thermal coupling, and a high chance of success, it is **recommended to operate** the heat switch as follows:

- Closing the heat switch should be done manually and not to the tightest position. For example, in the representative sample, a closed condition with 0.5 mΩ should be realized before ramping up, although the tightest condition is 0.3 mΩ. This ensures a reliable opening in full magnetic field.
- The implemented automation can be used after manual closing. Thus, the automation can open the heat switch, ramp down the magnet and regulate to a mK-temperature (next sect. 2.3.4).

To improve the performance, Entropy GmbH is developing a new heat switch design including this experience (Wernicke, 2013). Furthermore, a more sophisticated automation program could increase the reliability of the current design: Instead of using a fixed step size, the steps should be adjusted using the touch channels as feedback.

2.3.4. Performance of mK-environments

In this section, the performance of the cold pills is analyzed, which establish the mK-environment. Therefore, drifts and holds are considered after ramping down the magnet in a recharge cycle (sect. 2.3.1). The **analysis sample** includes drifts
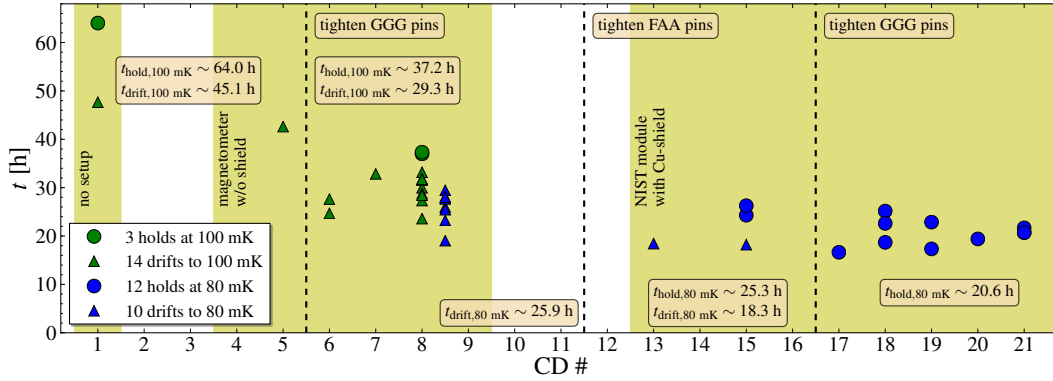
Figure 2.12.: Drift and hold times of different cool-downs: The figure shows drift times to 80 mK (blue triangles) and to 100 mK (red triangles), and hold times at 80 mK (blue circles) and at 100 mK (red circles) within cool-downs 1-21 in Hamburg (app. E.2). Different setups mounted to the cold finger are compared (yellowish areas): no setup during CD 1, the magnetometer at the detector bench with extension rod during CD 4-9, and the NIST module at the detector bench with extension rod with Cu-shield at the Al-plate from CD 13 (app. C). Furthermore, different adjustments of Vespel pins (app. E.3) are considered (divided by the dashed line): CD 1-5 first installation, CD 6-11 after tightening GGG pins, CD 12-16 after tightening FAA pins, and from CD 13 onwards after tightening GGG pins. In the boxes, the averaged times of drifts and holds for these four sections are given. The depicted drifts and holds form the analysis sample which is considered in this section.

and holds to or at a temperature of 80 mK or 100 mK for different setups and pill alignments (fig. 2.12).[30] To understand the behaviour of charged pills in the ADR environment, the discussion is split up in following subsections:

- The time evolution of the double-stage pills unit is explained (sect. 2.3.4.1).
- The energy of the FAA-pill is discussed (sect. 2.3.4.2).
- Power loads on the pills are considered (sect. 2.3.4.3).
- Finally, the temperature stability of a hold is considered (sect. 2.3.4.4), which is important to stably operate sensor modules.

2.3.4.1. Time evolution of double-stage pill unit

In principle, the **double-stage pills unit is a thermal system in series** (sect. 2.2.3). The FAA-stage has a thermal link to the GGG-stage due the six inner Vespel pins for mounting; in turn, the GGG-stage has a thermal link to the 4K-stage due to the six outer Vespel pins of the pills unit. Thus, the time evolution of each pill temperature can be described by the following differential equation, which results

---

[30]This sample includes data of CD 1-21 including different setups (app. E.2) and different adjustments of the Vespel pins (app. E.3). Using a self-written Python program, important values of drifts or holds are determined from the ADR logfiles.

(a) heat capacity of FAA   **(b)** heat capacity of GGG
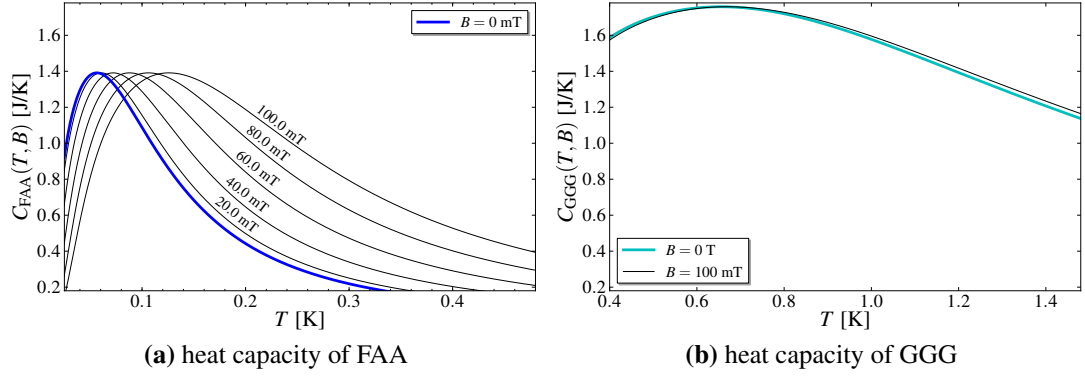
Figure 2.13.: Heat capacities of pills at mK-temperatures: Using the entropy model (fig. 2.5), the heat capacity is calculated for each pill. To understand the drift evolution of the pills unit (fig. 2.7a), the curve at $B = 0$ mT is helpful. While the heat capacity of FAA decreases rapidly at temperatures > 100 mK (a), the heat capacity of GGG decreases slowly (b). To understand the effect during holding a temperature (fig. 2.7b), the FAA curves at different magnetic fields are helpful (a). Regulating the magnetic field can hold a high heat capacity of FAA referred to its temperature.

from the power balance $P_{\text{cooling}} = P_{\text{heating}}$:

$$C\left(T(t)\right) \frac{\mathrm{d}T(t)}{\mathrm{d}t} = G(T(t)) \left| T_{\text{bath}}(t) - T(t) \right| + \Sigma P_{\text{load}_i}(t) \tag{2.14}$$

The left side represents the cooling power P_{cooling}, which is defined by the heat capacity C and the time derivative of the temperature. The right side summarizes the heating power P_{heating}: The heat conductance G multiplied by the temperature difference to the bath defines the power load of the bath due to the Vespel pins. Additional external power loads are thermal radiation, heat transfer through wiring, Joule heating of powered sensors, or even mechanical vibrations (White and Meeson, 2002, p. 82ff.). Power loads are considered in section 2.3.4.3. Furthermore, it is assumed that the 4K-stage is the heat bath for the GGG-stage, and the GGG-stage is the bath for the FAA-stage. In the following, the heat capacities of the pills are calculated with the entropy model (fig. 2.5).

Considering the differential equations for both pills (eqn. 2.14), the temperature evolution of drifting pills can be explained. In figure 2.7a, the GGG temperature increases almost linearly, while the FAA temperature increases considerably from $T_{\text{FAA}} \sim 200$ mK. This is mainly explained by two quantities in equation 2.14:

- the changing temperature difference to the bath, $\left| T_{\text{bath}}(t) - T(t) \right|$, and
- the changing heat capacity of the pills, $C(T(t))$.

This means for the **evolution of the GGG pill**: GGG's heat capacity (fig. 2.13b) and, therefore, the cooling power $P_{\text{cooling,GGG}}$ decrease slowly from maximum to

zero. In addition, the heating power $P_{\text{heating,GGG}}$ also decreases, since $T_{\text{bath,GGG}} = T_{\text{4K}} = const.$.

In contrast, the **evolution of the FAA pill** is: The cooling power of the FAA pill drops down considerably at a temperature of ~200 mK, due to the FAA heat capacity (fig. 2.13a). Additionally, the temperature difference to the GGG bath increases in the beginning of the drift (fig. 2.7a), which results in an increasing heating power. This explains the steep rise of the FAA temperature ~200 mK in this double-stage unit. The cooling power resulting from measurements is discussed in section 2.3.4.3. In the next section, the energy of the FAA-pill is considered.

2.3.4.2. Energy of FAA-pill

In this section, the cooling energy of the FAA-pill and the consequences for the mK-environment are considered.[31] At first, the **cooling energy** E_{cooling} is defined. Considering the left side of equation 2.14, the dissipated cooling energy is calculated by integration of the cooling power:

$$E_{\text{cooling}} = \int P_{\text{cooling}}(t)\,\mathrm{d}t = \int C\left(T(t)\right) \frac{\mathrm{d}T(t)}{\mathrm{d}t}\,\mathrm{d}t = \int_{T_{\text{min}}}^{T_{\text{end}}} C(T)\,\mathrm{d}T \qquad (2.15)$$

The energy can also be calculated via the change of entropy. It is:

$$E_{\text{cooling}} = \int C(T,B)\,\mathrm{d}T = \int T\,\mathrm{d}S(T,B) \qquad (2.16)$$

To determine the pill's energy of a hold, equation 2.16 is used, since the corresponding temperature related to the magnetic field is not measured. To compare the energy resulting from drifts and holds, the heat capacity and the entropy are assumed, which result from the theory (sect. 2.1.2) using the parameters of the salt pills unit (fig. 2.5). The energies are calculated numerically from the temperature evolution:

- For **drifts** with $B = 0$ T, the calculation results in

$$E_{\text{drift},T_{\text{end}}} = \sum_{T_0}^{T_{\text{end}}} C(\overline{T}_i)\Delta T_i = \sum_{T_0}^{T_{\text{end}}} \overline{T}_i \Delta S_i \qquad (2.17)$$

  where the bin is $\Delta T_i = T_{i+1} - T_i$, the corresponding mean temperature $\overline{T}_i = (T_{i+1} + T_i)/2$, and the entropy bin $\Delta S_i = S(T_{i+1}) - S(T_i)$. The summation starts with the minimum temperature of the drift $T_0 = T_{\text{min}}$, till the end temperature of the drift T_{end}.

---

[31]The focus is only on the FAA pill since the FAA-stage is the bath for superconducting sensors. Furthermore, the temperature evolution of the GGG was not always logged.

(a) theoretical sample   **(b)** analysis sample
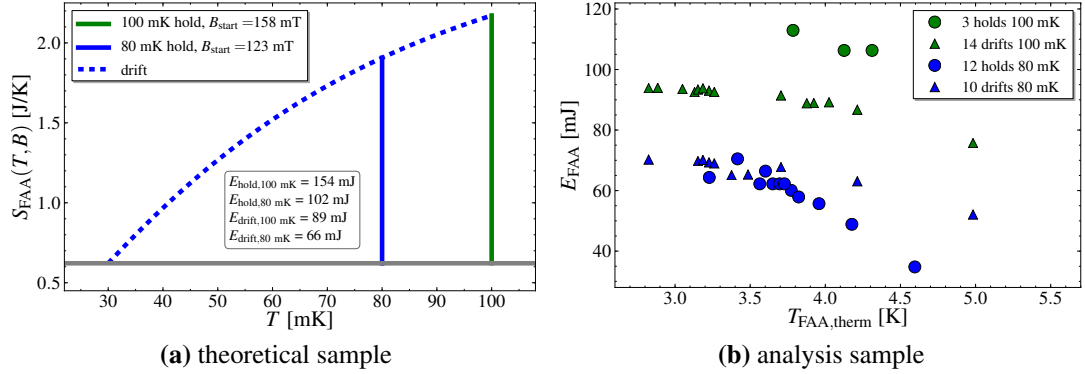
Figure 2.14.: Charged and dissipated energy of FAA pill: (a) shows the entropy of FAA calculated with the model (sect. 2.1.2 and fig. 2.5). Four mK-conditions are compared with the same initial entropy (grey line) which corresponds to a minimum temperature of 30 mK: Holds at 100 mK and 80 mK (vertical green and blue line) and drifts to 80 mK and 100 mK (dashed blue line). The calculated energy corresponds to the charged energy of the FAA pill. This forms a theoretical sample. (b) shows the calculated energies E_{FAA} of the analysis sample including drifts (triangles, green to 100 mK and blue to 80 mK) and holds (circles, green at 100 mK and blue at 80 mK). Each sample shows higher energies with lower thermalization temperature.

- For **holds**, the calculation of energy simply results in

$$E_{hold,T_{hold}} = T_{hold} \left(S \left(T_{hold}, B_{end} \right) - S \left(T_{hold}, B_{start} \right) \right) \tag{2.18}$$

where B_{start} is the magnetic field density at the beginning of the regulation and $B_{end} = 0$ T in the following, since only full holds are considered. The magnetic field is calculated by the measured current. It is assumed that 40 A corresponds to a 6 T magnetic field inside the solenoid, which is linearly dependent on current.

To understand differences and trends of drift and hold times, three samples are considered in the following:

- **Theoretical sample:** In figure 2.14a, energies of the theoretical sample are illustrated. Energies of considered drifts and holds are calculated using equations 2.17 and 2.18. For each mK-condition, a minimum entropy is considered which corresponds to a temperature of 30 mK. Since no losses are considered here, the calculated energy corresponds to the charged energy, $E_{charged}$. The charged energy is the theoretical maximum which can be used for cooling.

- **Analysis sample:** In figure 2.14b, energies of the analysis sample are de-
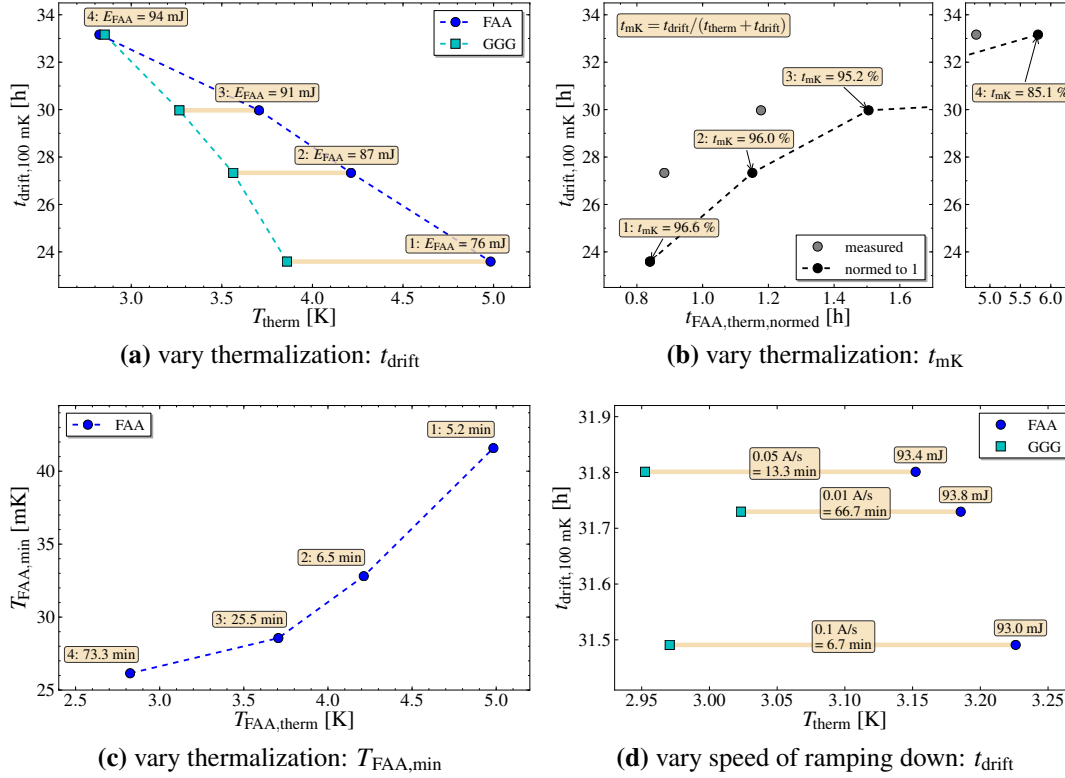
Figure 2.15.: Series of drifts varying the thermalization: (a)-(c) illustrates results of the specific sample of four 100 mK drifts. (a) shows drift times versus the thermalization temperature $T_{\text{therm.}}$ of the pills after opening the heat switch and before ramping down. (b) shows drift times versus the thermalization time. By considering the defined time ratio t_{mK} (upper box), recharge and drift 1 indicate the most efficient way of short thermalization and long drift time. (c) shows FAA minimum temperature versus thermalization temperature. The minimum is reached after a certain time after ramping down (boxes). (d) In a further series, the ramping down speed varies from fast 0.1 A/s to slow 0.01 A/s. No significant difference is indicated. All drifts are measured within the same cool-down including the same setup.

picted.[32] Energies are calculated by equations 2.17 and 2.18 using the temperature evolution, $T(t)$, from logfiles. These energies correspond to the total dissipated energy for cooling the FAA-stage, E_{cooling}.

- **Specific sample:** Figure 2.15 summarizes the results by analyzing a specific sample of 100 mK drift. The four drifts are from the same cool-down. Thus, it is assumed that the external power load is constant due to the same alignment and the same thermal load attached to the FAA cold finger.[33] Here, the

---

[32]Drift and hold times are found in figure 2.12.
[33]CD 8 after 2$^{\text{nd}}$ alignment with FAA extension rod, detector bench with magnetometer without

thermalization time is varied, which results in different thermalization temperatures $T_{\text{therm.}}$ before ramping down (sect. 2.3.1 and fig 2.6b).

By comparing these samples, the most important results are:

- **Longer hold times than corresponding drift times:** Considering the theoretical sample (fig. 2.14a) or the analysis sample (fig. 2.14b) indicates a higher energy for holding a constant temperature than the energy of a drift:[34] $E_{\text{hold}} > E_{\text{drift}}$. This explains longer hold times t_{hold} compared to corresponding drift times t_{drift} of the same setup (fig. 2.12).

- **Thermalization temperature before ramping down affects mK-times and mK-temperatures:** By analyzing the specific sample (fig. 2.15), it is indicated that drift or hold times strongly depend on the thermalization temperature $T_{\text{therm.}}$. This implicates the lower the thermalization temperature the higher the cooling energy (fig. 2.15a). This is caused by a lower entropy which is reached by longer thermalization during the recharge.

  A second consequence of lower $T_{\text{therm.}}$ are lower values in temperature. This is indicated by analyzing the minimum FAA temperature which is reached after ramping down (fig. 2.15c). For example, the lowest temperature of this sample is ~26 mK which is reached after ~73 min after ramping down due to thermalization time and the screening effect of the GGG pill.

- **Energy losses due to thermalization:** Comparing values of the theoretical sample (fig. 2.14a) and corresponding values of the analysis sample (fig. 2.14b) indicates $E_{\text{charged}} > E_{\text{cooling}}$.[35] This is presumably caused mainly by the thermalization of the cold mass mounted to the cold finger. Furthermore, the cooling energies of 80 mK holds (fig. 2.14b) are below the corresponding 80 mK drifts. This is caused by a different setup with a bigger cold mass (cf. fig. 2.12). Thus, thermalization energy $E_{\text{thermalize}}$ diminishes the charged energy which can be used for cooling.

- **Energy losses due to magnet regulation:** Another peculiarity is the relative lower energy for measured holds (fig. 2.14b) than expected (fig. 2.14a). For example, considering a 100 mK hold and a 100 mK drift without any cold mass attached to the cold finger[36], the energy ratio is ~77 %. The corresponding ratio from the theoretical sample results in ~58 %. This indicates an additional energy dissipation while regulating the magnet, $E_{\text{regulating}}$.[37]

---

shielding and Al-base plate.

[34] Apart from the 80 mK drifts in figure 2.14b. This is explained in the next bullet point.

[35] 30 mK minimum temperature corresponds approximately to $T_{\text{FAA,therm}} \simeq 4.0$ K. Since the model of the heat capacity is used for both samples equally, this comparison is valid.

[36] Within CD 1.

[37] A similar effect is observed if the magnet is ramped up and down shortly: Here, the final temperature is higher than the initial temperature. This energy loss is presumably caused by eddy currents while changing the magnetic field.

- **Energy losses due to ramping speed:** Entropy GmbH recommends a ramping down with decreasing speeds: From 40 to 10 A with 0.1 A/s, from 10 A to 2 A with 0.05 A/s and finally to 0 A with 0.03 A. This is a trade-off between a slow ramping resulting in a long time contribution and a fast ramping resulting in an energy loss due to higher eddy current heating. In one extra sample, three drifts with different ramping speeds 0.01, 0.05 and 0.1 A/s from 40 to 0 A are compared (fig. 2.15d).[38] In this analysis, no significant indications for an optimal speed of ramping down are found.[39] Therefore, the recommended ramping sequence is used for ramping down the magnet in a recharge.

The results of the previous analysis are summarized:

- The cooling energy for a hold is higher than for the corresponding drift: $E_{\text{cooling, hold}} > E_{\text{cooling, drift}}$.
- The mK-time, t_{drift} or t_{hold}, strongly depends on the thermalization temperature of the pills before ramping down.
- The charged energy during a recharge is dissipated by different mechanisms. Thus, the cooling energy is given by:

$$E_{\text{cooling}} = E_{\text{charged}} - E_{\text{ramping down}} - E_{\text{thermalization}} - E_{\text{regulating}}$$

where $E_{\text{regulating}}$ only contributes during holding a mK-temperature (sect. 2.3.4.4). Finally, an effective recharge cycle including a short thermalization time and a long mK-time can be found. By defining a ratio $t_{\text{mK}} = t_{\text{drift}}/(t_{\text{therm}} + t_{\text{drift}})$, sample 1 of the specific sample is the most effective recharge cycle (fig. 2.15b). This means that longer thermalization times increase the drift time absolutely; however, it is decreased relatively due to of the exponential evolution of thermalization. This is an important fact if the mK-environment is used to operate sensors as a detector. For example, if the detector is used in a 24 h cycle, an minimal thermalization time can be found, which is a dead time at the same time.

2.3.4.3. Power loads on the pills

In this section, power loads on the pills during an established mK-environment are considered. Firstly, the cooling power evolution during a drift is exemplary considered. Secondly, the analysis sample is evaluated to discuss different sources of power load.

---

[38]The thermalization temperature of FAA is nearly the same for each drift. The uncertainty is caused by opening the heat switch. While the heat switch is opened, the moment of complete uncoupled pills deviates.

[39]The slight difference between drift times t_{drift} could be caused by different thermalization temperatures.

(a) $P_{\text{FAA, cool}}$ and $G_{\text{FAA, eff}}$ **(b)** $P_{\text{GGG, cool}}$ and $G_{\text{GGG, eff}}$
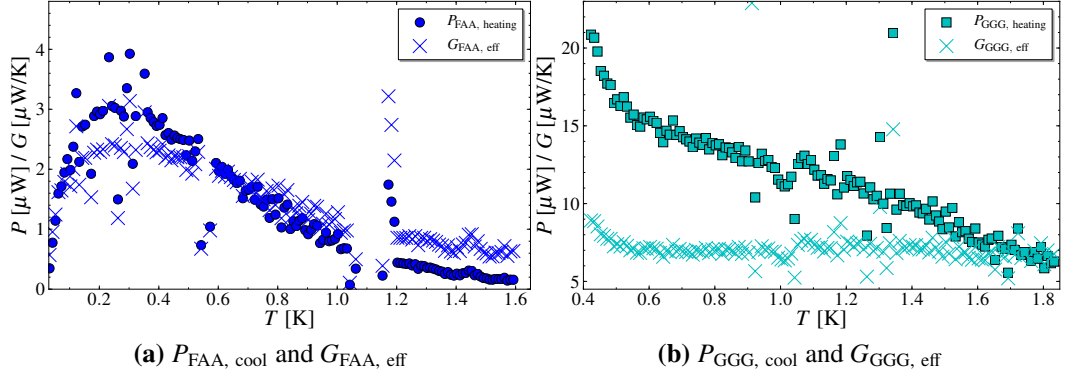
Figure 2.16.: Cooling power and effective heat conductance of GGG and FAA: For the drifting pills till a temperature above 1.5 K after a recharge (fig. 2.7a), the cooling power and the effective heat conductance is numerically calculated by equations 2.19 and 2.20. Deflections of individual data points are caused by discontinuities in the temperature measurement due to different resistance ranges of the thermometry (sect. 2.2.4).

According to equation 2.14, the **cooling power** is numerically calculated by:

$$P_{\text{cool}}(\overline{T_i}) = C(\overline{T_i}) \cdot \frac{\Delta T_i}{\Delta t_i} \tag{2.19}$$

where the temperature bin is $\Delta T_i = T_{i+1} - T_i$, the mean temperature bin $\overline{T_i} = (T_{i+1} + T_i)/2$, and the time bin $\Delta t_i = t_{i+1} - t_i$. The right side of equation 2.14, including the heat flow from the bath and external loads, can be described by an effective conductance G_{eff} times the temperature difference to the bath. This allows to calculate G_{eff} in order to estimate the thermal coupling to the environment:

$$G_{\text{eff}}(\overline{T_i}) = P_{\text{cool}}(\overline{T_i}) \left(\overline{T_{\text{bath}_i}} - \overline{T_i} \right)^{-1} \tag{2.20}$$

By applying equations 2.19 and 2.20 to measured temperature slopes, the evolution of cooling power and the effective heat conductance can be calculated. As an example, the **exemplary drift** in figure 2.7a is considered. Figure 2.16 illustrates the evolution of each pill which is in accordance with the description of the double-stage pills unit in section 2.3.4.1. The FAA cooling power reaches a maximum around 300 mK (fig. 2.16a). Afterwards it decreases because the cooling energy is dissipated. $G_{\text{FAA,eff}}$ shows a similar trend which is mainly caused by the cooling power evolution. The GGG cooling power decreases with higher temperature (fig. 2.16b). This is mainly caused by the decreasing temperature difference to the constant bath of the 4K-stage. $G_{\text{GGG,eff}}$ is quite constant with ~7.5 μW/K. This means that the GGG cooling power balances the temperature difference to the bath across the GGG temperature evolution (eqn. 2.20).

To compare the power during drifts and holds of the analysis sample, an **effective**

(a) $P_{\text{FAA,eff}}$ **(b)** $P_{\text{GGG,eff}}$
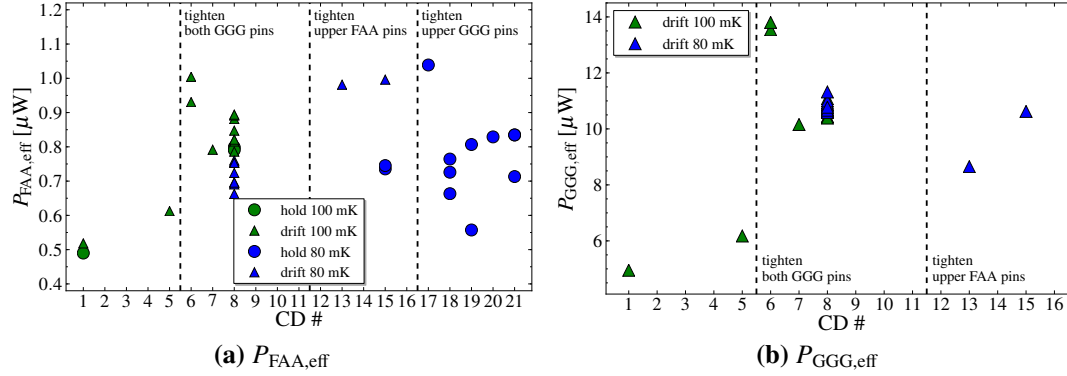
Figure 2.17.: Effective power load on FAA and GGG: The effective power of the FAA pill (a) and of the GGG pill (b) compared to the different alignments of the Vespel pins and setups at the cold finger. The effective power is calculated by dividing the dissipated energy with the drift respectively drift time. Interpretations are found in the text.

power, P_{eff}, is considered. It is defined by the cooling energy, which is given in figure 2.14b, and the corresponding mK-time, which is depicted in figure 2.12, of the analysis sample:

$$P_{\text{eff}} = E_{\text{cooling}}/t_{\text{mK-time}} \tag{2.21}$$

where $t_{\text{mK-time}}$ is t_{drift} or t_{hold}.

By applying equation 2.21 to the analysis sample, effective powers for the FAA and GGG pills are calculated.[40] Comparing the analysis sample in figure 2.17, two **effects due to the definition** of the effective power (eqn. 2.21) are observed:

- **Lower effective power of holds:** Since the mK-time is longer for holds than for drifts (fig. 2.12), the FAA effective power is lower for holds than for drifts (fig. 2.17a).[41]

- **Variation of effective power within the same setup:** The variation is observed for both pills (fig. 2.17). It is caused by the temperature dependence of the power (fig. 2.16).

Apart from these effects, a comparison of the analysis sample allows to evaluate the power loads on the pills:[42]

- **Heat transfer through Vespel pins** P_{Vespel}**:** Tightening the Vespel pins of

---

[40]$P_{\text{GGG,eff}}$ can only be calculated for drift data by equations 2.17 and 2.21. For hold data, the dissipated energy cannot be calculated, since the GGG temperature is not measured due to the regulation feedback (sect. 2.3.4.4).

[41]This is more distinctive for 80 mK data due to the cooling energy: For 100 mK data, $E_{\text{cooling, hold}}$ is 20 % larger than $E_{\text{cooling, drift}}$. For 80 mK data, cooling energies are nearly the same for a FAA thermalization temperature below 4 K (fig. 2.14b).

[42]It should be noted that this analysis cannot explain the absolute value of the calculated power.

the pills (app. E.3) increases the heat load, and thus, the effective power (fig. 2.17a).[43] It should be noted that tightening the GGG pins also affects the FAA pill. This illustrates the screening effect of FAA by GGG.

- **Heat transfer through wiring** P_{wiring}: Attaching sensor modules to the FAA-stage, which are weakly thermally linked to warmer parts of the ADR through cables, indicates an additional input.[44] Both stages are affected since the cable coming from 4K-stage is thermally coupled to the GGG- and FAA-stage. Furthermore, influences from the anchoring of the cables are observed.[45]

- **Thermal radiation** $P_{\text{radiation}}$: The higher power load after CD 13 can also be caused by a stronger thermal radiation on the FAA stage. From CD 13, the thermal shield is mounted to FAA-stage.[46]

Further power loads can be for example heat transfer through gas, mechanical vibrations, and Joule heating of thermometers and sensors (White and Meeson, 2002). It is estimated that such effects are negligible compared to the effects above.

It is concluded that the cooling power depends on temperature and therefore on time while the double-stage pills unit thermalizes to the 4K-stage-temperature. The cooling power of the pills compensates several external power loads: thermal link through Vespel pin mounting, thermal radiation, wiring to the stage, and further heat transfers:

$$P_{\text{cooling}} = P_{\text{Vespel}} + P_{\text{radiation}} + P_{\text{wiring}} + \cdots$$

2.3.4.4. Holding mK-temperature for measurement with sensors

In this section, the performance of holding a mK-temperature (fig. 2.7b) is considered. To operate sensors as TESs, a stable temperature is recommended, since the bath temperature can influence the sensor response (sect. 3.1.2.2). Since the FAA temperature is regulated to 80 mK for TES measurements (sect. 3.4), the stability for 80 mK drifts is analyzed in the following.

To regulate the temperature after a recharge, the magnet current is adjusted with a software-based feedback loop. The feedback is realized by proportional-integral-derivative (PID) control (sect. 2.2.4). After switching on the regulation with proper settings,[47] it takes ~4 min to be at (80 ± 1) mK and additional ~2 min till the tem-

---

[43] For example, for FAA and 80 mK drifts between CD 8 and CD 13/15. For example, for GGG and 100 mK drifts between CD 5 and CD 7/8.

[44] Here, CD 1 without sensor modules and CD 5 with electrical connections to the sensor modules (app. C.3) are compared.

[45] Considering 80 mK holds within CD 17-21 a significant higher power during CD 17 is indicated (fig. 2.17a). This was caused by a bad thermal anchoring of the electrical wiring at the 4K-stage.

[46] According to the Stefan-Boltzmann law (eqn. A.7), thermal radiation from 4K-stage to the thermal shield results in P = 0.5 μW.

[47] The following PID-parameters were used in the considered sample: `Kp` -0.5, `Ki` -0.001, `Kd` -0.1. These settings ensure the starting of the regulation and the quite short time in order to reach 80 mK (Phelan, 2012).
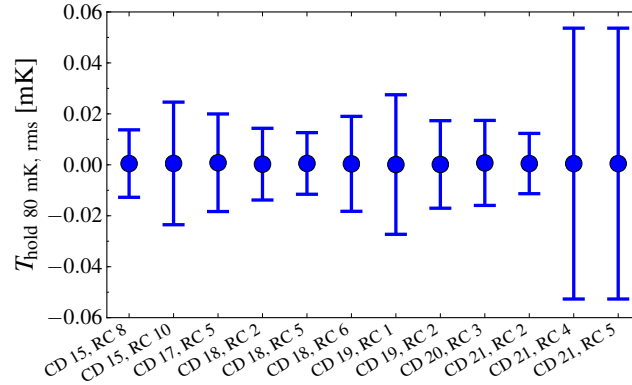
Figure 2.18.: Temperature stability during regulating to 80 mK: 80 mK holds of the analysis sample are shown. The RMS deflection is between 12-53 μK.

perature is stabilized within the root-mean-square (RMS) range. The RMS range is calculated with all measured temperatures of a full hold, and is the figure of merit of the temperature stability.

In figure 2.18, temperature stabilities of 80 mK holds from the analysis sample are depicted. The first ten holds have a RMS value <25 μK and fulfill the specification of the company offer (Entropy, 2011). The temperature stability depends on the feedback time of the regulation. Here, the FAA temperature is measured every ~2.4 sec. The higher RMS range of the latter two holds is mainly caused by a longer feedback time. Here, the FAA temperature is only measured every ~32 sec.[48] Furthermore, single heat-ups are observed occasionally: The FAA temperature spikes suddenly to 3 mK higher, before the regulation tunes the temperature back to 80 mK within ~30 mK. This is presumably caused by vibrations or mechanical stress relaxations, which could affect a heat input. Since the rate of such spikes is below one event per complete hold, these instabilities are uncritical for sensor operation.

---

[48]In these measurements, the GGG channel was activated. Therefore, the thermometry bridge required additional time to change the channels.

2.4. Summary and prospect for a TES detector

In section 2.1, it is explained that spin systems can be utilized to obtain a **cooling effect by adiabatic demagnetization**. A thermodynamic cycle allows to establish mK-environments. Using a quantitative description of an electron spin system allows to obtain equations describing the entropy, S, and the heat capacity, C.

In section 2.2, the **ADR cryostat system** is described which has been set up and characterized within this thesis. The ADR system incorporates a top-down cooling principle: A cold water cycle cools a double-stage pulse tube cryocooler for precooling below 4 K. The precooling is the bath for the adiabatic demagnetization cooling. The adiabatic demagnetization system incorporates a double-stage pills unit, a superconducting magnet to magnetize the pills, and a heat switch to couple and decouple the pill. For each pill, the heat capacity is calculated by theory (fig. 2.5) in order to characterize the system. The inner pill reaches mK-temperatures and forms the bath for superconducting sensors. The ADR system includes electronics and a control system to operate and monitor a cool-down.

The characterization of the ADR system concentrates on **thermalization times** and the **technical functionality** of the components (sect. 2.3.) A successful ADR run incorporates four phases (sect. 2.3.1):

- One cool-down from 300 K to $T_{\text{4K-stage}} \simeq 2.5$ K in $t_{\text{CD}} = 24.8 \pm 1.3$ h. After that time, the ADR reaches an equilibrium state with $T_{\text{70K}} \simeq 49.5$ K, $T_{\text{4K}} = T_{\text{pills}} \simeq 2.5$ K, and $p \simeq 3 \cdot 10^{-7}$ mbar.

- Recharges to load the pills in $t_{\text{recharge, FAA at 4 K}} \simeq 90 \pm 7$ min. The main part of the recharge time is due to the thermalization of the pills after magnetization.

- Subsequent drifts to 80 mK in $t_{\text{drift, 80 mK}} \simeq 18$ h or holds at 80 mK lasting $t_{\text{hold, 80 mK}} \simeq 25$ h.

- One warm-up to 300 K in $t_{\text{WU}} \simeq 19\text{-}26$ h.

The times mainly depend on the performance of the components as well as on the cold mass to thermalize.

Within this thesis, 35 runs were operated with different setups and alignments (app. E.2). The longest run took 22 days including 20 recharges. During the commissioning phase and from time to time during operation, various technical problems occurred which have been solved and optimized. It is indicated that the most critical component of the ADR is the **heat switch unit**. The analysis provides an understanding of the heat switch condition during recharge phases (fig. 2.9). This interpretation allows to explain different technical problems related to the heat switch and helps to find solutions. The most important results are:

- Slightly opened heat switch during cool-down (sect. 2.3.2): This ensures the movability of heat switch after precooling. Furthermore, the thermal coupling is satisfactory regarding the cool-down time.

- Closed condition before recharge is crucial (sect. 2.3.3.3): The closing condition of the heat switch is a trade-off between a sufficient thermal coupling and reliable opening in a full magnetic field. If the heat switch is closed too tight, the unit can reach an inappropriate condition due to the degree of freedoms and the forces during a recharge (sect. 2.3.3.1).

- After a proper alignment of the heat switch unit (app. D.1.1.3), the chance of a successful recharge is approximately 80 % (sect. 2.3.3.3). The performance gradually decreases due to loosening screws. Therefore, a regular realignment is required.

Furthermore, **mK-environments** are analyzed in detail (sect. 2.3.4). By considering drifts and holds, the evolution of the double-stage pills unit is described (sect. 2.3.4.1). Most important results are:

- The charged energy mainly depends on the thermalization temperature before ramping down (sect. 2.3.4.2).

- Holding a temperature show longer mK-times as drifting pills (sect. 2.3.4.2).

- The cooling power depends on temperature due to the heat capacity of the pills (sect. 2.3.4.3).

- Tightening the Vespel pins, cables to the FAA-stage, and the total mass attached to the FAA-stage decrease the mK-time (sect. 2.3.4.2 and 2.3.4.3).

Assuming proper parameters to calculate the heat capacity for the pills (fig. 2.5), the cooling energy and an effective cooling power can be estimated. Considering 80 mK holds for a setup of the ALPS TES detector with thermalization temperatures of ~4 K (sect. 3.4), typical values for the FAA pill are:

- holding times of ~20 h

- cooling energies of ~70 mJ

- effective cooling powers of ~0.9 μW

3. Superconducting sensors for photon detection and their environments

The goal of this chapter is a comprehensive understanding about TES detectors and the development of a TES detector system for ALPS. Therefore, superconducting sensors – TESs and SQUIDs – and their environments are considered which were used within this thesis. This chapter forms the second analysis of this thesis.

The first section 3.1 describes the TES theory in general. Equations of the signal and noise response are derived, as well as the SQUID theory which provides an understanding of transducing TES current into a voltage output. Sensor modules are described in section 3.2. Sensor modules incorporate TES and SQUID devices and were prepared and operated within this thesis. The NIST module is explained in detail which provides an application of the theory. Firstly, the realization for an operation in the ADR cryostat is given; secondly, the characterization of the module is described. Furthermore, other sensor modules are briefly described which were worked on within this thesis.

The environments of sensor modules are discussed in section 3.3. The electrical, magnetic, and thermal influences on sensors are studied and optimized to establish a sensitive and stable environment within the ADR cryostat in the ALPS IIa laboratory. In section 3.4, the TES detector setup for ALPS is summarized, which is called ALPS TES detector in the following. Furthermore, the working point of the ALPS TES detector and the corresponding parameters are given. This working point is used to study signals and backgrounds in chapter 4 of this thesis.

3.1. Theory on single photon detection with a TES

This chapter describes the physical basics to understand the working principle of TES based detectors. Firstly, features and properties of superconductivity are qualitatively explained (sect. 3.1.1). Secondly, and most prominently, TES physics is described (sect. 3.1.2). The mathematical framework of Irwin and Hilton (2005) is explained which allows to characterize TES devices and their response. Finally, the most important basics and properties of SQUIDs are discussed which work as TES read-out devices within this work (sect. 3.1.3).

3.1.1. Features of superconductivity

Superconductivity was first discovered by Kamerlingh Onnes (Onnes, 1911). For his investigations, he received the Nobel Prize in physics in 1913. 100 years later, the impact of superconductivity in science is immense. The prominent feature of zero-dissipative current flow of superconducting materials pushes forward many technical applications, for example strong magnets (sect. 2.2). Also, two main components of TES applications benefit from the properties of superconductivity: the TES itself and the SQUID for read-out.

Superconductivity is a unique property of certain conducting materials, which occurs if the material is below a specific **critical temperature** T_c: According to the BCS-theory,[1] two conducting electrons with antiparallel momentum and spin combine effectively to one so-called Cooper pair. Thus, these composite bosons underlie the Bose-Einstein statistics. Compared to conducting electrons, the Pauli exclusion principle is not valid. Therefore, all Cooper pairs are described by one wave function which results in the same quantum mechanical state. A current consisting of Cooper pairs is a supercurrent which flows without resistance.

Superconducting phase transitions occur typically in small temperature ranges depending on material properties. Considering the electrical resistance around the critical temperature T_c, a steep slope of the resistance occurs (e.g. fig. 3.1b). In the transition region, electrons and Cooper pairs occur both and the resistance does not follow Ohm's law anymore. With regard to the TES, the transition from normal conducting to superconducting looks like an *edge* (sect. 3.1.2).

Furthermore, superconductors exhibit a **critical super current density** j_c. The energy of a supercurrent in a superconductor corresponds to the kinetic energy of Cooper pairs. Above j_c the kinetic energy reaches the binding energy of Cooper pairs. Then, Cooper pairs break and the superconductivity fades away. This feature is important to bring superconducting sensors to their working point.

Another feature is the **expulsion of external magnetic flux** which is named Meissner-Ochsenfeld effect after the discoverers. External magnetic flux is expelled

---

[1] This theory is named after its originators J. Bardeen, L. N. Cooper, and J. R. Schrieffer. It is a microscopic description of superconductivity.

due to supercurrents within the superconductor which cancels the field. This flux expulsion is valid until the external magnetic field exceeds a critical value B_c which breaks Cooper pairs. This feature is important regarding superconducting magnetic shielding.

Finally, considering a **superconducting loop** structure, magnetic flux threading this loop is quantized. The magnetic flux is an integer multiple of the magnetic flux quantum $\Phi_0 = \frac{h}{2e} = 2.068 \cdot 10^{-15}$ Wb or J/A or Tm^2, where h is the Planck constant and e the elementary charge. This feature is important regarding SQUIDs.

Detailed explanations and theory on superconductivity are given in many text-books (Buckel and Kleiner, 2012, e.g.). Concerning phase transitions of metallic TES films, a comprehensive explanation is found in the thesis of Lindeman (2000).

3.1.2. Response of transition-edge sensors

In this chapter, the theoretical framework for the TES response is explained. Firstly, the basic working principle including a thermal and an electrical circuit is presented (sect. 3.1.2.1). According to Irwin and Hilton (2005), the mathematical framework of TES physics is described. Irwin and Hilton (2005) is the standard review about TES physics and is applied to characterize sensor modules (sect. 3.2). Thus, the thermal and electrical differential equations (sect. 3.1.2.2) and their solution describing signal and noise response (sect. 3.1.2.3) are explained.[2] Finally, it is summarized which mode and working point are aimed to operate a TES as a single photon detector (sect. 3.1.2.4). Therefore, it should be noted that the focus is on TES operation as a calorimeter – not as a bolometer[3] – with strong negative electrothermal feedback and with SQUID read-out.

In the following, the TES resistance appears in different notations, due to different meanings and values. Often R_{TES} is indicated by $R(T, I)$ which expresses the dependence on temperature T and current I. R_N means that the TES is in its normal resistance above the superconducting transition temperature. R_0 is the value at the working point.

3.1.2.1. Working principle

A Transition-Edge Sensor (TES) incorporates a thermal and an electrical circuit. The **thermal system** alone is a classical calorimeter (fig. 3.1a). It includes the heat capacity C of the sensor[4] and a thermal link to a bath with a constant temperature

---

[2]If it is not mentioned, the notation of quantities accords to Irwin and Hilton (2005).

[3]Bolometers are defined to measure power, calorimeters are defined to measure single pulses of energy (Irwin and Hilton, 2005).

[4]Here, the sensor material is simultaneously the absorber material. Basically, the sensor can be attached to a different absorber material to measure the change of energy.

T_{bath}. The link is given by the thermal conductance G.[5] As a closed system, it reaches a thermal equilibrium so that the absorber has the same temperature as the bath. If the sensor absorbs an energy input ΔE, it is heated up by

$$\Delta T = \frac{\Delta E}{C} \tag{3.1}$$

Because of the link to the bath, the sensor cools down again. After an instantaneous heat-up ΔT at time $t = 0$, the temperature evolution is described by $T(t) \sim \exp(-t/\tau)$. Here, τ is the natural thermal time constant which is given by the parameters of the thermal system:

$$\tau = \frac{C}{G} \tag{3.2}$$

To use the sensor as a **sensitive thermometer**[6], the temperature T has to correspond to an adequate measurable quantity. In many realizations, this is the electrical resistance; for example, such as in thermometers integrated at each temperature stage of the ADR (sect. 2.2). The TES as a thermometer benefits from a dramatic change in resistance R: The working point is between the normal and superconducting state of the sensor's material; in other words, within the *transition edge*. Since superconducting transitions $R(T)$ are mostly steep, TESs can reach a high sensitivity. Here, a small temperature change ΔT means a large resistance change ΔR (fig. 3.1b). How sharply the resistance changes with the temperature is expressed by

$$\alpha = \frac{T_0}{R_0} \frac{\partial R}{\partial T} \tag{3.3}$$

where α is called temperature sensitivity. R_0 and T_0 indicates a steady state, like the working point.

Otherwise, it is challenging to stably operate the TES in a sharp and narrow transition, just by regulating the temperature T_{bath}. Therefore, the TES is implemented in an electrical circuit, which is depicted by the upper part of figure 3.1a. If the TES is cooled and superconducting, so that $T_{\text{bath}} < T_{\text{c}}$, applying an electrical current I allows to set the TES within the transition. A high enough current provides a breaking of Cooper pairs. This results in a state between the superconducting and normally conducting phase. By analogy to α, the transition sensitivity referred to the current is defined by

$$\beta = \frac{I_0}{R_0} \frac{\partial R}{\partial I} \Big|_{T_0} \tag{3.4}$$

where R_0, I_0, and T_0 are the steady-state variables at the working point.

Thus, the TES resistance depends on temperature and current, $R_{\text{TES}} = R(T, I)$,

---

[5]The thermal link should be weak enough so that the absorber has time to thermalize when an energy input occurs.

[6]Technically speaking, it is a thermistor.

(a) TES thermal and electrical system
plus SQUID read-out

(b) transition and working point

(c) TES signal
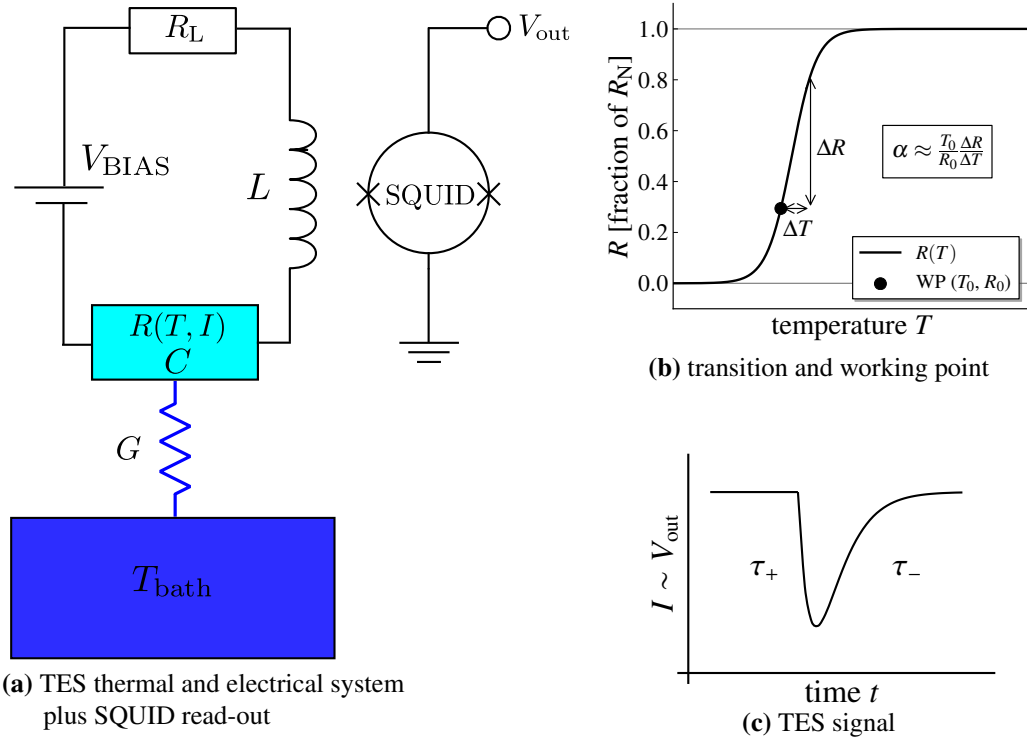
Figure 3.1.: TES in a nutshell: Electrical and thermal circuit, superconducting transition, resulting signal. (a) shows the coupled circuits of a TES with resistance $R(T, I)$ and heat capacity C (light blue). The thermal system (lower part) consists of the absorber (TES) with heat capacity C, a heat bath at a temperature T_{bath} , and a thermal link defined by the thermal conductance G. The electrical circuit (upper part) includes the resistive TES $R(T, I)$, a constant voltage source V_{BIAS}, a load resistance R_{L}, and an inductance L. The inductance magnetically couples to a SQUID which provides a low-noise read-out resulting in a voltage output V_{out}. (b) illustrates a superconducting transition of a TES, $R(T)$, and a working point. Below a certain temperature, the electrical resistance is zero and the TES is superconducting. By increasing the temperature, the resistance is increasing as well and is running through a steep slope, until the normal ohmic resistance R_{N} is reached. The TES working point (WP, black dot) lies within the phase transition. In realization, the working point is adjusted by applying a current, since the resistance also depends on current, $R(I)$. (c) shows a typical signal. The current change I and the corresponding voltage output V_{out} is negative if the TES temperature change is positive due to an energy input like a photon. The pulse response is described by a rise time τ_+, and after the peak by a fall time τ_-.

which allows a feedback mechanism providing advantages compared to a classical calorimeter. By applying a proper constant voltage V_{BIAS} (fig. 3.1a), the required current I_0 can be adjusted to bring the TES within the superconducting transition. The TES has a non-zero resistance R_0 and a certain temperature T_0. In an idealized picture without any influences, this is a stable equilibrium point where the Joule power corresponds to the power flow to the bath: $P_{\text{J}_0} = V_{\text{TES}}^2 / R_0 = P_{\text{bath}}$. It is

assumed that the TES voltage $V_{\text{TES}} = RI$ stays constant which is valid in a voltage bias condition (see below). If the TES heats up due to an external power or energy input, e.g. due to a photon, the resistance increases: $R_0 + \delta R$. An increase in resistance results in a smaller Joule power due to the constant voltage, and thus, the Joule heating is decreased. In turn, the TES relaxes back in the equilibrium state via the power flow to the bath. This principle is called **negative electrothermal feedback (negative ETF)**. Because of the constant voltage bias condition, it is a negative feedback. In comparison, a current biased TES would result in a positive feedback since the Joule heating would be increased at an external energy input.

Negative ETF provides several advantages compared to classical calorimeters or realizations with a constant current bias:

- Stable operation: The TES self-regulates and is less sensitive to thermal fluctuations. By comparison, a current biased TES results in a positive ETF. This can cause a thermal runaway, as a temperature increase causes an enhancement of the Joule power $P_{\text{J}} = I^2 R$ due to the constant current I.

- Faster signals: The natural time constant τ of the classical calorimeter is diminished due to negative ETF (sect. 3.1.2.3).

- Self-calibration: The energy input is "removed" by the ETF mechanism. This allows a calibration of the TES (sect. 3.1.2.3).

- Enhanced signal-to-noise ratio: Although the thermal response for signals and noise is comparably increased, all non-phononic noise components are suppressed within the ETF bandwidth (sect. 3.2.2.5).

Therefore, it is aimed to realize a strong negative ETF for sensitive photon TES detectors. Conditions for strong negative ETF are developed in the following sections and summarized in section 3.1.2.4.

In the following, components of the **electrical circuit** and their importance for TES realization are explained. The load resistance R_{L} defines the bias condition:

- The TES is strong current-biased – for positive ETF – if $R_{\text{L}} \gg R_0$.

- The TES is strong voltage-biased – for negative ETF – if

$$R_{\text{L}} \ll R_0 \tag{3.5}$$

  In fact, for a pure voltage bias, the inductance L should even vanish, $L \to 0$. Lindeman (2000) points out that the inductance can provide a current bias at high frequencies.

Since the load resistance is finite, the TES circuit appears in a mixed bias condition. The ratio between voltage and current bias is given by the ratio of the TES resistance in working point R_0 and R_{L}. In a strong voltage-biased condition with small inductance L, the voltage across the TES is given by the bias voltage:

$$V_{\text{TES}} = IR(T, I) \approx V_{\text{BIAS}} = const. \tag{3.6}$$
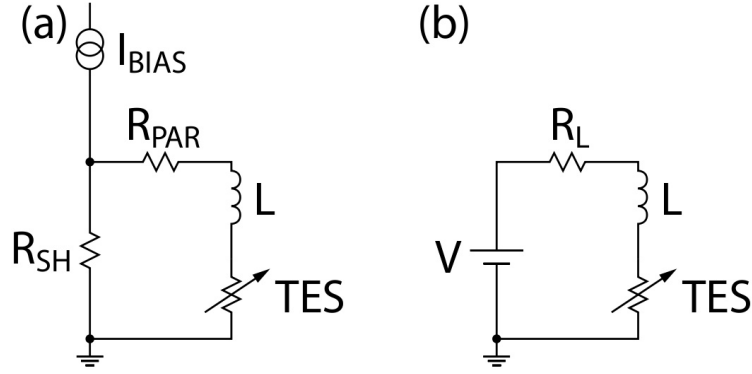
Figure 3.2.: Electrical TES circuit in two representations: (a) shows a circuit, how the wiring of a TES is mostly realized. (b) shows the equivalent circuit which is used for theoretical description and calculations. This circuit corresponds to the electrical circuit in figure 3.1a, with $V = V_{\text{BIAS}}$. [Taken from Irwin and Hilton (2005).]

According to the advantages above, it is aimed for a strong voltage-biased realization of the TES circuit with small L. This leads to simplifications of the response (sect. 3.1.2.3) and a stability criterion of the response (sect. 3.2.2.2).

To describe the TES physics in the next section 3.1.2.2, the electrical circuit in figure 3.1a is used. However, to realize a constant bias voltage, a current divider circuit is mostly used (fig. 3.2a). A constant current source I_{BIAS} is used, and the current is divided in two branches through a shunt resistor R_{SH} and through the TES branch with total resistance $R_{\text{TES branch}} = R_{\text{TES}} + R_{\text{PAR}}$. Here, R_{PAR} is a possible parasitic resistance due to non-superconducting parts in the circuit. R_{SH} defines, how much current of I_{BIAS} passes through the TES branch:

$$\frac{R_{\text{TES branch}}}{R_{\text{SH}}} = \frac{I_{\text{BIAS}}}{I_{\text{TES}}} - 1 \tag{3.7}$$

where I_{TES} is the current through the TES, which corresponds to the current of the whole TES branch according to Kirchhoff's law. The equivalence between the two circuits in figure 3.2 is given by Thevenin's theorem (Horowitz and Hill, 1989, e.g.):

$$R_{\text{L}} = R_{\text{SH}} + R_{\text{PAR}} \tag{3.8}$$

$$V_{\text{BIAS}} = I_{\text{BIAS}} R_{\text{SH}} \tag{3.9}$$

To read out the change of the TES resistance, the electrical circuit includes an inductance L (fig. 3.1a or 3.2).[7] When the TES resistance changes, the current through the TES changes vice versa, because of the voltage bias condition (eqn. 3.6). Hence,

---

[7]The inductance is composed of the stray inductance through wiring and the input inductance in the SQUID chip. Concerning the TES response, the total inductance has to be considered; concerning the SQUID read-out, only the input inductance has to be considered.

a TES heat-up results in a smaller current and a negative pulse out of equilibrium (fig. 3.1c). The inductance L translates the changing current into a changing magnetic field. This provides the coupling to a SQUID to read out the TES response. This results in a voltage output V_{out}. The read-out via SQUIDs is explained in section 3.1.3.

3.1.2.2. Thermal and electrical differential equation

In this chapter, the mathematical description of the electro-thermal system of a TES is explained according to Irwin and Hilton (2005). Therefore, differential equations are formulated. Due to non-linear terms, equations are linearized to obtain the TES response (sect. 3.1.2.3).

The thermal system (fig. 3.1a) and its dynamic can be described by considering all powers influencing the TES. The power flow to the bath P_{bath} equals all power inputs: $P_{\text{bath}} = P_{\text{TES}} + P_{\text{J}} + P$. P_{TES} is the energy change by time. This is given by the change of heat $dQ = CdT$ which is proportional to the change of temperature dT related to the heat capacity C. This results in: $P_{\text{TES}} = \frac{dQ}{dt} = C\frac{dT}{dt}$. Furthermore, $P_{\text{J}}(R(T, I))$ is the power dissipated by Joule heating of the resistive TES. P is an arbitrary power input, like photon signals or noise. This results in the **thermal differential equation**:

$$C\frac{\mathrm{d}T}{\mathrm{d}t} = -P_{\text{bath}} + P_{\text{J}}(R(T, I)) + P \tag{3.10}$$

Considering voltages of the electrical circuit (fig. 3.1a), it can be drawn up: $V_{\text{BIAS}} = V_{\text{L}} + V_{\text{ind}} + V_{\text{TES}}$. According to Kirchhoff's law, the applied bias voltage V_{BIAS} corresponds to the sum of voltages across the three components in series. The voltage across the load resistance is $V_{\text{L}} = I R_{\text{L}}$ and the voltage across the TES is $V_{\text{TES}} = I R(T, I)$. The voltage across the inductance L is $V_{\text{ind}} = L\frac{dI}{dt}$, where a current change induces a voltage due to self inductance. This results in the **electrical differential equation**:

$$L\frac{\mathrm{d}I}{\mathrm{d}t} = V_{\text{BIAS}} - I R_{\text{L}} - I R(T, I) \tag{3.11}$$

The two differential equations 3.10 and 3.11 describe the dynamic of the thermal and electrical circuit, and therefore, the response of the TES. They are coupled through the resistance $R(T, I)$. T and I are the time-dependent state variables of this system.[8] To describe the signal and signal response, the small-signal limit around the operating point is considered. R_0, T_0, and I_0 are the steady-state values at the working point.[9] A small deviation of the steady-state is indicated by a δ. Taking as

---

[8]In principle, the voltage V could be used instead of I (Lindeman, 2000).

[9]For the heat capacity C and the thermal conductance G, the steady-state values are used. This means that they are independent of temperature changes within this approximation.

an example, the temperature is $T = T_0 + \delta T$. This allows to linearize several terms in order to solve these coupled differential equations.

To linearize the TES resistance $R(T, I)$, it is expanded by Taylor series to the first order. Around the steady-state, it results in

$$R(T, I) \approx R_0 + \alpha \frac{R_0}{T_0} \delta T + \beta \frac{R_0}{I_0} \delta I \tag{3.12}$$

with equation 3.3 and 3.4. The Joule power of the TES is given by[10]

$$P_{\mathrm{J}} = I^2 R(T, I) \tag{3.13}$$

Similarly, this can be expanded and, using equation 3.12, it results in

$$P_{\mathrm{J}} \approx P_{\mathrm{J}_0} + 2I_0 R_0 \delta I + \alpha \frac{P_{\mathrm{J}_0}}{T_0} \delta T + \beta \frac{P_{\mathrm{J}_0}}{I_0} \delta I \tag{3.14}$$

where $P_{\mathrm{J}_0} = I_0^2 R_0$ is the quiescent power at the working point.

The power flow to the bath is described by a power law

$$P_{\mathrm{bath}} = \frac{G}{n\,T^{n-1}}(T^n - T_{\mathrm{bath}}^n) \tag{3.15}$$

where the exponent n defines the thermal link of the sensor to the bath. This includes the definition of the thermal conductance: $G \equiv dP_{\mathrm{bath}}/dT$. Equation 3.15 is linearized by the first order of Taylor series:

$$P_{\mathrm{bath}} \approx P_{\mathrm{bath}_0} + G\delta T \tag{3.16}$$

Here, P_{bath_0} is the steady-state power, which is directly given by equation 3.10:

$$P_{\mathrm{bath}_0} = P_{\mathrm{J}_0} + P_0 \tag{3.17}$$

where P_0 is the steady-state input power.

Using the expressions 3.2, 3.12, 3.14, and 3.16, and substituting the small-signal values δT and δI for the state variables T and I, equations 3.10 and 3.11 result in **linearized differential equations**:

$$\frac{\mathrm{d}\delta T}{\mathrm{d}t} = \frac{I_0 R_0 (2 + \beta)}{C} \delta I + \frac{1}{\tau_I} \delta T + \frac{\delta P}{C} \tag{3.18}$$

$$\frac{\mathrm{d}\delta I}{\mathrm{d}t} = -\frac{1}{\tau_{\mathrm{el}}} \delta I - \frac{\mathscr{L}_I G}{I_0 L} \delta T + \frac{\delta V}{L}, \tag{3.19}$$

Here, three variables are introduced:

---

[10]Joule power is $P = VI$ in general. Here, it is expressed in the state variable current I.

- The low-frequency feedback loop gain under constant current is

$$\mathscr{L}_I \equiv \frac{P_{J_0}\alpha}{GT_0} \tag{3.20}$$

This is a useful quantity to consider the strength of ETF: Strong negative ETF is given by (sect. 3.1.2.4):

$$\mathscr{L}_I \gg 1, \beta \tag{3.21}$$

Furthermore, it indicates the TES stability which is tested in section 3.2.2.2.
- The current-biased thermal time constant is

$$\tau_I = \frac{\tau}{1 - \mathscr{L}_I} \tag{3.22}$$

τ_I would give the exponential fall of temperature in the limit of $\delta I = 0$.[11]
- The electrical time constant is

$$\tau_{el} = \frac{L}{R_L + R_0(1 + \beta)} \tag{3.23}$$

τ_{el} would describe the exponential fall of current in a limit of $\mathscr{L}_I = 0$.[12]
In the next section, solutions of this mathematical TES description are presented.

3.1.2.3. Signal and noise response

The linearized differential equations 3.18 and 3.19 are coupled by δT and δI. A solution of the homogeneous form, where $\delta P = 0$ and $\delta V = 0$, is found by decoupling the equations. For example, this is done by diagonalizing a matrix representation of the coupled system. With the homogeneous solution, a specific solution can be found. Without presenting these calculations, two specific solutions are considered in the following:

- an impulse of energy (delta function) representing a **signal**, and
- a frequency-dependent power load (sinus function) representing a **noise**.

Additionally, simplifications are discussed which are caused by a strong negative ETF operation.

A **signal** can be approximated by an absorption in the TES material with an instantaneous thermalization. This is expressed by the initial conditions $\delta T(0) = \Delta T = \Delta E/C$ and $\delta I(0) = 0$. Together with the homogeneous solution, this results in

---

[11] This case is called hard current bias. Assuming $\delta I = 0$ and integrating equation 3.18 result in the time constant τ_I.

[12] By integrating equation 3.19.

equations for the temperature and the current for times $t > 0$:[13]

$$\delta T(t) \;=\; \left(\left(\frac{1}{\tau_I} - \frac{1}{\tau_-}\right)e^{-t/\tau_+} - \left(\frac{1}{\tau_I} - \frac{1}{\tau_+}\right)e^{-t/\tau_-}\right)\frac{\Delta T}{(1/\tau_+ - 1/\tau_-)} \tag{3.24}$$

$$\delta I(t) \;=\; \left(\frac{\tau_I}{\tau_+} - 1\right)\left(\frac{\tau_I}{\tau_-} - 1\right)\frac{1}{(2+\beta)}\frac{C\Delta T}{I_0 R_0 \tau_I^2}\frac{\left(e^{-t/\tau_+} - e^{-t/\tau_-}\right)}{(1/\tau_+ - 1/\tau_-)} \tag{3.25}$$

where τ_+ is the rise time and τ_- is the fall time of the signal pulse. These constants are the inverse eigenvalues resulting from diagonalization of the coupled system and are given by:

$$\frac{1}{\tau_\pm} = \frac{1}{2\tau_{\mathrm{el}}} + \frac{1}{2\tau_I} \pm \frac{1}{2}\sqrt{\left(\frac{1}{\tau_{\mathrm{el}}} - \frac{1}{\tau_I}\right)^2 - 4\frac{R_0}{L}\frac{\mathscr{L}_I(2+\beta)}{\tau}} \tag{3.26}$$

Equations 3.24 and 3.25 are complete solutions of a signal response of a TES microcalorimeter. A signal pulse is described by 11 independent parameters: four thermal parameters α, β, G, and C, three steady-state variables T_0, I_0, and R_0, three electrical parameters R_{SH}, R_{PAR}, and L, and the energy input ΔE (eqn. 3.1). These parameters are exemplarily determined for the NIST module in chapters 3.2.2.1 and 3.2.2.2. In chapter 3.2.2.4, a measured signal is compared to the linear small-signal theory.

Expressions of fall and rise time simplify under specific conditions. For small inductance L with $\tau_+ \ll \tau_-$, the time constants simplify to:

$$\tau_+ \;\rightarrow\; \tau_{\mathrm{el}} \tag{3.27}$$

$$\tau_- \;\rightarrow\; \tau_{\mathrm{eff}} \equiv \tau\,\frac{1 + \beta + R_L/R_0}{1 + \beta + R_L/R_0 + (1 - R_L/R_0)\mathscr{L}_I} \tag{3.28}$$

Furthermore, if the TES is operated in voltage bias condition (eqn. 3.5) and strong ETF (eqn. 3.21), τ_{eff} reduces to $\frac{\tau}{1+\mathscr{L}_I}$. If T_{bath} is small compared to the transition temperature T_0, equation 3.15 is approximated by $P_{\mathrm{bath}_0} \approx GT_0/n$. By assuming that P_{J_0} is described by P_{bath_0} due to small P_0 (eqn. 3.17), it is $\mathscr{L}_I \approx \alpha/n$. This results in the ETF time constant:

$$\tau_{\mathrm{eff}} \rightarrow \tau_{\mathrm{ETF}} \equiv \frac{\tau}{1 + \alpha/n} \tag{3.29}$$

The ETF time constant directly expresses the faster response compared to a classical calorimeter with time constant τ and without feedback. Therefore, it is often considered in TES literature. It is summarized, for strong negative ETF and sufficient cold bath T_{bath_0}, basically, the rise time is given by the electrical time constant

---

[13]In Irwin and Hilton (2005), equation 3.24 has a *plus* sign between exponential parts. A recalculation indicates a misprint, which is confirmed by one of the authors (Irwin, 2014).

τ_{el} and the fall time by the ETF time constant τ_{ETF}.

The current response corresponds to an energy due to the ETF mechanism. The time integral over a current pulse (eqn. 3.25) times the TES voltage results in the so-called ETF energy. In a voltage bias condition, the integral reduces to:

$$E_{\text{ETF}} = -\int_0^\infty V_{\text{TES}}(t)\, \delta I(t)\, \mathrm{d}t \approx -I_{\text{BIAS}}\, R_{\text{SH}} \int_0^\infty \delta I(t)\, \mathrm{d}t \tag{3.30}$$

This energy corresponds to the signal energy which allows to calibrate the TES. Since the ETF energy is independent of intrinsic TES parameters and only depends on electrical circuit parameters, the TES response is self-calibrating.

In the following, three TES noise components are presented to get the fundamental limit of the energy resolution. Fundamental **noise** sources of a TES device are:

- the Johnson-Nyquist noise[14] due to thermodynamic fluctuations associated with an electrical impedance (Johnson, 1928; Nyquist, 1928), here,

  - the TES resistance R_{TES} and
  - the load resistance R_{L}, and

- the thermal fluctuation noise (TFN) due to thermodynamic fluctuations associated with a thermal impedance, here, the thermal conductance G.

To express the frequency dependence of noise components, small sinusoidal fluctuations are considered. A fluctuation in power $\delta P = \mathrm{Re}(\delta P_0 e^{i\omega t})$ (eqn. 3.18) results in the general complex power-to-current sensitivity $s_I(\omega)$ by solving the differential equations 3.18 and 3.19:[15]

$$s_I(\omega) = -\frac{1}{I_0 R_0}\frac{1}{(2+\beta)}\frac{(1 - \tau_+/\tau_I)}{(1 + i\omega\tau_+)}\frac{(1 - \tau_-/\tau_I)}{(1 + i\omega\tau_-)}. \tag{3.31}$$

where $\omega = 2\pi f$. $s_I(\omega)$ is used to express noise components in spectral current density S^I in units of A^2/Hz.[16]

The Johnson-Nyquist noise of the TES resistance in the working point R_0 is:

$$S^I_{R_{\text{TES}}}(\omega) = 4k_{\text{B}} T_0 R_0 \cdot I_0^2 \frac{\xi(I)}{\mathscr{L}_I^2}(1 + \omega^2\tau^2)|s_I(\omega)|^2 \tag{3.32}$$

where the DC-component corresponds to the voltage noise of an ohmic resistor: $S^V = 4kTR$ with the Boltzmann constant k_{B}. The factor $\xi(I)$ describes the non-linearity of the TES resistance. For the linear case, it is $\xi(I) = 1$; for the first order

---

[14]Or just Johnson noise.

[15]A fluctuation in voltage $\delta V = \mathrm{Re}(\delta V_0 e^{i\omega t})$ (eqn. 3.19) would result in the general expression for the electrical impedance.

[16]For better clarity, the current referred noise S^I is indicated here by a superscript instead of a subscript as found in standard literature.

of non-linear resistance, it is $\xi(I) = 1 + 2\beta$. Analogously, the Johnson-Nyquist noise of the load resistance R_L is:

$$S^I_{R_\mathrm{L}}(\omega) = 4k_\mathrm{B}T_\mathrm{L}R_\mathrm{L} \cdot I_0^2 \frac{(\mathscr{L}_I - 1)^2}{\mathscr{L}_I^2}(1 + \omega^2\tau_I^2)|s_I(\omega)|^2 \tag{3.33}$$

The thermal fluctuation noise (TFN) is:

$$S^I_{G_\mathrm{TFN}}(\omega) = 4k_\mathrm{B}T_0^2 G \cdot F(T_0, T_\mathrm{bath})|s_I(\omega)|^2 \tag{3.34}$$

where the DC-component corresponds to the power noise across the thermal conductance G: $S^P = 4k_\mathrm{B}T_0^2 G$. $F(T_0, T_\mathrm{bath})$ is a dimensionless function which depends on the conductance exponent n. For operating TESs, it is between 0.5 and 1.

Thus, the total fundamental noise of a TES is:

$$S^I_{\text{TES fund.}}(\omega) = S^I_{R_\mathrm{TES}}(\omega) + S^I_{R_\mathrm{L}}(\omega) + S^I_{G_\mathrm{TFN}}(\omega) \tag{3.35}$$

Additional noise sources can occur, such as quantum, superconducting, or further thermal fluctuations. Furthermore, excess noise is observed by different groups. Additional components are discussed by means of the NIST module in section 3.2.2.5.

The noise defines the **energy resolution** of a TES calorimeter, which is given by:[17]

$$\Delta E_\mathrm{rms} = \left(\int_0^\infty \frac{4}{S^I(f)/|s_I(f)|^2} \mathrm{d}f\right)^{(-1/2)} \tag{3.36}$$

where $f = \omega/2\pi$. Here, Gaussian noise sources are assumed, which is valid for linear elements. Thus, for nonlinear TES resistance or thermal conductance, equation 3.36 is a first approximation. The total TES noise (eqn. 3.35) is a fundamental limit for the energy resolution. In the case of negative strong ETF, equation 3.36 reduces to

$$\Delta E_\mathrm{rms} = \sqrt{\frac{4k_\mathrm{B}T_0^2 C}{\alpha}\sqrt{\frac{n(1 + 2\beta)}{1 - (T_\mathrm{bath}/T_0)^n}}} \tag{3.37}$$

where $F(T_0, T_\mathrm{bath}) = 1$ (eqn. 3.34), and $\xi(I) = 1 + 2\beta$ (eqn. 3.32). For the NIST module, this fundamental limit is compared to measurements in section 3.2.2.5.

---

[17]Here, the root-mean-square (rms) value is given which represents one standard deviation. In literature, often the value of the full width at half maximum (FWHM) is given which is related to the rms-value by: $\Delta E_\mathrm{FWHM} = 2\sqrt{2\ln 2}\,\Delta E_\mathrm{rms} \approx 2.36\,\Delta E_\mathrm{rms}$.

3.1.2.4. TES operation mode and working point

The previous chapters have shown that it is beneficial to operate the TES in the limit of strong negative ETF. Strong negative ETF provides stable operation, faster signals and self-calibration (sect. 3.1.2.1). It is summarized that strong negative ETF is given if

- the TES is strong voltage-biased, $R_0 \gg R_L$ (eqn. 3.5),
- the low-frequency loop gain is larger than one and β: $\mathscr{L}_I \gg 1, \beta$ (eqn. 3.21).

From an experimental point of view, a high loop gain $\mathscr{L}_I$ is reached by strong Joule heating, since $\mathscr{L}_I \sim P_{J_0} \sim I_0^2$ (eqn. 3.20). The TES current at working point I_0 compensates the power flow to the bath. This means, the lower the bath temperature, the higher the required bias current to reach the superconducting transition. Therefore, a low operating bath temperature T_{bath} is favored. However, by using an ADR cryostat as bath, T_{bath} is constrained by the favored hold time for mK-temperatures (sect. 3.4).
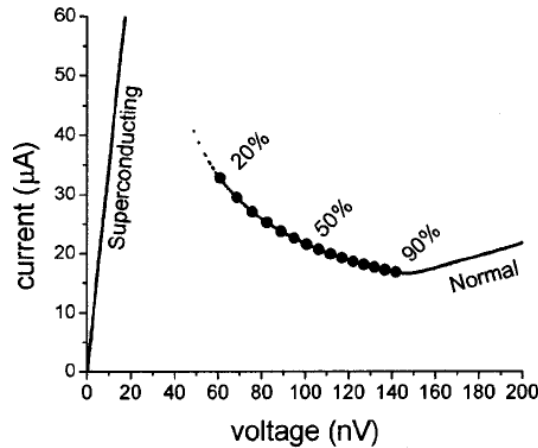
Figure 3.3.: *IV*-characteristic of a TES: Technically speaking, the voltage across the TES branch in the circuit is depicted against the current through this branch. The *IV*-curve incorporates three parts: At low voltages, the TES is superconducting and a small, parasitic resistance causes an ohmic slope. At sufficiently high voltages, the TES is normal resistive and causes an ohmic slope with the inverse R_N as gradient. In between, the superconducting transition occurs. Here, black dots illustrate working points in steps of ~5 % as a fraction of R_N. [Taken from Lindeman (2004)]

The working point of a TES is found by the **current-voltage characteristic or *IV*-curve** of a specific bath temperature $T_{\text{bath}} < T_c$. The superconducting transition can be passed through by applying different voltages across the TES. In figure 3.3, a typical *IV*-characteristic is depicted.[18] Beginning with high voltages, the TES is

---

[18] An *IV*-curve for a voltage-biased TES with strong Joule heating is shown. Lindeman (2000) gives a comprehensive overview of *IV*-characteristics of different bias conditions.

normal conductive at sufficient large voltages and the $I(V)$-dependence is linear due to Ohm's law. The normal resistance is directly given by the inverse gradient:

$$R_{\mathrm{N}} = \left(\frac{I_{\mathrm{TES}}}{V_{\mathrm{TES}}} \right)^{-1} \tag{3.38}$$

Since the resistance decreases within the transition (fig. 3.1b), the *IV*-characteristic shows large values of current with lower values of voltage till the TES is completely superconducting. At low voltages, a steep slope can occur which is caused by small non-superconducting parasitic resistances R_{PAR}.

The **working point** of a TES lies within the superconducting transition and has a specific resistance which is expressed in fractions of the normal resistance: $R_0 = \mathrm{frac.} \times R_{\mathrm{N}}$. The intersection between the line with gradient $(\mathrm{frac.} \times R_{\mathrm{N}})^{-1}$ and the *IV*-curve provides the corresponding voltage, which is needed for a specific working point (fig. 3.3). The working point with a constant voltage across the TES provides a stable equilibrium and defines the state variables R_0 and I_0. Furthermore, the working point sets the TES response.

In section 3.2.2, the NIST module is characterized for a specific working point. Exemplary *IV*-curves of the NIST module are shown in section 3.2.2.1. The measurement method of *IV*-curves is presented in the appendix D.3.2.2. The favored working point of the ALPS TES detector setup for background measurements is summarized in section 3.4.

3.1.3. Current read-out with SQUIDs

In principle, a superconducting quantum interference device (SQUID) is a sensitive magnetic flux sensor. The magnetic flux through the SQUID loop is converted into a voltage or current. As a prominent application, SQUIDs are used as low noise current sensors. To measure the current, a pickup or input coil is arranged to the SQUID. This allows to realize low noise read-out schemes for cryogenic detectors such as TESs.

Since the field of SQUIDs is rather wide, this chapter is focussing on the theoretical basics to understand the application for TES read-out. Therefore, single dc SQUIDs are considered here.[19] This does not restrict the understanding of more sophisticated devices like 2-stage SQUIDs which were operated within this thesis (sect. 3.2.1.3). In the following, reference is mainly made to the standard textbooks Clarke and Braginski (2004) and Clarke and Braginski (2006) which include an extensive look on SQUIDs and their applications. In this chapter, firstly, the working principle, the so-called SQUID modulation, and the working point are briefly explained (sect. 3.1.3.1). Secondly, basics of TES read-out are described (sect. 3.1.3.2).

3.1.3.1. Working principle and working point

A dc SQUID incorporates a superconducting ring with two Josephson junctions (fig. 3.4a). Therefore, firstly, properties of one **Josephson junction** are briefly considered. A Josephson junction consists of two weakly coupled superconductors which can be realized by a proper insulating layer between superconducting material. In 1962, B. D. Josephson predicts a supercurrent I_s across this junction by tunneling of Cooper pairs. This is given by the first Josephson equation:

$$I_s = I_0 \sin \delta \tag{3.39}$$

where δ is the phase difference of the wave functions of the two superconductors; I_0 is the maximum supercurrent and critical current at the same time. The second Josephson equation describes the time dependence of δ which results in a voltage U across the junction:[20]

$$\frac{\partial \delta}{\partial t} = \frac{2\pi}{\Phi_0} U \tag{3.40}$$

where Φ_0 is the magnetic flux quantum.

The whole dynamics of a Josephson junction can be developed by the so-called resistively- and capacitively-shunted junction (RCSJ) model. The junction is explained by an equivalent circuit which incorporates an ohmic resistor, a capacitor,

---

[19]Here, dc indicates SQUIDs with two Josephson junctions compared to RF (radio frequency) SQUIDs, which only consists of one junction.

[20]U indicates the real voltage; subsequently, V is the time averaged dc voltage across the junction.

and an element for the supercurrent in parallel (fig. 3.4a). Without describing calculations of the model in detail, the most important consequences are given. The total current across a Josephson junction I_J generally consists of three components:

- a supercurrent I_s due to Cooper pairs,
- a quasiparticle current I_{qp} due to electrons due to the resistive property of the junction, and
- a displacement current I_d due to the capacitive property of the junction.

In the static zero-voltage state, δ is constant (eqn. 3.40) and, according to equation 3.39, a dc supercurrent can flow. This implies that Josephson junctions show a nonlinear *IV*-characteristic due to the supercurrent which is distinctive for $I_J < I_0$. Finally, in the dynamic non-zero voltage state and for currents $I_J > I_0$, the supercurrent oscillates with the so-called Josephson frequency f_J. It is $f_J = V/\Phi_0 \approx$ 483 MHz/μV, where V is the time averaged dc voltage across the junction.

In a SQUID, two Josephson junctions are integrated in a superconducting ring, so that in each branch of the ring one junction is integrated (fig. 3.4a). According to the previous considerations, the two Josephson junctions of a SQUID define the maximum supercurrent I_c that can flow through the superconducting ring. Any external magnetic flux modulates I_c with a period of Φ_0. This **SQUID modulation** is caused by the interference of the superconducting wave functions and is the basis of the dc SQUID working principle. Reading out the voltage V across the SQUID allows to measure the applied magnetic flux Φ.[21] Thus, a SQUID is a sensitive magnetic field sensor.

The SQUID modulation is derived by considering the current components which flow through each Josephson junction expressed by the RCSJ model, and the difference of each phase difference δ of each junction. Considering symmetrically arranged and overdamped[22] Josephson junctions results in the voltage-flux ($V\Phi$) characteristic describing the SQUID modulation:

$$V = \frac{R}{2}\sqrt{I_b^2 - I_c^2} = \frac{R}{2}\sqrt{I_b^2 - \left(2I_0 \cos\pi\frac{\Phi}{\Phi_0}\right)^2} \tag{3.41}$$

where V is the time averaged voltage across the SQUID, I_b the bias current through the SQUID, $R/2$ the parallel resistance of the SQUID, and I_0 the average critical current of both junctions. Equation 3.41 indicates the Φ_0-periodicity of the modulation of the supercurrent I_c. It is valid for bias currents $I_b \geq I_c$. With currents between $I_b = I_c$ to $2I_c$, the $V\Phi$-characteristic has superconducting parts. With $I_b > 2I_c$,

---

[21]Φ the applied magnetic field corresponds to the magnetic flux B times the effective area A_{eff} of the SQUID loop: $\Phi = B A_{eff}$. Furthermore, it should be noted that the self-induced flux is negligible in most realizations.

[22]SQUIDs are usually operated in the strongly overdamped limit, where the so-called Stewart-McCumber parameter is small: $\beta_c = \frac{2\pi}{\Phi_0}I_0R^2C \ll 1$. Here, the voltage-current characteristic is non-hysteretic.

(a) equivalent circuit

(b) $V\Phi$-characteristic

(c) read-out scheme (FLL circuit)
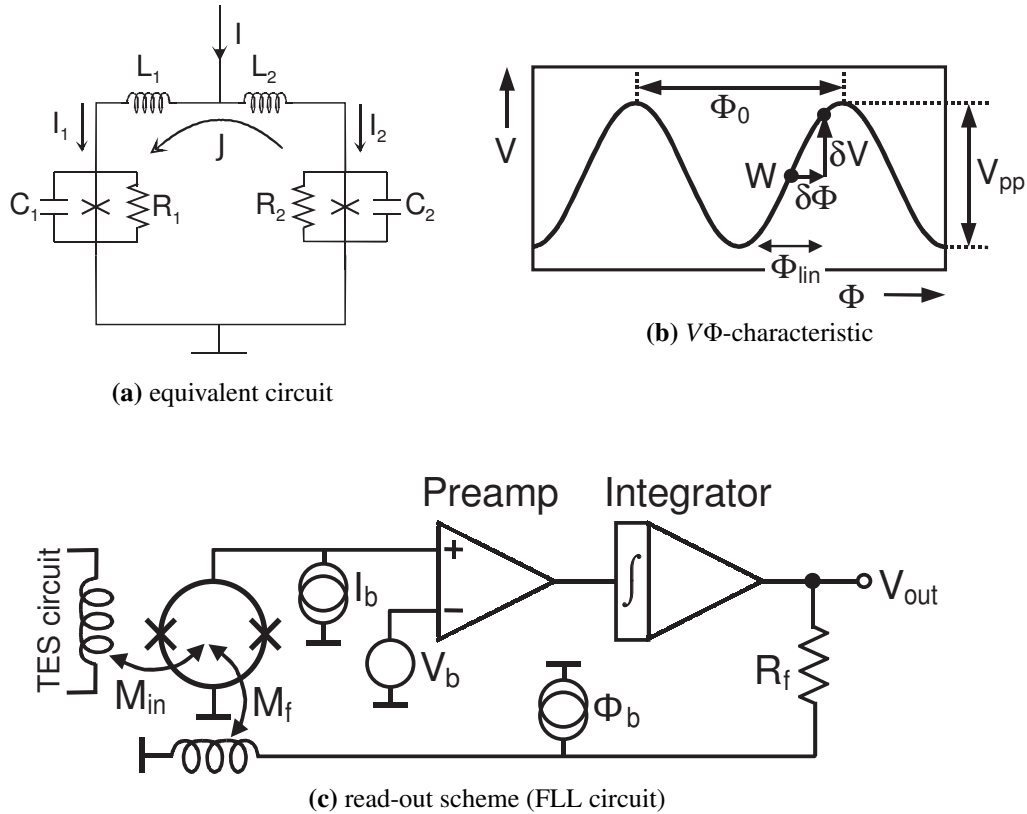
Figure 3.4.: SQUID in a nutshell: Equivalent scheme, $V\Phi$-characteristic and read-out scheme. (a) illustrates the equivalent circuit of a SQUID arrangement including two (1 and 2) Josephson junctions. A Josephson junction is described by an ohmic resistor (R), a capacitor (C), and an element for the supercurrent (black cross) in parallel (RCSJ model). I is the current through the SQUID, J is the circulating current in the ring, I_1 the current through junction 1 and I_2 through junction 2. An external magnetic flux couples to the SQUID inductance $L = L_1 + L_2$. (b) illustrates the $V\Phi$-characteristic or SQUID modulation with an applied flux Φ. The $V\Phi$-characteristic is given by equation 3.41 with a period of Φ_0 and a peak-to-peak value of V_{pp}. The working point (W) is set to the steepest point $\delta V/\delta \Phi$ in the positive slope. Around this point, the $V\Phi$-dependence is approximately linear (Φ_{lin}). (c) shows a typical read-out scheme of a TES with a dc SQUID current sensor operated by proper electronics. The TES circuit is inductively coupled to the SQUID (M_{in}), which is symbolized by a ring with two crosses. The SQUID is biased by current sources I_b, V_b, and Φ_b. The SQUID is operated in flux-locked loop (FLL) mode in which the preamplified (Preamp) and integrated (Integrator) voltage across the SQUID is negatively fed back via the feedback circuit (R_f and M_f). The negative feedback linearizes the SQUID and increases the dynamic range. [Adopted from Clarke and Braginski (2004)]

the $V\Phi$-characteristic is normal resistive for the whole period. An exemplary $V\Phi$-characteristic is depicted in figure 3.4b.

With the $V\Phi$-characteristic, a **working point** of the SQUID is found. By biasing the SQUID with a proper current I_b, a modulation is established (eqn. 3.41). By applying a proper magnetic flux Φ, the SQUID is set within the steep positive slope of the modulation (fig. 3.4b). Since the modulation is periodic, the working point is not unique. Therefore, SQUIDs are relative magnetic sensors. At the working point, the $V\Phi$-dependence is approximately linear and a change in magnetic flux $\delta\Phi$ results in a change of voltage δV, which defines the transfer coefficient:

$$V_\Phi = \left.\frac{\delta V}{\delta\Phi}\right|_I \qquad (3.42)$$

V_Φ defines the system bandwidth using a SQUID to read-out the TES current (sect. 3.1.3.2).

3.1.3.2. TES read-out

To use the SQUID as a current sensor for the TES, the SQUID has to be implemented in a proper circuit to bias and read out by proper electronics. Figure 3.4c shows a typical read-out scheme which incorporates the SQUID, an input circuit, a feedback loop, three bias sources, and further electronic elements to obtain a voltage output corresponding to the input TES current. Circuit components, the read-out mode, and system properties are explained in the following.

To use a SQUID as a current sensor, an input circuit is inductively coupled to the SQUID. Here, the **input circuit** is the electrical TES circuit including an input coil (fig. 3.1a): The current through the input coil, here I_{TES}, induces a magnetic flux in the SQUID, Φ_{in}. This inductive coupling is commonly expressed by the inverse mutual inductance:

$$M_{in}^{-1} = \frac{\delta I_{TES}}{\delta\Phi_{in}} \qquad (3.43)$$

M_{in}^{-1} only depends on the geometry and the distance between the input circuit and the SQUID.

To linearize the SQUID, a **feedback circuit** is arranged (fig. 3.4c). The feedback circuit incorporates a feedback resistance R_f and a feedback loop which is coupled inductively to the SQUID. Analogously, the coupling is given by:

$$M_f^{-1} = \frac{\delta I_f}{\delta\Phi_f} \qquad (3.44)$$

where I_f is the feedback current. This loop feeds back the output signal to the SQUID. This results in a negative feedback which linearizes the SQUID response and increases the dynamic range. This read-out mode is called **flux-locked loop (FLL)** mode which is depicted in figure 3.4c and explained in the following.

3. Superconducting sensors for photon detection and their environments

A SQUID allows to transduce the TES input current I_TES in an output voltage V_out. Firstly, the SQUID has to be set into a proper **working point**. The dc current bias I_b defines the SQUID modulation. Φ_b, realized as a current source, defines the magnetic flux bias through the feedback loop, and consequently a shift in Φ-direction (x-axis in fig. 3.4b). The voltage bias V_b sets a voltage offset, and consequently a shift in V-direction (y-axis in fig. 3.4b). This defines the SQUID working point.

Secondly, a TES current δI_TES causes a magnetic flux $\delta\Phi$ through the SQUID loop which causes a voltage across the SQUID given by the transfer coefficient (eqn. 3.42). The preamplified and integrated voltage is fed back to the SQUID via the feedback loop. Thus, the output voltage in FLL mode corresponds to $\delta V_\text{out} = R_\text{f}\,\delta I_\text{f}$. Since the negative feedback mechanism cancels the signal, $\delta\Phi_\text{f}$ corresponds to $\delta\Phi$ which is initially caused by the TES current. Therefore, according to equation 3.44, the flux is given by:

$$\delta\Phi_\text{f} = \frac{\delta V_\text{out}}{R_\text{f} M_\text{f}^{-1}} \equiv \delta\Phi \tag{3.45}$$

Finally, when combining equation 3.43 and 3.45, the input **TES current** is connected to the output voltage by:

$$\delta I_\text{TES} = \delta V_\text{out} \frac{M_\text{in}^{-1}}{R_\text{f} M_\text{f}^{-1}} \tag{3.46}$$

With a SQUID in FLL mode, the FLL loop gain is given by:

$$G_\text{S} = \frac{V_\Phi}{R_\text{f} M_\text{f}^{-1}} \tag{3.47}$$

which defines the total gain between FLL output and preamplifier input. Considering the SQUID electronics which is used in this thesis, the 3 dB point limiting the **system bandwidth** can be estimated by:

$$f_\text{3dB} \approx G_\text{S}\, GBP \tag{3.48}$$

where GBP is the FLL gain-bandwidth product which is a specific parameter of the electronics (Magnicon, 2011).

Considering a SQUID system reading out a TES, the **total current noise** referred to the TES current is given by:

$$S_\text{system}^I = S_\text{TES}^I + S_\text{read-out}^I \tag{3.49}$$

where $S_\text{TES}^I = S_\text{TES fund.}^I + S_\text{TES add.}^I$ is the intrinsic TES current consisting of fundamental and additional components (sect. 3.1.2.3). $S_\text{read-out}^I$ summarizes the noise

caused by the SQUID system. It mainly includes the intrinsic flux noise and the preamplifier noise.

The realization of a single-like 2-stage SQUID system, which is used to readout the NIST module, is described in section 3.2.1.3. SQUID parameters and the corresponding current-to-voltage factor are given in section 3.2.2.3. Explanations about operating the SQUID system used for ALPS are found in appendix D.3.1.

3.2. Realization and characterization of sensor modules

This chapter describes sensors which were operated and characterized within this thesis. Sensor modules are defined as a modular unit including TES chips for photon detection and SQUID chips for read-out. Both sensors are placed on a copper piece. A sensor module allows a useful mechanical installation and electrical connection in different cryostat setups. In cooperation with PTB (Physikalisch-Technische Bundesanstalt) in Berlin, Germany, different sensor modules were prepared. Sensor modules for ALPS were characterized in a dilution refrigerator at PTB and in the ADR cryostat at DESY.

Since the NIST module was used for extensive photon measurements in this thesis (app. 4), the following descriptions and results concentrate on this device. In section 3.2.1, the technical realization and, in section 3.2.2, the characterization of the NIST module is described in detail. This leads to practical insights into TES physics and allows to compare between the measured performance and theory prediction. The chosen working point and the determined parameters of the NIST module operated in the ADR cryostat are summarized in section 3.4. In section 3.2.3, further sensor modules are presented briefly which were also researched within this thesis. The AIST module is equipped with high-efficient 1064 nm TESs from AIST (sect. 3.2.3.1). Most important module parameters are compared to the NIST module. To measure the electro-magnetic environment (sect. 3.3.1 and 3.3.2), one module only equipped with a SQUID magnetometer was used (sect. 3.2.3.2). Furthermore, in cooperation with INFN[23] and the University of Camerino, a TES detector based on TES sensors from INRIM[24] was set up and operated (sect. 3.2.3.3).

3.2.1. Realization of the NIST module

The NIST module was assembled in cooperation with the PTB and NIST (Beyer, 2011-2013; Lita, 2013). The technical realization of the NIST module covers descriptions of:

- NIST W-TES chips (sect. 3.2.1.1),
- the fiber-to-chip coupling (sect. 3.2.1.2),
- PTB 2-stage SQUID chips (sect. 3.2.1.3),
- the copper module and the electrical connection (sect. 3.2.1.4).

A more detailed description about the specific installation in the ADR cryostat is given in the appendix C.

---

[23]Istituto Nazionale di Fisica Nucleare
[24]Istituto Nazionale di Ricerca Metrologica (Italian metrology insitute).

3.2.1.1. NIST W-TES chips

NIST has carried out the development and optimization of thin film tungsten-based TES from Cabrera's group in Stanford, U.S., in order to detect single near-infrared photons (Cabrera et al., 1998). Before describing NIST TESs used for ALPS, important properties of tungsten films are summarized. Firstly, the focus is on properties as a superconducting thermistor, secondly, as an absorber for photons.

Tungsten is a material which shows a distinctive **electron-phonon decoupling** at sufficiently low temperatures. This means that the electron system and the phonon system can be at two different temperatures, which is called the hot electron effect (Wellstood et al., 1994). This electron-phonon decoupling provides the required weak link. Thus, the W film can be directly deposited on silicon (Si) substrates (Irwin and Hilton, 2005).

In general, thermal conductance G, heat capacity C, and thermal noise of the TES depend on the temperature. Thus, the **superconducting transition temperature**, or critical temperature T_c, defines the response time and the energy resolution of the TES (Irwin and Hilton, 2005). In addition, the transition temperature has to match the cryogenic system. The cold bath temperature should be low enough with respect to the transition temperature. The temperature difference defines the ETF strength which provides stable operation, faster response time, and self-calibration (sect. 3.1.2.4).

Basically, tungsten films can form in one of **two crystal structures** resulting in different transition temperatures. The so-called single-phase α structure[25] results in a $T_c \sim 15$ mK; the single-phase β structure[26] results in a T_c between 1 and 4 K (Lita et al., 2005). Tuning the transition temperature was realized by different methods. Magnetic metal-ion doping can suppress T_c of the tungsten film (Young et al., 2002). Furthermore, it has been shown that a mixture of α and β phases of tungsten can tune T_c. The ratio of these two phases defines T_c, which depends on the deposition conditions during the fabrication process. Additionally, proximate underlayers and coating layers affect T_c (Lita et al., 2005). These methods allow to realize tungsten films with T_c in a range of 50-200 mK.[27] Such transition temperatures are matching cryogenic systems realized by adiabatic-demagnetization or dilution refrigerators.

In the following, the **energy efficiency of the ETF mechanism** and the **overall absorptivity (quantum efficiency)** are discussed. If a photon is absorbed in a tungsten film, a photoelectron is produced. The heat-up of the electron system is measured by the ETF mechanism (sect. 3.1.2.1). Because of the phonon decoupling, low losses of the heat-up through the phonon system are assumed. However, only a fraction of the photon energy is captured in the W electron system. During the initial cascade process, high energy phonons are produced and can escape the tungsten

---

[25]The structure is a bcc-lattice, where the unit cell is a body-centered cubic.

[26]The structure has an A15 phase, which is an intermetallic compound in a specific ratio.

[27]Uncertainties of aimed T_c are caused by the chip production method.
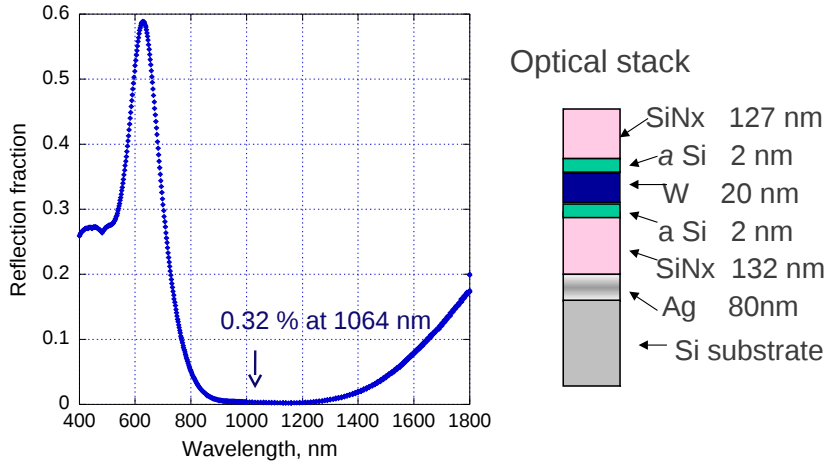
Figure 3.5.: Reflectance and NIST TES chip layout optimized for 1064 nm: The reflectance of the optical stack is measured in the warm (left). The reflectance of 1064 nm light is 0.32 % which allows to assume a high-efficient absorptivity in the tungsten film. The layer structure is optimized for 1064 nm light (right). The tungsten (W) layer is incorporated by anti-reflective coatings (a Si = amorphous silicon and SiN_x = silicon nitride) and a bottom metallic mirror (Ag = silver). These layers are deposited on a silicon substrate in different fabrication processes (Lita et al., 2010). [Taken from A. Lita, NIST]

film (Cabrera et al., 1998). Thus, the measured ETF energy E_{ETF} corresponds to a fraction of the real signal energy. The energy efficiency of the ETF mechanism is:

$$\eta_{ETF} \equiv \frac{E_{ETF}}{E_{photon}} \tag{3.50}$$

where E_{photon} is the single photon energy as a signal. η_{ETF} is calibrated by calculating the ETF integral of a photon event (sect. 3.1.2.3). Therefore, E_{ETF} corresponds to the energy input ΔE which causes the heat input ΔT to the TES (eqn. 3.1).

Thin metallic films can absorb radiation with a wavelength $\lambda \gg d$, where d is the thickness of the film. The absorptivity is broadband and has a maximum of 50 %. At this limit, 25 % of the radiation is transmitted and 25 % is reflected (Hadley and Dennison, 1947, e.g.).TESs with a bare tungsten film show a ~20 % quantum efficiency at 1310 and 1550 nm (Miller et al., 2003). To improve the absorptivity, the tungsten film is incorporated in an optical stack (e.g. fig. 3.5). An anti-reflective top layer diminishes the back reflection of photons. A high-reflective bottom mirror reflects light back which transmits the tungsten layer initially. Furthermore, non-absorbing dielectrics increase the light absorption into the tungsten layer for a specific wavelength band (Lita et al., 2010). Such a multilayer structure shows a 97 % absorptance of 1550 nm which is indicated by reflectance measurements in the warm (Rosenberg et al., 2004). A TES optimized for 1550 nm is measured to reach a (95 ± 2) % detection efficiency including all system losses (Lita et al., 2008).

(a) NIST TES chip

(b) fiber-to-chip coupling
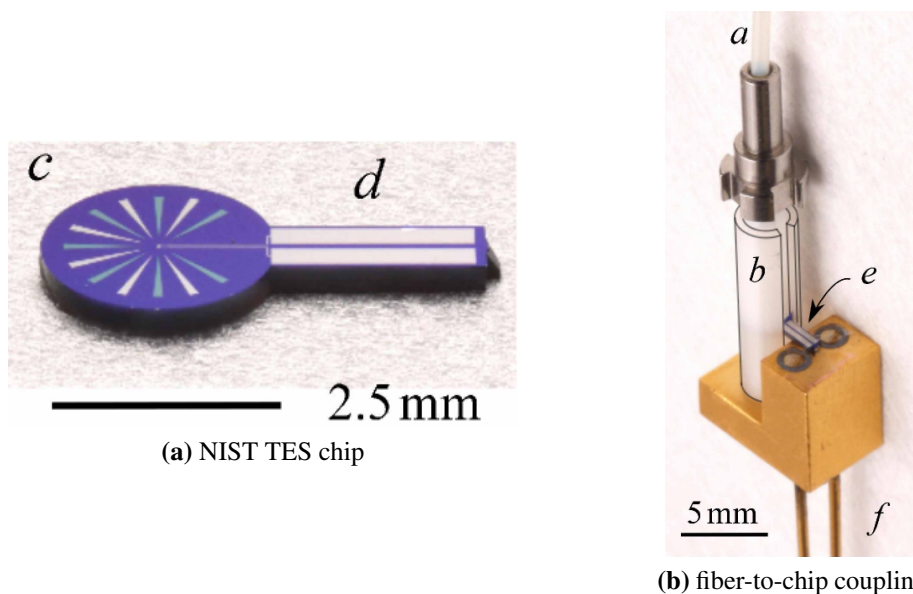
Figure 3.6.: NIST TES chip and fiber-to-chip coupling: (a) shows a sketch of a TES chip in a tennis-racket-like shape. In the center of the round left part 'c' the optical stack with the 25 μm × 25 μm sensitive tungsten area is located. This part has a (2.497 ± 0.001) mm diameter providing a damage-free assembly in fiber sleeve with a 2.5 mm diameter. The right part 'd' is used for the wiring supporting aluminum bond pads. The silicon substrate mainly defines the 275 μm thickness of the chip. (b) shows a realization of a fiber-to-chip coupling. The zirconia sleeve 'b' is fixed to a copper piece and surrounds the round part of the TES chip and the subjacent sapphire socket for sufficient thermal coupling. The single-mode fiber is attached by sticking the zirconia ferrule into the sleeve till it touches the chip surface. [Taken from Miller et al. (2011)]

Finally, NIST has developed near-unity high-efficient optical stacks of TES chips which are optimized for specific wavelengths (Lita et al., 2010).

ALPS benefits from this long-time chip development. The NIST module is equipped with two[28] **TES chips optimized for 1064 nm** (fig. 3.6a).[29] The tungsten film has a sensitive area of 25 μm × 25 μm and a 20 nm thickness. In figure 3.5, the detailed composition of chip layers and the resulting reflectance is depicted. The reflectance is measured with a spectrophotometer in the warm. This is comparable to the absorptance in the tungsten film due to the high-reflective Ag mirror. Additionally, NIST measured the overall system detection efficiency of approximately 97.5 % ± 2 % syst. ± 1 % stat. (Lita, 2013).

The overall system detection efficiency, including the quantum efficiency, depends mainly on optical losses within the optical fiber setup. These losses will be estimated for a specific setup (chap. 5). The transition temperature and the energy

---

[28]This means that two independent channels can be operated with the module.
[29]In NIST nomenclature: B6 and B7 from wafer AEL101810 (Lita, 2013).

efficiency of single photon absorption of the NIST module are determined in section 3.2.2.1 and 3.2.2.4.

3.2.1.2. Fiber-to-chip coupling

NIST has developed a low-loss method of a fiber-to-TES coupling (Miller et al., 2011). A standard fiber sleeve is used to connect a single mode fiber with a standard FC ferrule end to a TES chip. Therefore, the TES chip is prepared in a tennis-racket-like shape with a diameter fitting to the inside of the sleeve (fig. 3.6).

The coupling method has a cryogenic compatibility, reproducible assembly, and low component cost. Furthermore, this technique provides low optical losses. If the fiber ferrule is properly stuck into the sleeve until touching the chip surface, the ~9 μm diameter fiber core shows a mean lateral offset of 3 μm which is expected due to the slightly smaller chip diameter referred to the sleeve. If a Gaussian beam diameter of 10 μm and a 25 μm $\times$ 25 μm detector area is considered, this offset results in an optical loss of less than 0.1 % (Miller et al., 2011).

NIST has added to the 1064 nm chips for ALPS two pig-tail SMF28-fibers. Each fiber was 1 m long at the beginning[30] and has one fiber end with a FC ferrule in order to attach the fiber to the TES. Additionally, this end is AR-coated for 1064 nm which considerably diminishes losses through conventional 4 % back reflection at fiber ends.

3.2.1.3. PTB 2-stage SQUID chips

ALPS benefits from the longtime SQUID development of PTB-Berlin. In cooperation with PTB, a new generation of SQUIDs is tested to read-out single TES devices. The NIST module is equipped with a 2-stage dc SQUID chip working as a current sensor for the NIST TES.[31] The chip[32] has two channels, A and B, and a size of ~3.5 mm $\times$ 3.5 mm. In addition, the SQUID chip incorporates the input coil and the shunt resistor of the TES circuit (fig. 3.1a). Each channel has integrated shunt resistors with nominal values of 0.2, 2, 20 and 200 mΩ. Both NIST TES are shunted by a 20 mΩ resistor (sect. 3.2.1.4). In figure 3.7, a sketch of one channel is depicted. The complete SQUID circuit, including the SQUID electronics, is shown in the appendix in figure C.3. In the following, the most important properties are described.

One SQUID channel incorporates a 2-stage SQUID-cascade (fig. 3.7). The input coil, which is an element of the TES circuit, is inductively coupled to the so-called front-end single SQUID (SQ1). The front-end SQUID is read out by the 2nd

---

[30]During background measurements, the original length was diminished by splicing to extend the fiber.

[31]SQUIDs as current sensors have a special arranged input loop to be less sensitive to external magnetic fields.

[32]In PTB nomenclature: Type No. C6X114HW, Wafer: C648, Chip: J34
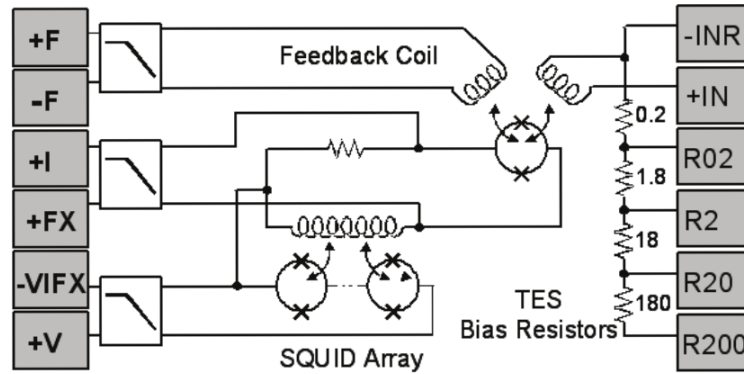
Figure 3.7.: Sketch of one channel of PTB SQUID chip 6X114HW: The sketch illustrates the electrical scheme as well as the bonding pads at left and right. In the middle is the front-end loop with the sensor single SQUID (1st stage) which is inductively coupled to the feedback coil (±F) and the input coil for the TES circuit (-INR, here R20). The input coil and the integrated shunt resistors allow a user-friendly connection to a TES chip. The 2nd stage SQUID array (-VFIX, +V) is inductively coupled to the front-end loop. The SQUID array is read out by proper electronics. Wiring details are found in appendix C.3. [Adopted from PTB.]

stage SQUID (SQ2), which is realized as an array of 14 single SQUIDs in series. The advantage of 2-stage SQUIDs compared to single SQUIDs or SQUID arrays is a lower noise due to a reduced SQUID electronics noise contribution. This read out cascade is dominated by the noise of the front-end SQUID, which determines the dynamic range. One disadvantage could be that 2-stage SQUIDs may have a complex combined, and therefore non user-friendly, $V\Phi$-characteristic compared to single SQUIDs (Beyer, 2011-2013).

The most important parameters are (Drung et al., 2007): The 2-stage SQUIDs has a low input inductance L of nominal 2 nH as design parameter which allows a stable TES response (sect. 3.2.2.2). It is working at mK-temperatures with a noise level at 100 kHz <2 pA/$\sqrt{Hz}$ referred to the input (Beyer, 2011-2013). This allows to place the SQUID chip near the TES chip and on one copper module (next. 3.2.1.4). Furthermore, the power dissipation due to bias currents is ~3 nW and lower compared to other SQUIDs. Finally, these 2-stage SQUIDs show a single-SQUID-like modulation (see fig. D.6).

The detailed wiring is found in appendix C.3. The used SQUID electronics is described in appendix C.5.1. The operation is explained in appendix D.3.1. The relevant SQUID parameters of channel A are given in section 3.2.2.3, and the values of the bias currents of the used working point in table 3.2.

3.2.1.4. Mechanical mounting and electrical connection

The NIST module was built in an agreement design between different groups.[33] A mechanical interface allows to mount the module in a cryostat, an electrical interface provides the operation of the module (fig. 3.8). This yields an easy exchange of sensor modules and their integration in different cryostat systems. Such a module has two independent detector channels. Using proper electronics allows to operate two TES detectors, each with a fiber channel, simultaneously.

The **mechanical interface** is a copper piece which allows an integration to the cold finger of a cryostat. The copper piece made of alloy Cu-17 is tempered to improve the thermal conductivity at low temperatures. Additionally, it is electroplated to avoid surface oxidation in order to ensure a sufficient thermal coupling to the cryostat mount. Hollows at the side of the copper piece allow to clamp NIST TES chips surrounded by a fiber (fig. 3.8b). The round part of a chip is fixed with silicone grease on a cylindrical socket made of sapphire for sufficient thermal coupling. This is plugged in a fiber zirconia sleeve which is clamped by an additional copper piece to the main copper piece. The SQUID chip is glued[34] directly on the copper surface near the printed circuit board (PCB). In addition, wire bonds connect the chip surface to the copper piece to improve the thermal flow during operation (see fig. 3.8b). Namely, it is assumed that the SQUID chip surface temperature is significantly higher than the bath temperature, as the chip is heated up by bias currents in operation (Beyer, 2011-2013).

The **electrical interface** is a Micro-D25 female connector which provides a cabling inside and out of the cryostat up to SQUID electronics. Bottom pins are soldered to a PCB, each being connected to a conducting path (fig. 3.8a). Aluminum bond wires connect conducting paths to bond pads of the SQUID chip. The SQUID front-end with integrated shunt resistors is connected to a TES chip, also with aluminum bonds, which forms the TES circuit. The length of aluminum bond wires affects the inductance L of the TES circuit. A rule of thumb is a parasitic inductance of 10 nH per centimeter (Beyer, 2011-2013). This results in 15-20 nH inductance through the bonds. Each TES of the NIST module is connected to the 20 mΩ shunt resistor which fits for a voltage-biased TES (sect. 3.2.2.2). The connection scheme is identical for both channels.

In the ADR cryostat, the module can be attached to the detector bench which is an extension of the cold finger (app. C.1). This ensures the thermal coupling to the FAA-stage. The detailed electrical connection scheme inside the ADR cryostat is found in appendix C.3.

---

[33]Originally between cryosensor group of PTB-Berlin and Zeilinger group of IQOQI, Vienna. Adopted for ALPS group at DESY, Hamburg.

[34]With GE 7031 varnish.
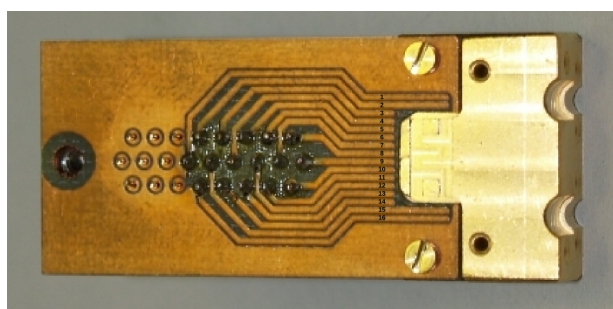
(a) Raw sensor module
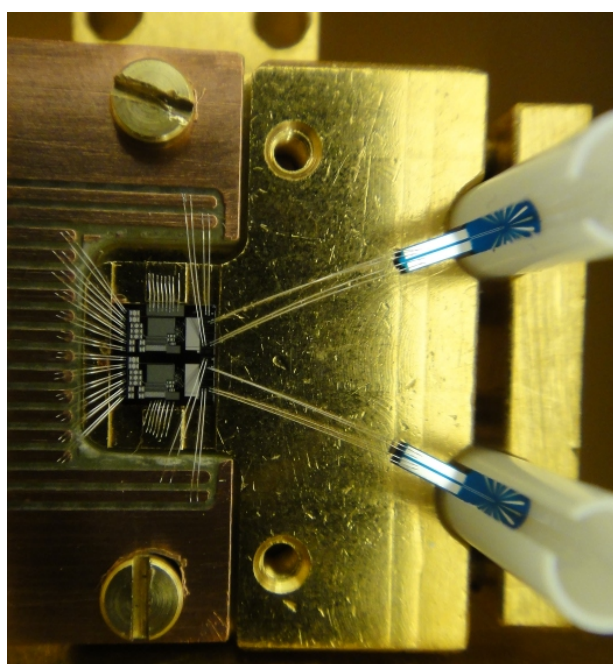
(b) NIST module with two channels

Figure 3.8: Assembling of the NIST module: (a) shows a raw module which is ready to assemble sensor chips and wiring. The copper piece on the right provides the space for the chips. On the left is a PCB with 16 conducting paths to pins of a Micro-D25 connector. This connector is the electrical interface for the cabling up to the SQUID electronics. The module including the PCB is ~5 cm long. (b) shows a zoom to the completed NIST module. TES chips surrounded by fiber sleeves are fixed by a copper clamp on the right. The two channel SQUID chip is glued near to the PCB. The chips are electrically connected by aluminum bonding wires. The 2nd stage of the SQUID is connected to PCB conducting paths. Such modules are attached to the cold bath of a cryostat. [(a) is taken from PTB.]

3.2.2. Characterization of the NIST module

The characterization and the performance of the NIST module is described in this section. Using different measurement methods, parameters of the module were determined within this thesis.[35] Measurement methods are *IV*-curves, current divider test, SQUID modulation, and noise spectrum analysis (app. D.3). The results covers

---

[35]The NIST module was operated one week in April 2013 at PTB-Berlin for the first time. Since that time it has been operated for detailed characterizations, for environment measurements in the ALPS laboratory (sect. 3.3), and for signal and background measurements (chap. 4). For a proof-of-principle, a similar sensor module was operated in the ADR cryostat in September 2012 in Berlin and in January 2013 in Hamburg. This module was equipped with NIST TESs optimized for 800 nm. PTB prepared the module for the Vienna group of IQOQI (Institute for Quantum Optics and Quantum Information).

the parameters which describe the NIST module:

- TES thermal parameters: critical temperature T_c, transition width ΔT_c, temperature sensitivity α, current sensitivity β, heat capacity C, thermal conductance G (sect. 3.2.2.1).
- TES electrical parameters: TES normal resistance R_N, parasitic resistance of TES branch R_{par}, shunt resistance R_{sh}, input inductance L (sect. 3.2.2.2).
- SQUID parameters: inverse mutual feedback inductance M_f^{-1}, inverse mutual input inductance M_{in}^{-1}, transfer coefficient V_ϕ, FLL loop gain G_S (sect. 3.2.2.3).

This allows a comparison of the TES response between the small-signal theory and measurements (sect. 3.1.2):

- Signal response (sect. 3.2.2.4).
- Noise response and bandwidth (sect. 3.2.2.5).

The values and results represent an exemplary measurement operating channel A of the NIST module at a bath temperature of 80 mK at a TES working point of 30 % R_N. This working point proves as suitable for single photon measurements (sect. 3.4 and 4). For Channel B, parameters are similar to the parameters of channel A. Therefore, a detailed characterization is not given here.

3.2.2.1. TES thermal parameters

Since TES thermal parameters depend on temperature, the following analysis considers the NIST module operated in a selected working point. The bath temperature is $T_{bath} = 80$ mK and the TES resistance is adjusted to $R_{TES} = 30$ % R_N. These settings are used for later single photon measurements (sect. 3.4). In figure 3.9, a representative measurement of *IV*-characteristic is depicted with the NIST module in its working point. From this *IV*-characteristic, values are derived to determine TES parameters, as it is shown in the following.

To measure TES parameters, different methods are used within the TES community. Firstly, the critical temperature T_c, the transition width ΔT_c, and the temperature sensitivity α of the superconducting transition can be identified by measuring the resistance $R(T)$ during a temperature change. Therefore, a four point wiring is needed to exactly measure the resistance. In addition, a proper regulation, e.g. a heater, is needed to adjust the bath temperature in a sufficient temperature resolution. Secondly, α, the current sensitivity β, the heat capacity C, and the thermal conductance G can be determined by impedance measurement (Lindeman, 2004; Taralli et al., 2012). With an adequate setup, the parameters result from fitting measurements to an impedance expression of the small-signal theory (Irwin and Hilton, 2005). Since such measurement infrastructures were not available, TES parameters of the NIST module are estimated with simpler methods,[36] which is sufficient for the purpose of this analysis:

---

[36]Based on e.g. Cabrera et al. (1998) or Lita et al. (2008).
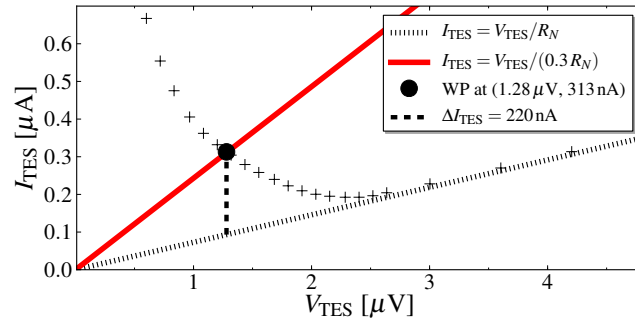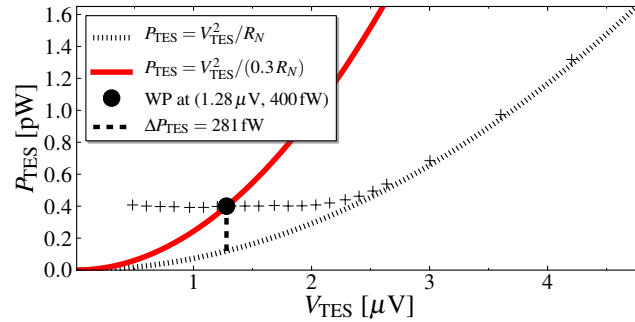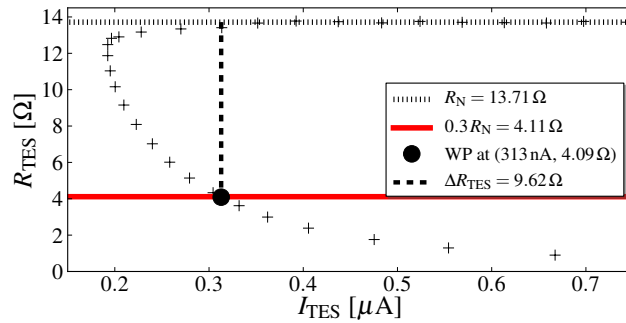
(a) *IV*-curve

(b) *PV*-curve

(c) *RI*-curve

Figure 3.9.: Different representations of the *IV*-characteristic: (a) shows a representative *IV*-curve. Data points (black crosses) are measured by sweeping the bias current I_{BIAS}. I_{BIAS} defines the bias and the voltage across the TES V_{TES} (eqn. 3.6 or D.9). TES current I_{TES} is measured by the SQUID output (eqn. 3.46 or D.4). The black thin dashed line illustrates R_{N}, TES normal resistance, the red line the 30 % fraction of R_{N} which is defining the working point. (b) shows the corresponding power across the TES P_{TES} versus V_{TES}. It is $P_{\mathrm{TES}} = V_{\mathrm{TES}} I_{\mathrm{TES}}$. Here, the quiescent power at the working point can be directly determined. (c) shows the corresponding TES resistance R_{TES} versus I_{TES}. It is $R_{\mathrm{TES}} = V_{\mathrm{TES}}/I_{\mathrm{TES}}$. This representation allows an estimate about the current sensitivity β (see text). In all representations the corresponding working point (WP, black dot) is given. In addition, each black thick dashed line illustrates the saturation of the TES, which is explained in section 3.2.2.4.

- To determine the **transition temperature** T_c, the noise level to different bath temperatures is observed. Therefore, the SQUID is operated in FLL and the TES circuit stays unbiased (app. D.3). Thus, the output noise level corresponds to the total resistance of the TES circuit due to Johnson noise (sect. 3.1.2.3). Channel A of the NIST module shows a transition from below 0.5 Ω till normal resistivity between ~139-141 mK.[37] This confirms a selective current divider test (app. D.3.2.1) at 140 mK which results in ~40% R_N. Following this rough measurement, for channel A of the NIST module a superconducting transition temperature $T_c = 140$ mK and a transition width $\Delta T_c = 1\text{-}2$ mK are assumed.

- The **current sensitivity** β is estimated by the *IV*-characteristic. By plotting the TES resistance against the corresponding TES current (fig. 3.9c), the working point and the corresponding gradient of this representation defines β (eqn. 3.4). The gradient is estimated by considering the line between the data point at $I_{TES} \approx 240$ nA and the working point. This corresponds to a 70 nA signal pulse amplitude (cf. fig. 3.10). This results in $\beta \approx 3.0 \pm 1.0$. The uncertainty is estimated by the uncertainty of the gradient.

- The **heat capacity** C is determined by values of experience from other groups. For the normal-metal phase, C is calculated by $C = V_m \gamma T V$, where V_m is the molar volume, γ the molar specific heat, T is the temperature and V the volume of the sensor (Irwin and Hilton, 2005; Lita et al., 2005, e.g.). Literature values are $V_m = 9.5 \cdot 10^{-6}$ m^3/mole and $\gamma = 1.3 \cdot 10^{-3}$ J/mole/K^2. The sensor volume is $V = 25\ \mu$m $\times 25\ \mu$m $\times 20$ nm. The temperature is assumed to be $T_{TES} \approx T_c = 140$ mK. In addition, since the TES is operated within the superconducting transition, the heat capacity is corrected by a factor of up to 2.43. This results from the BCS-theory, which describes the superconducting phase (Lindeman, 2000, e.g.). For the NIST TES at 140 mK, this results in a heat capacity of $C = 0.58$ fJ/K.

- The **thermal conductance** G is estimated with equation 3.15. By assuming a small external power load P_0 referred to the Joule heating power P_{J_0} (eqn. 3.17), the power flow to the bath P_{bath} is directly given by the quiescent power at the working point. This power is given by the power-versus-voltage curve of *IV*-representations in figure 3.9b. Here, it is $P_0 = 400$ fW at the working point. The bath temperature is $T_{bath} = 80$ mK and the TES temperature is again assumed to be $T_{TES} \approx T_c = 140$ mK. Exponent n, which describes the power law dependence between the electron system and the bath, is assumed to be $n = 5$. This is defined by the electron-phonon decoupling

---

[37]The bath temperature is regulated with the ADR magnet and it is swept in 1 mK steps (app. D.2.3). It is measured by the FAA-thermometer. Channel B shows a transition between ~140-142 mK. The transition at a slightly higher temperature for channel B is confirmed by *IV*-curves: Here, a higher bias current is needed to reach the same working point.

of tungsten (Cabrera et al., 1998; Irwin and Hilton, 2005, e.g.). The thermal conductance results in $G = 15$ pW/K.

- For a calorimeter without ETF, C and G define the thermal time constant (eqn. 3.2). Here, this results in $\tau \approx 38$ μs. Comparing τ with the ETF time constant allows to determine the **temperature sensitivity** α at the working point according to equation 3.29. Therefore, it is assumed that τ_{ETF} corresponds to the fall time $\tau_{\text{m}} = 1.53$ μs of a signal response of this setup (fig. 3.10). It results in a temperature sensitivity $\alpha \approx 360$ at the working point 30 % R_{N}.[38]

Results and values of this chapter are summarized in table 3.2. Furthermore, they are used for comparing the measured signal and noise response with the small-signal theory (sect. 3.2.2.4 and 3.2.2.5).

3.2.2.2. TES electrical parameters

Properties of the TES circuit define the bias condition as well as the electrical response (fig. 3.2, sect. 3.1.2.1, and sect. 3.1.2.2). For strong voltage-bias, the load resistance $R_{\text{L}} = R_{\text{SH}} + R_{\text{PAR}}$ has to be much smaller than the TES resistance in the working point, R_0. Assuming parasitic resistances are negligible, a small R_{SH} is needed referred to R_0. In turn, the normal resistance of the TES R_N should be high enough referred to the R_{SH}. If R_{SH} is chosen too small, high bias currents could be required to reach the working point. This could affect a high parasitic Joule heating, which is adverse for mK-application. The inductance of the circuit L should also be well chosen, otherwise the TES response can show sinusoidal ringing effects (Lindeman, 2000; Irwin and Hilton, 2005). These requirements are proofed, and the values of the TES circuit are discussed, in the following. One essential method to determine resistances of the circuit is the current divider test which allows to determine the resistance of the TES branch of the circuit $R_{\text{TES branch}} = R_{\text{TES}} + R_{\text{PAR}}$ (app. D.3.2.1).

- The **normal resistance** R_{N} is accurately determined by IV-characteristic (e.g. fig. 3.9a). For TES channel A of the NIST module, the normal resistance is $R_{\text{N}} = 13.78 \pm 0.09$ (stat.) ± 0.08 (sys.) Ω.[39] This mean value includes $\sim$60 IV-curves; the systematical uncertainty is caused by the measurement method (app. D.3.2.2). This value is used for further calculation in the following. For example, the 30 % working point results in $R_0 = 4.1$ Ω. With the current divider test, R_{N} is confirmed. An unbiased circuit above T_{c} results in

---

[38]The temperature sensitivity α can also roughly be estimated by the transition temperature and width. Following equation 3.3 and assuming approximately a linear $R(T)$ transition, it is $\alpha \simeq \frac{T_{\text{c}}}{R_{\text{N}}/2} \frac{R_{\text{N}}}{\Delta T_{\text{c}}} = 140\text{-}280$. This method includes the uncertainty about the real $R(T)$ dependence within the transition.

[39]For channel B, a slightly higher normal resistance is determined $R_{\text{N}} = 14.2 \pm 0.08$ Ω.

$R_{\text{TES branch}}$ = 13.5-14.0 Ω. At ~2.5 K, the operating temperature of the cry-ocooler, $R_{\text{TES branch}}$ = 40-44 Ω is observed. This is mainly caused by the aluminum bond pads of the TES chip since aluminum has its superconducting transition at 1.14 K.[40]

- The **shunt resistance** R_{SH} has been separately measured by PTB during the SQUID characterization. Here, a defined input circuit instead of the TES circuit was used. For channel A of the NIST module, it is R_{SH} = 24 mΩ.[41] This value is used to calculate the TES voltage according to equations 3.6 and 3.9. A current divider test with small currents below T_c allows an estimate of the parasitic resistance. The results fluctuate, presumably due to a Joule heating effect. Therefore, only a range can be given. For channel A at 80 mK, it is considered $R_{\text{PAR}} \approx$ 20-40 mΩ. This results in a **load resistance** of R_{L} = $R_{\text{SH}} + R_{\text{PAR}} \approx$ 40-60 mΩ.[42] By considering a 30 % R_{N} working point and $R_{\text{L}} \approx$ 60 mΩ conservatively, this indicates a strong voltage-bias condition for the NIST module: According to equation 3.5, it is $R_{\text{L}}/R_0 \approx 0.015 \ll 1$.

- The latter expression includes a TES stability criterion. This means, if $R_0 > R_{\text{L}}$, the TES relaxes back exponentially to the operating point after an energy input. This is only valid for an overdamped solution of the differential equations (sect. 3.1.2.2). Overdamped solutions are given if $\tau_+ < \tau_-$. This gives a requirement to the circuit inductance (Irwin and Hilton, 2005):[43]

$$L < L_{\text{crit}-} = 0.17 \frac{R_0 \tau}{\mathscr{L}_I} \approx 400 \text{ nH}$$

The **inductance** L of the NIST module combines the inductance of the SQUID input coil and the parasitic inductances of the lines (sect. 3.2.1.3 and sect. 3.2.1.4). Here, it is $L \approx$ 17-22 nH. This means, the inductance satisfies the requirement and the TES has a stable response.

- Finally, the **low-frequency loop gain** allows to rate the strength of the ETF mechanism (sect. 3.1.2.4). According to equation 3.20, it is $\mathscr{L}_I$ = 67 ≫ 1 and $\beta \approx 3$ (see above).

Results and values of this chapter are summarized in table 3.2. Furthermore, they are used for comparing the measured signal and noise response to theory (sect. 3.2.2.4

---

[40]The resistance of the Al-wire bonds is estimated to be small: ~20 mΩ (Beyer, 2011-2013).

[41]For channel B, it is R_{SH} = 26 mΩ. These values are found in PTB datasheet of the SQUID chip. Additionally, this indicates a slight deviation to the nominal value of the integrated shunt resistor of 20 mΩ.

[42]The noise level of an unbiased circuit with superconducting TES allows a cross-check. Here, the level is defined by R_{L} due to Johnson-Nyquist noise (eqn. D.11). The same order of magnitude is observed, $O(10 \text{ mΩ})$.

[43]This condition includes conservatively several simplifications. It treats the case of voltage-bias, where $R_{\text{L}} = 0$, of strong feedback, where $\mathscr{L}_I \gg 1$, and of the limit $\beta = 0$. It is noted that another comprehensive consideration about TES stability is given by Lindeman (2000).

and 3.2.2.5). It is summarized that the NIST module has a stable response and is operated in the negative strong ETF limit. This results in several simplifications of TES response, which are discussed in section 3.1.2.3).

3.2.2.3. SQUID parameters

PTB chips are exhaustively characterized after their production at PTB-Berlin. Values of SQUID parameters are listed in a datasheet for each chip. In the ALPS setup with an ADR cryostat, the most important parameters of the 2-stage SQUID of the NIST module (sect. 3.2.1.3) are confirmed and are presented in this section.

- The inverse mutual input inductance M_{in}^{-1} and inverse mutual feedback inductance M_f^{-1} are required to determine the TES current I_{TES} (sect. 3.1.3.2). For channel A of the NIST module, the input coupling is $M_{in}^{-1} = 5.792\ \mu A/\Phi_0$, which is determined by PTB characterization. The feedback coupling M_f^{-1} is determined by $V\Phi$-characteristics at 80 mK in the ADR (e.g. fig. D.6). The modulation shows the expected characteristic of a 2-stage SQUID (Drung et al., 2007). It is $M_f^{-1} = 44.04 \pm 0.07\,\text{(stat.)} \pm 0.13\,\text{(syst.)}\ \mu A/\Phi_0$. The systematic uncertainty is caused by the measurement method (app. D.3.1.1). According to equation 3.46, it results in a conversion factor between voltage output V_{out} and TES current I_{TES}

$$(I_{TES}/V_{out})_{NIST,A} = 1.315 \pm 0.036\,\text{(stat.)} \pm 0.067\,\text{(syst.)}\ nA/mV \quad (3.51)$$

  Here, the feedback resistance of the FLL circuit is $R_f = 100\ k\Omega$ which is used for TES operation.[44]

- The transfer coefficient V_Φ allows to estimate the FLL bandwidth. V_Φ indicates the voltage-flux-dependence at the SQUID's working point (fig. 3.4b). By applying a small alternating bias voltage in FLL mode, the transfer coefficient is determined (app. D.3.1.3). It is $V_\Phi = 2590 \pm 71\ \mu V/\Phi_0$.[45] According to equation 3.48, the SQUID system bandwidth is estimated: $f_{3dB} = 1.6 \pm 0.05$ MHz.[46] This value is compared to measurements in the next chapter 3.2.2.5.

The SQUID parameters and the used values of bias currents are summarized in table 3.2.

---

[44]The used feedback resistance is the highest possible value due to the SQUID electronics, which provides the highest gain.

[45]The measured value $V_{\Phi_{FLL}} = 8260 \pm 230\ \mu V/\Phi_0$ is corrected by the resistance of the activated input termination: $V_\Phi = \frac{R_{term}}{R_{term}+R_{dyn}} V_{\Phi_{FLL}}$. Here, $R_{term} = 50\ \Omega$ is the resistance of termination, and $R_{dyn} = 110\ \Omega$ is the dynamic resistance of the SQUID which is due to the current bias.

[46]This value depends on the chosen bandwidth option of the SQUID electronics. For measurements with the NIST module, a so-called gain bandwidth product of $GBP = 2.8$ GHz is selected (Magnicon, 2011).
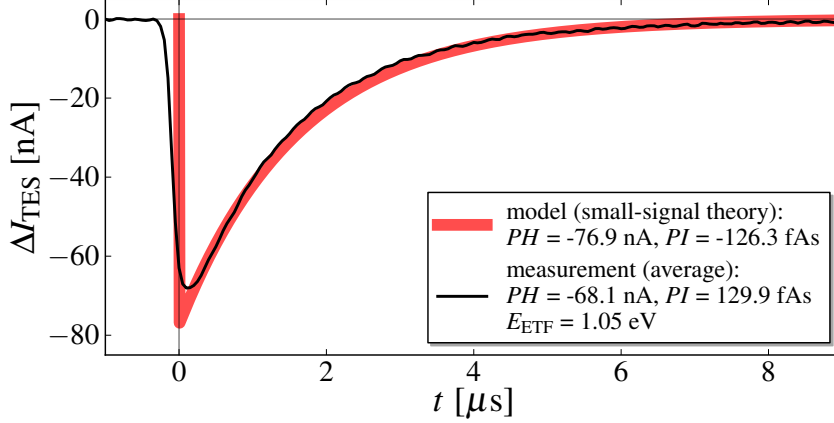
Figure 3.10.: Measured average photon signal and model pulse of the NIST module: The thin black line is an average pulse of 1064 nm single photons measured by channel A of the NIST module. The thick red line is the corresponding response according to the small-signal theory using determined parameters of the NIST module. For each pulse, *PH* is the pulse height, and *PI* the pulse integral. The measured pulse corresponds to E_{ETF} which calibrates the TES. Time constants of these pulses are found in table 3.1. The model and the data fit quite well apart from small deviations, which are discussed in the text.

3.2.2.4. Signal response

Considering the TES detector related to the ALPS experiment, single photon detection is most relevant. Signal photons and background sources are extensively studied by operating channel A of the NIST module in chapter 4. In this section, the measured signal response is compared to theory, and the energy resolution and further properties are discussed.

In figure 3.10, a measured average pulse of 1064 nm photons (thin black line) and the corresponding response according to the small-signal theory (thick red line) are depicted:

Table 3.1: Time constants of the NIST module: Rise and fall times from measurements and the small-signal theory are compared. Measured time constants are determined by analyzing an average photon pulse (fig. 3.10). Time constants from theory are calculated with the determined parameters in the previous sections, which are summarized in table 3.2.

rise times	calc.	$\tau_+ = 3$ ns	(eqn. 3.26)
		$\tau_{\mathrm{el}} = 3$ ns	(eqn. 3.23)
	meas.	$\tau_{\mathrm{p}} \approx 70$ ns	(fig. 3.10)
fall times	calc.	$\tau = 38.2\,\mu\mathrm{s}$	(eqn. 3.2)
		$\tau_- = 1.64\,\mu\mathrm{s}$	(eqn. 3.26)
		$\tau_{\mathrm{ETF}} = 1.53\,\mu\mathrm{s}$	(eqn. 3.29)
	meas.	$\tau_{\mathrm{m}} \approx 1.53\,\mu\mathrm{s}$	(fig. 3.10)

- **Measured average pulse**: By operating the NIST module at the working point (sect. 3.4) attached to a single 1064 nm photon source (sect. 4.1.2), an average pulse is measured. The rise time τ_p and fall time τ_m are determined by the time $\tau_{10,90}$ between 10 % and 90 % peak height. This time is connected by a factor 2.2 to the exponential time constant: $\tau_{10,90} = 2.2\,\tau_\mathrm{exp}$. The measured time constants are given in table 3.1. Calculating the pulse integral with equation 3.30 allows to calibrate the TES. Here, the measured energy is $E_\mathrm{ETF} = 1.05$ eV, which results in an energy efficiency of the ETF mechanism for a 1064 nm ($\hat{=}\ 1.165$ eV) absorption (cf. eqn. 3.50):

$$\eta_\mathrm{ETF} \approx 90\ \% \tag{3.52}$$

  Losses are presumably caused by high energetic phonons which can escape the absorber material (sect. 3.2.1.1).

- **Signal response according to small-signal theory:** Using the determined TES parameters (previous sect. 3.2.2.1 and 3.2.2.2, and summarized in tab. 3.2) and the determined calibration η_ETF, the signal response is described according to the small-signal theory (eqn. 3.25). Considering the calculated time constants in table 3.1, the approximations in a strong ETF limit are valid (sect. 3.1.2.3): The rise time τ_+ is described by the electrical time constant τ_el and the fall time τ_- by the ETF time constant τ_ETF.

In each case, the pulse shape shows a negative response since the current through the TES becomes smaller because of negative ETF operation (sect. 3.1.2.1). The pulse has a steep rising slope and an exponential fall relaxing to the zero baseline, as expected. Furthermore, the measured pulse is quite well described by the pulse resulting from theory (fig. 3.10). This means that the determination of thermal and electrical TES parameters, as shown in the previous sections 3.2.2.1 and 3.2.2.2, seems to be quite robust. Deviations between measurement and theory are caused by different effects:

- The measured pulse is affected by the system bandwidth (sect. 3.2.2.5). The system bandwidth is measured to be $f_\mathrm{3dB} \approx 0.9$ MHz, which affects times below $\tau_\mathrm{3dB} = \frac{1}{2\pi\,f_\mathrm{3dB}} \approx 180$ ns. Thus, the rising slope and the peak of a measured pulse are smeared in comparison to the real pulse. This is in accordance by comparing τ_el from theory and τ_p from measurement (tab. 3.1).

- The falling slope of the measured pulse is better described by introducing a second additional negative exponential time constant (app. B.2). In real, the TES is presumably a higher order thermal system and slightly deviates from the presented small-signal theory including one heat capacity and one thermal conductance. This deviation of the falling slope causes the 10 % deviation between the ETF time constant τ_ETF and the fall time τ_- (tab. 3.1).

One of the most important quantities of a calorimeter is the **energy resolution**. A high energy resolution allows a good discrimination between events with differ-

ent energies. Since the NIST module is operated in the strong negative ETF limit, the fundamental energy resolution can be determined by equation 3.37, assuming a perfectly linear TES. Using the determined TES parameters, it is $\Delta E_{\text{rms,model}} = 0.021$ eV including the factor of energy efficiency η_{ETF} (eqn. 3.52). As a fundamental limit, it results in $(\Delta E_{\text{rms,model}}/E)_{1064\text{ nm}} = 1.8$ % for 1064 nm photon signals. The real energy resolution of the setup is defined by the measured system noise spectrum (fig. 3.11). In addition, the value depends on the analysis method. Analyzing the pulse height distribution (sect. 4.2.1 or 4.2.2), it is determined $(\Delta E_{\text{rms,meas.,PHD/HIA}}/E)_{1064\text{ nm}} = \sim 7$ %. An improvement shows the pulse shape analysis (PSA). It results in $(\Delta E_{\text{rms,meas.,PSA}}/E)_{1064\text{ nm}} = \sim 6$ %. Further improvements could be expected by using the method of optimal filtering (McCammon, 2005).However, it is expected that the fundamental limit cannot be reached due to the simplification of theory (eqn. 3.52).

Finally, further properties of the NIST module are observed which are relevant for signal detection:

- **TES saturation:** The TES can be short-time saturated if an energy input heats up the TES until the resistance reaches R_{N} as a limit. In such a condition, the ETF power is maximal and constant, before the TES cools down and the resistance drifts to the working point again (Miller, 2001). The saturation corresponds to values which are derived from the representations of the *IV*-characteristic (fig. 3.9): $\Delta I_{\text{TES}} = 220$ nA, $\Delta P_{\text{TES}} = 281$ fW, or $\Delta R_{\text{TES}} = 9.6$ Ω each related to the considered working point. This corresponds to a single photon of 3.8 eV (330 nm) or corresponding multiple events. An example for this signal saturation is observed during background measurements (fig. 4.12b in sect. 4.3.2.2).

- **Linearity of signal response:** It is assumed that the signal response of the TES is linear till it is saturated. Signal linearity means here the linear dependence between the energy input of a signal and the pulse response of the TES. An indication shows the distribution of background events considering the peak and integral values of the events (fig 4.11). The linearity for photon signals has been tested within the ALPS collaboration (Bastidon and Januschek, 2014).

- **Pulse shape variation due to different working points:** The pulse shape is defined by the TES working point. Working points between $R_0 = 10\text{-}50$ % R_{N} are considered in measurements to optimize the working point of the NIST module (sect. 3.4 and app. B.1). In this range, the pulse height and the pulse integral increase with lower R_0. This is caused by the ETF thermal constant (eqn. 3.29), since the temperature sensitivity is approximately proportional to the inverse of the working point resistance: $\alpha \propto 1/R_0$ (cf. eqn. 3.3). Furthermore, it is observed, that the fall time shows a minimum for working points between 30-40 % R_{N} with $\tau_{\text{m}} < 1.6$ μs. This is presumably caused by the

shape of the superconducting transition which is expressed by α (eqn. 3.3).

- **Implications of lower bias currents for the same R_0:** In some runs, lower bias currents I_{BIAS} were needed to reach the same working point 30 % R_{N}. This is caused by external power loads to the TES while assuming a constant power flow to the bath (eqn. 3.17 and sect. 3.3.3). Having power loads, the quiescent Joule power P_{J_0} is smaller; thus, $\mathscr{L}_I$ is smaller (eqn. 3.20), and, with this, a stronger ETF is given (eqn. 3.21). Three observations are related to this:

  - Lower bias currents result in smaller pulse heights and larger pulse integrals (sect. 4.2.4). This is due to a larger effective time constant $\tau_{\text{eff}} \propto \mathscr{L}_I$ (eqn. 3.28) which describes the exponential fall time.
  - Lower bias currents result in a smaller energy efficiency of the ETF mechanism η_{ETF}.[47] This is mainly due to the linear dependence of $E_{\text{ETF}} \propto I_{\text{BIAS}}$ (eqn. 3.30).
  - Lower bias currents results in a higher correlation between pulse heights and integrals of monochromatic photon signals (fig. 4.4 in sect. 4.2.2). This is presumably caused by the strength of the ETF: At lower bias currents the variation of measured energy by ETF is supposed to be higher.

- **Detection efficiency:** The detection efficiency includes the quantum efficiency of the TES and all efficiencies related to the optics. The quantum efficiency is estimated by the NIST measurements (sect. 3.2.1.1). To evaluate the background of fiber-coupled TES, the total detection efficiency of the used setup, including optical and analysis efficiencies, is estimated in section 5. Detailed measurements are ongoing within the ALPS collaboration.

3.2.2.5. Noise response and bandwidth

The noise response defines the baseline deviations of a TES detector. Expressed as a spectral noise current density,[48] the frequency dependence allows an insight of the device's noise level and bandwidth simultaneously. The noise spectrum of the NIST module, operated in its working point (sect. 3.4), is discussed in the following.

In figure 3.11, the **measured system noise of the NIST module** S^I_{system} is depicted. Furthermore, in a first approximation, the read-out noise $S^I_{\text{read-out}}$ is illustrated by a one-pole transfer function, $\sqrt{S(f)} = \sqrt{S_0}/\sqrt{1 + (f/f_{\text{3dB}})^2}$, which is fitted to a measurement.[49] At mK-temperatures, for example, the read-out noise is

---

[47]Channel A of the NIST module shows $\eta_{\text{ETF}} \approx 75$ % for a bias current $I_{\text{BIAS}} \approx 46\,\mu\text{A}$. The presented performance, $\eta_{\text{ETF}} \approx 90$ %, is related to a working point which corresponds to $I_{\text{BIAS}} = 53\,\mu\text{A}$.

[48]Referred to the TES current in units of pA/$\sqrt{\text{Hz}}$.

[49]This is valid since the FLL acts as an low-pass element.
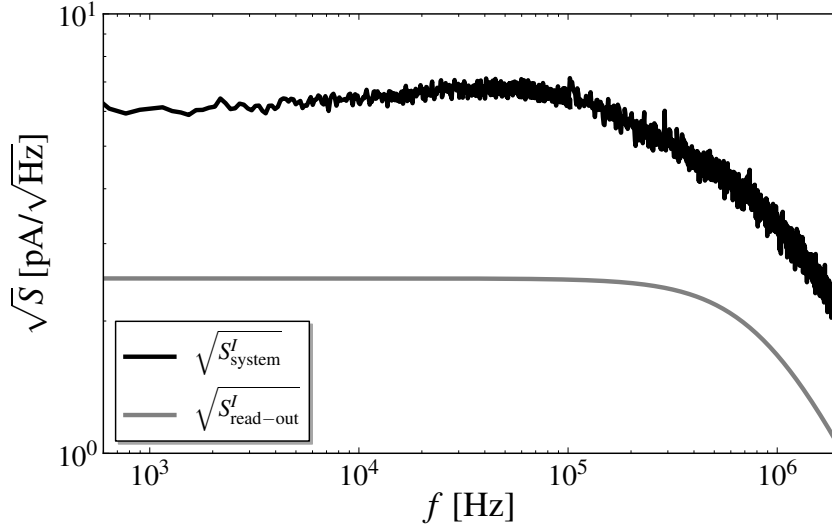
Figure 3.11.: Spectral noise current density and bandwidth of the NIST module: The NIST module is operated in the chosen working point $R_{\text{TES}} = 30\,\%\,R_{\text{N}}$ (sect. 3.4). The measured system noise S^I_{system} (black line) includes the TES noise S^I_{TES} and the noise due to SQUID read-out $S^I_{\text{read-out}}$ (grey line). The system bandwidth is determined by fitting a one-pole function to measurements: It is $f_{\text{3dB measured}} \approx 0.9$ MHz. Concerning the system noise, a slight bump around 100 kHz suggests excess electrical noise, which raises the noise floor locally.

measured by applying a sufficiently high TES bias current to obtain a normal resistive TES. This uncouples the TES circuit from the SQUID input (fig. 3.2), and therefore, the noise level correspond to the SQUID read-out noise. Such a noise spectrum of the NIST module, given in voltage units, is depicted in 3.13b.

As a first important result, it is indicated that the **noise level of the SQUID read-out noise is lower than the TES noise** (fig. 3.11). Considering the noise level at 10 kHz as a figure of merit, the read-out noise is $(S^I_{\text{read-out}})^{1/2} = 2.5$ pA/$\sqrt{\text{Hz}}$. The TES noise is determined by subtracting the read-out noise from the total system noise according to equation 3.49. With $(S^I_{\text{system}})^{1/2} = 6.5$ pA/$\sqrt{\text{Hz}}$, it results in $(S^I_{\text{TES}})^{1/2} = 6.0$ pA/$\sqrt{\text{Hz}}$. Thus, the system noise is dominated by the noise due to the TES single photon sensor and not by the SQUID read-out.

The read-out spectrum directly gives the **real system bandwidth**. Considering the one-pole function, it is determined $f_{\text{3dB measured}} \approx 0.9$ MHz. This is in the same order of magnitude to the estimated value in section 3.2.2.3: The SQUID read-out system bandwidth is estimated by $f_{\text{3dB estimate}} \approx 1.6$ MHz. The deviation is presumably due the approximation by a one-pole roll-off or the method of estimating the bandwidth including parameters of the SQUID electronics.

The measured system spectrum **slightly deviates in amplitudes from a one-pole spectrum** due to different time constants. The spectrum can be qualitatively

explained due to the following processes:

- $f \lesssim 5$ kHz: The noise is dominated by the thermal noise, since the ETF mechanism strongly suppresses the TES Johnson noise by a factor of $\frac{1}{1+\mathscr{L}_l(1+i\omega\tau)}$ according to equation 3.32 (Irwin, 1995). In other words, "at low frequency, the Johnson noise is reduced due to partial cancellation of the Johnson voltage in the electrical circuit by the Johnson noise power in the thermal circuit" (Lindeman, 2000).

- $f \approx 5\text{-}105$ kHz: A rise with a peak around 70 kHz is indicated. This deviation from a perfect one-pole trend is presumably caused by additional intrinsic noise sources of the TES: It is typically referred to as excess electrical noise with the same behaviour of Johnson noise (Irwin and Hilton, 2005). The thermal constant $\tau \approx 38$ μs defines the frequency $f_{\text{th}} = 1/2\pi\tau \approx 5$ kHz, at which the TES Johnson noise and, with it, a possible excess noise increase.

- $f \gtrsim 105$ kHz: The ETF time constant $\tau_{\text{ETF}} = 1.53$ μs defines the frequency roll-off of the thermal noise component of the TES:

- $f \gtrsim 900$ kHz: The spectrum shows an additional roll-off of the read-out bandwidth of the SQUID system given by $f_{\text{3dB measured}}$.

- $f \gtrsim 30$ MHz: The electrical time constant of the TES circuit fundamentally limits the bandwidth at $f_{\text{el}} \approx R_0/2\pi L \approx 30$ MHz. This roll-off is negligible due to the read-out bandwidth.

It is summarized that the noise response slightly affects a 1064 nm signal due to the bandwidth (sect. 3.2.2.4). Furthermore, comparing spectra from different measurement runs, it is observed that the noise response stays constant within the uncertainty of measurement by the spectrum analyzer (sect. D.3.2.3). Additionally, no significant difference between measurements inside the ADR and the dilution refrigerator at PTB-Berlin are observed. Only, 200 kHz harmonics are occasionally observed, however, which are uncritical for single photon measurements (see sect. 3.3.1). In addition, it is measured that the noise level at a bath temperature of 80 mK is 90 % lower than the level at 110 mK due to thermal noise. At temperatures below 80 mK, the thermal noise does not decrease significantly.

3.2.3. Further sensor modules

3.2.3.1. AIST module

Within this thesis, a second module to detect single photons was arranged for ALPS purposes: the AIST module. The setup is similar to the NIST module apart from the TES chips and the fiber-to-chip coupling. The module was operated and characterized in a dilution refrigerator at PTB in April 2013.

The AIST module was assembled in cooperation with PTB and AIST (Beyer, 2011-2013; Fukuda, 2012). The copper mounting was equipped with 2-stage PTB SQUIDs[50] and was sent to AIST to attach TES chips and single mode fibers. The mechanical mounting and electrical connections are the same as in the NIST module (sect. 3.2.1.4). Slight modifications were necessary because of the different fiber-to-chip coupling. Different from the NIST module, the fiber end is glued to the TES chip with resin. An additional Teflon mounting provides a stress relief to the fiber.

Optical-infrared TESs of AIST have a titanium film as sensor material. By using a multilayer structure with dielectric mirror layers around the TES layer, a near-unity detection efficiency for specific wavelengths is achieved (Fukuda et al., 2011). The AIST module is equipped with 1064 nm optimized chips (Fukuda, 2012). For each channel, a fiber end of a 1 m long fiber of a UHNA7[51] was glued to the chips. The UHNA7 fiber is extended by a 1.5 m long SMF28 fiber.

Due to a damaged SQUID input of channel B, only channel A of the AIST module was characterized. In the following, important parameters are summarized and compared to values of the NIST module:

- **Thermal parameters:** The superconducting transition is between T_c = 303-317 mK including a non-monotonous, steplike shape. Compared to NIST TES, the transition temperature is a factor 2 higher, which would allow to choose a bath temperature > 80 mK for longer hold times at mK temperatures in the ADR (sect. 2.3.4.4).

- **Electrical parameters:** The normal resistance above the transition is R_N = 3.7 Ω. The shunt resistor is R_{SH} = 22 mΩ, and a small parasitic resistance is indicated $R_{PAR} \approx 8$ mΩ. By considering a working point of 30 % R_N and $R_L \approx 30$ mΩ, the voltage-bias condition is given by $R_L/R_0 \approx 0.027 << 1$. Compared to the NIST module, it is a factor 2 larger, but still in the strong voltage-bias limit.

- **Working point:** At T_{bath} = 100 mK, the working point of 30 % R_N corresponds to $I_{BIAS} \approx 190$ μA. As a reminder, channel A of the NIST module requires $I_{BIAS} \approx 52$ μA for the same working point at 80 mK. A higher bias current provides a stronger Joule heating and, therefore, a stronger ETF, but it can diminish the hold time of an ADR at the same time (sect. 2.3.4.4).

---

[50]In PTB nomenclature: Type No. C6X114HW, Wafer: C638, Chip: L34
[51]This kind of fiber has a high NA> 0.4, see e.g. www.nufern.com

- **Noise response:** At this working point, the system noise level is $(S^I)^{1/2} =$ 5.8 pA/$\sqrt{\text{Hz}}$, the TES noise is $(S^I_{\text{TES}})^{1/2} = 5.7$ pA/$\sqrt{\text{Hz}}$. This is slightly lower than for the NIST module (sect. 3.2.2.5). The 3 dB frequency is at 1.2 MHz. For working points > 0.4 and < 0.2 R_N, a significant excess noise around 1 MHz is observed.

- **Signal response:** 1064 nm signals have an averaged pulse height of $PH \approx$ 60 nA and a measured fall time of $\tau_m \approx 310$ ns. This is nearly a factor 5 faster than the NIST module (sect. 3.2.2.4). The energy efficiency is $\eta_{\text{ETF}} \approx 70$ %.

The AIST module is suitable for low-noise single infrared photon detection. On the one hand, the glued fiber is a practical disadvantage compared to the NIST technique (sect. 3.2.1.2). On the other hand, faster pulses cause a better time resolution, which could provide a better pile-up discrimination (sect. 4.3.3).

3.2.3.2. Magnetometer

Additionally, a magnetometer was prepared to measure the magnetic environment inside the ADR and in the ALPS IIa laboratory. It is a dc SQUID from PTB[52] with a SQUID loop perpendicular to the chip plane. The sensitivity is 2 μT/ϕ_0 as a design parameter. The chip was glued on a modular copper piece and bonded to the circuit board (sect. 3.2.1.4). The magnetometer is operated at the base temperature of the pulse tube cooler in the ADR at ~2.5 K. Operating the magnetometer, influences of the ambient magnetic field in the ALPS IIa laboratory as well as influences due to the ADR magnet at the location of the sensors have been characterized (sect. 3.3.2).

3.2.3.3. INRIM module

In cooperation with INFN[53], the ALPS collaboration started their research on single photon detection with TESs. In 2011 a TES setup was operated in a dip-in dilution refrigerator at the University of Camerino (Natali, 2011; Cantatore, 2011). A successful operation at mK-temperatures and a single photon detection was achieved (Cantatore, 2013).

The sensor module was equipped with a Ti/Au TES from the INRIM group, Turin, Italy (Lolli et al., 2011). For read-out, a commercial SQUID array from the company Magnicon, Germany, was used. The SQUID was placed on a different base plate as the TES chip and was surrounded by a niobium can for magnetic shielding. Optical fibers were fed into the cryostat and the inner fiber ends pointed to the sensor area. The whole operation and measurement time was limited due to the amount of He4 which gradually evaporated for 4.2 K precooling.

---

[52]In PTB nomenclature: Type No. La70J025R14, Wafer: C403, Chip: D35. Inverse mutual feedback inductance: $M_f^{-1} = 40.8 \, \mu$A/ϕ_0.

[53]G. Cantatore (University of Trieste) and D. Vitali (University of Camerino)

3. Superconducting sensors for photon detection and their environments

Due to problems with the cryostat, no sufficient thermal shielding of the TES, and no sufficient coupling of the wires in the beginning, the superconducting transition was observed after several cool-downs. Besides cryogenic experience, the qualitative result was that single photon detection with a TES setup can be successfully established. Quantitative results and details about INRIM TESs are found in the thesis of Lolli (2012), for example. INRIM TESs have shown photon number discrimination, signal fall times <0.5 μs, and ~4 % overall detection efficiency (Lolli et al., 2011, 2012). The INRIM group, Turin, is developing new chip generations with multilayer structures and improved fiber-to-chip coupling in order to increase the detection efficiency (Lolli, 2013).

3.3. Environments of sensor modules for ALPS

In this chapter, environments of superconducting sensors are described. The focus is on an operation within the ADR cryostat (sect. 2.2) in the ALPS IIa laboratory.[54] For low-flux single photon detection and background measurements (app. 4), it is essential to understand the detector environment and to know its long-term stability. Therefore, the following environments are studied:

- the electrical setup is optimized (sect. 3.3.1),

- possible magnetic influences are considered (sect. 3.3.2),

- and the thermal mK-environment is optimized (sect. 3.3.3).

3.3.1. Electrical setup

The electrical setup of a TES detector system is rather complex. Superconducting sensors as well as the cabling of signal and power lines of the components can potentially couple in electro-magnetic interferences (EMIs). An optimized setup of operating a sensor module in the ADR cryostat has been found (fig. 3.12).[55] This setup is proven as having less electrical interference by ground loops. This was tested without operating the ADR cryostat to exclude influences from that. This is confirmed by operating the NIST module, which is briefly discussed in the following.

To assess the electronic environment, the **spectral noise density of** the SQUID electronics output is observed using a spectrum analyzer.[56] Basically, the system is set up as for photon measurements: The NIST module is operated at 80 mK inside the ADR cryostat.[57] The SQUID is operated in FLL. However, to observe only the read-out noise, the TES circuit is decoupled by setting the TES normal resistive, for example, with $I_{\text{bias}} = 250\ \mu\text{A} \sim 1.0\,R_{\text{N}}$. This allows to assess the electrical environment of different setups.

In the basic setup, signal cables of the ADR infrastructure and the measurement side are connected to the ADR dewar (fig. 3.12). Therefore, they have the same ground level. In addition, if the ADR infrastructure and the measurement side is powered by the same supply, a ground loop is established. This arrangement causes considerable **50 Hz harmonics** (fig. 3.13). Interrupting the ground loop diminishes 50 Hz harmonics to a satisfying level: The noise peak at 50 Hz is decreased by one

---

[54]The laboratory is located in the first basement floor of HERA-West at the DESY site, building 50, room 607.

[55]The focus is on the detector infrastructure outside the ADR cryostat. A detailed wiring scheme between SQUID electronics and sensor modules inside the cryostat are given in the appendix C.3.

[56]The spectrum analyzer is a HP 89410A borrowed from the PTB group. The device directly illustrates an averaged spectrum in units of V/$\sqrt{\text{Hz}}$.

[57]The mK-operation was established with and without ADR temperature regulation which indicated no difference (sect. 3.3.2.2).
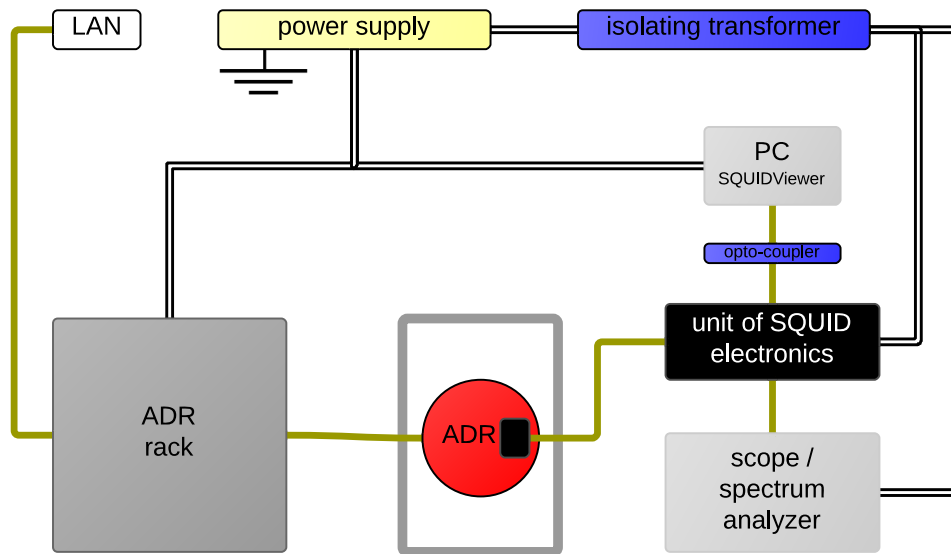
Figure 3.12.: Optimized electrical setup of the ALPS TES detector: This simplified sketch illustrates the signal (brownish lines) and power (double black lines) cabling of the TES detector setup. Basically, on the left is the ADR infrastructure, on the right the measurement side. In general, a ground loop could be established because the ADR rack and the SQUID electronics are connected to the same power supply and the ADR provides the same ground level. Since the controlling PC for the SQUID electronics is galvanically isolated by an opto-coupler element, in addition, an commercial isolating transformer (upper right) is used as galvanic isolated power supply for the SQUID electronics and the measurement device (oscilloscope or spectrum analyzer). This avoids a ground loop.

order of magnitude and there are nearly no higher harmonics. The best galvanic isolation is found by separating the ground loop with an isolating transformer for the power supply of the measurement side (fig. 3.12).

In addition, **200 kHz harmonics** are observed (fig. 3.13). These harmonics are measured if the complete 2-stage SQUID is biased. Operating only the SQUID array in FLL mode and an unbiased front-end, the 200 kHz harmonics do not occur. Additionally, these harmonics are only observed in the ADR setup at DESY. During the characterization at PTB-Berlin, 200 kHz peaks were not measured. Presumably, a current source of the SQUID electronics or its switching power supply cause these interferences (Barthelmess, 2013). However, these harmonics have shown to be uncritical for single photon and background measurements (chap. 4). Firstly, the peaks are relatively diminished when the NIST module is operating in the working point for single photon detection. The higher noise level due to a corresponding TES bias of 30 % R_N is shown in figure 3.13b. This spectrum corresponds to the presented noise response in section 3.2.2.5. Secondly, the noise level is much smaller than the level of a signal.

(a) no isolation   **(b)** galvanic isolation
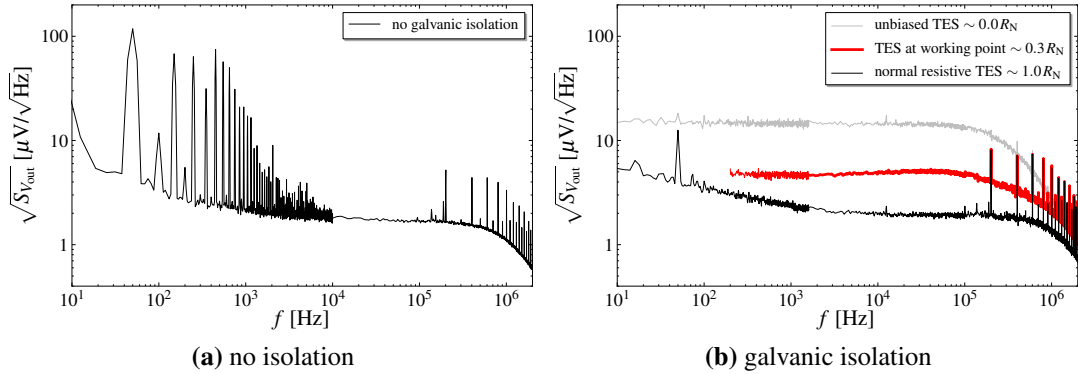
Figure 3.13.: Noise spectrum without and with galvanic isolation: The NIST module is operated. To observe only the read-out noise by the SQUID system, the TES circuit is uncoupled (black spectra). (a) shows considerable 50 Hz harmonics without galvanic isolation of the measurement side (fig. 3.12). (b) shows the effect of using a galvanic isolation: The 50 Hz harmonics are significantly diminished. In addition, 200 kHz harmonics couple to the biased SQUID of the NIST module. The peaks of the 200 kHz harmonics are relatively diminished if the TES is in working point (red spectrum in the middle). This spectrum corresponds to the noise response of the NIST module, which is discussed in section 3.2.2.5. In addition, the upper (grey) spectrum results from an completely unbiased superconducting TES at which the noise level is mainly caused by the low impedance load resistance R_L of the TES circuit.

Additional tests provide no improvements. Neither a differential signal amplifier between the SQUID electronics and the spectrum analyzer, nor different mass connections between the components show any improvement. Furthermore, the network connection of the ADR computer (LAN) feeds in interferences like 50 Hz oscillations. With the isolating transformer, these oscillations are not measured. Further small noise peaks around 12.5-16.0 kHz are caused by the microcontroller of the SQUID electronics. These peaks are sufficiently diminished by setting the SQUID electronics in sleeping mode (Magnicon, 2011).

3.3.2. Magnetic influences

SQUIDs are naturally sensitive to magnetic influences (sect. 3.1.3.1). Although SQUIDs realized as current sensors are designed to be less sensitive to magnetic fluxes, strong external influences can degrade the performance. For example, if a SQUID traps magnetic flux due to external fields, the SQUID characteristic is deformed, and the operation as a linear sensor is not guaranteed anymore. Therefore, in this section the magnetic environment (sect. 3.3.2.1) and influences of the ADR magnet (sect. 3.3.2.2) are discussed. In front, the location of the sensor module inside the ADR and possible magnetic influences are discussed as well as critical

Figure 3.14: Magnetic influences on sensors inside the ADR: The chip (dark grey) illustrates the location and orientation of the SQUID sensor inside the ADR cryostat. Possible magnetic influences on the SQUID are an ambient magnetic field, such as the earth's magnetic field (red arrow), the ADR magnet (light grey), and the bucking coil (black lines). By approximation, the ADR magnet couples parallelly to the chip plane; and the bucking coil perpendicularly to the chip. The orientation between the ambient magnetic field and the sensor plane is defined by the position of the ADR cryostat in the laboratory (fig. 3.15a).
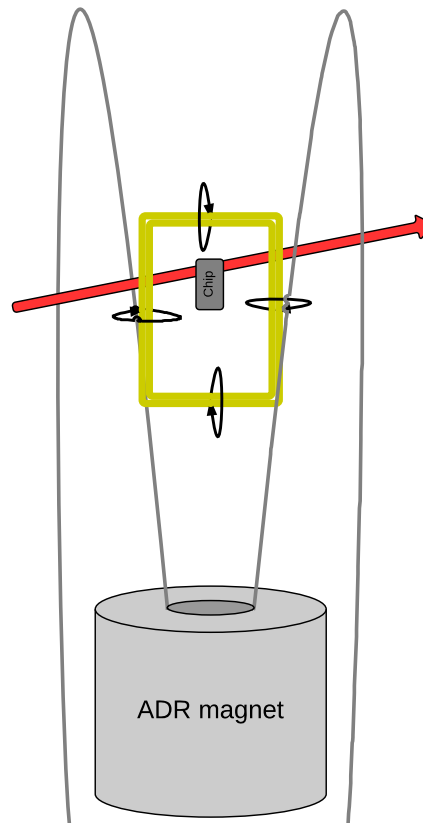
fields of SQUID operation are defined.

The location of the sensor modules is illustrated in figure 3.15a. In the ALPS IIa laboratory the ADR cryostat is surrounded by different metallic and electric components which can affect the magnetic environment. Inside the ADR, the sensor module is placed along the z-axis of the solenoid ADR magnet. Here, the z-axis lies along the SQUID chip plane.[58] In addition, a bucking coil (app. C.1) surrounds the sensor which allows to compensate ambient fields during defluxing the SQUID (see below). These **possible magnetic influences** on sensors are sketched in figure 3.14. Main sources are the earth's magnetic field as ambient field (sect. 3.3.2.1) and the active ADR magnet (sect. 3.3.2.2). To characterize magnetic couplings to SQUIDs, the orientation of the chip plane related to the flux lines is important. In this setup, flux lines of the ADR magnet are approximately parallel to the chip plane, flux lines of the bucking coil approximately perpendicular. In section 3.3.2.2, magnetic couplings to the sensors are discussed.

For the following discussion, **two field parameters** of a SQUID are important. Three cases of a SQUID in a constant ambient magnetic field B_{amb} are considered:

---

[58]The distance from the upper part of the magnet to the sensor is about ~27 cm. The distance includes the width of the 4K-stage, the length of the FAA cold finger, the FAA extension rod, and the length on the detector bench.

(a) in ALPS IIa laboratory
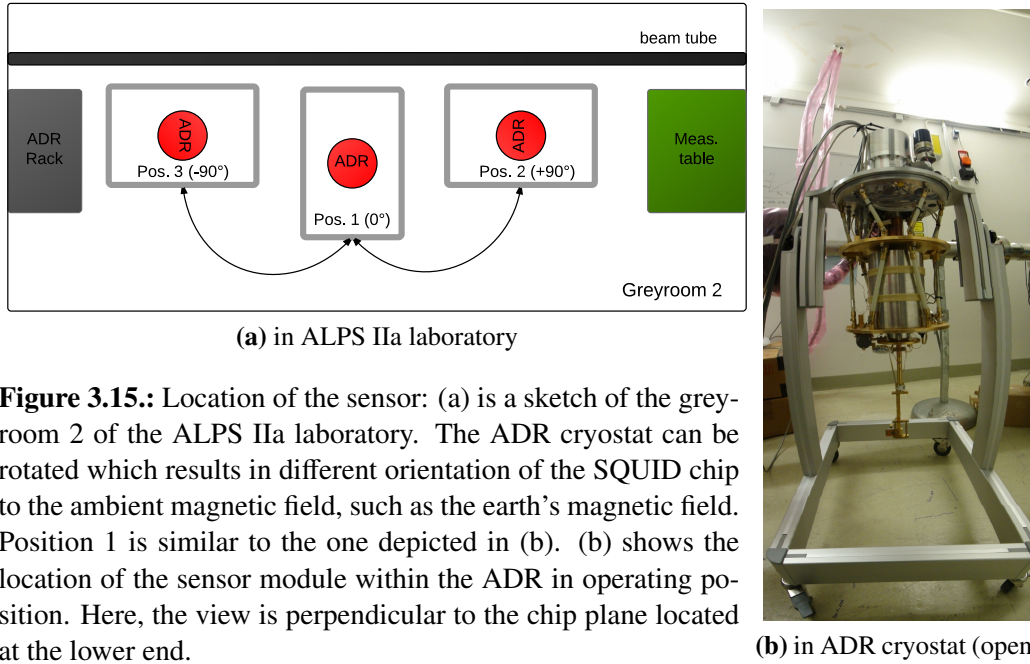
Figure 3.15.: Location of the sensor: (a) is a sketch of the greyroom 2 of the ALPS IIa laboratory. The ADR cryostat can be rotated which results in different orientation of the SQUID chip to the ambient magnetic field, such as the earth's magnetic field. Position 1 is similar to the one depicted in (b). (b) shows the location of the sensor module within the ADR in operating position. Here, the view is perpendicular to the chip plane located at the lower end.

(b) in ADR cryostat (open)

- $B_{amb} < B_{coolmax}$: The SQUID is cooled below T_c. The SQUID becomes superconducting and no flux is trapped in the SQUID. This defines the first parameter $B_{coolmax}$. If the superconducting SQUID includes trapped flux, the SQUID can be defluxed by short-time heating (app. D.3.1.2).

- $B_{coolmax} < B_{amb} < B^*$: The SQUID traps flux if it becomes superconducting. Trapped flux can be removed by defluxing the SQUID while applying a compensating field. If the resulting field at the sensor is below $B_{coolmax}$, the SQUID can be defluxed. If the SQUID is superconducting without trapped flux, the compensating field can be switched off since the SQUID expulses fields smaller than B^*. Thus, B^* defines the maximal tolerable field for a proper SQUID operation.

- $B_{amb} > B^*$: The SQUID is always affected by the ambient field.[59]

PTB SQUIDs are designed to work in an ambient DC magnetic field comparable to the earth's magnetic field (Beyer, 2011-2013). Therefore, $B_{coolmax}$ is larger than the strength of the earth's magnetic field. This is tested in the next section.

3.3.2.1. Ambient magnetic field

The DC component of the ambient magnetic field is estimated by operating the magnetometer (sect. 3.2.3.2).[60] Rotating the ADR cryostat more than 180° results

---

[59]Only a permanent compensating field could lower the resulting field sufficiently.

[60]As a reminder, the magnetometer is operated at the base temperature of the pulse-tube cooler. The ADR magnet is switched off.

in a peak-to-peak value of the ambient field (fig. 3.15a). Fluxes between Φ_{pp} = 39-44 Φ_0 are measured. This results in a magnetic field density of B_{pp} = 78-88 μT with the design parameter $2\,\mu\mathrm{T}/\Phi_0$ of the magnetometer. This value corresponds to the horizontal component of the ambient field, assuming that only magnetic changes perpendicular to the magnetometer chip plane are measured. In the following, the half of the peak-to-peak value is conservatively considered as the maximum possible ambient magnetic field in the laboratory $B_{\mathrm{amb,max}} \approx 45\,\mu\mathrm{T}$.

Uncertainties of the measurement are caused by the non-perfect rotation around one axis. As shown in figure 3.15a, a rotation of the ADR corresponds to different locations at the same time since the movement is constrained by the helium tubes of the pulse tube cooler (sect. 2.2). Furthermore, it is observed that the result deviates depending on the end locations. This implies that metallic components in the laboratory are influencing the ambient magnetic field.

In the laboratory of PTB-Berlin, an ambient field of about B_{amb} = 19 μT is measured by rotating the magnetometer. This is comparable to the horizontal component of the earth's magnetic field. For example, in northern regions of Germany, the earth's magnetic field density is $B_{\mathrm{total}} \approx 50\,\mu\mathrm{T}$, $B_{\mathrm{horizontal}} \approx 18\,\mu\mathrm{T}$, and $B_{\mathrm{vertical}} \approx 45\,\mu\mathrm{T}$.[61] Comparing this to the determined value in Hamburg, $B_{\mathrm{amb,max}} \approx 45\,\mu\mathrm{T}$, indicates that the horizontal component of the ambient field is higher in the ALPS IIa laboratory. This is presumably caused by the metallic environment which can squeeze and deflect the ambient field.

According to the datasheet, it is B_{coolmax} = 94.8 μT for channel A of the 2-stage SQUID of the NIST module, which is below the estimated value above. That means that the NIST module is working in the magnetic environment of the ALPS IIa laboratory without magnetic shielding[62], which is confirmed by successful SQUID defluxing and proper operation of the NIST module. Furthermore, it is observed that SQUID sensors are sensitive to moving metal, such as chairs or the door of the ADR rack. This is uncritical for sensitive long-term measurements with nobody in the laboratory. Finally, considering the noise spectrum of the NIST module, no AC influences related to magnetic fields are observed.

It is summarized that **the ambient magnetic field of the ALPS IIa laboratory is uncritical to operate the NIST module**.

3.3.2.2. ADR magnet

Since the cooling principle is due to magnetic fields within an ADR, stray fields of the ADR magnet can affect magnetically sensitive sensors such as SQUIDs. Especially, the holding of a mK-temperature by regulating the ADR magnet can influence the SQUID read-out during measurements. Thus, the magnetic influence of

---

[61] Values are taken from `http://www.ngdc.noaa.gov/geomag/magfield.shtml`.
[62] Results of superconducting shielding inside an ADR is found in the appendix C.2.

the ADR magnet on the location of the sensors is studied. The results referred to the NIST module are presented.

Similarly as the inverse mutual feedback inductance of a SQUID (sect. 3.1.3.2), the coupling of the ADR magnet is defined as the corresponding inverse mutual inductance:

$$M_{\mathrm{ADR}}^{-1} = \frac{\delta I_{\mathrm{ADR}}}{\delta \Phi}$$

For the NIST module, a weak coupling $M_{\mathrm{ADR,NIST}}^{-1} = 15$ A/Φ_0 is determined in a current range up to $I_{\mathrm{ADR}} = 1$ A, which is relevant for regulating mK-temperatures.[63] The coupling includes the effect due to the passive cryoperm shield around the ADR magnet; in this range the shield is not saturated, which expresses as a linear coupling dependence. Thus, this total shift corresponds to a small SQUID flux change of $\Delta\Phi = 0.07$ mΦ_0 or to a baseline shift of ~40 mV. During a temperature regulation, this coupling causes a slow, gradual shift of the baseline. In principle, this could be gradually compensated by adjusting the bias source Φ_{b} (sect. 3.1.3.2). However, since photon measurements are operated in AC-coupling mode (sect. 3.4), this shift is uncritical for sensitive photon detection.[64]

Furthermore, the AC component is measured during temperature regulation. No significant influences are observed by comparing noise spectra.

Finally, it is noted that the SQUID is highly affected and traps flux during a recharge with full magnetic field. After ramping down the ADR magnet and reaching mK-temperatures, the SQUID can be defluxed by a short-time Joule heating, which is explained in the appendix D.3.1.2). The tolerable magnetic field B^* of the SQUID of the NIST module corresponds to an ADR magnet current of ~5 A.[65] Thus, it is unproblematic to deflux the SQUID even while regulating a mK-temperature.

It is summarized that **the influence of the ADR magnet is uncritical to operate the NIST module at mK-temperatures**.

3.3.3. Thermal environment

Proper cooling of superconducting sensors is a necessary condition for their operation. Although the bath temperature of the ADR cold finger, $T_{\mathrm{bath}} = 80$ mK, is below the transition temperature of the NIST TES, $T_{\mathrm{c}} \approx 140$ mK, it is observed that the cooling effect by the bath is not stable or even not sufficient due to external

---

[63]For example, the temperature regulation to 80 mK by the ADR magnet corresponds to magnet currents between $I_{\mathrm{ADR}} \approx 500$ until 0 mA while a ~20 h hold (cf. fig. 2.7b).

[64]The AC-coupling of the SQUID electronics sets the baseline to zero by averaging the voltage output with a frequency of about 0.5 Hz (Barthelmess, 2013), which is fast compared to the shift of the baseline.

[65]This is an important insight using superconducting magnetic shielding made of aluminum which are attached to the FAA-stage. This is discussed in appendix C.2.

power loads. This cooling of the NIST TES[66] as well as the setup optimization is discussed in the following.

An indicator for the thermal condition of the TES is the required bias current to set the TES from a superconducting state in its working point by Joule heating. According to the steady-state power balance (eqn. 3.17), it is

$$P_{J_0} = I_0^2 \cdot R_0 = P_{\text{bath}_0} - P_0 \tag{3.53}$$

where R_0 is the TES resistance in the working point – here 30 % R_N – and I_0 the TES current which is related to the adjusted bias current I_{BIAS} of the TES circuit (sect. 3.1.2.4). Therefore, in an ideal scenario, I_{BIAS} directly indicates an effect of external power load P_0, assuming that P_{bath} is constant.[67] Thus, lower bias currents appear as a lower effective cooling of the bath due to higher external power loads P_0.

During setting up the TES detector system of ALPS, three different cases were observed:

- **Non superconducting TES with $I_{\text{BIAS}} \geqq 0\,\mu$A:** The thermal mK-shield with little holes and a not completely attached fiber end to the sleeve show an insufficient cooling. This is caused by an external power load due to thermal radiation of the 4K-stage. Using the Stefan-Boltzmann law (eqn. A.7), the black body radiation of the 4K-stage results in $P_{\text{black body, 4K-stage}} \approx 3000$ fW reaching the TES chip.[68] Compared to the Joule power $P_{J_0} \approx 400$ fW to reach the TES working point in a shielded setup (fig. 3.9), black body radiation from the 4K-stage causes a too high power load.

- **Reaching the TES working point with I_{BIAS} = 40-50 μA:** Using a proper mK-shield but an improper thermal coupling of the fiber shows an irreproducible condition after recharges within one cool-down. The deviation in the required I_{BIAS} to reach the TES working point is caused by an insufficient thermal coupling of the fiber. Parts of the fiber or the fiber-to-chip coupling could act as a heat store. In addition, it is observed that the bias current for the same working point gets slightly higher about 1-2 μA within the first hours after a recharge. This points to a thermalization effect.[69] Furthermore, since the fiber is mechanically not fixed within the ADR 4K-room, vibrations could cause undefined power loads.

- **Reaching the TES working point with I_{BIAS} = 52-54 μA:** Using a mK-shield and a proper thermally and mechanically fixed fiber, a stable condition

---

[66]Here, channel A of the NIST module.

[67]Deviations to this ideal scenario are self-heating due to Joule power and a change of the thermal coupling due to the fiber attached to the TES.

[68]Here, the TES chip area (fig. 3.6) facing a 2.5 K black body radiation from the 4K-stage (sect. 2.3.2) is considered.

[69]This effect is observed in a similar setup by the Vienna group of IQOQI (Giustina, 2013).

is observed. The bias current deviates between 52-54 μA. This deviation includes the measurement uncertainty of the *IV*-curve and probably tiny thermalization effects. These values of current bias are also required without fiber to the TES. This confirms a proper thermal coupling of the fiber and a proper thermal environment for the TES.

It is concluded that the last setup is suitable for single photon detection and dark count determination. A detailed discussion about the deviation of the signal response is found in section 4.2.4.

3.4. Summary and working point of the ALPS TES detector

It is summarized that a TES detector system for ALPS is set up and optimized. Therefore, the TES physics according to Irwin and Hilton (2005) is described (sect. 3.1). This provides an understanding of the TES response concerning noise and signals. The NIST module is extensively characterized (sect. 3.2). The determined TES and SQUID parameters are found in the right part of table 3.2. The measured signal response fits to the theory using the determined TES parameters (fig. 3.10). Furthermore, the environment of the ALPS IIa laboratory and the environment in the ADR cryostat is suitable to operate TES detectors (sect. 3.3).

The setup which is used for single photon and background studies in the next chapter 4 is named *ALPS TES detector* in the following. The components and the setup are summarized according to the studies of the previous chapters:

- The **ADR cryostat** is operated in the ALPS IIa laboratory at position 1 (fig. 3.15a). At this position, the electrical and magnetic environments are known (sect. 3.3.1 and 3.3.2).

- The **NIST module** is attached to the detector bench which extends the FAA cold finger of the ADR (app. C.1). Thus, the sensor is placed as far as possible away from the ADR magnet to minimize magnetic influences during regulation. The ADR temperature regulation is uncritical to operate the NIST module (sect. 3.3.2.2).

- A **copper shield** surrounding the NIST module is attached to the FAA-stage (app. C.2). The shield provides a mK-environment and screens thermal radiation of the 4K-stage (sect. 3.3.3). In addition, cables and fibers are thermally and mechanically anchored at the FAA-stage before reaching the NIST module.

- Different **fiber installations** are used which are described in section 4.1.1. Fibers have to be thermally coupled to the mK-stage, before reaching the TES in order to diminish thermal influences (sect. 3.3.3).

- Measurement and SQUID electronics are **galvanically isolated** from the ADR infrastructure, in order to avoid interferences (fig. 3.12 in sect. 3.3.1). Furthermore, the SQUID electronics is switched on 2 hours before measurements in order to reach a stable condition (Barthelmess, 2013).

The nominal **working point** of the ALPS TES detector operating channel A of the NIST module:

- **ADR cryostat:** The bath temperature is set to 80 mK by regulating the FAA temperature with the ADR magnet (sect. 2.3.4). This temperature has shown a good trade-off between ~20 h hold time (sect. 2.3.4.4) and sufficient temperature difference to T_c of the NIST TES which provides an operation in strong ETF (sect. 3.2.2.2).

- **NIST TES:** The bias current is set to a value which corresponds to 30 % R_N. In addition, different working points between 10 to 50 % R_N were considered. In this range no significant excess electrical noise is observed which could affect the response (sect. 3.2.2.5). In a series, different working points were studied with 1064 nm photon signals (app. B.1). It is indicated that working points between 10 and 30 % R_N have a good signal-to-noise ratio as well as similar energy resolutions. For single photon operation, 30 % R_N is chosen. A discussion about systematical uncertainties and deviations to the nominal working point is found in sections 3.2.2.4 and 4.2.4.

- **PTB 2-stage SQUID:** The SQUID device provides a low-noise current read-out of the TES (sect. 3.2.2.5). The bias currents are given in table 3.2. The values are selected to obtain the steepest slope in the modulation which corresponds to a high dynamic range (sect. 3.1.3.2). A description to adjust the 2-stage SQUID in its working point is found in appendix D.3.1.1. Further adjustments of the SQUID electronics are (app. C.5.1): The feedback resistance is set to $R_f = 100$ kΩ; the gain-bandwidth product is set to $GBP = 2.8$ GHz; for single photon detection, AC-coupling and the sleeping mode are active.

The working point of the ALPS TES detector as well as its noise and signal response are summarized at left in table 3.2. The signal and noise response is described in detail in section 3.2.2.4 and 3.2.2.5. A manual like description to operate the ALPS detector setup is found in appendix D.

Working point of the ALPS TES detector and noise and signal response		TES and SQUID parameters of the NIST module (ch A)	
T_{FAA} (I_{ADR})	80 mK (~0-500 mA)	T_{bath}	80 mK
I_{b}	12.5 μA	T_{c}	140 mK
V_{b}	120.8 μV	ΔT_{c}	1-2 mK
I	30.0 μA	α	360
Φ_{X}	10.0 μA	β	3
GBP	2.8 GHz	C	0.58 fJ/K
R_{f}	100 kΩ	G	15 pW/K
R_{TES} (I_{BIAS})	30 % R_{N} (~52-54 μA)	R_{N}	13.8 Ω
$\sqrt{S^I_{\text{system}}}$ at 100 kHz	6.5 pA/$\sqrt{\text{Hz}}$	R_{SH}	24 mΩ
f_{3dB}	0.9 MHz	R_{PAR}	20-40 mΩ
τ_{rise}	~70 ns	L	17-22 nH
τ_{fall}	~1.53 μs	M_{in}^{-1}	5.792 μA/Φ_0
$PH_{1064\text{ nm}}$	~70 nA	M_{f}^{-1}	44.04 μA/Φ_0
$(\Delta E/E)_{1064\text{ nm}}$	6-8 %	$I_{\text{TES}}/V_{\text{out}}$	1.315 nA/mV

Table 3.2.: Working point and corresponding response of the ALPS TES detector and parameters of channel A of the NIST module: The left table summarizes the working point – ADR temperature, SQUID adjustment, and TES bias – of the ALPS TES detector for single photon and background measurements (chap. 4). The bottom part are corresponding values of noise and signal response (sect. 3.2.2.5 and 3.2.2.4). The right table summarizes parameters of the NIST module: thermal parameters (sect. 3.2.2.1), electrical parameters (sect. 3.2.2.2) and SQUID parameters (sect. 3.2.2.3).

4. Near-infrared signal photons and dark counts

The goal of this chapter is to determine a dark count rate of 1064 nm photons using the ALPS TES detector, which is developed within in this thesis (chap. 2 and 3). Firstly, the optical setup including different fiber setups and measurement settings is described (sect. 4.1). Secondly, 1064 nm photons are analyzed which represent a signal of the ALPS II experiment and calibrate the detector (sect. 4.2). Three analysis methods are developed each one allowing to define a signal region and to obtain different insights into single photon measurements. Furthermore, analysis strategies for background measurements are developed.

The last part examines noise and backgrounds seen by the NIST module (sect. 4.3). Noise and background events which cannot be distinguished from signals result in dark counts of the detector. Basically, two dark count rates of 1064 nm photons using the ALPS TES detector are considered:

- a detector dark count rate of a TES with optical fiber link to the experiment,
- an intrinsic dark count rate of a dark TES.

It is expected that the detector dark count rate is dominated by thermal infrared photons from the room temperature end of the fiber. This is observed by other groups and is summarized in section 4.3.1; results of this thesis are found in section 4.3.3. The intrinsic dark count rate could be caused by different background contributions:

- Cosmic rays: Most of cosmogenic components are absorbed by overburden such as the ceiling of the ALPS IIa laboratory or the ADR shields (Beringer et al., 2012). However, muons could directly reach the TES or, due to absorption, induce scintillation light, which could be detected by the TES.

- Radioactivity: Environmental radioactivity is expected to be screened by the ADR shields. Radioimpurities in detector or shielding components could cause TES signals. For example, aluminum is often found to contain radioactive sources (Beringer et al., 2012). As above, direct absorption or scintillation photons are possible.

- Thermal photons: Material at a certain temperature is found to show a black body spectrum (sect. 4.3.1). Thermal photons of warm surfaces inside the cryostat could reach the TES.

- Electro-magnetic interference (EMI): External interferences can couple to the read out system including the magnetically sensitive SQUID (sect. 3.3.1 and

3.3.2).

- Fundamental noise: The fundamental TES noise including the resistive John-son noise and the thermal fluctuation noise by phonons (sect. 3.2.2.5) could result in a dark count.

- Exotic particles: In principle, it cannot be excluded that exotic particles are measured. For example, if magnetic monopoles would exist, they could interact with SQUIDs (Eidelman et al., 2004).

Non-photon like background is expected to be suppressed by the analysis. The intrinsic dark count rate is the fundamental limit of this specific detector setup. This is discussed in section 4.3.2. In section 4.4, all results are summarized.

Units of data

In this chapter the TES response is treated as the SQUID output in voltage units. The negativity of pulses conserves the character of smaller TES currents due to an increase in temperature after an energy input (sect. 3.2.2.4). As a reminder here, the voltage output directly corresponds to the TES current by formula 3.46. For channel A of the NIST module the conversion factor is (sect. 3.2.2.3):

$$(I_{\text{TES}}/V_{\text{out}})_{\text{NIST,A}} = 1.315 \pm 0.036\,(\text{stat.}) \pm 0.067\,(\text{syst.})\,\text{nA/mV} \quad (4.1)$$

Another helpful formula is related to the calibration. The sensor is calibrated to photon energies within the signal analysis. In a form of practical units, the conversion from photon wavelength λ to energy E is given by:

$$E = 1\,\text{eV}\left(\frac{1240\,\text{nm}}{\lambda}\right) \quad (4.2)$$

(a) standard   (b) inside   (c) no fiber
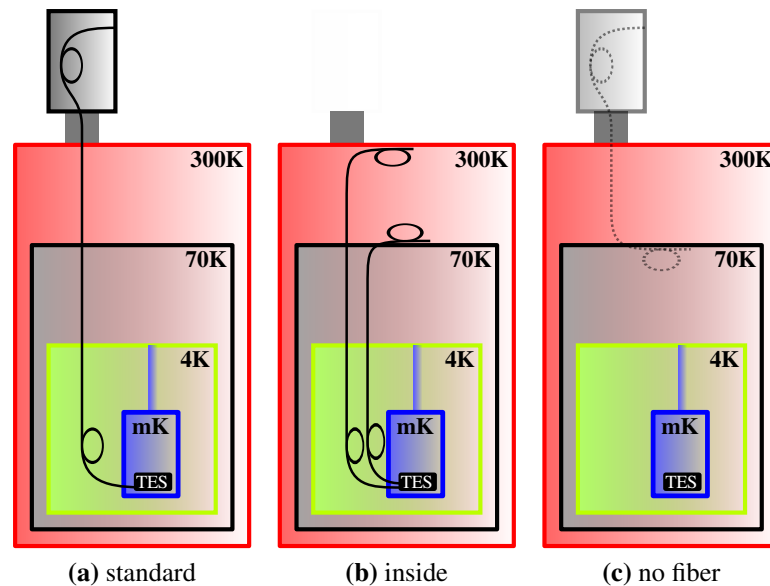
Figure 4.1.: Optical fiber installations: Basically, three fiber installations are studied: (a) illustrates the signal configuration, where the fiber is fed through the ADR to the fiber interface at the black box outside of the ADR. (b) shows the configuration, where the fiber stays inside the ADR, connects the TES and is looking in the 300K-room of the ADR. As illustrated, two fiber channels are tested: one fiber channel with the warm fiber end at the outside of the 70K-stage and one channel with the warm end at the 300K-stage at the bottom side of the ADR top flange. In (c) the TES is not connected to a fiber. Optionally, a fiber is fed in the ADR, but its cold end is stored at the 70K-stage (dotted line).

4.1. Experimental setups

To analyze signals and backgrounds, the NIST module is operated in its favored working point within the optimized setup for ALPS (sect. 3.4). A detailed explanation about operation of the TES detector is found in the appendix D. In this section important experimental setups are briefly described: To determine signals and to discriminate background sources, different fiber setups are required. Three different installations are studied which are described in section 4.1.1. Photon sources to establish a single signal photon flux and methods to reduce environment light are briefly explained in section 4.1.2. Finally, different measurement settings are used to determine signals or backgrounds which are summed up in section 4.1.3.

4.1.1. Fiber setups

For the following studies, different fiber setups are required. For signal calibration the TES has to be connected to a single photon source outside the ADR cryostat. To explore background, different fiber setups can provide a discrimination. In prin-

ciple, three different fiber setups are studied in this work (fig. 4.1):

a) **Standard configuration:** The fiber connects the TES and the connector of the black box outside the ADR (app. C.4). Thus, a photon source can be attached for signal measurements. Optionally, for background measurements, the fiber end at the black box is sufficiently covered to prohibit stray light from the environment (fig. 4.1a). At the same time the standard configuration represents a realization to use the TES detector for the ALPS experiment (fig. 4.1a).

b) **Fiber inside the ADR:** The TES is connected to a fiber. The warm fiber end is placed inside the ADR. Two fiber channels are tested: one with the end fixed outside the 70K-stage, but looking in the 300K-room; one with the end fixed at the 300K-stage at the bottom side of the ADR top flange (fig. 4.1b).

c) **No fiber:** No fiber is installed. There is no optical link between the inside and the outside of the ADR (fig. 4.1c). Optionally, a fiber is fed in the ADR, but its cold end is stored at the 70K-stage (dotted line in fig. 4.1c) and is not attached to the TES.

Fibers which are used in these setups are from the type SMF28 (app. C.4). Each fiber is prepared to be "naked": The plastic tubing along the fiber is removed, thus, only two cladding layers surround the core. The NIST technique (Miller et al., 2011) is used for a high-efficient fiber-to-TES-coupling (sect. 3.2.1.2). Since black body photons as background are considered, the temperature and the length of the fiber are crucial. It is assumed that the temperature of the fiber outside the ADR and inside the 300K-room of the ADR is the same as in the laboratory. The laboratory is climatized at 22 °C, which corresponds to 295.15 K. Therefore, 300 K is a conservative estimate for black body considerations. Exact fiber lengths and configurations are found in section 4.3.3.

4.1.2. Signal sources and environment light

As the ALPS II laser is used to set up and characterize the production cavity, test lasers are used for the calibration of the TES. Two **attenuated monochromatic laser sources** are available with wavelengths of 1063.9 nm and 1066.7 nm.[1] These photon energies deviate <0.25 % of 1064 nm photons, which is the nominal ALPS II wavelength. This is uncritical to calibrate ALPS signals, because this deviation is small compared to the energy resolution about 6-8 % (sect. 4.2). Thus, using these sources, the wavelength is named 1064 nm for convenience in the following. In addition, to reach a suitable single photon flux, the lowest laser power of ~1 μW is

---

[1]The sources are fiber-coupled diode lasers of the model "51nanoFCM" or "58FCM" from the company Schäfter+Kirchhoff. Additional emission of wavelengths between 600 to 1100 nm is not observed. The intensity of other wavelengths is measured to be <0.2 % related to the nominal wavelength.

used together with several fiber attenuators in series. This leads to a suitable rate of 100-1000 photons per second to analyze single signal photons.

In addition, in order to prohibit **environment light**, the setup is covered as well as possible. The laser source with the attenuators is placed in a dark box.[2] Laboratory lights are switched off during measurements. Furthermore, remaining light sources like control lamps or displays are screened as well as possible. This leads to a sufficient dark environment with a defined signal source to calibrate the TES detector (sect. 4.2). The same method to reduce environment light is used during long-term background measurements with a fiber outside the ADR. With the fiber end inside the ADR or no installed fiber, a vacuum flange instead of a fiber feedthrough on top of the ADR is used. This naturally leads to a sufficient screening of environment light (see light-tightness of the ADR in sect. 4.3.3).

4.1.3. Measurement settings

To record the voltage output of the SQUID electronics, the oscilloscope DPO7104C from Tektronix is used. The sampling interval is set to $\Delta t = 50$ ns and the digitization step to 0.4 mV. Two acquisition options are used:

- **Time series to analyze signals:** A proper single photon source is applied (sect. 4.1.2). Time series for seconds allow to extract signal photons offline to define a signal region (sect. 4.2).

- **Events on trigger to measure background:** For long-term background measurements (sect. 4.3) a data window is saved on trigger. The window is set from -5 to 15 μs and from -80 to 20 mV, which is suitable to scan the 1064 nm signal region.[3] The time window and the read-out time define the dead time of the detector. To reach a high record efficiency, the trigger rate should be sufficiently below the inverse dead time. Thus, the trigger level has to be well chosen:

    - A trigger level of $TL = -40$ mV is adjusted to determine the intrinsic background (sect. 4.3.2). This includes the whole 1064 nm signal region up to a 3σ-level (e.g. fig. 4.4).

    - A trigger level of $TL = -52$ mV is adjusted to determine the background of fiber-coupled TES with 300 K warm fiber end (sect. 4.3.3). It is observed that at lower trigger the near-infrared black-body spectrum causes a critical rate, which leads to dead time effects. Approximately, this includes the half high-energetic 1064 nm signal region.

---

[2]For example, more photon events are observed, if connections and fibers are not covered.

[3]Actually, the adjusted time window is from -5 to -20 μs. In the analysis, only data points from -5 to -15 μs are considered, which allows a valid comparison to signals (e.g. sect. 4.2). Furthermore, in one measurement, see section 4.3.2, the range until saturation of the NIST TES (sect. 3.2.2.4) is scanned. Here, the acquisition window is extended to 100 μs times 0.5 V and the digitization step is 2 mV.

4. Near-infrared signal photons and dark counts

It is noted that the scope has a non-zero trigger efficiency below the absolute value of the trigger level. Thus, there are triggered events near below the trigger level which are not exceeding the trigger level in real. These events are excluded by the offline analysis.
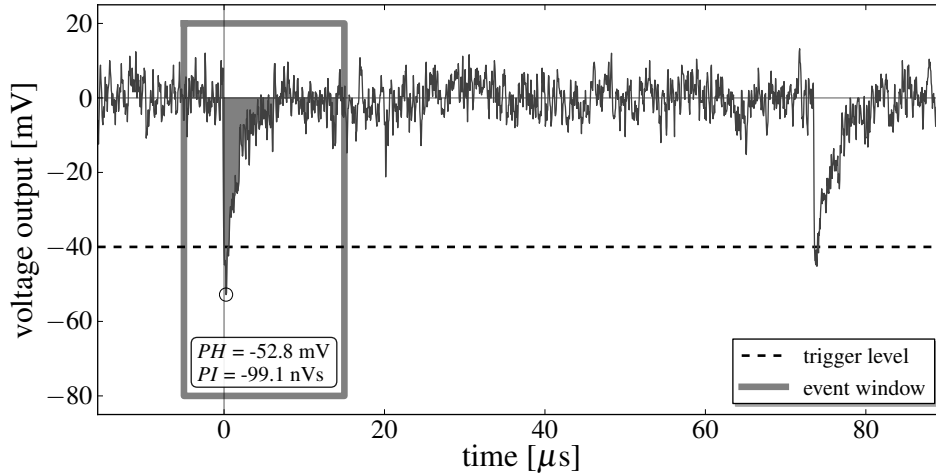
Figure 4.2.: Exemplary time series with event window: This extract of a time series illustrates the voltage output of the SQUID electronics. Exemplary, an offline trigger of -40 mV is applied. This defines an event window. From this, the pulse height (*PH* and circle) and the pulse integral (*PI* and grayish area) are determined. Here, a second event occurs at ~75 μs.

4.2. Signal photons and regions

In this chapter 1064 nm signal photons are analyzed. Analyzing the distribution of signal photons allows to define a signal region. This permits to judge about single events if they are related to signal photons. Different offline analysis are considered within this thesis which are developed in the following:

- pulse height analysis (PHA) (sect. 4.2.1),
- pulse height and integral analysis (HIA) (sect. 4.2.2), and
- pulse shape analysis (PSA) (sect. 4.2.3).

Firstly, for each analysis, the method and the corresponding representation is explained. Secondly, the signal region is defined which describes the location of signal events. Finally, the impact on measurements is evaluated and summarized.

To define a valid signal region of 1064 nm photons, one **representative signal sample** is studied in the following. This signal sample is taken to define signal regions which are compared to dark measurements in section 4.3.[4] Therefore, the TES detector is operated in the favored working point (sect 3.4) and in standard fiber configuration (fig. 4.1a). A single photon flux with a rate between 100-1000

---

[4]During data acquisition of this sample a stable run was established, which means a sufficient thermal coupling of the fiber and reliable performance of the precooling system. In addition, measuring several *IV*-curves results in a bias current deviation of less than ± 0.25 μA. This provides a valid assumption to be close at 30% of R_N (see sect. 4.2.4). The mean of this sample is illustrated by the blue cross with a 1σ-contour around in figure 4.7.

photons per second is applied (sect. 4.1.1).[5]

A time series is acquired and analyzed offline with a Python program. Setting a trigger level defines an **event window** if the output exceeds the level (fig. 4.2). To consider signals, the trigger level TL is chosen to a 3σ-level referred to the peak of the signal distribution (see next sect. 4.2.1).[6] An event window is defined from -5 μs before and +15 μs after trigger.[7] This allows to extract single events from the time series. The sample of all extracted events defines the signal sample.[8]

Furthermore, the **system noise** is estimated from this signal sample. Therefore, voltage entries from -5 to -1 μs of all event windows are assumed to present the baseline of the sample. All noise entries distribute around μ_{noise} = 0.6 mV with a standard deviation of

$$\sigma_{\mathrm{noise}} = 5.0 \pm 0.1 \text{ mV} \tag{4.3}$$

Each event is corrected by the offset μ_{noise}. σ_{noise} is used as an error estimate of a single data point, which is relevant for fitting single events (sect. 4.2.3). The baseline distribution is depicted in figure 4.10a for the discussion of noise events. The offset μ_{noise} and systematic uncertainties are discussed in more detail in section 4.2.4.

These settings and definitions result in a representative signal sample.[9] By analyzing time series from other valid runs, similar results are observed. The different analyses are summarized and strategies are developed to analyse background measurements (sect. 4.2.5), which allows to determine dark count rates of different setups (sect. 4.3).

4.2.1. Pulse height analysis (PHA)

4.2.1.1. Method

From each event window the maximum height in absolute values is extracted. Here, the pulse height PH is defined as the minimum of the window, due to negative

---

[5]By applying a proper trigger level, this rate dominates the trigger rate of the TES detector. It is shown to be suitable to analyze single signal events. Furthermore, few pile-ups are observed, since single photons arrive the TES randomly.

[6]It is $TL_{3\sigma,\mathrm{PHD}} = \mu_{PH} + 3\sigma_{PH} \simeq -43.7$ mV. This ignores low-energy events with a smaller absolute value of pulse heights.

[7]Depending on the sampling interval of $\Delta t = 50$ ns, the event window has 400 entries of voltage V_i, 100 before and 300 after trigger.

[8]The used time takes 5 seconds and results in 2275 events. Since it is assumed that this sample contains few non signal events, this results in a signal rate of approximately 450 signal photons per second (see next sections).

[9]The uniformity of the sample is proven by splitting the data set in two parts randomly. Each part shows the same distribution within statistical variations.

(a) laser off
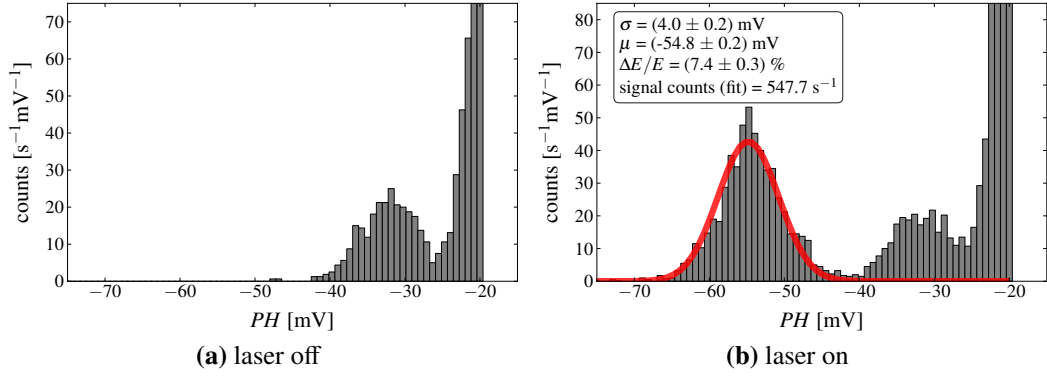
(b) laser on

Figure 4.3.: Pulse height distribution of laser off and on: (a) With laser off, events related to thermal background (peak around -35 mV) and sensor noise (around 0 mV cut by an offline TL = -20 mV) are observed. (b) With laser on, it is assumed that 1064 nm photons are normally distributed. The red line is a Gaussian χ-squared-fit to the signal distribution. It is χ^2 = 12.5. The mean, the standard deviation, and the resulting energy resolution is given in the box. The uncertainty results from the fit.

voltage response:

$$PH = \min(V_i) \tag{4.4}$$

Defining proper, equally sized voltage bins allows to illustrate events in a histogram. Each bin has a corresponding count of events. *PH* in units of voltage are plotted along the *x*-axis, corresponding counts along the *y*-axis normed by the bin width. This method is called pulse height analysis (PHA), the corresponding representation is a pulse height diagram or distribution (PHD).

4.2.1.2. Signal region

By applying PHA to the signal sample, it is assumed that signal events distribute normally (fig. 4.3b). This is caused by the noise of the TES detector system (sect. 3.2.2.4) which results in a limited energy resolution. By fitting a one-dimensional Gaussian distribution to the signal distribution, the signal region can be described by the mean μ and the standard deviation σ.

4.2.1.3. Evaluation and summary

PHA allows a quick localization and discrimination of signal pulses related to the pulse height of trigger events.[10] Choosing a $TL = -20$ mV and comparing PHDs of samples with laser on and laser off (fig. 4.3b), results in the following event classes:

---

[10]The used DAQ have a option to save trigger events in a PHD directly. This allows an online calibration of signal sources in the laboratory.

- **Signal peak:** The signal peak around -54.8 mV is caused by 1064 nm single photons of the test laser (fig. 4.3b). An energy resolution of 1064 nm signal is defined by:

$$\Delta E / E_{\text{PHD}} = |\sigma/\mu| = (6.8 \pm 0.3) \; \%$$ (4.5)

- **Noise peak:** The signal peak is significantly discriminated from the steep falling noise peak with pulse heights > -25 mV (sect. 4.3.2.1). The noise peak is caused by the system baseline (sect. 3.2.2.5).

- **Thermal peak:** Events between these two peaks are related to thermal photons. This is proven by measurements without fiber (sect. 4.3.2) and with different fiber setups (sect. 4.3.3). Thermal photons result in a peak, due to the black-body spectrum and the optical transmittance (sect. 4.3.1). The optical transmittance includes the TES absorptance (fig. 3.5 in sect. 3.2.1.1) and the fiber transmittance (app. C.4). This results in a peak, due to a reasonable infrared cut-off for wavelengths $\gtrsim 2000$ nm.

4.2.2. Pulse height and integral analysis (HIA)

4.2.2.1. Method

Basically, the pulse height and integral analysis (HIA) is an extension of a PHA which results in a two-dimensional event distribution. Therefore, a second variable is extracted from event windows. The integral of the pulse is defined as the sum of all voltage entries of an event window:

$$PI = \sum V_i \Delta t$$ (4.6)

Events are now plotted in the *PI-PH*-plane. By defining proper binning, each bin represents a count. This representation is a two-dimensional histogram, as it is shown in figure 4.4.

4.2.2.2. Signal region

By applying HIA to the representative signal sample, it is assumed that signal events normally distribute in the *PI-PH*-plane. This distribution can be described by a **two-dimensional Gaussian function**:

$$N(x,y) \sim \exp\left(-\frac{1}{2(1-\rho^2)}\left[\frac{(x-\mu_x)^2}{\sigma_x^2} + \frac{(y-\mu_y)^2}{\sigma_y^2} - \frac{2\rho(x-\mu_x)(y-\mu_y)}{\sigma_x\sigma_y}\right]\right)$$ (4.7)

$N(x,y)$ is the count of the corresponding location (x,y). μ_x and μ_y are the corresponding means, and σ_x and σ_y the corresponding standard deviations. ρ is the correlation coefficient, which is a degree of the statistical correlation of the two data
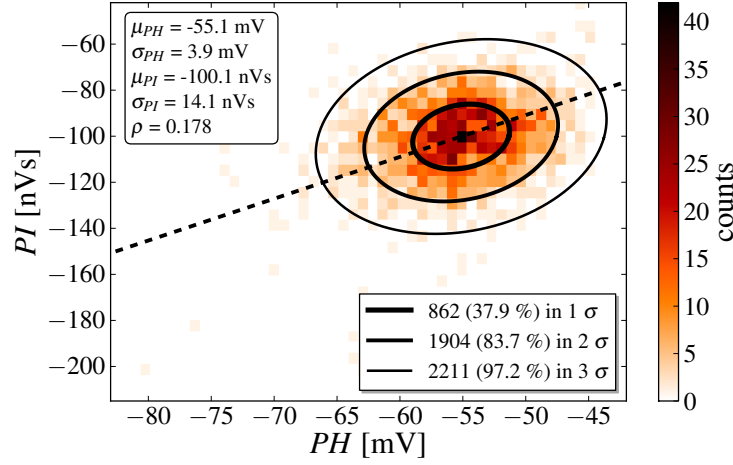
Figure 4.4.: Two-dimensional signal region according to HIA: The two-dimensional histogram illustrates the event distribution of the signal sample. The means and the standard deviations are determined by fitting a two-dimensional Gaussian distribution. The results are given in the upper left box. Therefore, n-time-σ elliptic contours are defined which correspond to signal regions of the HIA. The fractions of events lying in a contour are given in the lower right box. The dashed line illustrates the linear TES response. This line is given by the point of origin and the mean value of the signal sample and is called photon line. If the TES response is linear, the mean value of photons with different energies should be on this line.

sets. ρ is a real number between -1 and 1 corresponding to total anti correlated or total correlated data sets. $\rho = 0$ means that the data sets are uncorrelated.

A signal region can be defined by a n-σ **elliptic contour** which represents a n-fold tolerance interval. Here, n is a positive number, and in the following $n = 1, 2, 3$. The unrotated ellipse is given by a parametric form $x = \mu_x + n\,\sigma_x \cos(t)$ and $y = \mu_y + n\,\sigma_y \sin(t)$ with the parameter t running from 0 to 2π. If the data are correlated, $\rho \neq 0$, the ellipse has to be rotated and the axes have to be transformed. The rotation of the ellipse around its center is given by the angle θ, which is calculated by:[11]

$$\tan(2\theta) = \frac{2\,\rho\,\sigma_x\,\sigma_y}{\sigma_x^2 - \sigma_y^2} \tag{4.8}$$

This relation results from an orthogonal transformation.

Here, x and y are the data sets of all pulse heights *PH* and integrals *PI*. By fitting the two-dimensional Gaussian distribution to the histogram, μ_{PH} and σ_{PH}, μ_{PI} and σ_{PI}, and ρ are determined. It should be noted that the means and the standard deviations can also be determined by calculating the moments of each data set. However, fitting a Gaussian distribution is more robust due to the not perfect

---

[11]Here, the quantities are without units. For the calculation of pulse height in V and integrals in Vs the data are normalized.

signal sample. Finally, using equation 4.8, the transformed elliptic contours are determined surrounding the data points of the signal sample (fig. 4.4). The depicted contours define the **1-, 2- and 3σ signal region** resulting from HIA.

4.2.2.3. Evaluation and summary

The most important results are:

- **Signal photons:** Because of the system noise (sect. 3.2.2.5), single photon events deviate from an ideal pulse without noise (sect. 3.2.2.4). Here, 1064 nm signal photons scatter around $\mu_{PH} = -55.1$ mV and $\mu_{PI} = -100.1$ nVs. By applying HIA to single events, it is tested if triggered events are lying in the signal region and can be referred to signal photons. Events with different energies, pile-ups, or baseline shifts can be discriminated, as it is observed by background measurements (sect. 4.3).

- **Energy resolution:** The energy resolution of 1064 nm signals results in:

$$\Delta E / E_{\mathrm{HIA,PH}} = |\sigma_{PH}/\mu_{PH}| = (7.1 \pm 0.3)\ \% \quad \text{or} \tag{4.9}$$

$$\Delta E / E_{\mathrm{HIA,PI}} = |\sigma_{PI}/\mu_{PI}| = (14.1 \pm 0.6)\ \%. \tag{4.10}$$

  Compared to the PHA (eqn. 4.5), the energy resolution calculated by *PH* is in the same order of magnitude and shows no improvement. The energy resolution calculated by *PI* is even a factor of 2 higher.

  This is presumably caused by more frequency contents of the baseline noise in the 20 μs event window from which *PI* is calculated (fig. 3.11). Thus, the relative standard deviation $|\sigma_{PI}/\mu_{PI}|$ is larger than $|\sigma_{PH}/\mu_{PH}|$ since a *PH*-value is determined in a time window smaller than $\sim$0.5 μs (see fig. 4.2).

- **Correlation:** The Gaussian fit to the signal sample results in $\rho = 0.18$, which points to a correlation between *PH* and *PI*. The correlation results in a rotation of the elliptic signal region in the *PI-PH*-plane (fig. 4.4).[12]

  The correlation is explained as follows. Assuming the TES would always measure a constant energy induced by a signal photon, no correlation, $\rho = 0$, would be expected. However, since there is no total energy absorption (sect. 3.2.1.1), it is assumed that the measured energy deviates. Assuming a variation in energy and considering an ideal signal response without noise, *PH* and *PI* should be totally correlated, $\rho = 1$. Thus, a correlation in between is expected.[13]

---

[12]It is noted that the photon line (dashed black in fig. 4.4) and the major axis of the ellipse are not parallel.

[13]For the 1064 nm signal photons detected with channel A of the NIST module in its favored working point, correlations with $\rho = 0.18$-0.30 are observed. There is an indication that higher bias currents result in lower correlation, which is presumably caused by the corresponding stronger ETF (sect. 3.2.2.4), which means that more energy is measured by the ETF mechanism.

- **Purity of signal sample:** To evaluate the signal sample, the fractions of the events lying in the sigma regions (fig. 4.4) are compared to the nominal fractions of a perfect two-dimensional Gaussian distribution:[14]

  - 1σ-region: measured (37.9 ± 3.4) % to nominal 39.3 %
  - 2σ-region: measured (83.7 ± 2.3) % to nominal 86.5 %
  - 3σ-region: measured (97.2 ± 2.1) % to nominal 98.9 %

  Although the fractions nearly fit to the Gaussian assumption within in the uncertainties, slight deviations to the normal distribution are indicated. These deviations are presumably caused by few impurities of the signal sample. Pile-up events can explain a deviation from the Gaussian assumption. The sample contains such events apart from 1064 nm photons, which is confirmed by the PSA in section 4.2.3. Furthermore, the deviation could be associated with a non-perfect Gaussian noise response of the TES.

It is summarized that HIA considers two variables of an event window: the pulse height *PH* and the pulse integral *PI*. By applying HIA to signal photons, a signal region in the *PI-PH*-plane is defined. The HIA method allows a deeper insight to the distribution of signals compared to the PHA.

4.2.3. Pulse shape analysis (PSA)

4.2.3.1. Method

An expected photon pulse shape is fitted to a single event. As expected pulse, the average pulse of the signal sample is used. A proper shifting and scaling of the average pulse provides a best fit to a single event. This allows to determine if a single event can be related to a photon or not. This method is called **pulse shape analysis** (PSA).

The following **fit function** describes a shifted and scaled average pulse:

$$f(a, j) = a \cdot \text{avg}[j] \tag{4.11}$$

Here, a is the scaling factor, and $\text{avg}[j]$ is the average pulse shifted by the index j. A discrete index shift $j = 1$ corresponds to a shift in time of $\Delta t = 50$ ns due to the sampling interval of the DAQ. Shifts of the pulse are considered before and after the trigger with indexes $j = -50 \ldots 50$. With a Python program[15], a fit routine is written which fits the parameter a to the considered pulse for each index i. As figure

---

[14]Each uncertainty is calculated by $\sqrt{N}$, where N is the absolute count.

[15]Here, the fit routine `optimize.curve_fit` from the package "SciPy" is used. To shift the index the function `roll` of the "NumPy" package is used.

(a) test on average

(b) pulse shape fit to single pulse
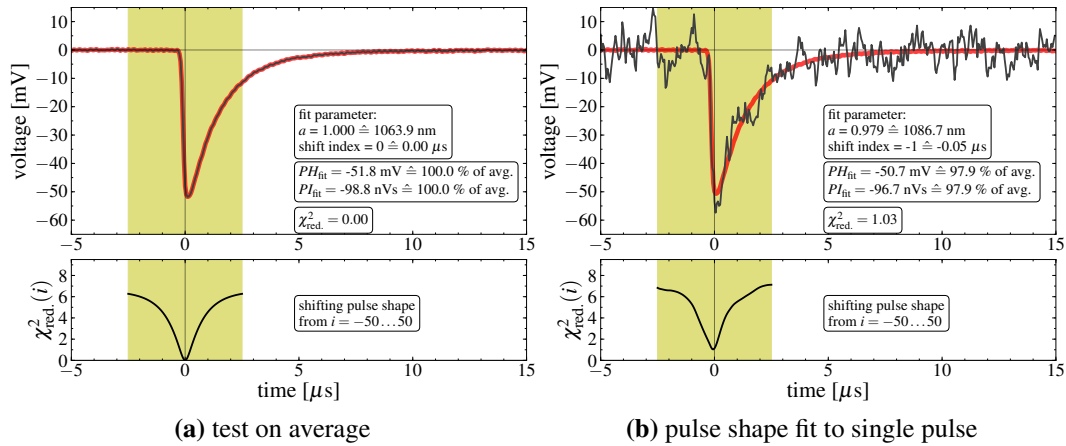
Figure 4.5.: Pulse shape analysis of single events: (a) proves the perfect fit by applying the pulse shape fit to the average pulse itself. It results in unity fit parameters $a = 1$ and $i = 0$. The yellowish area illustrates the range of shifting the index i from -50 to 50. $\chi^2_{\text{red.}}$ is calculated for each i and the smallest value gives the best fit. (b) illustrates the application to a typical single event. The lower plot in both examples illustrates the significant minimum of chi-squared for the best fit, compared to fit results of shifted shapes.

of merit, the reduced chi-squared $\chi^2_{\text{red.}}$ for each index i is calculated.[16] This provides the determination of the best single event fit which shows the minimal value of $\chi^2_{\text{red.}}$.

A test on the average pulse itself shows the expected result of a perfect fit (fig. 4.5a). By applying this fit routine to an exemplary event, a criteria of the goodness of fit is given by $\chi^2_{\text{red.}}$ (fig. 4.5b). The scaling factor a directly provides a energy calibration of a single event (see sect. 4.2.3.3). Therefore, events are plotted in the $\chi^2_{\text{red.}}$-a-**plane**.[17]

By defining proper binning, each two-dimensional bin represents a count. The representation is a two-dimensional histogram, as it is shown in figure 4.6.

4.2.3.2. Average pulse and signal region

PSA requires a **valid average pulse** of signal photons. Therefore, all events of the signal sample are averaged which are lying in the two-dimensional 3σ-region of the HIA (fig. 4.4).[18] The average pulse is depicted in figure 4.5a.

---

[16]It is $\chi^2 = \sum_j^N \left(\frac{y_i - f(x_i)}{\mathrm{d}y_i} \right)^2$, where y_i is the voltage entry and $\mathrm{d}y_i$ the uncertainty of the i-th data point of the single event. $f(x_i)$ is the voltage entry of the ith data point of the average pulse according to equation 4.11. The reduced chi-squared is calculated by $\chi^2_{\text{red.}} = \frac{\chi^2}{\nu}$, where ν is the degree of freedom. Here, it is $\nu = N - n = 400 - 1 = 399$, which includes all $N = 400$ data points of an event window and $n = 1$ due to one free fit parameter a for a fixed shift index j.

[17]It should be noted that plotting the pulse height and integral resulting from the pulse shape fit would result in a straight line in the *PI-PH*-plane. Since a scales the whole pulse shape, *PH* and *PI* change with different values of a uniformly.

[18]The resulting pulse averages 2211 single events within the 3σ-region of 2275 total events.
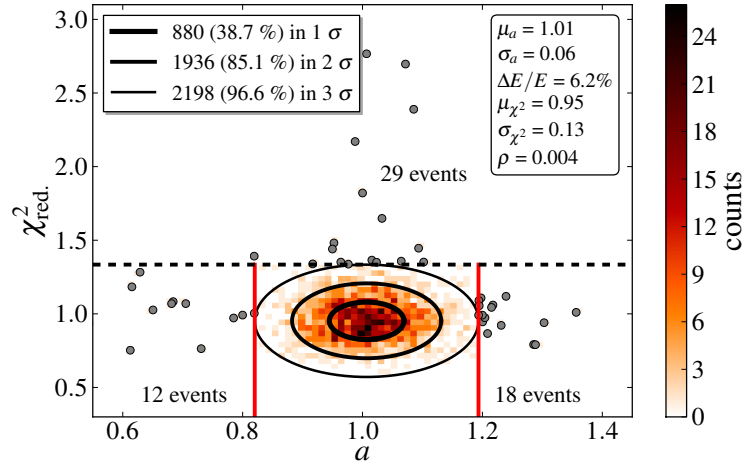
Figure 4.6.: Two-dimensional signal region according to PSA: Events of the signal sample are plotted in the $\chi^2_{\text{red.}}$-a-plane. By fitting a two-dimensional Gaussian distribution the signal region is defined. Using cuts, impurities of the signal sample are figured out: A proper cut provides a discrimination to pile-up events, $\chi^2_{\text{red.}} > \mu_{\chi^2_{\text{red.}}} + 3\sigma_{\chi^2_{\text{red.}}}$. Cuts along the a-axis discriminate photons with lower energy or higher energy.

By applying PSA[19] with the valid average pulse to the representative signal sample, it is assumed that signal events normally distribute in the $\chi^2_{\text{red.}}$-a-plane (fig. 4.6). Analogously to HIA (sect. 4.2.2.2), a two-dimensional Gaussian distribution is fitted to the signal histogram. Here, x and y are the data sets of all scaling factors a and reduced chi-squared $\chi^2_{\text{red.}}$. Elliptic contours allow to define the **1-, 2- and 3σ signal regions** resulting from PSA, as it is depicted in figure 4.6.

4.2.3.3. Evaluation and summary

The most important results are:

- **Events of signal sample:** PSA allows to discriminate between different event classes of the signal sample (fig. 4.6):

  - **Signal events** (events in the 3σ-region): 2198 of 2275 events of the signal sample lie in the 3σ-region.[20] It is assumed that these events are single signal photons from the laser source. This is validated by analyzing a sample with laser off. Analogously to HIA (sect. 4.2.2), signal photons are normally distributed; here, around $a = 1.0$ and $\chi^2_{\text{red.}} = 0.95$. The correlation coefficient is $\rho < 0.01$. Thus, a correlation between a

---

[19]To determine $\chi^2_{\text{red.}}$ the standard deviation of the system noise (eqn. 4.3) is used as the uncertainty of each data point. Since similar values are observed for other signal samples, this value stays fixed for the PSA.

[20]Compared to 2211 events lying in the 3σ-region of HIA (fig. 4.4), this value is slightly smaller which is presumably caused by a better discrimination through PSA.

	a	E [eV]	λ [nm]
μ	1.01	1.165	1064
σ	0.06	0.072	–
1σ-region	0.95-1.07	1.093-1.237	1002-1134
2σ-region	0.88-1.14	1.021-1.309	947-1214
3σ-region	0.82-1.20	0.948-1.382	897-1308

Table 4.1.: Energy calibration of the fit parameter a: The calibration results from 1064 nm single photons. The standard deviation σ and the corresponding regions result from the PSA of the representative signal sample. Since the wavelength depends on the energy reciprocally, the corresponding borders of the σ-regions are calculated by formula 4.2.

and $\chi^2_{\text{red.}}$ is excluded. This is an indication for the linearity of the TES response around energies of 1064 nm photons.

– **Low-energetic photon-like events** ($\chi^2_{\text{red.}} < \mu_{\chi^2_{\text{red.}}} + 3\sigma_{\chi^2_{\text{red.}}}$ and $a < \mu_a - 3\sigma_a$): Few events of the signal sample are presumably related to low-energetic photons between ~1300-1950 nm. If these events are dedicated to single photons, they presumably originate from thermal background due to the fiber (sect. 4.3.3) or from the 4σ-region of the signal sample. Furthermore, it is possible that these events are related to pile-up events, when two low-energetic photons are detected in a small enough a time window (see below).

– **High-energetic photon-like events** $\chi^2_{\text{red.}} < \mu_{\chi^2_{\text{red.}}} + 3\sigma_{\chi^2_{\text{red.}}}$ and $a > \mu_a + 3\sigma_a$: Few events of the signal sample are presumably related to high-energetic photons between ~600-900 nm. If these events are dedicated to single photons, they presumably originate from stray light of the laboratory environment (sect. 4.3.3) or from the 4σ-events of the sample.

– **Pile-ups or background** ($\chi^2_{\text{red.}} > \mu_{\chi^2_{\text{red.}}} + 3\sigma_{\chi^2_{\text{red.}}}$): Few events within the signal sample are determined as a first-order pile-up event. A first order photon-like pile-up event is defined as two photon-like events that are detected within the same time window. It is shown that such events are well discriminated by PSA if the two constituents occur within a time window $\gtrsim 0.5\,\mu$s. If they occur within $\lesssim 0.5\,\mu$s, PSA cannot distinguish the pile-up event from a single photon-like event. This is important for the analysis of thermal background in section 4.3.3.3. Also background events result in a high $\chi^2_{\text{red.}}$ (sect. 4.3).

This analysis confirms the impurity of the signal sample (sect. 4.2.2.3). Furthermore, it suggests, following definition: events with $\chi^2_{\text{red.}} < \mu_{\chi^2_{\text{red.}}} + 3\sigma_{\chi^2_{\text{red.}}}$

are defined as photon-like events.

- **Energy resolution:** The energy resolution results in:

$$\Delta E/E_{\text{PSA}, a} = |\sigma_{\text{a}}/\mu_{\text{a}}| \approx 6.2\ \% \tag{4.12}$$

Compared to HIA (sect. 4.2.2), PSA shows a slight improvement.

- **Calibration:** The scaling factor a provides a calibration. Here, $a = 1$ is calibrated to the nominal energy of 1064 nm photons of the used laser source. Thus, the fit parameter a determines the energy of a well fitted single event. Energies and corresponding wavelengths for 1,2,3-σ-regions are listed in table 4.1.

It is summarized that the PSA provides a fit routine which is independent of the TES response resulting from the small-signal theory (eqn. 3.25). It includes the deconvolution of the TES detector output due to the system response and bandwidth (fig. 3.10) which avoids an additional process in a fit analysis. It is assumed that the TES response is linear around energies corresponding to 1064 nm photons. If the TES response is linear, a scaling of the expected pulse is valid. The linearity is indicated by background measurements (sect. 4.3.2) and confirmed by measurements with several photon energies within the ALPS collaboration (Bastidon and Januschek, 2014). Furthermore, $\chi^2_{\text{red.}}$ allows a discrimination between different event classes. PSA provides a definition for photon-like events. Finally, the energy is calibrated and described by the scaling parameter a.

4.2.4. Systematic uncertainties

Although the NIST module is always set to the favored working point for valid measurements (sect. 3.4), it is observed that different effects can change the pulse response (sect. 3.2.2.4). If the photon signal pulse changes, the location of the signal regions defined by analysis methods in the previous chapters also change. Therefore, systematic uncertainties of the ALPS TES detector are discussed in the following.

Figure 4.7 shows the observed deviations of 1064 nm signal regions analyzed by HIA (sect. 4.2.2.2). The crosses represent mean values of pulse height and integral, μ_{PH} and μ_{PI}, of different runs. Here, three representative measurements are shown which differ in the thermal anchoring setup of the fibers (sect. 3.3.3). The solid blue elliptic contour represents the 1σ-signal region which corresponds to the statistical deviation of the analyzed representative signal sample (sect. 4.2.2) which is defined as best guess in the next section 4.2.5. Although variations of mean values, which result from a favored working point setup with well coupled fibers, are within this statistical deviation, significant trends of systematic uncertainties are observed. In the following, three effects are discussed:
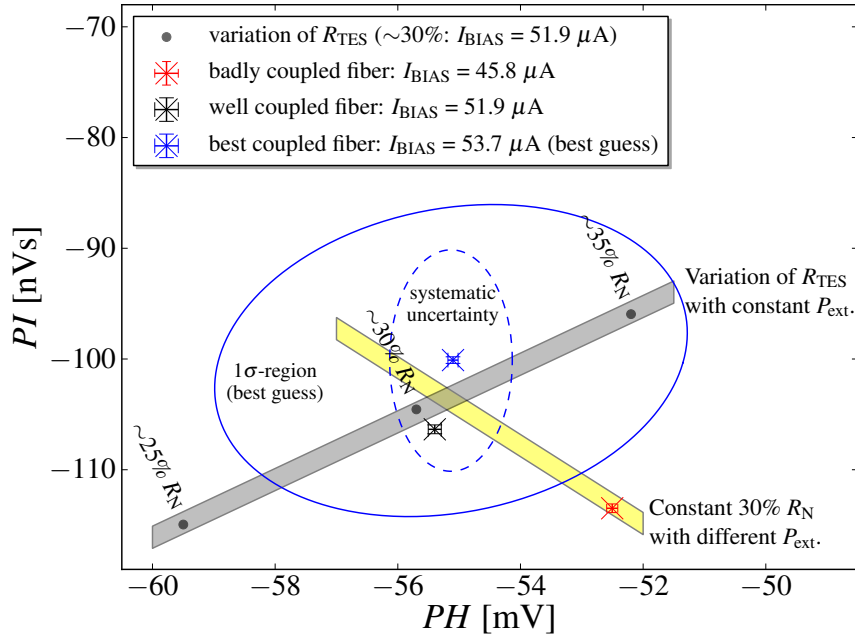
Figure 4.7.: Signal region and systematic uncertainties: In the *PH-PI*-plane, the crosses represent mean values from different measurements. The blue sample is the best guess with the 1σ-region (solid ellipse), which is presented in section 4.2.2.2. In addition, an estimate for the systematic uncertainty (dashed ellipse) is given (see text). The grayish trend illustrates the change of the resistance R_{TES}, the yellowish trend illustrates the change of the bias current I_{BIAS} for reaching the favored working point. Details are found in the text.

- **Variation of the bias current I_{BIAS} between different setups:** Due to the external power load P_0, the bias current is adjusted to reach $R_{TES} = 30\% \, R_N$ as working point (sect. 3.3.3). P_0 variations are mainly caused by the thermal coupling of the fiber (sect. 3.3.3). As shown in figure 4.7, the measurement with $I_{BIAS} = 45.8 \, \mu A$ (red cross) has a lower absolute value of pulse height but a higher absolute value of pulse integral, compared to the representative signal sample (blue cross). The yellowish area illustrates this trend in variations of I_{BIAS} for the same $R_{TES} = 30\% \, R_N$. The trend is explained in section 3.2.2.4.

  For valid signal and background measurements with a sufficient coupled fiber or without fiber, the adjusted bias currents of channel A of the NIST module vary from 51.8 to 54.5 μA. Therefore, absolute variations of < 0.75 mV for *PH* and < 7.5 nVs for *PI* are estimated to be caused by this effect.

- **Deviation between the adjusted and the real TES resistance R_{TES}:** This can be caused by three effects:

  - The method of the *IV*-curve includes an uncertainty. The TES resistance is defined by the adjusted bias current which is determined by an *IV*-

130

curve measurement (app. D.3.2.2). The determination of the *IV*-curve deviates approximately ±0.3 μA due to the accuracy of the method.[21]

– The current binning of the SQUID electronics provides an uncertainty. The adjusted bias current can deviate from about maximal ±0.5 μA related to the determined value.[22]

– A long-term thermalization effect causes an uncertainty (sect. 3.3.3). It is observed that the bias current corresponding to 30% of R_N before a long-term measurement is ~1.0 μA smaller than the value which is determined by an *IV*-curve after the measurement. This results in a deviation of R_{TES} about 1% of R_N.

All these effects cause an uncertainty on the TES resistance R_{TES}. According to theory (sect. 3.1.2), the lower the resistance the higher the absolute values of *PH* and *PI*. This trend is confirmed by a measurement (black dots) and is illustrated by the grayish area in figure 4.7. However, the effect on *PH* and *PI* is smaller than the deviation due to external power loads (see above).

• **Non-zero baseline:** Although the SQUID electronics is set to AC-coupling, the mean of the baseline deviates between -0.5 to +0.5 mV for different measurements. It is observed that the deviation is low-frequent. This is presumably caused by the whole DAQ setup and the interplay between different components. In figure 4.7, each data point of measurement is corrected by the shift of the corresponding data sample. Since the baseline is not observed during long-term measurements (sect. 4.1.3), an uncertainty is assumed for single events: ±0.5 mV for *PH* and ±10 nVs for *PI*.

Summarizing all these effects, a systematic uncertainty for the pulse height and integral is conservatively estimated by the largest deviation:

$$\sigma_{PH_{sys.}} = \pm 1.0 \text{ mV}$$
$$\sigma_{PI_{sys.}} = \pm 10.0 \text{ nVs}$$

These systematic deviations can be integrated in the PHA or HIA method (sect. 4.2.5). For the PSA method, the whole average pulse would be needed to describe a deviation. It is observed that systematical variations of the average pulse due to different bias currents between 51.8 to 54.5 μA are negligible compared to the statistical variations for a single event. Therefore, the PSA is used as best guess analysis with the representative signal sample in the following (sect. 4.2.5).

---

[21]This includes an uncertainty, due to the reading of the data points, due to the linear interpolation between the single points, and due to an uncertainty of fitting a linear slope to the normal resistance R_N.

[22]This absolute maximal value of 0.5 μA only occurs in the option of "high current range" of the SQUID electronics. In the option "low current range" it is < 0.1 μA.

4.2.5. Summary and analysis strategies

In sections 4.2.1-4.2.3 three analysis methods are developed. Each analysis is applied to a representative signal sample of the ALPS TES detector in the favored working point (sect. 3.4). By this, signal regions of 1064 nm photons are defined. The different methods bring along different advantages and insights to measurements. The TES detector has systematic uncertainties which can affect signal regions (sect. 4.2.4).

In the next section 4.3, dark count rates of different optical setups are determined. During long-term background measurements with fiber inside the ADR or even without fiber, no calibration signal can be brought to the TES. Therefore, to determine dark count rates, different analysis strategies are applied. The following analysis strategies are applied to long-term background measurements:

- **HIA best guess:** Events are compared to the signal region in the *PH-PI*-plane defined by HIA (sect. 4.2.2.2). HIA gives a quick discrimination between event candidates lying in the signal region and background events lying outside the region.

- **HIA conservative guess:** Events are compared to the signal region resulting from HIA best guess extended by systematic uncertainties (sect. 4.2.4). The region of the systematic uncertainty alone is illustrated by the dashed blue line in figure 4.7. HIA with a systematic uncertainty is an upper limit for dark count rates.

- **PSA (best guess):** Events are compared to the signal region in the a-$\chi^2_{\text{red.}}$-plane defined by PSA (sect. 4.2.3.2). PSA allows to distinguish photon-shaped events from other events. At the same time, the scaling factor a corresponds to the photon energy.

This allows to determine dark count rates depending on the analysis. Furthermore, it allows to compare the methods. The PHA method is only used to check the location of signal photons (sect. 4.2.1). In addition, two signal regions are considered and the corresponding results are compared in the following:

- **3σ-region:** The 3σ-region includes 98.9 % of signal events. This results in an elliptic contour within *PH-PI*-plane for HIA or within the a-$\chi^2_{\text{red.}}$-plane for PSA.

- **(High-energetic) half** 3σ-region: Only the high-energetic half is considered which includes 49.5 % of signal events. This provides an indication about the dark count distribution. For HIA, due to the linear TES response, events with different energies lie along the photon line in the *PH-PI*-plane (fig. 4.4). For the high-energetic half, the energy cut is perpendicular to this line and goes through the mean of the signal. For PSA, a cut on energy means just a cut on the scaling factor a. For the high-energetic half, the energy cut is $a > \mu_a$.

Finally, the adjusted trigger level can provide a cut through the signal region.

Such a cut is necessary for long-term background measurements with attached fiber to the 300 K environment (sect. 4.3.3). Here, the adjusted trigger level is set to $TL = -52$ mV which goes through the 3σ-region.[23] Otherwise the trigger rate is too high and causes dead time issues due to the thermal photons. This additional cut changes the nominal signal content. With the distribution of the representative signal sample (sect. 4.2.2 and 4.2.3), each content of the corresponding reduced signal region is calculated. Thus, with $TL = -52$ mV, the defined signal regions are diminished by the following fractions:

- HIA signal region:
    - The 3σ-region contains 79.3 % of nominal signal events.
    - The half 3σ-region contains 82.4 % of nominal signal events.

- PSA signal region:
    - The 3σ-region contains 79.7 % of nominal signal events.
    - The half 3σ-region contains 78.1 % of nominal signal events.

Deviations are presumably caused by statistical uncertainties and the difference of the analysis methods since TL only set a cut on PH. Therefore, it is assumed that the considered signal regions contain approximately 80 % of the signal if applying a cut with $TL = -52$ mV. This is used in section 4.4.

---

[23]Because of the non-zero trigger efficiency of the DAQ near below the adjusted TL, an corresponding offline TL is additionally applied. Therefore, only events with $PH < -52$ mV are considered.

4.3. Noise, background and dark counts for 1064 nm

In this chapter, different dark count rates for 1064 nm photons are determined, measured with the ALPS TES detector (sect. 3.4). Firstly, a brief overview of the current state of research is presented which concentrates on considerations about fiber-coupled TES to detect near-infrared single photons (sect. 4.3.1). Secondly, an examination follows about the intrinsic dark count rate of 1064 nm photons for non-fiber-coupled and dark TES operated in the ADR (sect. 4.3.2). This will provide an understanding of what intrinsic noise and background components are. It follows the study of dark count rates of 1064 nm photons for fiber-coupled TES. This is crucial for using the TES detector for applications like the ALPS experiment (sect. 4.3.3).

4.3.1. Current state of research

Since the field of near-infrared TES detectors is relatively new and small, so far only few groups investigated dark count rates. In this chapter, results of publications are briefly summarized, which are mainly referenced to two American university groups[24], the NIST group and the AIST group. All are concentrating on the telecommunication wavelength of 1550 nm. A dark count rate for 1064 nm is not explicitly determined, as far as the author of this thesis knows.

In one of the first publications on optical tungsten TES, the authors have emphasized the difference to other detectors: A TES has no equivalent to a dark current as with a CCD (Cabrera et al., 1998). Therefore, dark counts are given by possible backgrounds. They report about "infrared photons from the room temperature end of the fiber" which qualitatively results in a peak due to the infrared cutoff of the fiber.

In his thesis, Miller (2001) considers a fiber-coupled TES which is looking at a black body. A 300 K black body radiates 459.3 W/m^2, which is calculated with the Stefan-Boltzmann law (app. A.3). By taking into account the properties of the optical fiber[25] and the absorptivity of the TES device[26], Miller (2001) estimates a remaining photon power of 3.5 fW: this corresponds to a black body photon rate of 700 s^{-1}. The measured rate about 200-400 s^{-1} could be explained by losses due to the optical setup. The light is spread over the sensitive sensor area due to the used technique of fiber-to-TES coupling.

Rosenberg et al. (2005) end up with a similar number. They investigate the system efficiency of a fiber-coupled TES device with a 1550 nm laser. The improved design of the tungsten TES (sect. 3.2.1.1) mainly provides an overall efficiency of

---

[24]Cabrera's group from Stanford university and Miller's group from Albion college.

[25]Here, the multi-mode fiber has a core diameter of 200 μm, a N.A. of 0.22 (12°), and a transmittance for 0.5-4 eV photons.

[26]Here, the absorption is 50 % for the tungsten TES.
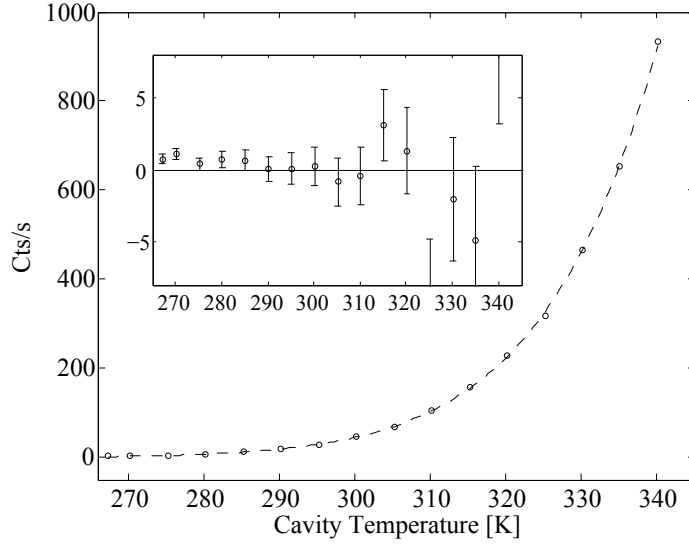
Figure 4.8: Thermal photon rates of different temperatures: The counts received from a temperature controlled cavity (circles) fit to the integrated dark count rate of a one-dimensional black body model (eqn. 4.13). The inner figure shows the fitting errors marking the expected 2σ statistical errors. [Taken from Miller et al. (2007)]

about 88 %. They observe a background rate of approximately 400 s^{-1} "due to black body radiation from room-temperature surfaces".

In a proceeding note, Miller et al. (2007) emphasize that the thermal background is the limiting factor of detecting low-rate photons with fiber-coupled TES:

> "In operating our devices we noticed that whenever the devices were coupled to a fiber the 'dark count' rate was several orders of magnitude higher than the theoretical expectations. Even when completely blackening the input end of the fiber at room temperature the devices count hundreds to thousands of photons per second. These photons were confirmed to be coming from the high-energy tail of the black-body distribution for the 300 K environment of the fiber end." (Miller et al., 2007, p. 3)

For a theoretical description, Miller et al. (2007) consider a black-body cavity at the fiber end which couples to the fiber only in one dimension. The wavelength dependent rate is given by (app. A.1):

$$\tilde{L}_{\lambda,1d}(\lambda, T) = \frac{2c}{\lambda^2} \frac{1}{e^{hc/kT\lambda} - 1}$$

By considering near-infrared and optical photons, the following approximation is valid: $E_\gamma = \hbar\omega = hc/\lambda \gg kT$. Thus, it is $e^{E_\gamma/kT} - 1 \approx e^{E_\gamma/kT}$ and the integration reduces to (Miller et al., 2007):

$$\bar{R}(T) = \int_{\lambda_0}^{\lambda_1} \eta \, \tilde{L}_{\lambda,1d} \, d\lambda \approx \frac{2\eta kT}{h} e^{-hc/\lambda kT} \Big|_{\lambda_0}^{\lambda_1} \tag{4.13}$$

where η is an energy independent free parameter including the non-unity emissivity of the one dimensional cavity and the non-unity detection efficiency of the detector.
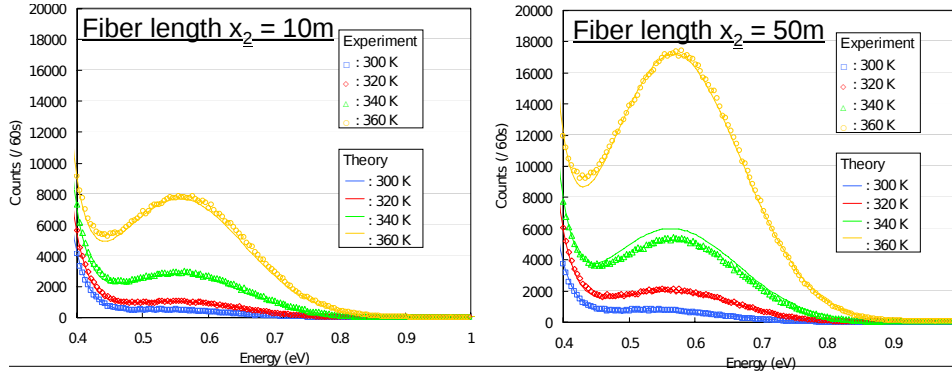
Figure 4.9.: Thermal photon rates of different temperatures and different fiber length: Fujii et al. (2011) measure the count rate of different fiber length, in different temperatures. With a model including Planck's law and the fiber transmittance, they fit the measurements (eqn. 4.14). This explains the peak shape: For lower photon energies, the transmittance of the fiber decreases (e.g. fig. C.4). [Taken from Fujii et al. (2011)]

By a variation of the cavity temperature between 0° and 70° C, Miller et al. (2007) have found $\eta = 0.15$ to fit their measurements (fig. 4.8). Therefore, the integration borders are 0 to 1966 nm, which corresponds to the absorption edge of the fiber here. This provides a total integrated count rate. For example, for a 300 K cavity they measure $\bar{R} \approx 50$ counts/s. Miller et al. (2007) end with a fundamental dark count limit of 0.01 s^{-1} via formula 4.13, by considering a 1 nm band around 1550 nm for an ideal 300 K cavity with a perfect detector ($\eta = 1$).

The recent study about dark counts of fiber-coupled TES is from AIST group Fujii et al. (2011). They measure photons coming from an optical fiber to the TES. The fiber type is a SMF28, the standard single mode fiber for telecommunication wavelengths, which is also used in the ALPS TES detector setup in this work (sect. 4.1.1). They vary the fiber length and the temperature of the fiber in a dark environment. In addition, the outer fiber end is put in liquid nitrogen, in order to diminish black-body photons from the fiber end. This setup provides a test of how many black body photons couple from outside to the fiber core, which depends on the fiber length. The number should for example include photons which come from outside the whole fiber or are emitted in the fiber cladding. The results and the dependency on fiber length and bath temperature are depicted in figure 4.9.

Fujii et al. (2011) fit their measurements with the following formula[27] for the spectral distribution f of photons:

$$f(E, T, x) \sim \int_0^\infty \frac{DE(\epsilon)R(\epsilon, T, x)}{\sqrt{2\pi}\sigma} e^{-\frac{1}{2}\left(\frac{E-\epsilon}{\sigma}\right)^2} d\epsilon \qquad (4.14)$$

The variables are energy E, temperature T and fiber length x. The rate R is folded

---

[27]This formula is adopted from the poster and the typing error is corrected.

with distribution due to the energy resolution σ of the TES and with the energy-dependent detector efficiency *DE*. The rate *R* is a combination of the fiber transmittance (fig. C.4) and the spectral distribution of the black body (app. A.4). Furthermore, *R* contains the fit parameter which includes the coupling efficiency of photons to the fiber core.

The resulting fit parameter is not given on the poster. Since the plot is non-logarithmic and ends at an energy of 1 eV, an extrapolation of a rate for 1064 nm photons is difficult. According to a private communication, the fit results in a differential rate at 1 eV of 10^{-4} $s^{-1}eV^{-1}$ for a 10 m long fiber at 300 K (Fukuda, 2012). However, it should be noted that the factor between a 10 m and a 50 m long fiber is approximately 2 by comparing the peaks of both measurements (fig. 4.9).

It is summarized that thermal photons as a background for fiber-coupled TES are confirmed by different groups and measurements. A detailed examination of intrinsic dark counts with a dark, non-fiber-coupled TES, has not been performed so far. Furthermore, a closer look at the dark count rate for 1064 nm signals for fiber-coupled TES has not been performed. The next chapters covers this with measurements using the ALPS TES detector.

4.3.2. Intrinsic noise and backgrounds

This chapter provides a closer look at the intrinsic noise and background of the NIST module. Intrinsic means that the TES is operated in the dark: There is no optical link via a fiber which connects the TES to a source outside the ADR or to the warm environment (fig. 4.1c). Basically, sources of noise or background can cause a trigger, which results in a dark count for 1064 nm photon signals. In the following, four **event classes** are distinguished:

- **Noise events** are trigger events which are caused by the whole electronic system or by EMI to the system (sect. 4.3.2.1).

- **Non-(single) photon events** are trigger events which differ from photon-like events. Analyzed by HIA, such events are not lying along the photon line in the *PI-PH*-plane (fig. 4.4). Analyzed by PSA, such events do not fit to the single photon average pulse ($\chi^2_{\mathrm{red.}} > \mu_{\chi^2_{\mathrm{red.}}} + 3\sigma_{\chi^2_{\mathrm{red.}}}$). Thus, pile-ups consisting of two or more single photon-like events are also referred to this class by PSA.

- **(Single) photon-like events** are trigger events which correspond to a single photon response. Analyzed by HIA, such events lie along the photon line (fig. 4.4). Analyzed by PSA, such events fit to single photon average pulse ($\chi^2_{\mathrm{red.}} < \mu_{\chi^2_{\mathrm{red.}}} + 3\sigma_{\chi^2_{\mathrm{red.}}}$).

- **Dark count events** are trigger events which lie in the 1064 nm signal region of the corresponding analysis.

4.3.2.1. Noise events

Two sources are considered in the following:

- Internal sources: A first potential source are peaks due to the electronic system noise which shortly reach a high amplitude out of the baseline. Such an event is called noise glitch in the following. The probability for a noise glitch reaching the signal region is discussed below.

- External sources: A second potential source are electro-magnetic interferences (EMI). It is observed, for example, that switching the light on or off in laboratory causes a trigger event. In addition, it is observed that EMIs can shift the whole baseline. Therefore, results of long-term measurements are discussed.

The sensor module as an electronic device has a specific noise spectral density (sect. 3.2.2.5) which define deviations of the baseline. The baseline noise distributes in a Gaussian manner around the nominal zero line. From this distribution, the probability can be derived for a noise peak which reaches the 1064 nm signal region. In figure 4.10a, the time series of the signal sample is depicted representing the system baseline distribution for the fiber-coupled NIST module in its working point.[28] The noise component around zero fits to a normal distribution. By extrapolating, a rate for noise events reaching the trigger level is estimated: **Noise glitches** with a pulse height of $PH \leq -40$ mV occur with a count rate of $\lesssim 10^{-8}$ s^{-1} (cf. caption of fig. 4.10a). Therefore, a noise trigger is statistically expected every 3 years. This results in a negligible contribution of dark counts for 1064 nm photon signals.

Events caused by EMI are tested by operating only the SQUID, since the SQUID is sensitive to external electro-magnetic influences (sect. 3.3). In two long-term measurements, the SQUID was set in the working point and during the TES circuit was decoupled from the SQUID input by operating the TES in normal resistive condition.[29] The measurements are analyzed by HIA and events are depicted in the *PH-PI*-plane in figure 4.10b. During the ~38 h long measurements three single trigger events and, in one case, one excess of noise were observed. The single events are presumably due to short-time baseline deviations. The noise excess is located around the trigger level at PI = -600 to -300 nVs (fig. 4.10b). These ~100 trigger events occurred within 20 seconds on Monday morning around 7:00 am. During this noise excess, the mean baseline level was shifted to -25 mV, which provided noise glitches reaching the trigger level. This short-time baseline shift could be caused, for example, by a starting machine adjacent to the laboratory. However,

---

[28]This distribution contains all data points of the 5 seconds time series, which are given by the sampling interval $\Delta t = 50$ ns.

[29]Two base temperatures were tested. During the first measurement it was $T_{bath} = 2.8$ K. Here, the TES was naturally normal resistive. During the second measurement it was $T_{bath} = 80$ mK. Here, the TES was set normal resistive by applying $I_{BIAS} = 400$ μA. Both measurement took place over night, one measurement was nearly 24 h long covering a whole day.

(a) estimated noise glitches

(b) measured noise events (analyzed by HIA)
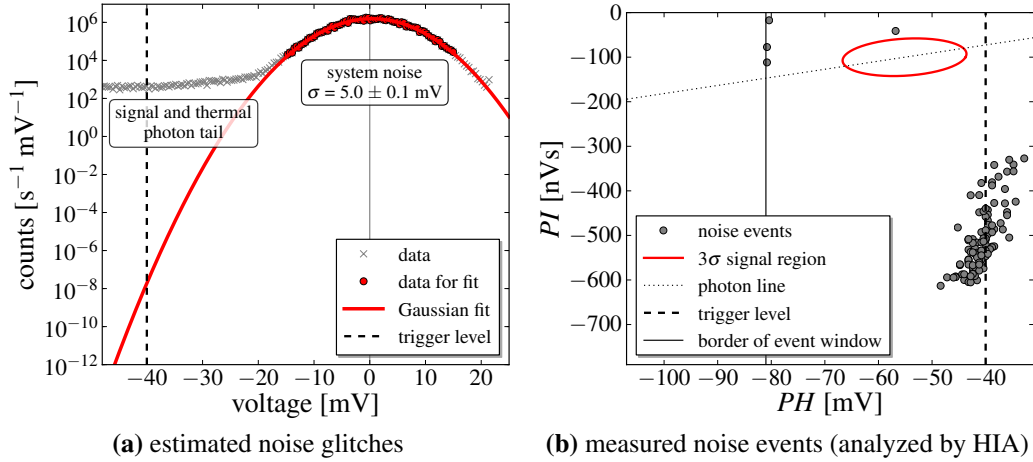
Figure 4.10.: Estimated and measured noise events: (a) illustrates the probability for a noise glitch of the baseline which could reach the trigger level. The noise of the sensor module is normal distributed around zero which represents the baseline. By extrapolating the normal distribution, a noise glitch reaches the trigger level with an integrated rate of $(9.0 \pm 6.0) \cdot 10^{-9}$ s^{-1}, where the eroor is estimated from the noise deviation σ. Counts below -20 mV are related to signal and thermal photon peaks (sect. 4.3.3). (b) shows noise events from two long-term measurements. Here, events can only couple to the SQUID or the electronics, because the TES was operated in normal resistive condition. No event within a total measurement time of 38 h lies in the 3σ signal region of HIA (red ellipse). The dotted line illustrates the photon line.

no events are in the 3σ signal region. This is confirmed by PSA.

It is concluded that noise events are uncritical: Single noise glitches or baseline shifts are discriminated by the analysis. Therefore, this is no contribution to the dark count rate. Only the measurement time is diminished because noise events are dead time periods for signal counts. The presented measurement above results in a small dead time contribution of <0.02 %.[30]

4.3.2.2. Non-photon events

In one measurement,[31] the full sensitive window of the TES module was tested. Therefore, the digitization step and the size of the event window of the DAQ was adjusted. In this measurement, 497 trigger events occurred (fig. 4.11). This corresponds to a trigger rate of $1.2 \cdot 10^{-2}$ s^{-1}.

---

[30]The dead time contribution is defined as the quotient of total event time and measurement time. This is equal to the product of the triggered event rate times the time of the event window, neglecting potential saving time of the DAQ.

[31]The measurement took 11.5 h. The event window was $100\,\mu$s long and 500 mV high. Furthermore, both channels A&B were in its corresponding working point at 30 % R_N. The trigger level was set to -40 mV for channel A.
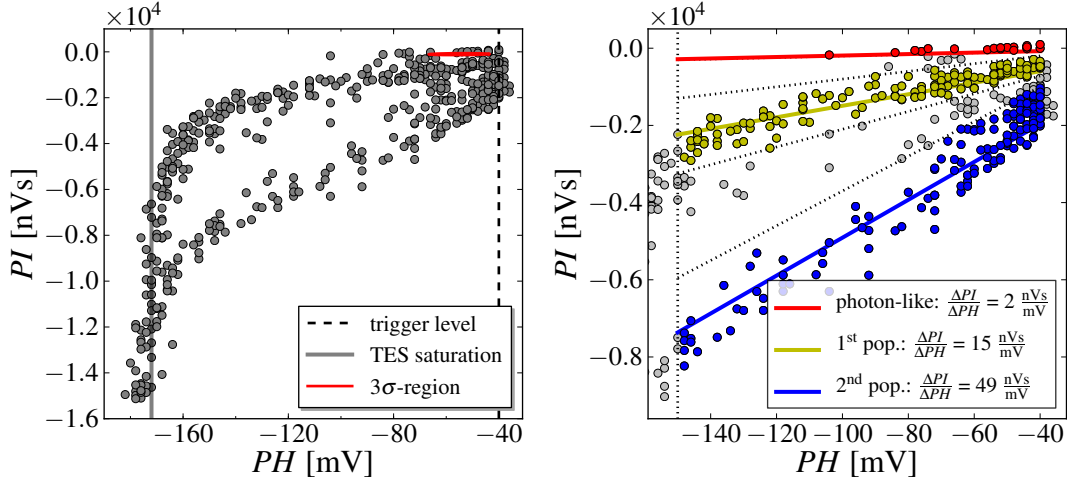
Figure 4.11.: Distribution of two populations of non-photon events: The measurement is analyzed by HIA. On the left, the whole *PH-PI*-plane is depicted. Due to the ETF range of the TES, around -170 mV the TES is saturated. Two non-photon populations are distinguished which are lying along different slopes. The photon region, with the 1064 nm signal region around $PH \sim 55$ mV and $PI \sim 100$ nVs, is at the upper border of each figure. On the right, a zoom is shown. The population are distinguished by box cuts (dotted lines). Lines with different gradients describe the populations within the linear range. For the pulse analysis, events around these linear trends are considered: 20 photon-like events are counted (red line and dots), 139 events are associated with the 1st population (yellow line and dots), and 143 events with 2nd population (blue line and dots).

Analyzed by HIA, **two background populations** are distinguished which differ significantly from photon-like events along the photon line (sect. 4.2.2.2).[32] Both populations show a linear trend above the trigger level, before they saturate around $PH \approx -170$ mV (fig. 4.11). This is caused by the TES saturation (sect. 3.2.2.4); and corresponds to a TES current $I_{\text{TES}} \sim 220\,\mu$A calculated by equation 4.1 which fits to the estimate from the *IV*-curve analysis (fig. 3.9 or sect. 3.2.2.4). Assuming that these single events are distributed due to different energy inputs to the TES, the saturation in the *PH-PI*-plane can be explained: During the pulse height *PH* reaches a limit, the pulse integral *PI* can still rise due to a high-energetic event. The relation between *PH* and *PI* is not linear anymore at this saturation limit. This is also illustrated by single events of one population in figure 4.12b.

In the following, only events within the linear range are considered. Linear cuts by eye provide a **separation of the populations**, which is illustrated by the dotted lines in figure 4.11.[33] By fitting a line through the point of origin, a gradient for each population in the *PH-PI*-plane is determined. 20 photon-like events are

---

[32] Analyzed by PSA, the two populations are similarly distinguished in the $\chi^2_{\text{red.}}$-a-plane.

[33] It is estimated that the linear range is up to > 150 mV. The cuts which border the populations are lines through the point of origin.

(a) average pulses of different event classes

(b) 1st population singles
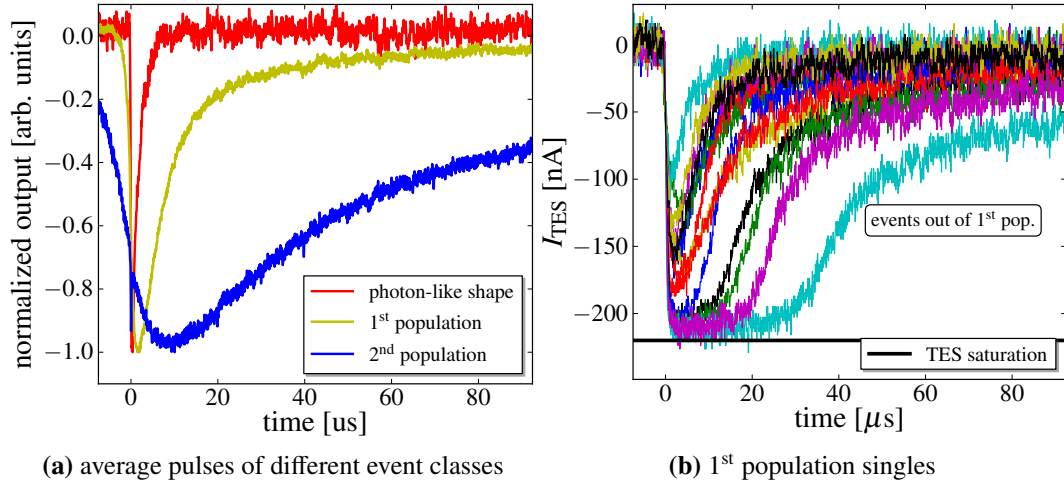
Figure 4.12.: Average and exemplary single pulses of non-photon events: (a) shows the average pulses of different event classes. Each average pulse results from each sample of single events which are lying in the linear range of each population (fig. 4.11). The red shape illustrates the average of photon-like events, the yellow shape the average of 1st population events, and the blue shape the average of 2nd population events. (b) shows a sample of single events of the 1st population. This illustrates events of different energies and the TES saturation. The output is related to the TES current: The maximal current change in the TES circuit is approximately 220 μA, which fits to *IV*-curve analysis (fig. 3.9).

determined, which are located along a line with a gradient of ~2 $\frac{nVs}{mV}$. Within the statistical uncertainty, this fits to the photon line with a gradient of $1.8\frac{nVs}{mV}$, which is determined with HIA for the representative signal sample (sect. 4.2.2.2). The first (1st) non-photon population has a gradient of ~15 $\frac{nVs}{mV}$, the second (2nd) of ~49 $\frac{nVs}{mV}$.

The different populations are caused by **different pulse shapes**. By normalizing and averaging the events of each population lying in the linear range, the pulse shapes are significantly different (fig. 4.12a). Compared to the photon-like pulse, 1st population events are broader due to larger time constants. 2nd population events are even more broader. This explains the different values of *PI*s referred to an equal *PH*. In table 4.2, a quantitative estimate for the time constants is given. Here, the rising time constant $\tau_{rise_{10,\,90}}$ is defined as the time from 10 % to 90 % of peak height, and vice versa for the falling time constant $\tau_{fall_{10,\,90}}$.[34]

In addition, possible **coincidence events** of channel A and channel B of the NIST module were tested. Coincident events are defined as events which show an indication of an event for channel B at a trigger of channel A. The offline event level is set to *PH* < −30 *mV* for channel B. Within this sample of 497 trigger events of channel A, seven coincident events were observed in channel B. A quick analysis by eye results in four event combinations:

---

[34] This time constant is connected by a factor 2.2 to an exponential time constant τ if the trend is exponential: $\tau_{10,\,90} = 2.2\tau$.

	$\tau_{\mathrm{fall}_{10,\ 90}}$ [μs]	$\tau_{\mathrm{fall}_{10,\ 90}}$ [μs]
photon-like events	0.3	3.5
1st population events	2.2	28.8
2nd population events	11.8*	160.7*

Table 4.2.: Time constants of non-photon events: The rising and falling time constants of the two background events are compared to photon-like events. The time constants are given as the time between 10 % to 90 % peak height. By calculating the exponential value[34], time constants of photon-like average fit to the values which are determined for 1064 nm signal photons (tab. 3.1 in sect. 3.2.2.4). *Since the normalized pulse shape of 2nd population events exceeds the time window, the value is calculated from the time between 40 % to 90 % pulse height.

- 3 coincident events show an overall baseline shift at both channels which causes the trigger by a noise glitch. These events occurred within 1 minute, and are presumably related to an excess noise (sect. 4.3.2.1).
- 2 events show a 2nd population event for each channel.
- 1 event shows for channel A a 1st population event and for B a photon-like event.
- 1 event shows for channel A a photon-like event and for B a 2nd population event.

Such three latter coincidence events suggest particles which pass both channels and deposit some energy, which is measured by the TES.

The **origin** of the non-photon events is not clarified. However, the previous analysis suggests different assumptions. Since these events show a pulse shape with a rising and falling time constant, it is assumed that the short-time energy input to the TES is related to a single energy input, like a particle. Furthermore, the distribution shows a uniform broad energy spectrum. This could be caused either by a broad band source or by a broad band distributed energy input to the TES. Furthermore, the two different pulse shapes suggest that there are either two kinds of sources or two different energy inputs to the TES. One consideration is that these events are related to cosmic muons. Passing muons could thermalize the silicon substrate of the sensor chips – SQUID and TES – causing a heat input to the TES. Photons could be induced by this process (see next section). Another source could be radioactive materials.

It is concluded to determine dark count rates of 1064 nm photons events, these two background populations are uncritical. Since the pulse shape differs, these events are discriminated by the analysis methods. This is confirmed by the following analysis in the next sections 4.3.2.3 and 4.3.3. This non-photon background only

	run 1	run 2	run 3	run 4
time [s]	55520	33435	50820	76752
trigger events	559	289	510	758
photon-like events	30	13	37	31
HIA (conservative guess), 3σ-region	16	4	8	11
HIA (conservative guess), half 3σ-r.	3	2	0	3
HIA (best guess), 3σ-region	14	4	5	10
HIA (best guess), half 3σ-r.	3	2	0	3
PSA, 3σ-region	10	3	1	8
PSA, half 3σ-region	4	2	0	0

Table 4.3.: Absolute intrinsic dark counts of 1064 nm photons of non-fiber-coupled TES: The corresponding rates of four long-term measurements are illustrated in figure 4.14. Photon-like events are defined with $\chi^2_{\text{red.}} < \mu_{\chi^2_{\text{red.}}} + 3\sigma_{\chi^2_{\text{red.}}}$ according to PSA.

affects the measurement time as a dead time period. Assuming that both classes of events occur roughly with the same rate and taking a generous dead time window of $\sim 150\,\mu$s, this ends up with a dead time contribution of 0.0002 %. The photon-like events are studied in the next chapter.

4.3.2.3. Photon-like events

Photon-like events depend on the used analysis method, HIA or PSA, with the definition given at the beginning of this section 4.3.2. It should be noted that a photonic origin for a photon-like event is assumed, but another origin cannot be excluded in this analysis. In this section, measured dark counts result in an intrinsic dark count rate for 1064 nm photons for the ALPS TES detector.

To determine the intrinsic dark count rate of 1064 nm photons, results of **four long-term measurements**[35] are considered. In all runs no fibers were attached to the TES. However, in run 1 and 2, two fiber channels were fed into the cryostat. The covered[36] fiber ends inside the ADR were stored in the 70K-room by fixing them at the inner side of the 70K-stage (see dotted line in fig. 4.1c). In run 3 and 4, absolutely no fibers were in the ADR (fig. 4.1c). During run 4, the lab light and additional light sources were switched on.

---

[35]Each measurement had the same event window and digitization steps. The same DAQ adjustments are used as for the determination of the signal region (sect 4.1.3). This diminishes systematical uncertainties between the measurements.

[36]With a plastic cap for FC ferrules.
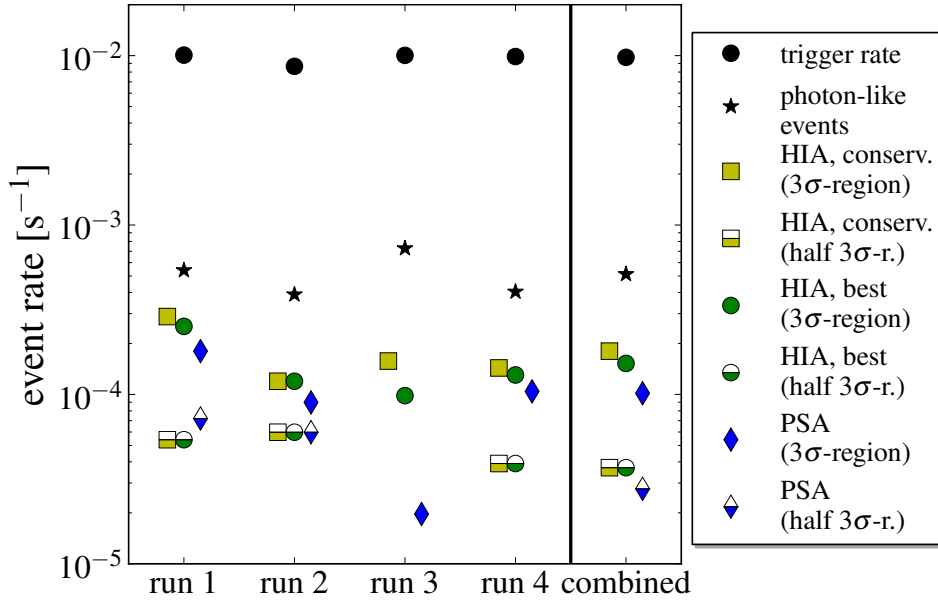
Figure 4.13.: Intrinsic dark count rate of 1064 nm photons for the ALPS TES detector: The rates of four long-term measurements (run 1-4) and the overall rate of all four measurements (combined) are depicted. The rates are calculated with the absolute values of each run (tab. 4.3): Trigger rates (black dots), rates of photon-like events (black stars), and the dark count rates of 1064 nm photons which result from different signal regions according to the developed analysis strategies in section 4.2.5. The conservative guess (yellow squares) and the best guess (red dots) are related to HIA, fit analysis (blue diamonds) to PSA. Each half filled marker represents the corresponding low-energy cut, which considers only the high-energetic half of each 3σ-region (sect. 4.2.5).

An **overall trigger rate** of $(9.8 \pm 0.6) \cdot 10^{-3}$ s^{-1} is observed. This is in the same range as the trigger rate of $1.2 \cdot 10^{-2}$ s^{-1} during the measurement for non-photon like events (sect. 4.3.2.2). The deviation is presumably caused by differently adjusted digitizations which result in a different trigger efficiency (sect. 4.1.3).

The **absolute dark counts** are listed in table 4.3, the corresponding **dark count rates** are illustrated in figure 4.14. The dark count rates of each run within each analysis method are in the same order of magnitude for all four runs. Deviations are presumably caused by a systematic error related to a deviation of the nominal working point (sect. 4.2.4). A difference related to the different setups cannot be confirmed due to low statistics. Thus, a possible dark count contribution, due to a fiber from outside up to the 70K-stage of the ADR or light in the laboratory, is negligible.

Hence, a **combined dark count rate** is considered. Therefore, total counts are divided by the total time of all four measurements. This results in intrinsic dark count rates of 1064 nm photons $DC_{\text{intr., 1064 nm}}$ for the ALPS TES detector, according

to different analysis methods and signal regions (sect. 4.2.5):[37]

- HIA conservative guess:

    - $DC_{\text{intr., 1064 nm, HIA conserv., full } 3\sigma} = (1.80 \pm 0.29) \cdot 10^{-4} \text{ s}^{-1}$
    - $DC_{\text{intr., 1064 nm, HIA conserv., half } 3\sigma} = (3.69 \pm 1.31) \cdot 10^{-5} \text{ s}^{-1}$

- HIA best guess:

    - $DC_{\text{intr., 1064 nm, HIA best, full } 3\sigma} = (1.52 \pm 0.27) \cdot 10^{-4} \text{ s}^{-1}$
    - $DC_{\text{intr., 1064 nm, HIA best, half } 3\sigma} = (3.69 \pm 1.31) \cdot 10^{-5} \text{ s}^{-1}$

- PSA:

    - $DC_{\text{intr., 1064 nm, PSA, full } 3\sigma} = (1.02 \pm 0.22) \cdot 10^{-4} \text{ s}^{-1}$
    - $DC_{\text{intr., 1064 nm, PSA, half } 3\sigma} = (2.77 \pm 1.13) \cdot 10^{-5} \text{ s}^{-1}$

The results allow to **compare different analysis methods**. As for the rates resulting from HIA, best guess rates are by trend lower than conservative guess rates as expected due to a larger signal region. In addition, PSA rates are lower than HIA rates. This is caused by a harder cut of low-energy events, which is presented in the next chapter 4.3.3 in more detail. Furthermore, comparing the results of the full 3σ-region and of the high-energetic half 3σ-region indicates an asymmetry. If the photon-like counts would distribute uniformly, the cut should provide half of the counts. However, approximately 75 % of dark counts are lying in the low-energy half region. The observation is in agreement with all analysis methods. This asymmetry suggests a low-energy source for the observed dark counts.

Two possible sources of dark counts are discussed in the following: photon-like events from thermalization processes of material or thermal photons of black body radiation. Dark counts could be events related to the non-photon background (sect. 4.3.2.2). It cannot be excluded that the non-photonic background can induce photons or photon-like events during the **thermalization process** of a substrate of the TES chip. Two coincidence events during the background measurement suggest such a processes (sect. 4.3.2.2). Even spontaneous emission from other parts in the 4K-room could induce photon-like events which reach the TES. For example, it is observed that a running piezo-motor of the heat switch induces photon-like events.

Finally, **thermal photons** as a source are considered. Thermal photons resulting as 1064 nm dark counts from low-temperature surfaces are implausible. The TES module faces mainly a 80 mK black body radiation due to the thermal copper shield attached to the bath temperature (app. C.2). From these surfaces, no events are expected because thermal radiators with a temperature < 30 K result in a rate < 10^{-100} s^{-1}.[38] Possible sources of thermal photons are the 300 K parts within the

---

[37]Each uncertainty is calculated by $\sqrt{N}$, where N is the absolute count.

[38]This is estimated conservatively for a 3σ-region around 1064 nm including the sensitive area of the TES and the half space of a Lambertian radiator (app.A.4).

ADR. It is observed that photons reach the TES from fibers stored at the 70K-stage. As mentioned above in run 1 and 2, a fiber connects the outside to the 70K-room (see dotted line in fig. 4.1c). By applying a laser source with a power of < 1 mW including the attenuation of the plastic cap at the fiber end, a photon rate of ~0.8 s^{-1} is measured. This demonstrates that photons from the 70K-room can arrive at the TES, which is caused by a non-perfect light-tight 4K- and mK-shield. Therefore, it is possible that thermal photons from 300 K surfaces could pass the 70K- and also the 4K-, and the mK-shield to finally reach the TES. It should be noted that two or more low-energetic thermal photons could cause a dark count as a pile-up (see 4.3.3).

It is summarized that the determined intrinsic dark count rate is a **fundamental limit** of the dark noise of this TES detector setup. The dead time contribution is the same as in the previous chapter 4.3.2. In the next section 4.3.3, it is presented that for fiber-coupled TES, this rate is surpassed by the background of thermal photons from the warm fiber. Therefore, the intrinsic dark count rate is uncritical at this stage of the TES detector development for ALPS.

4.3.3. Thermal photon background of fiber-coupled TES

Thermal photons from warm environments are the dominant contribution for dark counts of fiber-coupled TES (sect. 4.3.1). Because of the fiber transmittance acting as a bandpass, the low-energy contribution of the black body spectrum is suppressed (fig. C.8a): This results in a thermal photon peak, which is observed with an attached fiber to the TES (fig. 4.3). In the following, the different setups and measurement results are described (sect. 4.3.3.1). These results are discussed in section 4.3.3.2-4.3.3.4, concerning different setups, used analysis methods, and the comparison to the expected dark count rate.

4.3.3.1. Setups and results

The dark counts of 1064 nm photons for fiber-coupled TES is studied for **three different fiber setups**. For each setup, two valid long-term measurements are considered. Each run lasted between 14-20 h. For each setup, the warm fiber end, which is not attached to the TES, was in the dark 300 K environment, however, the length and the location of the fiber differed.[39] The setups are – from cold to warm or from short to long fiber:

- **Setup 1**: The warm fiber end was inside the ADR cryostat at the outside of the 70K-stage according to figure 4.1b. 80 cm of the fiber were in the 300K-room of the ADR.

---

[39]See figure 4.1b. The exact fiber setup is described in appendix C.4.3.

146
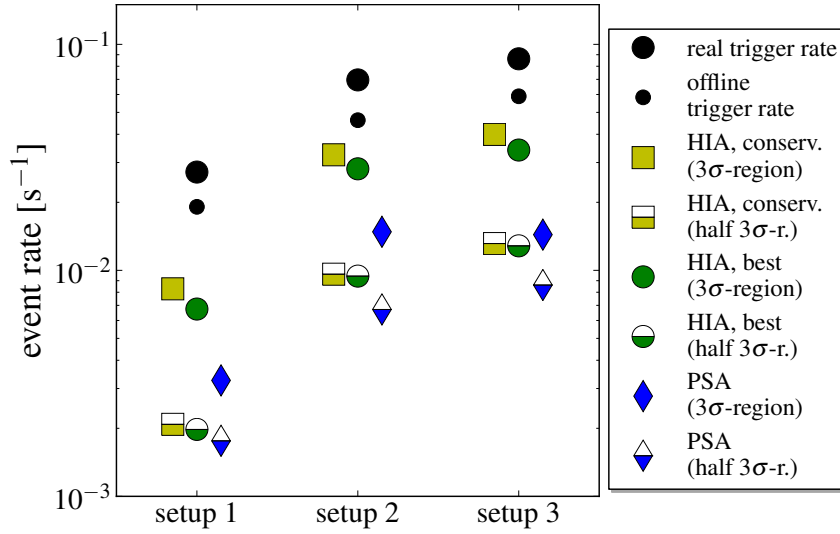
Figure 4.14.: Measured dark count rates of 1064 nm photons for different fiber setups: The combined rates of three different fiber setups (setup 1-3) are depicted. The real trigger rate is depicted in big black dots including events with a pulse height below the trigger level due to the trigger efficiency of the DAQ (sect. 4.1.3). The offline trigger rate is depicted in small black dots, which is only considering events exceeding the trigger level $TL = -52$ mV. The measured dark count rates of 1064 nm photons are depicted according to the analysis methods: HIA conservative guess (yellow squares), HIA best guess (red dots), and PSA (blue diamonds). For each analysis the high-energetic half 3σ-region is depicted in half-filled dots. Different results are caused by different couplings to the thermal radiation (see text).

- **Setup 2**: The warm fiber end was inside the ADR cryostat at 300K-stage at the bottom side of the top flange according to figure 4.1b. 157 cm of the fiber were in the 300K-room of the ADR.
- **Setup 3**: The warm fiber end was fed outside the ADR and stored in the black box (standard configuration in fig. 4.1a). 220 cm of the fiber were in the 300 K environment.

Furthermore, the trigger level was set to $TL = -52$ mV for these long-term measurements. This ensures not to be constrained by dead time due to a higher rate of low-energetic thermal photons. However, the nominal signal content is reduced, which is explained in section 4.2.5. Thus, the measured rates has to be corrected to compare to expectations (sect. 4.3.3.4) and to estimate the detection efficiency (sect. 4.4).

Since the deviations between each two measurements of one setup are <18 %, in the following, **combined dark count rates** for each setup are considered. Therefore, total counts are divided by total time of measurement for each setup. In figure 4.14, the combined rates of each setup and each analysis method are depicted.

4. Near-infrared signal photons and dark counts

These results are discussed in the following:

- Firstly, conclusions due to different setups are discussed (sect. 4.3.3.2).
- Secondly, conclusions due to the used analysis methods are considered (sect. 4.3.3.3).
- Finally, the results are compared to the expected rate and to measurements from other groups (sect. 4.3.3.3).

4.3.3.2. Conclusions due to different setups

A first indication are **different rates** between different setups. This is explained by different couplings to thermal photons from black body radiation. The coupling efficiency includes the coupling of the fiber end and along the fiber due to a specific length at a certain temperature, and further possible couplings related to connectors or splice protectors along the fiber. This is in accordance with the measurements (fig. 4.14):

- The rate of setup 1 is the lowest one. This is caused by the warm fiber tail attached to the 70K-stage.
- The rate of setup 2 is significantly higher. Here, the warm fiber tail of setup 2 is stored at the 300K top flange and the fiber is longer in comparison to setup 1.
- Finally, the rate of setup 3 is even slightly higher. This is presumably caused by a longer fiber and the warm fiber end attached outside the ADR. Therefore, stray light could be a possible source, although the fiber end was covered as best as possible.[40]

Another result is the **ADR light-tightness** from outside. In setup 2, the fiber end was placed in a direction of the vacuum tight connection of the ADR dewar. During one run of this setup, the laboratory light and additional light sources were switched on. No significant difference is observed, which suggests the light-tightness of the ADR from outside.

4.3.3.3. Conclusions due to analysis methods

As in the previous section 4.3.2.3, the determined dark count rates depend on the used analysis method (fig. 4.14). Within one setup, the different analysis methods show the same trend:

- The HIA conservative guess shows higher rates as the best guess, as expected. This is caused by the size of the signal region.
- PSA rates are lower than HIA rates. This is explained by a harder cut on low-energy events, which is discussed in the following.

---

[40]In setup 3, the coupling efficiency between two fiber parts is an additional factor (see details in app. C.4.3). This should lower the photon rate which comes from the outer fiber part.

(a) HIA method (best guess): full and zoom view

(b) PSA method: full and zoom view
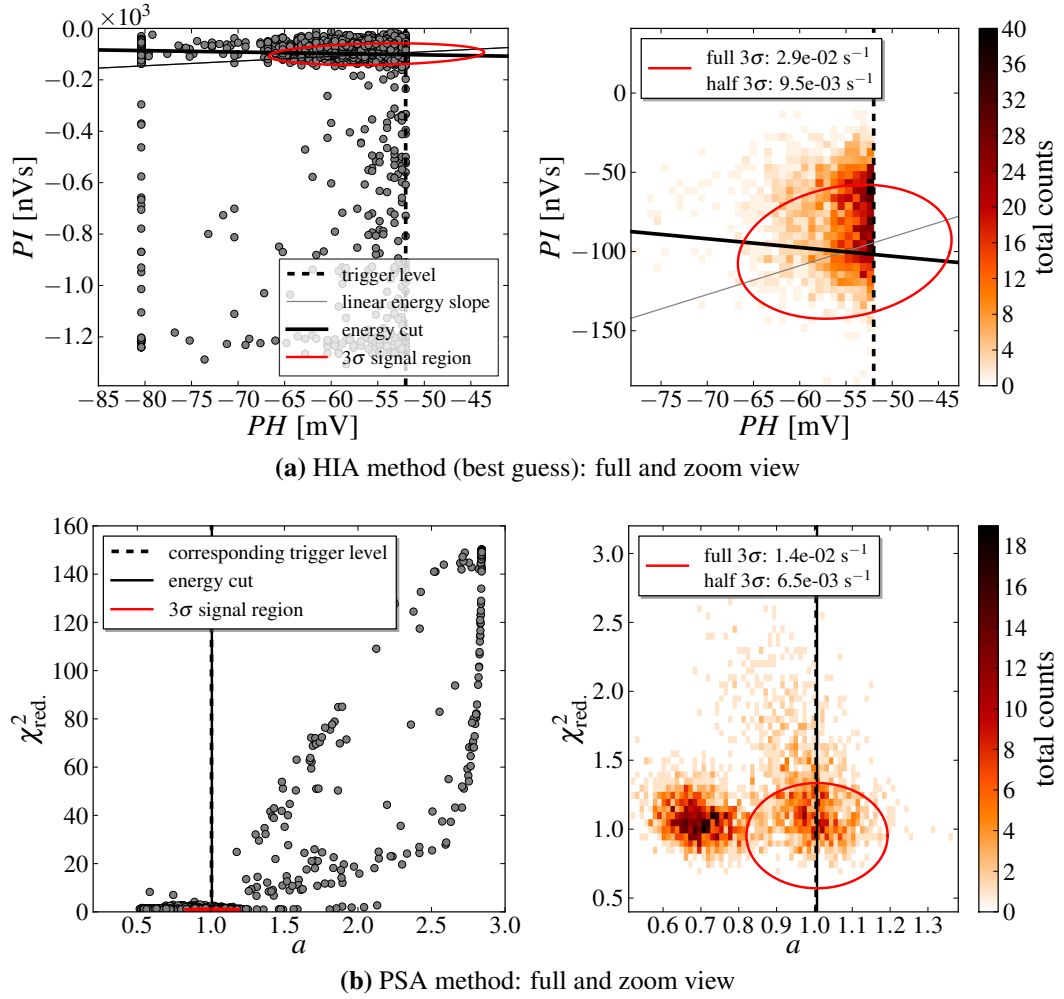
Figure 4.15.: Event distribution of fiber-coupled TES and comparison of the analysis methods: This is an exemplary result from a long-term measurement with fiber setup 2.

(a) The measurement is analyzed by HIA, and the result is illustrated in the *PH-PI*-plane. Left, the full plane is depicted, trigger events are illustrated by grey dots, and the event window border affects a maximal pulse height of $PH = -80$ mV. Apart from the signal region (red ellipse), the two populations of the non-photonic background are identifiable (sect. 4.3.2.2). Right, a zoom of the signal region is shown. Trigger events are illustrated by a histogram. The distribution hints at two photon-like populations, which is confirmed by PSA.

(b) The same measurement is analyzed by PSA, and the result is illustrated in the a-$\chi^2_{\text{red.}}$-plane. Left, in the full plane, the two populations of non-photonic background (sect. 4.3.2.2) are split due to the fit analysis with a photon-like shape. Right, in the zoomed view around the signal region, photon-like events split in two populations significantly. This is caused by different trigger events (see text).

4. Near-infrared signal photons and dark counts

In both analysis methods, **two photon-like populations** in and around the signal region are identified (fig. 4.15). Analyzed by PSA, these populations are significantly isolated (fig. 4.15b):

- **"1550 nm" noise glitch trigger:** This population is around $a = 0.7$ ($\hat{=}$ 1520 nm) with a $\chi^2_{\text{red.}} < 1.5$ (fig. 4.15b). Considering single events, these events are related to low-energy photon-like events which reach the trigger level by a coincidental noise glitch near the real peak height. A typical example is shown in figure 4.16a. Together with the HIA picture (fig. 4.15a), it is estimated that these events could be related to the 3-4σ-region of 1550 nm photons. Furthermore, the rate of this population $\sim 2 \cdot 10^{-2}$ s^{-1} is in the same order of magnitude of the positive 3σ-region for 1550 nm photons calculated with the simple model in appendix A.5. This strengthens the assumption that these photon-like events are caused by thermal photons.

- **Pile-up trigger:** This population is around $a = 1.0$ with a range of $\chi^2_{\text{red.}} = 0.7 \ldots 3.0$. Considering as exemplary a single event with a $\chi^2_{\text{red.}} \sim 1.7$ (fig. 4.16b), it obviously appears as a first-order pile-up event (sect. 4.2.3.3). By considering pile-up events close to the 3σ-region cut of $\chi^2_{\text{red.}} \geq \mu_{\chi^2_{\text{red.}}} + 3\sigma_{\chi^2_{\text{red.}}} \approx 1.3$, a time resolution of the PSA method can be estimated. This results in a time resolution of $\tau_{\text{PSA}} \approx 0.5$ μs. This means, if two photon-like events occur within this time window τ_{PSA}, this first-order pile-up event cannot be discriminated by PSA and is counted as a single photon-like event.

This consideration explains the **lower rates analyzed by PSA** compared to HIA due to better discrimination. Using PSA, the "1550 nm" noise glitch triggers are better distinguished from the signal photon region. In addition, pile-up events within a time window $\gtrsim 0.5$ μs are also discriminated by the pulse shape fit. Furthermore, considering the pile-up population reaching uniformly the signal region of 1064 nm (fig. 4.15b) suggests that the dark count rate of 1064 nm is pile-up dominated. This assumption is discussed in the following.

4.3.3.4. Comparison to expected dark count rate

Finally, the measured rates are compared to an expected dark count rates which result from different estimations. Therefore, one **conservative value** of a measured dark count rate is considered. The choice is:

- setup 3 as standard setup with a warm fiber end outside the ADR (fig. 4.1a)
- PSA method due to better discrimination of thermal photons (sect. 4.3.3.3)
- half 3σ-region due to the corresponding trigger level in the a-$\chi^2_{\text{red.}}$-plane which is below the half energetic cut (dashed line in fig. 4.15b)

150

(a) "1550 nm" noise glitch trigger   **(b)** pile-up trigger
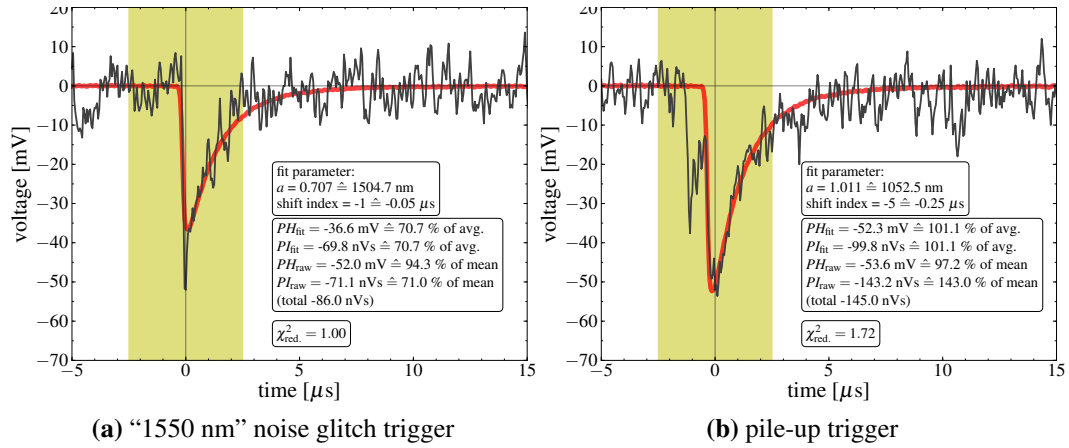
Figure 4.16.: Exemplary trigger events related to thermal photons: Two photon-like events are illustrated which are assumed to be related to thermal photons (see text). (a) shows a typical trigger event due to a noise glitch. The trigger level is reached by a noise peak on top of a thermal photon peak. (b) shows a typical first-order pile-up event. Obviously, two thermal photons reach the TES nearly simultaneously. Therefore, the overall pulse height is influenced by these two events, which results in a high enough peak height to reach the trigger level.

This dark count rate corresponds to the half-filled blue diamond in figure 4.14:[41]

$$DC_{\text{fiber, 1064 nm, PSA, half } 3\sigma} = (8.6 \pm 1.1) \cdot 10^{-3} \text{ s}^{-1} \tag{4.15}$$

This measured value corresponds to the integrated differential rate for photons with energies from 1.165 eV to 1.410 eV, which cover the half 3σ-region of 1064 nm photons with an energy resolution of <7 % (sect. 4.2.3). However, the real rate is expected to be higher if it would include the overall detection efficiency and the corrected signal region, due to the chosen trigger level (sect. 4.2.5). Thus, this value is a conservative estimate for the following considerations.

Firstly, this measured rate is compared to the **expectation of a black body spectrum**. In appendix A.5, a simple model of a fiber-coupled TES is derived where the warm fiber end couples to a 300 K spectrum. Assuming conservatively an energy resolution of 10 %, no optical losses, and overestimated fiber parameters, the integrated rate of the high-energetic half 3σ-region results in (cf. tab. A.1):

$$DC_{\text{fiber model}} = 3.4 \cdot 10^{-4} \text{ s}^{-1}$$

Although both values are estimated conservatively, the measured rate is one and a half orders of magnitude higher than the estimate of this fiber model.

---

[41]Here, the error is the standard deviation of the 2 runs within setup 3.

Secondly, a possible contribution of **counts along the fiber** is considered. In chapter 4.3.1, the measurement of AIST is explained which considers black body photons coupling along the fiber into the core and reaching the TES (Fujii et al., 2011). The extrapolated differential rate for 1 eV photons is $\sim 1 \cdot 10^{-4}$ for a 10 m fiber setup (sect. 4.3.1). For an integrated rate of the half 3σ-region, it is conservatively estimated

$$DC_{\text{along fiber}} < 1 \cdot 10^{-3}$$

Since <2.5 m of the fiber are in the 300 K environment at setup 3, the expected rate is assumed to be even smaller. Although this estimate is quite uncertain, the measured rate is nearly one order higher than the estimate along the fiber.

Taking both estimates into account, the measured rate is still too high for a valid explanation with the current fiber models. This leads to different possibilities of explanation:

- **Additional thermal photon source:** The setup has an additional source of photons which couples into the fiber. For example, the source could be a "hot" surface, which provides more thermal photons. For example, the upper part of the cold head unit of the pulse-tube cooler is a warm component in the environment of the fiber (sect. 2.2.1).

- **Additional thermal photons due to fiber parts:** There is a higher coupling along the fiber into the core, as it is assumed by AIST results (Fujii et al., 2011). This could be caused by elements like fiber connectors or splice protectors along the used fiber channel (app. C.4.3).

- **Pile-up events:** The measured rate is caused by pile-up events. Since the photon rate of the black body spectrum increases strongly for low-energetic photons, the chance for pile-up events increases. The limit to resolve pile-ups depends on the time resolution of the detector and the analysis. Therefore, the real intrinsic spectrum of black body photons changes with the detection, and for example, a fraction of low-energetic events combines to counts of high-energetic events.

The first and second explanation has to be tested experimentally.

The **pile-up explanation seems to be plausible**. As the rate of black body photons increases strongly for lower energies (app. A.4), the possibility for pile-up combinations within the event window increases. For an estimate, the resulting first-order pile-up rate $\dot{n}_{\text{res}}$ can be estimated by a formula describing accidental coincidences (Eckart and Shonka, 1938, e.g.):

$$\dot{n}_{\text{res}} = 2\,\tau\,\dot{n}_1\,\dot{n}_2$$

where τ is the resolving time and $\dot{n}_1$ and $\dot{n}_2$ uncorrelated rates. Considering the PSA, the time resolution is $\tau_{\text{PSA}} \approx 0.5\ \mu\text{s}$ (see above). For $\dot{n}_1$ and $\dot{n}_2$, the thermal photon spectrum from a measurement of this thesis is considered which includes

the fiber transmittance (fig. 4.3). By splitting the resulting thermal peak containing black body photons into two parts, from -40 mV to -30 mV and from -30 mV to -20 mV, an integrated rate of approximately 10^2 s^{-1} is derived for each part. The two parts correspond approximately to mean photon energies of 0.7 eV and 0.5 eV respectively. By including the energy resolution, these two contributions can roughly combine to a 1064 nm-like event. Thus, it is $\dot{n}_1 = \dot{n}_2 \approx 10^2$ s^{-1} and the rate for first order pile-ups imitating 1064 nm events is:

$$\dot{n}_{\text{res}} = 2 \times 0.5 \cdot 10^{-6} \text{ s} \times 10^2 \text{ s}^{-1} \times 10^2 \text{ s}^{-1} \simeq 10^{-2} \text{ s}^{-1}$$

This roughly estimated rate $\dot{n}_{\text{res}}$ is in the same order of magnitude as the observed dark count rate including the half 3σ-region (eqn. 4.15). Furthermore, it is shown that pile-up contributions are measured and they explain directly one of the two photon-like populations (fig. 4.15). Finally, this would explain the sustained tail of the near-infrared spectrum of fiber-coupled TES, which is also observed by other groups (sect. 4.3.1).

Finally, the dark count rate is evaluate for signal measurements. Considering the possible signal content of the corresponding dark count rate (eqn. 4.15), it has to be corrected by a factor ~80 % due to the cut of the chosen trigger level (sect. 4.2.5). This results in an analysis detection efficiency for the half 3σ-region analyzed with PSA:

$$DE_{\text{analysis, 1064 nm, PSA, half } 3\sigma} \approx \frac{3\sigma_{2\text{d}}}{2} \, 80.0 \text{ \%} = 39.6 \text{ \%} \tag{4.16}$$

The combination of this efficiency (eqn. 4.16) and the dark count rate (eqn. 4.15) results in a dead time contribution of $< 10^{-4}$ %.

4.4. Summary

It is summarized that the ALPS TES detector is working as a single photon detector (sect. 3.4). In section 4.1, the **experimental setup** is described to analyze signal photons and to research corresponding dark count rates. In section 4.2, the ALPS TES detector is calibrated by **signal photons**. Methods are developed which allow to analyze signal photons. A representative signal sample of 1064 nm photons is used to define corresponding signal regions. Two methods are used for background measurements with the following properties:

- **Pulse height and integral analysis (HIA)** (sect. 4.2.2):

    - HIA is an extension of a pulse height diagram. This allows a quick localization of events depicted in a plane spanned by the integral and height of an event.
    - The energy resolution of 1064 nm signals is $\Delta E / E_{\mathrm{HIA}} = (7.1 \pm 0.3)$ %.

- **Pulse shape analysis (PSA)** (sect. 4.2.3):

    - PSA uses an averaged photon signal pulse to judge single events. This allows to distinguish single photon-like events from non-single-photon-like events. In addition, a comfortable calibration is given.
    - The energy resolution of 1064 nm signals is $\Delta E / E_{\mathrm{PSA}} = (6.3 \pm 0.3)$ %. This fits to the HIA value and is slightly better.

Furthermore, the detection stability is discussed (sect. 4.2.4). It is indicated that the systematic error is below the 1σ-uncertainty of the statistical distribution of signal photons. Furthermore, signal regions and strategies to determine dark counts are discussed (sect. 4.2.5).

In section 4.3, **backgrounds and dark count rates** are considered. As a baseline, an overview of the current state of research about dark count rates of TES detectors for NIR signals is given (sect. 4.3.1). By using the developed analysis methods, dark count rates of different setups for 1064 nm photon signals are determined:

- **Intrinsic dark count rate:** With a dark, non-fiber coupled TES and using PSA, it is (sect. 4.3.2):

    - $DC_{\mathrm{intr.,\ 1064\ nm,\ PSA,\ full\ }3\sigma} = (1.0 \pm 0.2) \cdot 10^{-4}\ \mathrm{s}^{-1}$
    - $DC_{\mathrm{intr.,\ 1064\ nm,\ PSA,\ half\ }3\sigma} = (2.8 \pm 1.1) \cdot 10^{-5}\ \mathrm{s}^{-1}$

    where the first value includes the total 3σ-region ($\hat{=} 98.9$ % of signal photons), the second the high-energetic half of the 3σ-region ($\hat{=} 49.5$ % of signal photons).

- **Dark count rate of fiber-coupled TES:** Using PSA, the result is (sect. 4.3.3):

    - $DC_{\mathrm{fiber-coupled,\ 1064\ nm,\ half^{*}\ }3\sigma} = (8.6 \pm 1.1) \cdot 10^{-3}\ \mathrm{s}^{-1}$

where only the half 3σ-region is given due to the chosen trigger level. Therefore, only 39.6 % of signal photons are within this region (sect. 4.2.5).

It is confirmed that **thermal photons** are the main dark count contribution of fiber-coupled TES. It is indicated that the dark count rate of 1064 nm is dominated by pile-up events of low-energetic thermal photons (sect. 4.3.3). Due to the time resolution of the analysis, pile-ups with constituents occurring in a time window <0.5 μs cannot be resolved.

Finally, **two non-photonic populations** are indicated which show a broad energy distribution (sect. 4.3.2.2). Their origin could be related to cosmic ray events; however, this is not confirmed. These backgrounds are no dark count contribution for 1064 nm signals because they are discriminated due to different pulse shapes. Finally, considering background sources apart from thermal photons, baseline deviations can make up the main part of **dead time contribution** with <0.02 % of the total measurement time (sect. 4.3.2.1).

5. Conclusion

Searches for physics beyond the standard model (SM) require new experiments incorporating extremely high-developed machines (chap. 1). To explore the existence of weakly interacting sub-eV particles (WISPs), a high experimental precision has to be established. Any Light Particle Search (ALPS) II is a light-shining-through-a-wall (LSW) experiment which will exploit a WISP-photon coupling. WISPs are motivated by astrophysical observations as well as the fact that they could form cold dark matter. One technical improvement of ALPS II will be a superconducting microcalorimeter instead of a Si-CCD camera used at ALPS I. In this thesis, a superconducting microcalorimeter based on a transition-edge sensor (TES) has been successfully set up and optimized for ALPS II: It has been proven to work as a low-noise single photon detector for 1064 nm light and is named *ALPS TES detector*. In the following, the main results of this thesis are summarized with respect to an operation at the ALPS II experiment; detailed results are found in section 2.4 concerning the performance of a milli-kelvin (mK) cryostat, in section 3.4 concerning the performance of superconducting sensors for photon detection, and in section 4.4 concerning signal and background analyses.

An adiabatic demagnetization refrigerator (ADR) was set up during the work of this thesis. The **ADR cryostat system** was proven to be an adequate mK-environment to operate superconducting sensors (chap. 2). The ADR system was successfully set up and optimized for a stable operation. Using the ADR cryostat as mK-environment for the ALPS TES detector, the most important conclusions are:

- It is recommended to operate cool-downs and warm-ups over weekend. This provides a safe thermalization of the ADR and superconducting sensors.

- Main technical problems are due to the heat switch which couples and decouples the 4K-stage with the mK-stages. With the analysis, the operation of the heat switch at low temperatures is explained. A proper alignment in the warm could be found which results in ~80 % chance of success in the cold.

- Holding a 80 mK-temperature is stable to <25 μK (RMS) over ~20 h. Thus, a 24 h detector cycle could be established: ~20 h measurement time and ~4 h dead time which consists of recharge time and the time to adjust sensors.[1]

Sensor modules which were developed in this thesis were proven to be adequate for single photon detection (chap. 3). The NIST module incorporating two channels

---

[1]The cycle can be optimized for a specific setup (fig. 2.15b).

5. Conclusion

with fiber-coupled tungsten TESs and 2-stage SQUIDs is extensively characterized (sect. 3.2). Important results are:[2]

- The transition temperature is $T_c = 140$ mK.
- The heat capacity is estimated with $C = 0.58$ fJ/K.
- The system bandwidth is $f_{3dB} = 0.9$ MHz.
- The TES noise is higher than the SQUID noise. Thus, the used SQUID setup is adequate for TES current read-out.
- The measured signal response fits to the theory using the determined TES parameters (fig. 3.10).
- The environment of the ALPS IIa laboratory and the environment in the ADR cryostat is suitable to operate TES detectors (sect. 3.3).

Further TES and SQUID parameters, which have been determined, are found in the right part of table 3.2.

The NIST module operated in the ADR cryostat forms the **ALPS TES detector**. The NIST module is operated at 80 mK and is thermally shielded by a copper shield. The detailed setup and the working point for single photon detection are summarized in section 3.2. The ALPS TES detector is used for 1064 nm single photon (signal) and background studies (chap. 4). Most important results of the **signal** analysis and the detector calibration are:

- Different analysis methods are developed. Fitting an averaged signal pulse to trigger events shows the best results concerning the energy resolution and the discrimination of non-single-photon-events.
- The energy resolution is $(\Delta E/E)_{1064\,\text{nm}} = $ 6-8 % depending on the analysis.
- The exponential fall time of single photons is $\tau_{\text{fall}} = 1.53\ \mu$s.

Concerning the **background**, most important results are:

- Using the pulse shape analysis (PSA), dark count rates are:

  - Intrinsic dark count rate for a TES without optical fiber link to warm environments:

    * $DC_{\text{intr., 1064 nm, PSA, full } 3\sigma} = (1.0 \pm 0.2) \cdot 10^{-4}\ \text{s}^{-1}$
    * $DC_{\text{intr., 1064 nm, PSA, half } 3\sigma} = (2.8 \pm 1.1) \cdot 10^{-5}\ \text{s}^{-1}$

    where the first value includes the total 3σ-region ($\hat{=}$ 98.9 % of signal photons), the second value the high-energetic half of the 3σ-region ($\hat{=}$ 49.5 % of signal photons).

  - Dark count rate for a standard fiber setup with fiber-coupled TES and fiber end outside the ADR:

    * $DC_{\text{fiber, 1064 nm, PSA, half}^* 3\sigma} = (8.6 \pm 1.1) \cdot 10^{-3}\ \text{s}^{-1}$

---

[2]For channel A.

where only the half 3σ-region is given due to the trigger level. Therefore, only 39.6 % of signal photons are within this region (sect. 4.2.5).

- The main dark count contribution of a fiber-coupled TES are thermal photons from a 300 K black body spectrum. Furthermore, it is indicated that the dark count rate of 1064 nm is dominated by pile-up events of low-energetic thermal photons (sect. 4.3.3).

- The electrical system noise shows no dark count contribution.

- Two non-photonic populations are indicated which show a broad energy distribution (sect. 4.3.2.2). Their origin could be related to cosmic ray events; however, this is not confirmed. These backgrounds are no dark count contribution for 1064 nm signals because they are discriminated due to different pulse shapes.

$$\star \quad \star \quad \star$$

Finally, the results are used to estimate the detector impact on the ALPS II experiment (sect. 1.2). To compare the ALPS TES detector system with the Si-CCD camera (von Seggern, 2014), the detector sensitivity is defined as (cf. eqn. 1.5):

$$\mathcal{S}_{\text{detector}} = \frac{\sqrt{DC_{\text{detector}}}}{DE_{\text{detector}}} \left[\sqrt{\text{s}^{-1}} \right]$$

where DC is the detector dark count rate and DE the detector efficiency. The smaller this figure of merit the higher the gain for the ALPS experiment. Using the Si-CCD as the detector in ALPS II with $DC_{\text{CCD}} = 1.2 \cdot 10^{-3}$ s^{-1} and $DE_{\text{CCD}} = 1.2$ % for 1064 nm signals (von Seggern, 2013),[3] it results in:

$$\mathcal{S}_{\text{CCD}} = 2.9 \ \sqrt{\text{s}^{-1}}$$

For the ALPS TES detector, a dark count rate of $DC_{\text{TES}} = 8.6 \cdot 10^{-3}$ s^{-1} is considered (eqn. 4.15). The detector efficiency is a product of the analysis efficiency and the optical efficiency. The analysis efficiency is given by the considered signal region with 39.6 % (eqn. 4.16). The optical efficiency is estimated as the product of the fiber-to-TES coupling, the fiber transmittance, and the beam-to-fiber coupling. The fiber-to-TES coupling is assumed to be 95 % according to the NIST technique (sect. 3.2.1.2). The fiber transmittance is estimated 60 % conservatively.[4] The beam-to-fiber coupling is conservatively assumed as 80 % which has been shown

---

[3]This rate is an effective rate including the read-out noise and assuming a typical 1 hour long exposure. Correctly, the dark current is in the units electron per pixel and seconds $\frac{\text{e}}{\text{px s}}$. It is considered the focus one pixel and the read-out gain to be one for one electron.

[4]Due to the two fiber parts of this setup and the losses at the FC connector (app. C.4.3).

5. Conclusion

within the ALPS collaboration (Ghazaryan, 2013). Therefore, the overall detection efficiency is assumed to be $DE_{\text{TES}} \approx 18\%$. This results in:

$$\mathcal{S}_{\text{TES, ALPS 2013}} = 0.5 \ \sqrt{\text{s}^{-1}}$$

Considering the sensitivity of the ALPS experiment $\mathcal{S}(g_{a\gamma}) \propto \sqrt[4]{\mathcal{S}_{\text{detector}}}$ (cf. eqn. 1.5), this results in a **sensitivity gain by a factor of 1.55** compared to the CCD. This proves the gain of using a TES-based detector instead of the CCD camera system to detect single 1064 nm photons.

This motivates to optimize the current setup of the ALPS TES detector in order to reach the aimed sensitivity gain for the ALPS II experiment (see tab. 1.1 in sect. 1.2). The present analysis only uses the high-energetic half of the signal region due to high rates for low-energetic thermal photons. Therefore, the most promising strategy is to reduce the thermal background which results from a 300 K black body spectrum. Two experimental improvements and one analytic improvement are proposed:

- Filter around 1064 nm photons: This filter should be placed in the cold. One realization could be a high-pass coated filter at the cold fiber end which reflects low-energetic thermal photons (Miller, 2011; Fukuda, 2012). A second realization would be a TES chip development. By multilayer structures, it is possible to raise and lower the detection efficiency of certain wavelengths.

- Cooling the fiber or the collimating optics: This would reduce the black body spectrum which is coupled into the fiber. With regard to ALPS IIc, a fiber-coupled TES detector could benefit from the cold environment of superconducting HERA magnets.

- Pile-up rejection: Events imitating 1064 nm dark counts by pile-ups could be rejected within an improved analysis or harder cuts. A filter, as described above, should also reduce the pile-up possibility of thermal photons imitating 1064 nm signals.

$$\star \ \ \star \ \ \star$$

The ALPS TES detector has been successfully set up as a sensitive single photon detector. As introduced, the ALPS TES detector is an extreme machine. The author of this thesis is confident that it will provide an success in sensitive WISP searches and for physics beyond the standard model.

160

Appendices

A. Black body photons and optical fibers

A black body is often modeled with a closed cavity. In thermal equilibrium, the cavity emits and absorbs electromagnetic radiation. The spectrum only depends on the temperature of the body. In nature, the most well-known black body is the universe itself: A black body with a temperature of 2.7 K fits to the observed cosmic microwave background.

For fiber-coupled TES detectors, it has been shown, that 300 K black body radiation is a reasonable background (sect. 4.3.1): The fiber end that is coupled to an optical setup in the warm provides a window for thermal photons reaching the TES in the cold. Therefore, the following chapters provide a closer look to derive a photon rate from a black body source for fiber-coupled TES.

A.1. Rollback of Planck's radiation law

Since photons are spin 1 particles, they follow the Bose statistic. Following Schwabl (2000) the Bose distribution is given by the number of states:

$$N(\epsilon_p) = \frac{1}{e^{\beta(\epsilon_p - \mu)} - 1}$$

with the one particle energy $\epsilon_p = p^2/2m$, the inverse energy $\beta = (kT)^{-1}$ with temperature T and Boltzmann constant k,[1] and the chemical potential μ, which expresses the relative change of states due to the change of the particle number.[2] The chemical potential of a photon gas is $\mu = 0$ because the number of photons is not constant due to emission and absorption. This distribution is applied to a fixed volume. By considering the momentum space d^3p, the number of occupied states is given by:

$$N(\epsilon_p)\frac{g}{\Delta}d^3p$$

The factor of degeneracy is here $g = 2$ because the spin of ultrarelativistic particles like photons is either parallel or antiparallel along the direction of momentum p.

---

[1]This is called the Boltzmann factor $e^{-\beta\epsilon_p}$.

[2]The chemical potential is defined as partial derivative of the free energy F and the particle number N, during temperature T and volume V stay constant: $\partial F/\partial N|_{T,V}$

Δ is the volume in momentum space given by $\Delta = \frac{(2\pi\hbar)^3}{V}$, with the space volume V and $\hbar = h/2\pi$, which includes the Planck constant h. In spherical symmetry, d^3p becomes $4\pi p^2 dp$. This results in:

$$\frac{1}{e^{\epsilon_p/kT} - 1} \frac{V}{\pi^2 \hbar^3} p^2 dp$$

By considering the frequency with $\epsilon_p = pc = \hbar\omega = h\nu$, this results in the number of states in an interval $[\nu, \nu + d\nu]$:

$$\frac{1}{e^{h\nu/kT} - 1} \frac{8\pi V}{c^3} \nu^2 d\nu$$

Multiplying with $1/V$ and considering only the factor without frequency interval, this results in the spectral number density of a cavity or a black body:

$$\tilde{u}_\nu(\nu, T) = \frac{8\pi}{c^3} \frac{\nu^2}{e^{h\nu/kT} - 1} \tag{A.1}$$

with the units number of photons per volume and frequency $[\text{m}^{-3}\text{Hz}^{-1}]$. Multiplying $h\nu/V$ results in the spectral energy density u_ν with the unit $[\text{J m}^{-3}\text{Hz}^{-1}]$. In the following, number quantities are labeled with a tilde, energy quantities without a tilde.

A.2. Different representations

Since photons can be described by frequency, wavelength, or energy; in the following, different representations of the spectral number radiance are derived. The spectral number radiance is connected with the spectral number density (eqn. A.1) by $\tilde{L}_\nu = \frac{c}{4\pi} \cdot \tilde{u}_\nu$ (Schneider, 2006, p. 411). This results in spectral number radiance in frequency representation:

$$\tilde{L}_\nu(\nu, T) = \frac{2}{c^2} \frac{\nu^2}{e^{h\nu/kT} - 1} \tag{A.2}$$

with the units photons per seconds, area, hertz and steradian $[\text{s}^{-1}\text{m}^{-2}\text{Hz}^{-1}\text{sr}^{-1}]$.

The wavelength is connected with the frequency via $\lambda = c/\nu$. Therefore, the differential factor $|\frac{d\nu}{d\lambda}|$ is added if the spectral number radiance is expressed in wavelength:

$$\tilde{L}_\lambda(\lambda, T) = \frac{2c}{\lambda^4} \frac{1}{e^{hc/kT\lambda} - 1} \tag{A.3}$$

with the units $[\text{s}^{-1}\text{m}^{-2}\text{m}^{-1}\text{sr}^{-1}]$.

The energy is connected with the frequency via the relation $\epsilon = h\nu$. Using the

differential factor $|\frac{d\nu}{d\epsilon}|$, this results in:

$$\tilde{L}_\epsilon(\epsilon, T) = \frac{2}{h^3 c^2} \frac{\epsilon^2}{e^{\epsilon/kT} - 1} \tag{A.4}$$

with the units $[\text{s}^{-1}\text{m}^{-2}\text{J}^{-1}\text{sr}^{-1}]$. To calculate with the energy in electronvolt (eV), it is helpful to use the Planck constant $h = 4.14 \cdot 10^{-15}$ eV s and the Boltzmann constant $k = 8.62 \cdot 10^{-5}$ eV/K in these units.

A.3. Lambert radiator and Stefan-Boltzmann law

If radiation is emitted from surfaces dA in a solid angle dΩ, this is called a Lambertian radiator. For the calculation, an additional factor $\cos\theta$ is needed, which ensures the right intensity level for each angle of view. This is called Lambert's cosine law. This is illustrated in figure A.1.
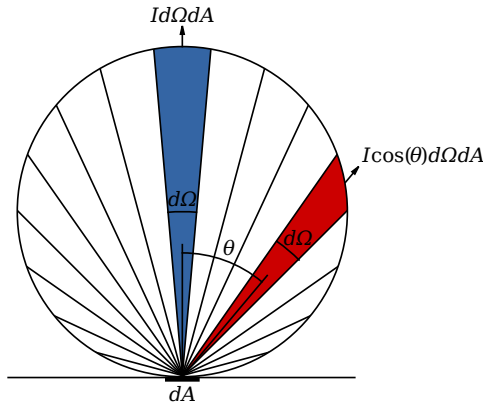
Figure A.1: Lambertian radiator: A Lambertian radiator is a surface dA which has the same radiance for any angle. By considering the radiation of such a surface at different angles $\theta = 0° \dots + 90°$, the factor $\cos\theta$ is necessary to correct the intensity related to the normal direction. A black body is such a radiator. [Taken from Wikimedia Commons]

The solid angle dΩ of a Lambertian radiator results in

$$\begin{aligned} d\Omega &= \cos\theta \cdot \sin\theta d\phi d\theta \tag{A.5} \\ \Omega &= \int_0^{2\pi} d\phi \cdot \int_0^\theta \cos\theta' \sin\theta' d\theta' \\ \Omega(\theta) &= \pi/2 \left(1 - \cos(2 \cdot \theta)\right) \tag{A.6} \end{aligned}$$

where the angle of view θ is between $0°$ and $90°$. Considering the half space, the solid angle results in $\Omega_{\text{half−space}} = \pi$ by plugging in $\theta = 90°$ in equation A.6. For comparison, a normal integration over the half space results in 2π.

The Stefan-Boltzmann law expresses the total radiation of a black body. Therefore, the spectral density is integrated over all energy states. The Stefan-Boltzmann law is usually given in units of power per area. Thus, the calculation is done with

the spectral energy radiance $L_\nu = \frac{c}{4\pi} \cdot u_\nu$ (sect. A.1):

$$
\begin{aligned}
j &= \int_0^\infty L_\nu \, \mathrm{d}\nu \, \theta(90°) \\
j &= \sigma T^4
\end{aligned}
\tag{A.7}
$$

where the solid angle results from the half space of a Lambertian radiator. $\sigma = 5.67 \cdot 10^{-8} \, \frac{\mathrm{W}}{\mathrm{m}^2\mathrm{K}^4}$ is the Stefan-Boltzmann constant. This provides the total radiation in units of $[\mathrm{Wm}^{-2}]$, which only depends on the black body temperature T to the power of 4.

A.4. Near-infrared spectrum of a room-temperature black body

In most fiber-coupled TES applications, the optical setup is at room temperature. Therefore, the spectral number radiance $\tilde{L}_\lambda$ for a 300 K black body is considered (fig. A.2). It is shown that small temperature deviations and wavelength change the rate by orders of magnitudes:

- The differential rate for 1064 nm decreases about three orders of magnitude if the black body temperature changes from 300 K to 250 K.
- For a 300 K black body, the differential rate for 1550 nm photons is about five orders of magnitude higher than for 1064 nm photons.
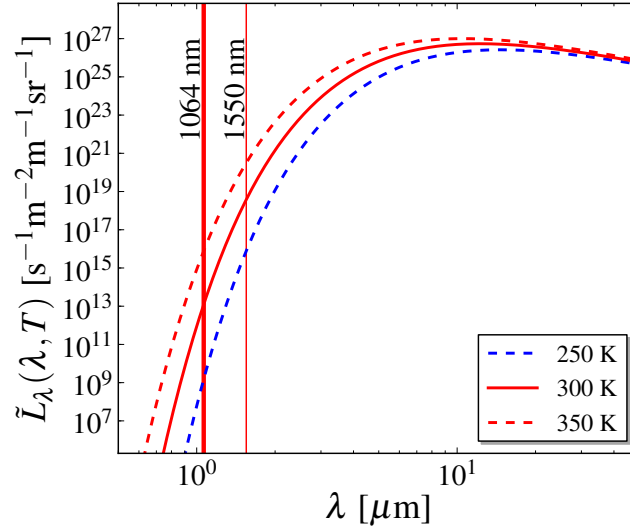
Figure A.2: Near-infrared spectrum of a room-temperature black body: The differential spectral number radiation is plotted for different temperatures: 250, 300 and 350 K. The peak for the 300 K black body spectrum is at ∼12 μm.

A.5. Calculating a photon rate

To determine a photon rate in units of $[\text{s}^{-1}]$, the spectral number radiance has to be integrated over the solid angle $d\Omega$, the surface dA, and the photon band of interest. The photon band is considered in the energy representation in the following. Thus, the integration is:

$$d\tilde{N}(T) = \tilde{L}_\epsilon(\epsilon, T)\, d\epsilon\, dA\, d\Omega \tag{A.8}$$
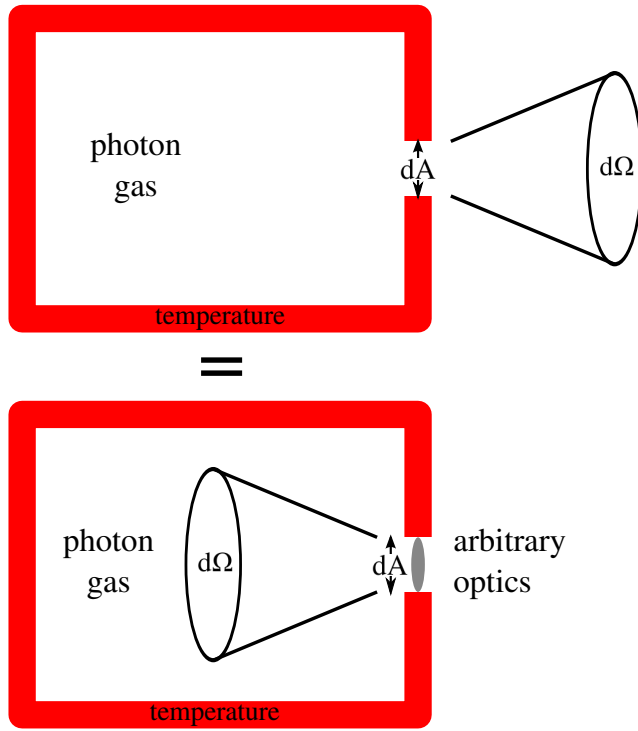
Figure A.3: An optics faces a black body: The radiation of a black body can be described by a cavity at a certain temperature with a little hole (top). The radiation which is emitted by the hole is described with a black body spectrum. An observer has to consider the solid angle $d\Omega$ and the area dA to calculate the photon flux. This is corresponds to an optics which looks into the black body (bottom). Therefore, the area and the divergence of the optics is used to determine the photon flux of the black body.

This is applied to a fiber-coupled TES detector, which is used for detecting 1064 nm photons, in the following. Therefore, some additions are considered for a simple model. The warm fiber end as an optical element faces a black body at room-temperature. This is illustrated in figure A.3. The diameter of the fiber core defines dA and the numerical aperture (NA) defines $d\Omega$. In principle, this is folded by an efficiency profile $\eta(A)$ and $\eta(\Omega)$, where $\eta \in [0, 1]$.

Considering the energy, an efficiency has to be added $\eta(\epsilon)$ which expresses the overall system efficiency. For a fiber-coupled TES, it includes optical losses at the fiber end and through the fiber, and the detector efficiency. Furthermore, the TES detector has an energy resolution. It is assumed that the signal is normally distributed:

$$\text{res}(E, \epsilon) = \frac{1}{\sqrt{2\pi}\sigma} \exp\left(-\frac{(E - \epsilon)^2}{2\sigma^2}\right) \tag{A.9}$$

Combining everything results in a modified formula for the spectral distribution of

A. Black body photons and optical fibers

black body photons which are detected by a fiber-coupled TES detector:

$$\mathrm{d}\tilde{N}(T) = \tilde{L}_\epsilon(\epsilon, T)\, \eta(\epsilon)\, \mathrm{res}(E, \epsilon)\, \mathrm{d}\epsilon\, \mathrm{d}E\, \eta(A)\, \eta(\Omega)\, \mathrm{d}A\, \mathrm{d}\Omega \qquad \text{(A.10)}$$

The following conservative assumptions and values are considered to calculate a photon rate:

- The room temperature is assumed to be 300 K.
- Each efficiency is set to one: $\eta(\epsilon) = 1$, $\eta(A) = 1$, and $\eta(\Omega) = 1$.
- A fiber core of diameter 10 μm is assumed. This results in $\mathrm{d}A = 7.9 \cdot 10^{-11}$ m.
- A NA of 0.15 is assumed. This results in $\mathrm{d}\Omega = 0.07$ sr.
- An energy resolution of $\Delta E / E = 10\,\%$ is assumed. This results in $\sigma = 0.1 \cdot \epsilon$.

The folding integration over ϵ runs from 0.1 to 4.0 eV. This is sufficient for the integration of a 3σ-band around 1064 nm. The calculated[3] rates are listed in table A.1. These rates can be considered as the fundamental dark counts for 1064 nm resulting from a 300 K fiber end since the parameters are chosen conservatively. However, this simple model does not account for photons which couples from along the fiber inside the core (sect. 4.3.1). In addition, it is noticed that this consideration only holds for a single photon detector which has a zero time resolution or a infinite bandwidth. Otherwise, not resolvable pile-up events could be an additional effective source of dark counts.

1064 nm	band [eV]	band [nm]	$\tilde{N}_{(\frac{\Delta E}{E}=10\,\%)}$ [s^{-1}]	$\tilde{N}_{(\frac{\Delta E}{E}=0)}$ [s^{-1}]
1σ-region	1.048-1.282	1182-967	$1.0 \cdot 10^{-2}$	$1.3 \cdot 10^{-4}$
2σ-region	0.932-1.398	1330-886	$3.1 \cdot 10^{-1}$	$9.1 \cdot 10^{-3}$
3σ-region	0.816-1.515	1520-818	$1.0 \cdot 10^{+1}$	$6.4 \cdot 10^{-1}$
half 3σ-region	1.165-1.515	1064-818	$3.4 \cdot 10^{-4}$	$1.7 \cdot 10^{-6}$

Table A.1.: Dark count rates for 1064 nm photons resulting from a warm fiber end: Rates for a fiber-coupled TES detector with an energy resolution of 10 % are compared to a perfect detector with a zero energy resolution. The half 3σ-region only includes the high-energetic half of events (sect. 4.2.5).

---

[3]The calculation was done with the integration routine `scipy.integrate.quad` from the Python module SciPy.

B. TES working point and photon pulse fit

B.1. Selecting a TES working point

In a series of measurements with the ALPS TES detector (sect. 3.4), different TES working points were studied. Therefore, a 1064 nm photon single photon source was attached to channel A of the NIST module. Using a histogram mode of the oscilloscope DPO7104C, which is similar to the PHA method (sect. 4.2.1), pulse height histograms were analyzed. The trigger level was set within the falling slope of noise events in order to get a comparable signal rate. An example for a 30 % R_N is depicted in figure B.2a.

Assuming and fitting a Gaussian distribution to the signal peak, the signal mean value μ and the energy resolution for 1064 nm signals $\Delta E/E = \sigma/\mu$ is determined from histograms (fig. B.2a). By fitting an exponential rise to the noise distribution $N(V)$, a signal-to-noise quantity is determined together with the signal distribution $S(V)$. Here, as figure of merit, the signal-to-noise is arbitrarily defined by a 3σ cut:

$$\text{"S/N"} = \frac{\sum_{V_i=-\infty}^{\mu+3\sigma} S(V_i)}{\int_{-0.1}^{\mu+3\sigma} N(V)\,dV}$$

These quantities are determined for different TES working points between 10 % and 50 % R_N. The results are depicted in figure B.2b. μ shows a nearly linear trend of smaller peak heights in absolute values at higher working points. The signal-to-noise value is high and stable between 10 and 30 % R_N, before it is decreasing. The energy resolution scatters between 7.0 to 8.5 %. For the photon analysis in this thesis (chap. 4), a working point of 30 % R_N is chosen (sect. 3.4).
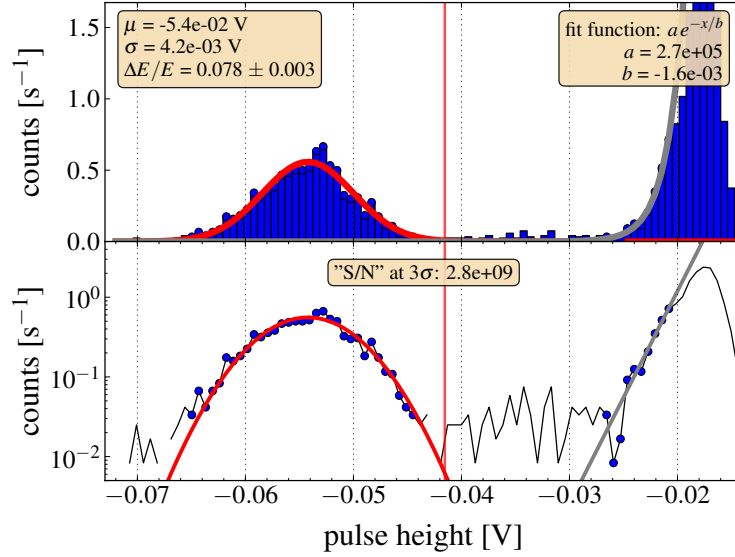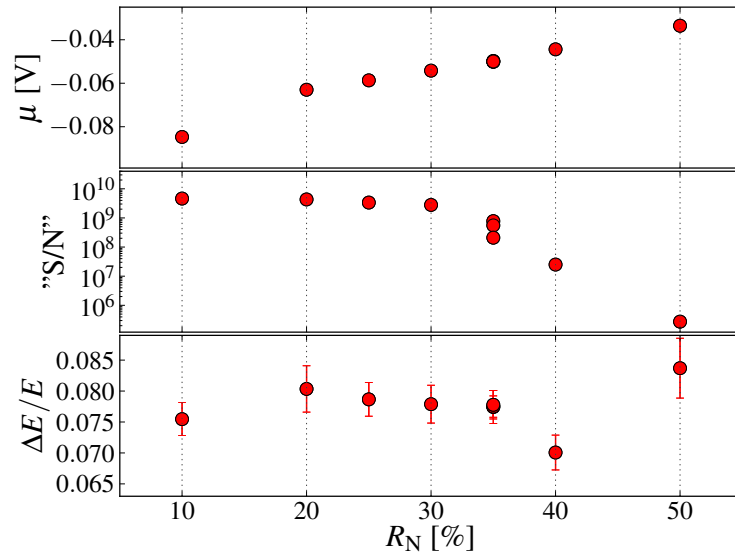
(a) histogram

(b) comparison of working points

Figure B.1.: Selecting a TES working point: (a) shows an analysis of a histogram recorded by an oscilloscope. (b) depicts the comparison of different TES working points. The mean pulse height, a signal-to-noise ratio in arbitrary units, and the energy resolution or 1064 nm signals are considered.

(a) 4 parameter fit   **(b)** additional time constant

Figure B.2.: Fitting the average pulse: (a) shows a 4 parameter fit (eqn. B.1) to the average pulse. The results are given in the boxes. The lower plot shows the normed residuals of the fit related to the average pulse. (b) shows a 5 parameter fit by adding a second negative time constant t_{m2} to the fit function (eqn. B.2). This fit describes the pulse better. It is $\chi^2_{red.}$.

B.2. Fitting an average pulse

In section 3.2.2.4, the average signal pulse measured by the ALPS TES detector is well described by theory using determined TES parameters. In this appendix, fitting the average pulse is discussed. The average signal pulse is fitted to two different functions and compared.

The first function is a simplified version of the signal response from theory (eqn. 3.25):

$$V(t) = a \left(e^{-(t-t_0)/t_p} - e^{-(t-t_0)/t_m} \right) \tag{B.1}$$

The second function is extended by an additional negative exponential term including a second negative time constant t_{m2}:

$$V(t) = a \left(e^{-(t-t_0)/t_p} - e^{-(t-t_0)/t_m} - e^{-(t-t_0)/t_{m2}} \right) \tag{B.2}$$

To evaluate the fit, the reduced chi-squared is calculated with $\chi^2_{red.} = \sum \delta_i^2 / \nu$, where ν is the degree of freedom[1]. The normed residuals are calculated with $\delta_i = (V_{fit_i} - V_{avg_i})/\sigma_{avg}$, where σ_{avg} is defined as the standard deviation of the data points of the first $4\,\mu$s which represents the baseline noise.

In figure B.2a, the result is depicted by using equation B.1. The pulse height of the fit shows a small deviation of <1 % to the pulse height of the average pulse. The integral of the fitted pulse is ~8 % lower than the integral of the average pulse. This

---

[1]The degree of freedom is defined as the difference of data points N and free parameters n of the fit, which is here $\nu = N - n = 300 - 4 = 296$.

B. TES working point and photon pulse fit

is explained by as follows. Firstly, since the fit start is the trigger time $t = 0$ μs, the content of the rising edge before the trigger is not included. Secondly, the fit deviates from the average pulse, which is illustrated by the normed residuals δ_i for each point (B.2a). The fit results in $\chi^2_{\text{red.}} = 6.5$.

Using equation B.2 results in figure B.2b. The falling slope as well as the points around the peak are better described by the fit. The residuals are smaller, which reduces chi-squared to $\chi^2_{\text{red.}} = 2.0$. This is presumably caused by the real thermal system of the TES, which slightly deviates from the small-signal theory.

C. Components of the ALPS TES detector

In this appendix, further components of the ALPS TES detector are described. ALPS TES detector components, which are described in previous sections and in the following, are:

- ADR cryostat system (sect. 2.2)
- Sensor modules (sect. 3.2.1, 3.2.3.1 and 3.2.3.2)
- Detector bench and bucking coil (app. C.1)
- Thermal and magnetic shielding (app. C.2)
- Electrical wiring for sensor modules inside the ADR (app. C.3)
- Fiber optics (app. C.4)
- Measurement electronics (app. C.5)

C.1. Detector bench and bucking coil

In order to attach sensor modules to the cold finger of the FAA-stage, a detector bench was manufactured.[1] A bucking coil can be attached to compensate background magnetic fields at the location of the sensors (sect. D.3.1.2).

The pieces of the detector bench and sensor modules (fig. C.1) are made of the standard copper alloy Cu-ETP[2]. After manufacturing, the pieces were aftertreated to improve thermal properties at low-temperatures: Firstly, they were tempered[3] to improve the heat conductivity at low-temperatures. Secondly, the pieces were electroplated to obtain a smooth surface in order to increase the thermal coupling. The detector bench is mounted to the cold finger of the FAA-stage. At the detector bench, sensor modules can be fixed by two screws. Basically, there is space for up to six sensor modules. The length was chosen that the upper sensor position is as far away as possible due to the experimental space in the inner 4K-chamber. At this location, the remnant ADR magnet fields are assumed to be small.

---

[1]A modular design from PTB was adopted.

[2]Cathode copper with the European norm CW004A, DIN1787, and the old abbreviation 'E-Cu'.

[3]Following the tempering recipe from PTB: 1.) Heat up with normal speed inside the vacuum oven to 750 Celsius. 2.) 10 hours tempering at this temperature. 3.) Switch off oven and leave closed for cooling down.
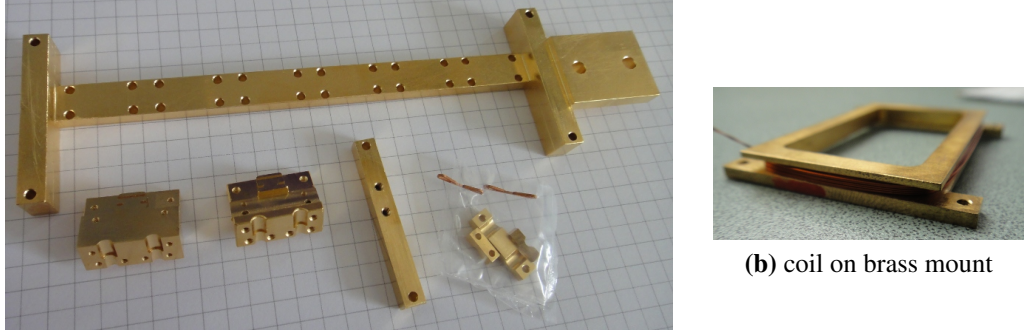
(a) detector bench and pieces for sensor module

(b) coil on brass mount

Figure C.1.: Completed detector bench and bucking coil: (a) Tempered and electroplated copper pieces: detector bench with six locations for sensor modules (top), pieces for NIST sensor module, and bar for coil (from left to right). (b) magnetic coil: coiled superconducting wire around the brass mount.

The bucking coil mount is made of brass. The coil itself is made of a superconducting wire: NbTi (Cu)[4]. A copper matrix for sufficient thermal conductance surrounds niob/titanium lines for electrical conductance. The coil has about $n \approx 100$ turns and a length of about 50 mm and width of about 31 mm. The formula for a short cylindrical coil is

$$|B| = \mu_{\mathrm{r}}\mu_0 \frac{nI}{2R} \approx I\,[\mathrm{mA}] \times 3.14\,\mu\mathrm{T} \tag{C.1}$$

where the relative magnetic permeability is $\mu_{\mathrm{r}} \approx 1$.[5] Furthermore, it is estimated an effective radius $R \approx 20$ mm. At the end of the coil, a 2 pin connector is soldered for electrical connection (sect. C.3). A resistance of about $R = 6.1\,\Omega$ is measured in the warm.

Using the magnetometer, the bucking coil was characterized. Appying a current, I_{buck} results in an inverse mutual inductance of $M_{\mathrm{buck}}^{-1} = 1.12\,\mathrm{mA}/\Phi_0$. Thus, the coil inductance is: $L_{\mathrm{buck}} = 1/M_{\mathrm{buck}}^{-1} = 1.8\,\mathrm{pH}$. With the design parameter $2\,\mu\mathrm{T}/\phi_0$ of the magnetometer, the maximum magnetic flux density at the sensor location is: $|B| = I_{\mathrm{max}} \frac{2\,\mu\mathrm{T}/\phi_0}{M_{\mathrm{buck}}^{-1}} = 44.6\,\mu\mathrm{T}$, where $|I_{\mathrm{max}}| = 25$ mA due to the current source of the SQUID electronics. Calculating the theoretical value by using formula C.1, it results in a maximum magnetic flux density of $|B| = 78.5\,\mu\mathrm{T}$. The deflection can be caused by the assumption for a short coil, the uncertainty of the real number of turns, n, or the non-central SQUID chip position within the plane of the bucking coil. The use of the coil is explained in section D.3.1.2.

---

[4]From the company California Fine Wire: www.calfinewire.com

[5]The wire of the coil is a NbTi wire in a 48% Cu Matrix with a diameter of 200 μm. With the magnetic susceptibilies of the materials $\chi_{\mathrm{m_{Cu}}} = -5.46 \times 10^{-9}$, $\chi_{\mathrm{m_{Nb}}} = 195 \times 10^{-9}$ and $\chi_{\mathrm{m_{Ti}}} = 153 \times 10^{-9}$ it is assumed $\mu_{\mathrm{r}} = \chi_{\mathrm{m_{tot}}} \approx 1$.
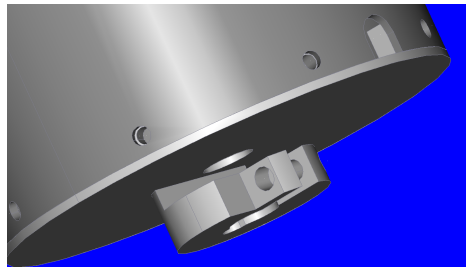
(a) sketch of base with mount

(b) manufactured pieces
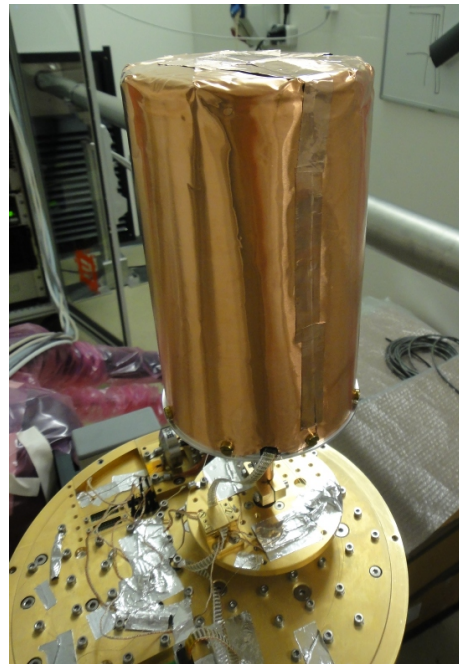
(c) copper shield

Figure C.2.: Aluminum and copper shield: (a) Zoom to the bottom of the aluminum shield with mount to the FAA extension. (b) Picture of manufactured aluminum shield made of AlMg3. The cup has a height of 170 mm, diameter of 110 mm, and a thickness of 2 mm. A 10 mm gap provides a feed out of the cabling and fibers. (c) Shield made of thin copper sheet and copper tape, mounted to the aluminum base plate and fixed to the FAA extension [(a) taken from R. Stromhagen]

C.2. Thermal and magnetic shielding

Different shields were manufactured and tested: shields made of copper and shields made of aluminum. The copper shield acts as a thermal shield. The aluminum shield acts as thermal and magnetic shield if it is operated below the critical temperature of aluminum T_c = 1.14 K. A thermal shield surrounding the sensors and coupled to the base temperature is necessary to screen thermal radiation from the 4K-stage (sect. 3.3.3). A magnetic shield screens external magnetic influences which could affect sensitive SQUID sensors. A magnetic shield can be established by using a superconducting material (Claycomb and Miller, 1999): A superconducting shield in a tube or cup shape defines a screening factor along the center of the tube, which depends only on the ratio of length to tube radius. Three kinds of shields were realized and tested:

- By using commercial aluminum foil, an enclosed volume was manufactured which surrounds the sensors. The self-made shield was fixed by wires to the FAA-stage. One disadvantage is the non-reusability.

Aluminum foil shielding was used in PTB DR cryostat, and in the ADR cryostat for several tests. In the DR cryostat the SQUID performance was unrestricted. In the ADR, a foil shield results in a defined orientation: By turning the ADR, only in a certain range of the SQUID orientation, defluxing is possible if the shield is superconducting. It seems that the shield freezes the ambient field including the earth field. Probably due to the foil geometry, the field is squeezed so that the local magnetic flux is larger than the tolerable field of the sensor, B^* (sect. 3.3.2).

- A massive aluminum shield was manufactured which is stable, reusable, and easily to install (fig. C.2). It incorporates a one-piece base plate which can be fixed to the FAA extension rod, and a one-piece cup. This provides a better flow of a superconducting shielding current (sect. 3.1.1). One disadvantage is the cold mass.

  By using this shield in the ALPS TES detector, it was indicated that this shield is inappropriate in the current ADR setup. The temperature of uncoupled and charged pills corresponds to a magnetic field. Thus, a corresponding stray field of the ADR magnet is freezed when the critical temperature of aluminum, $T_c = 1.14$ K, is surpassed. In a regular recharge, the corresponding magnet current is ∼12 A when the aluminum shield becomes superconducting. At a bath temperature of the 4K-stage, it was indicated that magnetic fields above a corresponding current of ∼5 A affect the SQUID modulation, which is associated with B^* (sect. 3.3.2). Therefore, the shield is inappropriate.[6]

- By using a copper sheet, a thermal shield was manufactured (fig. C.2). The copper cup fits to the aluminum base plate.

However, it is indicated that magnetically unshielded sensor modules shows an adequate and unrestricted performance in the ADR and ALPS IIa laboratory (sect. 3.3.2).

---

[6]Only if the pill has less charged energy, resulting in a corresponding magnet current of <5 A when passing Al T_c, the SQUID can be properly defluxed. However, this results in short mK-times. Possible options for future tests using a magnetic shielding are:

- Using a warm magnetic shield around the ADR dewar, for example, a mu- metal ton.
- Superconducting shield with lower T_c due to the material.
- Heat out or deflux option for the massive Al shield including less Joule heating.
- Active bucking coil with less Joule heating when using the massive Al shield.

C.3. Electrical wiring for sensors modules inside the ADR

In this section, the electrical wiring for sensors is described. Sensors are operated by a suitable electronics from Magnicon GmbH (sect. C.5.1). The wiring from the electronics to the sensor modules equipped with two channels of SQUIDs and TESs is considered. In figure C.3, a circuit scheme is shown including the used 2-stage SQUIDs, the TES circuit, and electronic bias sources.

In the following, the cabling between the ADR top flange, where the electronics is connected, and the sensors is described (illustrated in fig. C.4):

- cryocable from Magnicon
- 4K-connection from Entropy
- Micro-D cable from Entropy for the sensors and a twisted pair for the coil
- Micro-D socket on PCB with bonding wires to SQUID and the coil itself

All parts include a screening of the wires: This is realized by stainless steel braids from 300 K to the 4K-stage and by superconducting wires from the 4K-stage to the sensors.

The **cryocable from Magnicon**[7] incorporates a vacuum tight flange and three EMI shielded and 120 cm long strands. The flange has a 24 pin LEMO socket for the electronics (fig. C.5a) and a 9 pin LEMO connector is at each strand end. Two strands include two channels to operate a TES with SQUID read-out, each with 9 wires of Alloy30 (fig. C.5b). The third strand is for the current supply of the bucking coil with 2 wires of Alloy30 (fig. C.5c).

The **4K-connection** is a PCB connector interface:[8] Two 9 pin LEMO sockets[9] are connected to a 25 pin Micro-D socket. The 4K-PCB is the interface between the cryocable and the sensor module which is equipped with a Micro-D connector. Near the 4K-PCB, a 9 pin LEMO socket is placed which connects the third strand of the cryocable to the bucking coil.

From the 4K-connection, **two cables** connect the sensor module and the bucking coil (fig. C.7e). The connection between the 4K-PCB and the sensor module is a 50 cm long ribbon cable with 2x12 NbTi/CuNi twisted pair wires and two 25 pin Micro-D connectors[10]. The connection between the 9 pin LEMO socket and the bucking coil is a twisted pair cable of NbTi/CuNi wires[11] with a 9 pin LEMO connector and a 2 pin connector.[12]

---

[7]The serial number is CC0035 (Magnicon, 2010).
[8]The cryocable and the 4K-PCB are installed in the ADR as a permanent installation (fig. C.7).
[9]LEMO EYG.0B.309
[10]For one line, a resistance of about 44 Ω is measured in the warm.
[11]0.06 mm diameter
[12]For one line, a resistance of about 17 Ω is measured in the warm.
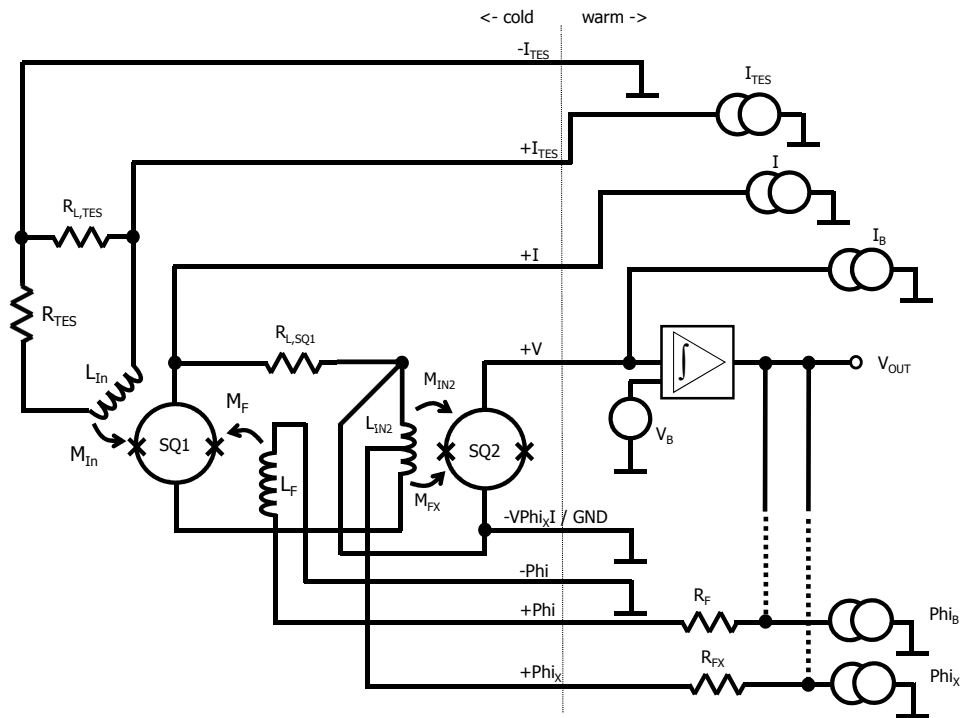
Figure C.3.: Circuit scheme for sensor modules: On the left "cold" side, the circuit scheme of the 2-stage SQUID and TES circuit is shown. On the right "warm" side, the scheme of the bias sources integrated in the SQUID electronics is depicted (sect. C.5.1). [Taken from PTB]

The connection scheme of a sensor module including a Micro-D25 socket, copper tracks on the PCB, and aluminum bond wires to sensor chips is depicted in figure C.6. In table C.1 the complete pin assignment of a **sensor module** and the **bucking coil** inside the ADR is summarized (fig. C.6d). Total resistances of the lines in the warm are given in section D.1.2.2.
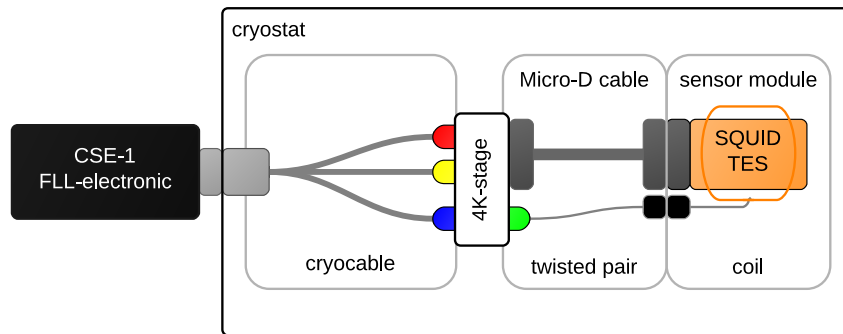
Figure C.4.: Wiring of sensor modules inside the ADR: At the ADR top flange, the SQUID FLL-electronics is connected. Inside the cryostat, the so-called cryocable connects the electronics to the 4K-connection by 3 strands (red for channel 1, yellow for channel 2, and blue for the bucking coil). The 4K-connection placed at the 4K-stage is a PCB interface with LEMO to Micro-D. A Micro-D cable connects the PCB interface and the sensor module equipped with a Micro-D socket. In addition, a simple twisted pair cable supplies the bucking coil current.

(a) socket at top of ADR

(b) Channel 1/2
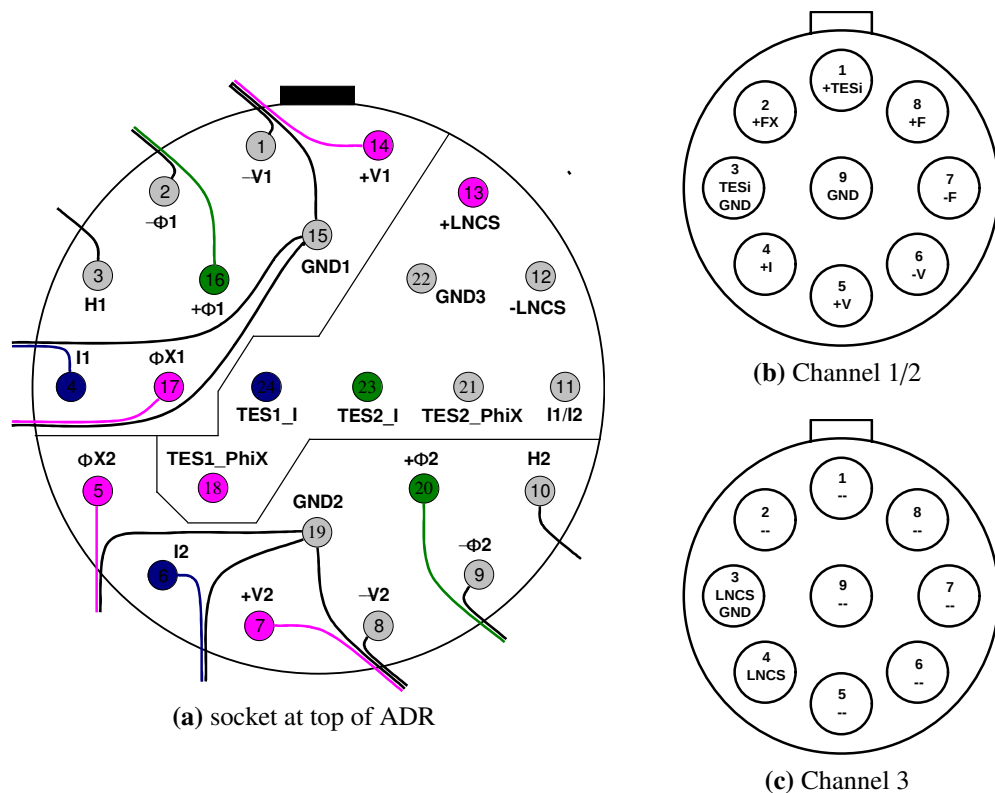
(c) Channel 3

Figure C.5.: Pin assignment of the cryocable:(a) illustrates the assignment of the 24 pin LEMO socket of the cryocable top flange. (b) illustrates a LEMO 9 pin connector at the strand end of the cryocable for one sensor channel. (c) illustrates a LEMO 9 pin connector for the coil. [Adopted from Magnicon]

179

(a) Sensor module with PCB for Micro-D

(c) TES and SQUID bonds

(b) Pin assignment of Micro-D socket

(d) SQUID chip 6X114HW
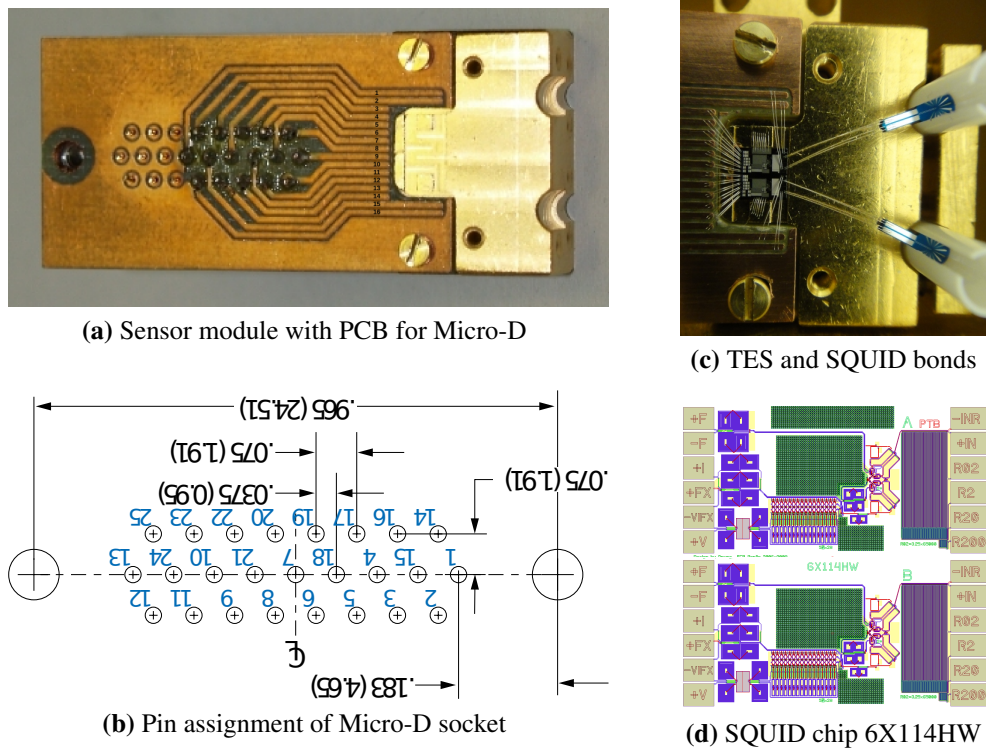
Figure C.6.: Pin assignment of the sensor module: (a) sensor module with circuit board: A Micro-D25 connector is soldered to copper tracks on the PCB. (b) pin assignment of the Micro-D25 connector in the same orientation to (a). (c) aluminum wire bonds from copper tracks to chip. (d) sketch of the 2-stage SQUID chip incorporating two channels: On the left and right side the bond pads are located. The connection scheme is given in table C.1. The 16 copper tracks are numbered from 1-16 from top to down in the orientation of (a) and (c). [(a), (d) PTB / (b) Glenair]
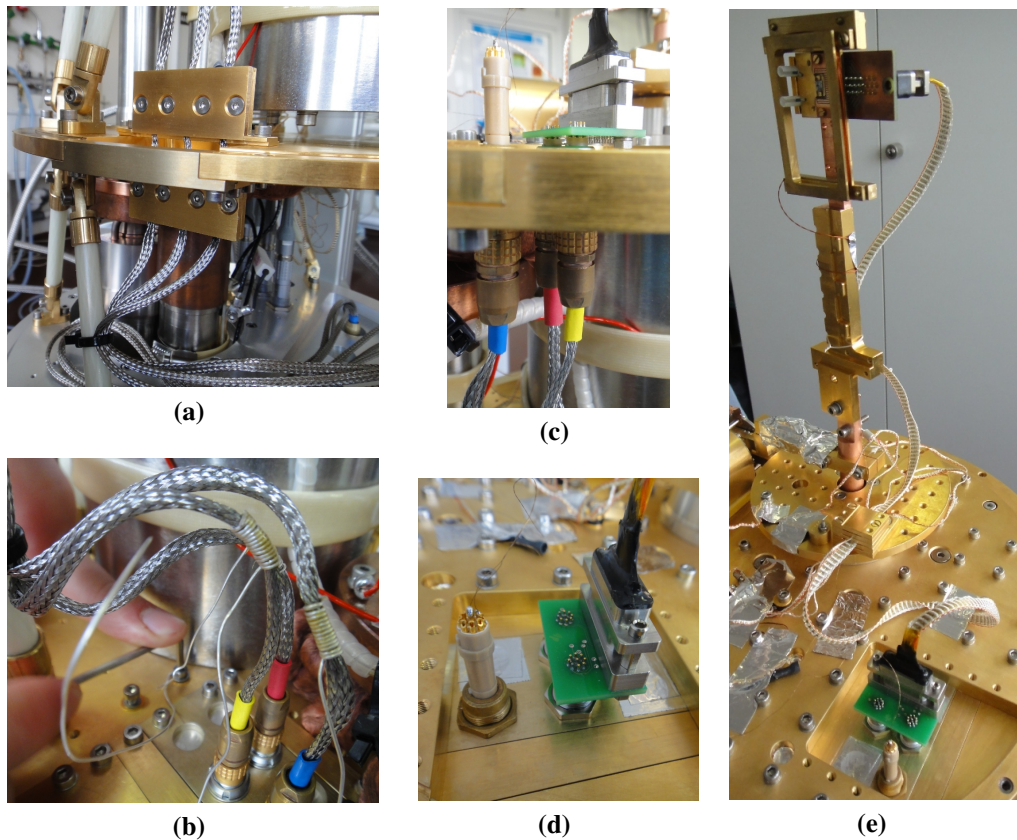
Figure C.7.: Pictures of sensor module wiring inside the ADR: (a) The cryocable is fixed and thermally coupled at the 77K-stage with copper clamps. (b) 4K-PCB at the 4K-stage with connected strands of the cryocable: channel 1 (red), channel 2 (yellow) and LNCS (blue). Each steel braid is thermally coupled with silver wires attached to the 4K-stage. (c) Side view of the 4K-connection: Channel 1/2 is connected to the Micro-D-cable and the LEMO to the twisted pair for the coil. (d) Top side of installed 4K-PCB. (e) Micro-D cable to the sensor module and twisted pair cable to the bucking coil which are both attached to the detector bench.

name	LEMO24	ch.	LEMO9	MD25	PCB	ch.	6X114HW	TES
$+\phi2$	20	2	8	1	9	B	+F	
$-\phi2$	9	2	7	2	10	B	-F	
I2	6	2	4	3	11	B	+I	
ϕX2	5	2	2	4	12	B	+FX	
-V2	8	2	6,9	5	13	B	-VIFX	
+V2	7	2	5	6	14	B	+V	
TES2_I	23	2	1	7	15	B	R20	*in*
GND3	22	2	3	8	16	B	-INR	
							+IN	*out*
+V1	14	1	5	14	8	A	+V	
-V1	1	1	6,9	15	7	A	-VIFX	
ϕX1	17	1	2	16	6	A	+FX	
I1	4	1	4	17	5	A	+I	
$-\phi1$	2	1	7	18	4	A	-F	
$+\phi1$	16	1	8	19	3	A	+F	
TES1_I	24	1	1	20	2	A	R20	*in*
GND3	22	1	3	21	1	A	-INR	
							+IN	*out*
name	LEMO24	ch.	LEMO9					coil
+LNCS	13	3	4					*in*
-LNCS	12	3	3					*out*

Table C.1.: Pin assignment of sensor modules and bucking coil: pin assignment from the SQUID electronics at the ADR top flange to the sensor module and the bucking coil in the cold. The left part till the first double line gives the connection scheme of the cryocable ends (fig. C.5) and the next part is the connection scheme of the sensor module (fig. C.6). The last column gives bond connections between the SQUID and TES chip and connections to the coil.
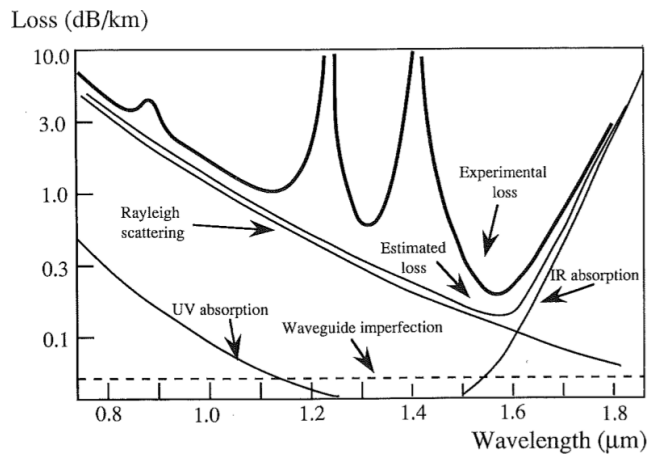
(a) loss spectrum

(b) vacuum feedthrough

Figure C.8.: Fiber loss spectrum and fiber vacuum feedthrough: (a) illustrates the loss spectrum of SiO_2 fibers. The loss in dB/km is plotted against the photon wavelength. Two fundamental attenuation mechanisms mainly define the transmittance: the intrinsic Rayleigh scattering causes attenuation for shorter wavelengths, the IR absorption is caused by molecular vibrations. [Taken from Midwinter and Guo (1992)] (b) Vacuum feedthrough for two fibers surrounded by a quite light-tight black box, here open at the front side. Swagelok connectors with a Teflon gasket provide the vacuum tight fiber feedthrough (see text).

C.4. Fiber optics

This section describes:

- fiber types used in this work (sect. C.4.1)
- fiber vacuum feedthrough (sect. C.4.2)
- fiber setups for long-term measurement (sect. C.4.3)
- optical coupling to ALPS IIa experiment (sect. C.4.4)

The fiber installation inside the ADR is described in app. D.1.2.3.

C.4.1. Fiber type

The optical setup of the ALPS TES detector utilizes SMF28 fibers. SMF28 fibers are made of glass based on silica and work as single mode fibers for near-infrared wavelengths. It is the standard fiber in telecommunications. 1310 nm and 1550 nm wavelengths are used due to low losses. The fiber has a certain wavelength-dependent bandwidth due to the glass material SiO_2. The loss spectrum and fundamental attenuation mechanisms are illustrated in figure C.8a. The numerical aperture is N.A. = 0.14 and the fiber core diameter is 8.2 μm. Using a SMF28 for 1064 nm results in the following properties:

- The attenuation is ~1 dB/km, which is negligibe for 1-10 m long fibers, as used in the ALPS TES detector.
- SMF28 is not a pure single mode fiber because the single mode field diameter of 1064 nm is 6.2 μm. However, this is irrelevant for TES operation.

C.4.2. Fiber vacuum feedthrough

A vacuum feedthrough was manufactured within this thesis. Up to two fibers can feed out the ADR vacuum dewar what matches the two channels of a sensor module. The vacuum tight realization is done by commercial screw fittings and self-made Teflon gaskets with a 250 μm hole fitting the fiber diameter (Abraham and Cornell, 1998). The two feedthroughs are surrounded by a quite light-tight box to diminish stray light to the fiber outside the ADR. Additionally, the box is equipped with two FC couplers to extend the fiber or connect fiber-coupled laser sources. The whole box is mounted to a free KF40 port of the ADR vacuum dewar (fig. C.8b).

C.4.3. Fiber setups for long-term measurement

For long-term measurements, in order to study the dark count rate of fiber-coupled NIST module, three setups are considered (sect. 4). The detailed fiber setups are:

- **Setup 1**: The warm fiber end was inside the cryostat at the outside of the 70K-stage (fig. 4.1b). 80 cm of the fiber were in the 300K-room.

  Details: The fiber is 190 cm long in total, 80 cm are in the 300K-room fixed outside of the 70K-stage, at the end is an FCA connector. This fiber setup includes two splices at 80 cm and 145 cm measured from the coupler at the 70K-stage. The splice protector of the first splice is clamped at the 4K-feedthrough. Thus, 110 cm are in the 4K-room or mK-room.

- **Setup 2**: The warm fiber end is inside the cryostat at the 300 K top flange (fig. 4.1b). 157 cm of the fiber are in the 300K-room.

  Details: The fiber is 250 cm long in total, 157 cm are in the 300K-room of the ADR and ~110 cm are coiled and fixed at the inside top flange. The warm end is simply cut and has no fiber connector. The fiber setup includes two splices each with a 4 cm long plastic protector. They are located at 157 cm and 216 cm measured from the cut end. The protector of the first splice is clamped at the 4K-feedthrough. Thus, 93 cm are in the 4K-room and mK-room, which are coiled and thermally fixed to the mK-shield.

- **Setup 3**: The warm fiber end is feed outside the ADR and stored in the black box (standard configuration in fig. 4.1a). 220 cm of the fiber are in the 300 K environment.

  Details: The inner fiber of setup 2 is extended with a 150 cm long fiber with FCA connectors at each end. It is connected to the connector at the outside of

the 70K-stage, the warm end is connected inside the black box. 80 cm of this fiber extension are in the 300K-room of the ADR, the remaining part of 70 cm in the black box outside the ADR. A splice with a 4 cm long splice protector is ~36 cm away, measured from the coupler at the 70K-stage. Thus, the overall length from the connector at the black box to the TES is here 340 cm, with 220 cm in the 300 K environment. For the FCA connection at the 70K-stage, a coupling efficiency of (60 ± 8) % for 1064 nm is estimated by measuring the power with a power meter in the warm.

C.4.4. Coupling to the experiment or test signal

The signal of ALPS IIa will be coupled to the detector through the planar inner end mirror of the regeneration cavity (Bähre et al., 2013). At this position, the ALPS beam waist[13] is about $w_0 = 4$ mm. Within the ALPS collaboration, free space to fiber coupling has been tested in a separate optical setup. An efficiency of about 83 % has been reached (Ghazaryan, 2013).

C.5. Measurement electronics

In the following, electronics are briefly described which were used for measurements within this thesis:

- SQUID electronics to operate SQUID and TES devices (sect. C.5.1)
- measurement electronics to digitize the analog signal from the SQUID electronics (sect. C.5.2)

C.5.1. SQUID electronics

To operate SQUIDs, a SQUID electronics from Magnicon GmbH was purchased.[14] The system incorporates different components including the FLL[15] electronics which is attached to the ADR top flange. The FLL electronics incorporates low-noise current sources in order to operate 2-stage SQUIDs connected to TESs (two channels):

- I_B, V_B and *Phi*$_B$ for the 2nd stage SQUID array (SQ2)
- I and *Phi*$_X$ for the front-end single SQUID (SQ1)
- I_{TES} for the TES

For each current source, a generator signal can be applied. In addition, a low-noise current source to operate the bucking coil is integrated. The electronics provides a maximum FLL bandwidth of about 20 MHz. The analog output signal[16] has a

---

[13]Radius of a Gaussian beam where power drops to $1/e$.
[14]Magnicon develops SQUID systems in a license agreement together with PTB-Berlin.
[15]flux-locked loop
[16]V_{OUT} in figure C.3.

voltage range of ±10 V. The electronics can be computer-controlled via an optically isolated RS-232 interface. Using the "SQUID Viewer" software, bias sources are adjusted (Magnicon, 2011).

C.5.2. Data Acquisition

For the measurements in the ALPS IIa laboratory, an oscilloscope and spectrum analyzer were used to digitize the voltage output of the SQUID electronics:

- An oscilloscope DPO7104C from Tektronix was used to characterize TESs and SQUIDs to acquire TES signals in photon measurements (sect. 4).

- Using fast fourier transform (FFT) spectrum analyzers 89410A DC-10 MHz and 35670A DC-102.4 kHz from Agilent Technologies,[17] spectra of sensor modules were digitized (sect. 3.2.2.5). By observing the spectrum online, the electro-magnetic environment was optimized (sect. 3.3).

---

[17]The spectrum analyzers were borrowed from PTB-Berlin to compare measurements between Berlin and Hamburg.

D. Installation and operation manual of the ALPS TES detector

This appendix presents a kind of manual to set up components and operate them as the ALPS TES detector. It is written in chronological installation and operation order. Here, laboratory experience is collected including the support of Entropy GmbH, PTB, and IQOQI. This appendix is divided into three sections:

- In section D.1, required installations before a cool-down are explained.
- In section D.2, the operation of the ADR cryostat is described to establish mK-environment: cool-down to 4 K, a recharge cycle, holding mK-temperature, and stopping the ADR.
- Section D.3 describes the operation, functionality tests, and the adjustment of the sensor module in order to use the whole setup as a single photon detector.

D.1. Installations before cooling down

The installations in the warm are split up in three sections:

- Firstly, the ADR system is set up (sect. D.1.1).
- Secondly, sensor modules, shields, and fibers are integrated into the ADR (sect. D.1.2).
- Thirdly, read-out and DAQ electronics are set up (sect. D.1.3).

D.1.1. Installation of the ADR system

To operate an ADR cryostat, three steps of preparations in the warm are basically required:

- installation and connection of the ADR components (sect. D.1.1.1)
- adjustment of the pills and the heat switch unit (sect. D.1.1.3)
- connection and check the ADR electronics (sect. D.1.1.2)

D.1.1.1. Hardware installation

Since the ADR cryostat system has to be moved in the future of ALPS, the basic installation of the ADR system is described. If the ADR system is to be moved, it

Figure D.1.: Exemplary setup of ADR system at PTB-Berlin: Compact view of the whole installation of the ADR system including three main components: Left, the red dewar with top flange placed in a trolley. In the back, the ADR rack with electronics and the ADR computer. Right on the bottom close to the basin, the compressor connected to water and heavy current. The compressor and the ADR are connected by thick silver flexlines filled with Helium. Most of the 20 m long flexlines are stored in the brown cardborads.

is recommended to contact Entropy GmbH for support (Entropy, 2012, p. 5). In figure D.1, the installed system at PTB-Berlin is exemplary depicted.

Firstly, proper locations for the three main components, compressor, cryostat, and electronic rack, are needed. The location of the compressor is constrained to its external supplies: cooling water and heavy power supply. An admissible quality and flux of the cooling water are required (SHI, 2008). Furthermore, the compressor emits a loud noise in operation due to 1.3 Hz alternating pump. It is recommended to place the compressor as far as possible away from the ADR dewar. A separate room for working comfort or a different platform to prohibit vibrational effects could help.

The maximum distance between the rotary valve of the cryocooler at the ADR dewar and the compressor is 20 m due to the Helium flexlines and one electrical connection. If the ADR trolley is located less than 20 m away from the compressor, it is necessary to find space for the remnant parts. It is uncritical to roll up the lines with a radius not smaller than 0.5 m. A vertical installation is also possible as done at the installation at ALPS IIa.

Close to the ADR trolley, space is needed for the electronic rack within a radius of 5 m due to the cabling. Close to the ADR, space is also needed for the DAQ,
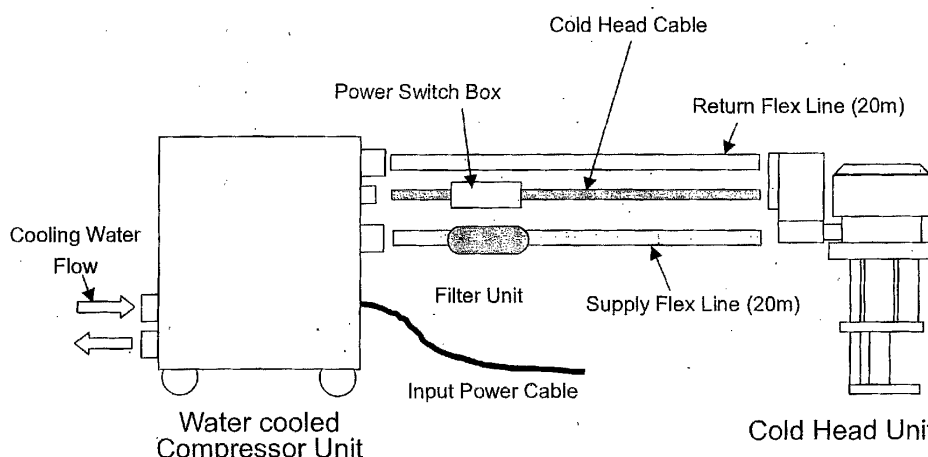
Figure D.2.: Sketch of components and connections of the precooling system: On the left, there are the connections for the water. The supply and return flexlines are connected to the rotary valve of the cold head unit where the 2-stage pulse tube cooler is attached to. A filter unit is installed at the beginning of the supply flexline. The cold head cable synchronizes the rotary valve. [Taken from SHI (2008)]

including the computer to operate the SQUID electronics. Furthermore, a vacuum pump or a leak detector should be connected to the ADR dewar during cooling down (sect. D.2.1).

Finally, the Helium cycle of the precooling system can be established by connecting the compressor unit, the filter unit, one short and two 20 m long flex lines (supply and return), the cold head unit with the rotary valve, and the cryocooler on top of the ADR (fig. D.2). Each component contains ~17 bar Helium gas and is equipped with special security valves which open when connecting. During the connection of the components, small amounts of Helium can escape. The supply barometer at the compressor should show ~17.2 bar if the cycle is closed. If Helium loss has occurred, Helium may be refilled at an inlet valve at the compressor. Helium 4 with 99.999 % purity is needed (SHI, 2008).

D.1.1.2. Electrical connections

The precooling system needs only two connections. The compressor has to be connected to a heavy power supply.[1] The cold head cable has to be connected between compressor and rotary valve (fig. D.2).

Inside the electronic rack, the hardware components of electronics are usually connected to the power supply and via suitable interfaces to the ADR computer.

---

[1]32 A. The installation must be carried out by an electrician. During the installation in ALPS IIa lab, it is indicated that the current is alternating clockwise at DESY. Furthermore, before connecting, it must be confirmed that the compressor is switched off!

The rack is connected to a conventional power supply to power all integrated components. From the rack to the ADR, the following cables are connected:

- one cable with LEMO 10pin for the magnet
- one cable with LEMO 2pin for the heat switch unit
- one Ethernet cable for the vaccuum gauge
- two cables each with LEMO 16pin for 2x4 channels for thermometry

Inside the ADR cryostat, the wiring of the thermometry, the magnet and the heat switch was established in Entropy's commissioning phase. After establishing the connection between the rack to the connectors at the ADR top flange, connections can be checked by the "Adiabatic Control" software:

- The magnet circuit is correctly connected if the software does not complain during start.
- The correct thermometry connection is checked by resistance measurement:

    - Channel 1, FAA: ~800 Ω
    - Channel 2, GGG: ~3.9 kΩ
    - Channel 3, 4K: ~80 Ω
    - Channel 4, 70K: ~1.0 kΩ
    - Channel 5 and 6, Touch GGG and FAA: due to the heat switch status between ~0.1 mΩ and `overrange` (sect. D.1.1.3).

- The pressure display should show 1000 mbar.
- The heat switch is working if it is possible to move the piezo actuator using the "Entropy Piezo Knob" software (sect. D.1.1.3).

D.1.1.3. Adjustment of salt pills and heat switch unit

The adjustment of the pills and heat switch is required if the pills unit has to be dismantled or if Vespel pins have to be tightened. The heat switch unit has to be removed to fix Vespel pins (fig. D.3a). Furthermore, if the heat switch unit does not work properly, a re-alignment of the heat switch units and bars will improve the performance.

Vespel pins should be tightly screwed in a moderate way that the pills are elastically moveable in a small range: When turning the GGG-stage around the axis of the cold finger (pills axis) slightly, after releasing, it should move back into the initial position (fig. D.3b). If this behaviour is not indicated, Vespel pins are presumably loose. To reach the Vespel pins, the heat switch unit, the bars, and the GGG copper plate have to be removed (fig. D.3a). To tighten the Vespel pins, three

(a) pills unit with Vespel pins

(b) movability

(c) alignment
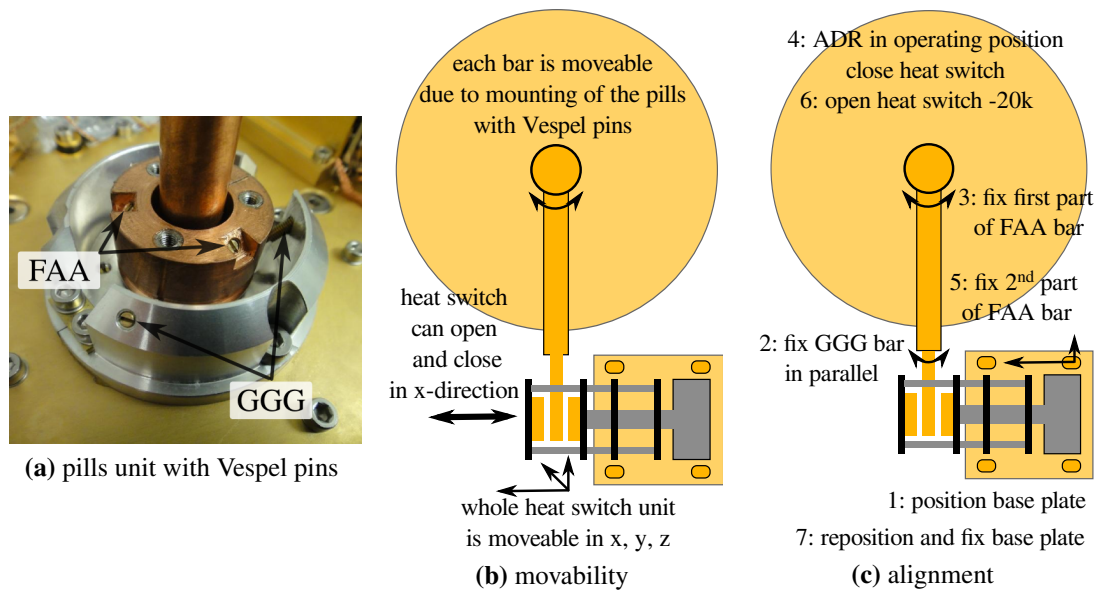
Figure D.3.: Adjustment of the heat switch: (a) shows the upper Vespel pins of the installed pills unit. Here, the bars to the heat switch and the GGG-stage are removed. (b) and (c) illustrate the heat switch unit (at bottom), the bars (orange rectangle), the GGG-stage (big orange circle), and the cold finger of FAA-stage (small orange circle) in a topview of the 4K-stage. (b) illustrates the movability of the whole unit. (c) describes the alignment in short.

pins at one side of GGG or FAA should be screwed carefully and symmetrically. Vespel pins should not to be too tight,[2] since mK-times are shortened (sect. 2.3.4).

In figure D.3b, the movability of the whole unit is illustrated; in figure 2.4, names of the heat switch units are given. During ADR operation, different forces act on the heat switch unit due to the degrees of freedom of the mechanics (fig. 2.9a). Together with Entropy GmbH, it turned out from experience of several alignments (app. E.3), that the following alignment procedure is successful to reach a satisfactory performance (fig. D.3c):

- **Coarse alignment 1:** Bring the ADR in mounting position. Open the heat switch (-20-30 k steps) and bring the heat switch base plate into its middle position, so that each of the 4 screws are in the middle of the corresponding boring of the plate. Leave the screws loosely. Fix the GGG bar, so that the coupling areas of the bar and the heat switch copper pads are in parallel (fig. 2.9a).

- **Coarse alignment 2:** Fix the first part of the FAA bar by the clamp around the cold finger; in parallel to the GGG bar. The second part should be mounted,

---

[2]A hint for the tightness of the Vespel mounting is the resistance in the warm between the components. Using a multimeter, between FAA and GGG a resistance of 11.5 kΩ and between GGG and 4K-stage a resistance of >1 MΩ is measured for the 4th alignment (app. E.3).

but with loose screws. Bring the ADR in operational position and close the heat switch tight (fig. 2.9b). Now, fix the FAA bar and the heat switch base plate. Tightening the 4 screws of the base plate should be done step by step to ensure that the base plate does not warp.

- **Fine alignment:** In mounting position, the heat switch should be opened by less than -20 k steps. If the heat switch does not symmetrically open or requires a lot more steps to open, the heat switch unit can be aligned by shifting the base plate. Closing the heat switch indicates asymmetrically decreasing touch values due to the inclination of the heat switch unit (fig. 2.9a). However, the values should show a symmetrical behaviour below ~2 mΩ till a closed condition.[3]

- **Fine tuning:** The significant test of the alignment is the performance in the cold: The reproducible and reliable movement of the heat switch during recharges indicates a successful alignment of pills bars and the heat switch unit (sect. 2.3.3.1). The time of thermalization of each pill indicates the coupling to the 4K-stage (sect. 2.3.3.2).

  If long thermalization times or moving problems occur, a slight shift of the base plate can dramatically improve the performance in the next cool-down.

Finally, it is summarized that a proper alignment of bars and heat switch unit in the warm should result in the following performance:

- parallelism of clamping FAA and GGG bar: parallel opening by eye, with the help of the touch measurements: symmetrical values below 2 mΩ when nearly closed

- opening in the warm: -20 k steps, closing: +25 k steps

- no increasing touch values (ΔR_{touch} <0.5 mΩ) during ramping up to 40 A

- no heating >11 K of FAA after reaching 40 A

- satisfactory thermalization time

- reproducibility (steps and thermalization) with a chance of success of >75 % for automatic recharges

D.1.2. Preparing the ADR with a sensor module

The installation of a sensor module is described. Exemplary, the NIST module is used (sect. 3.2.1).

The installations should be done with clean hands or even with gloves in order to avoid dirt which could worsen the vacuum performance. Regularly, it is recommended to clean pieces below the 4K-stage with isopropanol. It is indicated that for thermal coupling, the mechanical contact of clean copper surfaces with tighten

---

[3]If the heat switch reaches the closed condition, the buzzing sound will change, which indicates that the piezo-ceramic actuator cannot move the pads anymore.

screws is sufficient. Occasionally, cryogenic vacuum grease is used in between if cables are thermally coupled. Furthermore, aluminum tape is irreplaceable in the lab in order to fix and couple cables and fibers.

D.1.2.1. Mounting

The following components are mounted to the cold finger:

1. FAA extension rod with base plate of the mK-shield (sect. C.2):

   After mounting the FAA extension rod, the aluminum base plate of the shield is clamped (fig. D.4a). Here, a suitable height has to be chosen: The mK-shield should not touch the upper end of the detector bench and the 4K-shield.

2. Detector bench with mounted sensor module (sect. C.1 and sect. 3.2.1):

   Before mounting the detector bench, it is equipped with the sensor module. Therefore, the sensor module has to be handled with care in order not to break wire bonds or damage the SQUID chip by electrostatic discharge (ESD).[4] After screwing the sensor module to the bench, the supporting bar and the bucking coil are mounted. Finally, the detector bench is mounted to the FAA extension rod (fig. D.4a). Here, three hands are advantageous for holding and screwing.

D.1.2.2. Wiring

The wiring for sensors as a permanent ADR installation is described in appendix C.3. After mounting the detector bench with the sensor module to the FAA-stage, the Micro-D cable is connected to the sensor module and the twisted pair cable to the bucking coil. By connecting the sensor module, the sensor is grounded to the ADR.[5]

If everything is properly connected, the following resistances in the warm should be measured at the top flange of the cryocable. Figure C.5a illustrates the pin assignment and figure C.3 explains the notations:

- -V/GND: ~4 Ω (only cryocable, because short)
- +V/-V, +V/GND: ~0.6 kΩ (SQUID array SQ2)
- +Φ/−Φ: ~170 Ω (feedback coil L_F)
- I/GND: ~170 Ω (load resistor of single SQUID $R_{L,SQ1}$)
- +ΦX/GND: ~170 Ω (half of coupling coil to SQ2 L_{IN2})
- TES1_I/GND3, TES2_I/GND3: ~120 Ω ($R_{L,TES}$ of TES circuit)
- +LNCS/-LNCS: ~80 Ω (compensating coil)

---

[4]The experimenter should be optimally grounded with ESD-safe shoes or wristband. If these are not available, wearing socks and touching for example the ADR copper stage as electrical grounding also provide a safe condition.

[5]ESD-safety of the experimenter is no longer important.
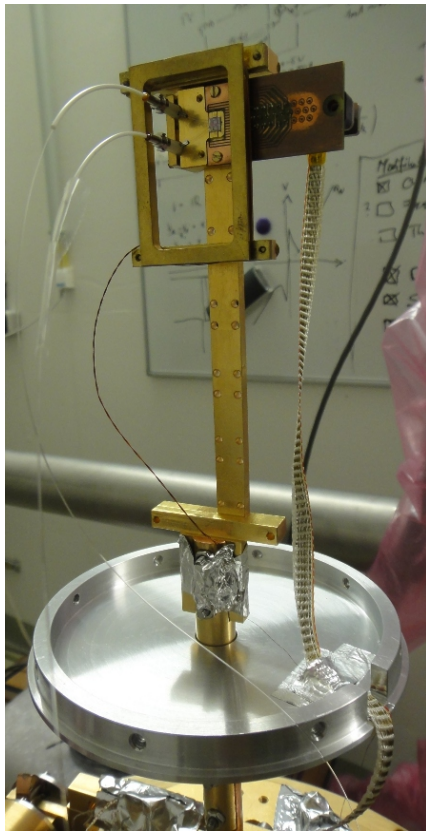
(a) cold finger installations
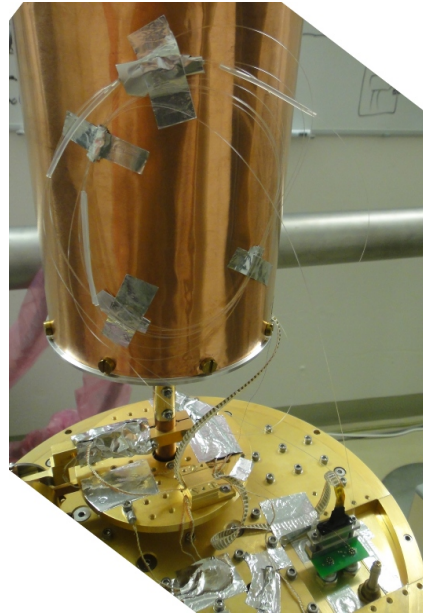
(b) anchored fibers to mK-stage

Figure D.4.: Sensor installations: (a) shows the installations to the FAA cold finger: extension rod with aluminum base plate for the mK-shield and detector bench with mounted sensor module and bucking coil. All cables are connected and are thermally fixed cables. Fibers are already attached to the TES. (b) Thermal coupling of fibers by taping them to the mK-shield.

Each other combination, as well as, a pin connection related to the earthed ADR housing should be high-ohmic due to no electrical connection.

All cables should be mechanically fixed to the 4K-, the GGG-, and the FAA-stage for thermal anchoring (fig. D.4). To fix cables to the 4K-stage, aluminum tape is sufficient. To fix cables to GGG, copper clamps with a cryogenic grease in between are used. To anchor cables to the FAA-stage, cables can be fixed to the detector bench or shield base plate with aluminum tape.

D.1.2.3. Fiber installation

A standard fiber installation (fig. 4.1a) is explained using the NIST module and a continuous single mode fiber without plastic tubing and with a FC connector at one end (app. C.4.1). The fiber should be installed inside the ADR and fixed to each

ADR stage. Additionally, the fiber should not be under tension and the bending radius should be >5 cm in the cold.[6]

To have a continuous fiber from TES to the outside of the ADR, the fiber should be at least 1.5 m long. It is recommended to install the fiber from inside to outside with the ADR in mounting position without shields:

- Fiber-to-TES: The fiber-to-TES technique of the NIST module is explained in section 3.2.1.2. The fiber is attached to the chip by carefully sticking the ferrule of the fiber end into the sleeve surrounding the TES chip till the ferrule touches the chip surface. Tentatively, the ferrule end has to be cleaned with proper cleaning stuff and the sensor surface can be very carefully cleaned with the use of compressed air.

- Fiber-to-stages: Now, the fiber is guided through the corresponding copper feedthroughs of the 4K- and the 70K-stage. Additionally, it is mechanically fixed with aluminum tape and the remaining gaps should be screened with aluminum tape. Furthermore, the fiber should be fixed to the FAA-stage before reaching the TES. Thus, after closing the mK-shield (app. D.1.2.4), the remaining coiled fiber parts can be taped to the mK-shield outside (fig. D.4b).

- Fiber vacuum feedthrough: The bare fiber end has to be guided through the Teflon gasket of the vacuum feedthrough (app. C.4.2). The screw fitting is hand-tightly screwed which is sufficient for leak tightness. Finally, remaining fiber parts can be coiled and fixed to the inside of the ADR top flange.

D.1.2.4. Closing ADR

If everything is properly mounted and working, the ADR cryostat can be closed. The shields are screwed from inside to outside: mK-, 4K-, and 70K-shield. The red vacuum dewar is the last shield before bringing the cryostat in operating position (fig. D.5). Here, the black gasket ring should be properly placed in its groove. Tentatively, if the ring does not fit, it can be stretched by hand using a little bit of vacuum grease.

D.1.3. Installation of measuring electronics

Figure 3.12 shows the recommended cabling of the detector setup developed in this thesis. A galvanic separation of the measurement side including the power supply of the SQUID electronics and the measurement instruments (app. C.5) prohibits strong influences due to ground loops (sect. 3.3.1). Galvanic separation utilizes a commercial isolating transformer.[7]

---

[6]It was observed that the cladding of a bended fiber can spall from the core after cooling down and warmin up again.

[7]Isolating transformer Vit 1000 from the company Voltcraft.

| **(a)** mK | **(b)** 4K | **(c)** 70K | **(d)** vacuum | **(e)** operating |
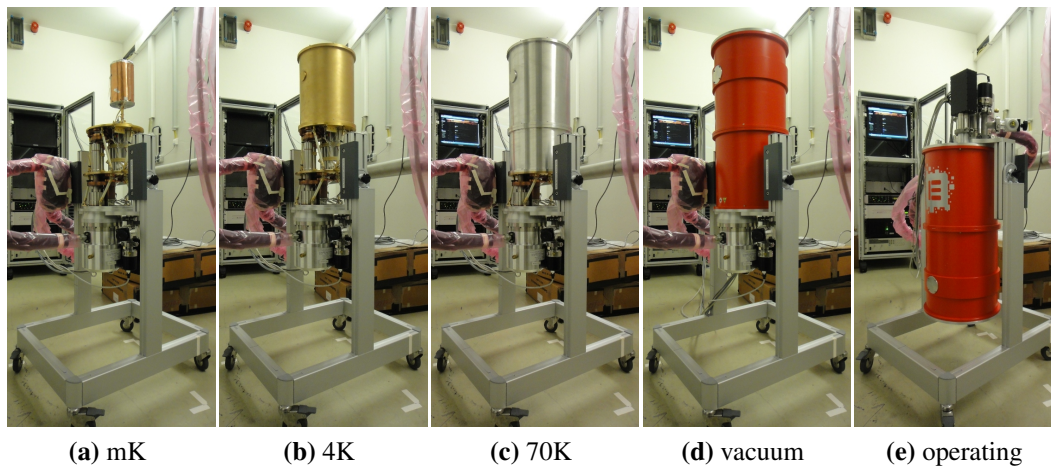
Figure D.5.: Closing the ADR shield: (a)-(e) show the order to close the ADR shields: mK-shield, 4K-shield, 70K-shield, and red vacuum dewar. In (e), the ADR is in operating position and ready for cool-down.

The SQUID electronics should be switched off when it is connected to the top flange connector. Furthermore, before plugging into the connector, it should be discharged. Thus, the connector jackets should be touched in order to bring the ADR and the electronics to the same potential (Beyer, 2011-2013). During cool-down, everything should be connected. The SQUID electronics should be switched off. After reaching 4 K, the SQUID electronics can be switched on at the connector box.

D.2. Operation of ADR system

In this section, the ADR operation is described to reach mK-temperatures (sect. 2.3.1):

- cool-down from 300 K to 4 K
- recharge cycle from 4 K to mK
- regulation to hold mK operating temperature
- warm-up back to 300 K

The following description is a summary of the ADR system operation during this thesis. Heat switch steps and time are related to an operation without technical problems. Specific results and detailed explanations are found in section 2.3. In the following, the temperature 4 K indicates the base temperature of the 4K-stage. The real temperature depends on the performance of the precooling system (sect. 2.2.1).

D.2.1. Cool-down: from 300 K to 4 K

Before starting a cool-down, the heat switch is brought into a proper condition: After the heat switch has been totally closed in the warm,[8] it is slightly opened by -2 k steps.

Now, the ADR dewar is pumped. An oil-free pumping station is recommended including a turbomolecular pump. A leak test can be carried out when the pressure is low enough. Without no leak and reaching a pressure $< 5 \times 10^{-2}$ mbar, the precooling system is switched on:

- switch on the water cycle
- switch on the compressor:[9] `DRIVE` to `ON`

After ~5 min, the 70K-stage should begin to cool. The "Adiabatic Control" software recognizes a cool-down when the 4K-temperature falls below 273 K.[10] The pump can be uncoupled if the pressure is in the 10^{-6} mbar range and the pressure drops if the pump is temporary uncoupled by closing the ADR evacuation port.[11]

Until the pills unit and the 4K-stage is thermalized to the base temperature, it takes approximately 25 h (sect. 2.3.1). If the 4K-stage has already reached <4 K and the cooling rate of the pills is very slow, the heat switch can be closed by +3-5k steps more for a better thermal coupling. After thermalizing, a heat switch test is recommended in order to test the movability of the heat switch unit and to determine the steps to open and close without magnetic field.

D.2.2. Recharge: from 4 K to mK

After reaching the base temperature, a recharge brings the cold finger to mK- temperatures. A manual recharge is described which splits up into five operational phases (sect. 2.3.1). The "Piezo Knob" software which moves the heat switch and the "Adiabatic Control" software for magnet operation and system monitoring are used (sect. 2.2.4):

a) **Closing the heat switch:** Using "Piezo Knob", the heat switch is closed with standard parameters: `Temperature` 3 K, `Torque` 1, and `Frequency` 200 Hz. A closed heat switch `Touch GGG` and `Touch FAA` should show values below 1.0 mΩ. The steps to close depend on the steps to open the heat switch. As a exemplary value, +75 k steps are considered (sect. 2.3.3.1).

---

[8]If the piezo motor is warm (300 K), it should not be moved at pressures between 1 to 10^{-2} mbar. In this range, a gas conduction can damage the piezo element.

[9]If the compressor is switched off, it is necessary to wait ~5 min before switching on again (Phelan, 2012). This is recommended to ensure that the oil flow is completely stopped.

[10]This is the starting point in the "Diagnostic"-file, which is stored in `C://Entropy/logs`. Important temperatures and corresponding times are saved during the cool-down and subsequent recharges.

[11]Approximately, after ~15 h.

b) **Ramping up the magnet:** Using "Adiabatic Control", the magnet current is ramped up by setting `Target (A)` to 40 A and `Rate (A/s)` to 0.1. During the ramping, pills will heat up till ~10 K. If the pills exceed 12 K, the ramping should be stopped and the heat switch has to be readjusted for better thermalization.

c) **Thermalization of the pills:** Due to the coupling, it takes 50-90 min to cool down both pills below 4 K (sect. 2.3.3.2). In order to increase the holding time, pills can be thermalized longer and closer to the 4K-stage temperature (sect. 2.3.4).

d) **Opening the heat switch:** Using "Piezo Knob", the heat switch is opened by using -60-80 k steps in the magnetic field. Settings are `Temperature` 3 K, and `Torque` 2. The heat switch is open if `Touch GGG` and `Touch FAA` measure `overrange`.

e) **Ramping down the magnet:** Using "Adiabatic Control", ramping down the magnet takes place in three steps: Firstly, ramp down to 10 A with 0.1 A/s, secondly, to 2 A with 0.05 A/s, and thirdly, to 0 A with 0.03 A/s.

Step a) is not necessary if the heat switch is already closed. Steps a) to e) and a subsequent mK-regulation can also be automatically operated by "Adiabatic Control". Therefore, settings like ramping speed and steps to close and open the heat switch have to be adjusted.

D.2.3. Regulation: holding mK-temperature

After ramping down, a temperature can be regulated by using "Adiabatic Control":

- Choose proper PID values: `Kp` -0.5, `Ki` -0.001, `Kd` -0.1 show a sufficient performance (sect. 2.3.4.4).

- Enter the setpoint: For example, set for `Set point (K)` 0.08 for 80 mK and press the return key.

- Start the regulation by pressing the `start/stop` button. The background of the button should change to green. After a few seconds, the magnet current and the FAA temperature should increase. After ~3 min, the FAA stage stabilizes to the setpoint temperature.

- Stopping the regulation: Enter 0.0 as `Set point (K)` and press the return key. After the magnet current has been dropped to 0 A, pressing the `start/stop` stops the regulation.

If the FAA-temperature exceeds the regulation temperature during active regulation, the magnet current has reached 0 A and FAA begins to heat up.

D.2.4. Warm-up: switch off ADR

To stop the cooling cycle of the ADR, two things should be ensured:

- The magnet must be switched off and the current must be 0 A.
- The heat switch must be closed and the pills must be coupled to the 4K-stage.

The precooling system is stopped by:

- switching off the compressor: `DRIVE` to `OFF`
- closing the water cycle

Before opening the cryostat for modifications, the inner stages should be thermalized to room temperature. Otherwise, air can condensate or freeze to cold parts. At worst, this can damage components. There are different ways of thermalization to 300 K:

- Long and safe method: Leave the cryostat. It takes >24 h for the pills to reach room temperature. This is recommended e.g. over the weekend.

- Standard method: Let in a little amount of ambient air acting as exchanging gas. Therefore, the evacuation port is shortly opened up to three times. This is recommended e.g. for warming up over night.

- Short method: Let in an amount of air and after an hour another amount and so on. Open the dewars at a temperature of >250 K at the 4K-stage. Use a heating fan with maximum 50° C to warm the cold mass as the ADR magnet and inner stages to reduce condensed water. Dry the components with lab towels regularly. Ask Entropy GmbH before applying this method. This is only recommended for quick ADR maintenance without sensors inside. It takes 4-5 hours.

If the temperature of the 4K-stage and pills has nearly reached room temperature, the cryostat is ventilated by opening the evacuation port. Now, the red dewar and shields can be removed for modifications. If the ADR cryostat is switched off for more than 3 days, it is recommended to leave the dewar closed with low pressure.

D.3. Adjustment of the sensor module

In this section, the adjustment and operation of the NIST module is exemplary described (sect. 3.2.1). The adjustments are done with the SQUID electronics using the "SQUID Viewer" software (Magnicon, 2011). It is a manual-like summary to operate a sensor module as a single photon detector. Furthermore, it includes a short description of functionality checks. It is assumed that the bath temperature of the FAA stage is regulated to 80 mK.

D.3.1. SQUID operation

Reproducing important datasheet values and establishing a SQUID modulation are functionality tests (sect. 3.1.3). After a cool-down and before a recharge, functional-
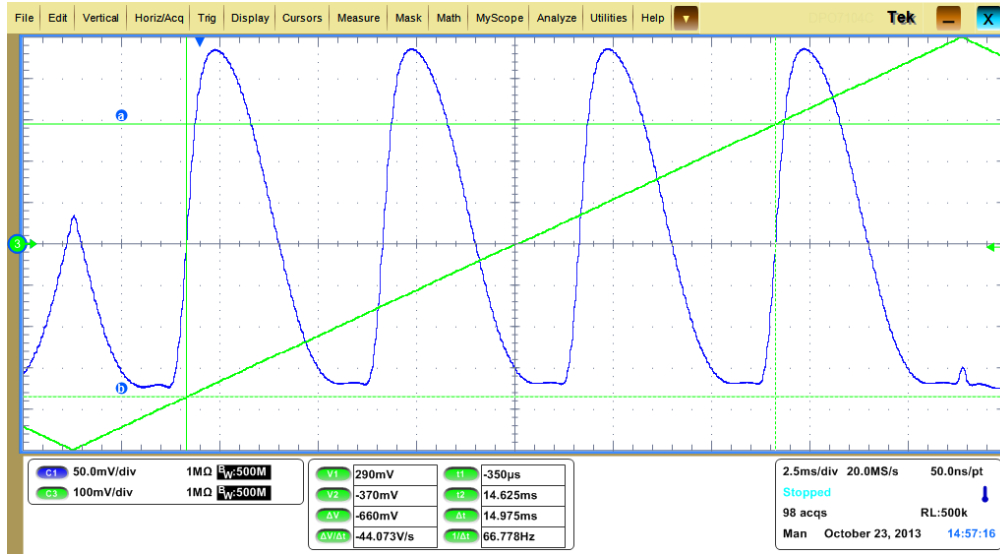
Figure D.6.: Exemplary SQUID modulation measured with an oscilloscope: Overall 2-stage SQUID characteristic or $V\Phi$-modulation (blue) with triangle monitor signal (green). From peak to peak of the triangle signal, the modulation includes ~4 periods. One period corresponds to one flux quantum. Counting the flux quanta within the current range of the monitor signal results in the inverse mutual feedback inductance M_f^{-1} (eqn. D.1). A SQUID working point crosses the x-axis and is at the positive edge of the modulation. The steepness at the working point is expressed by the transfer coefficient V_Φ (eqn. D.2).

ity tests at 4 K are recommended. In the following, 2-stage SQUIDs are considered (sect. 3.2.1.3 and fig. C.3).

D.3.1.1. SQUID modulation: $V\Phi$-characteristic

To set the working point of a 2-stage SQUID, both stages have to be biased: `Ib` and `Vb` for the SQUID array (SQ2) and `I` and `PhiX` for the front-end single SQUID (SQ1). Adjustment steps are:

1. **Preparation:** After switching on the electronics, the SQUID can be controlled with the "SQUID Viewer" software. Select a channel and set in amplifier mode, input termination should be switched on (`Mode palette`). Connect the corresponding channel output and the monitor signal to an oscilloscope.

2. **SQUID offset:** If every bias source is set to zero and the baseline of the channel output is not at a zero level, the baseline should be adjusted in the `Hardware Palette`: After pressing the `Io Adjust` button, the voltage output can be fine-tuned using the `Vo (uV)` slider.

3. **SQUID array characteristic (SQ2):** In the `Bias Palette`, adjust the bias values from datasheet; firstly, for `Ib (uA)`, secondly, for `Vb (uV)`. By ap-

plying a triangle waveform at source `PhiX` in the `Generator Palette`, the modulation of the array is established. Therefore, the scope should trigger to monitor output. The frequency of 22 Hz as a standard and a peak-to-peak value between 200-250 μA can be chosen.

4. **SQUID defluxing:** If the modulation shows little side peaks caused by trapped flux, the SQUID should be heated out (see next section D.3.1.2).

5. **Overall characteristic:** Set the values for `I` and `PhiX` from datasheet in the `Source Palette`. By applying a triangle signal at source `Phib` in the `Generator Palette`, the overall SQUID modulation is established. Again the frequency of 22 Hz as standard and a peak-to-peak value between 200-250 μA can be chosen.

Now, the scope should display a modulation as in figure D.6. The working point of the SQUID is the intersection between the zero line (x-axis) and a positive slope of the modulation. The working point can be optimized.[12] The SQUID is locked at the working point for FLL read out (next sect. D.3.1.3). By analyzing the $V\Phi$-characteristic, two SQUID parameters of the working point are determined:

- **Inverse mutual feedback inductance** M_{f}^{-1}**:** The applied triangle modulation of `Phib` in the `Generator Palette` runs through a certain number of flux quanta Φ_0. A flux quantum is one period of the modulation. By counting the flux quanta, the innverse mutual feedback inductance is determined:

$$M_{\mathrm{f}}^{-1} \, [\mu\mathrm{A}/\Phi_0] = \frac{\Delta\mathrm{Phib}_{\mathrm{peak-to-peak}} \, [\mu\mathrm{A}] \times \Delta V_{\mathrm{out}} \, [\mathrm{V}]/1 \, \mathrm{V}}{\#\,\Phi_0} \qquad (\mathrm{D}.1)$$

  With that, the TES current is calculated in FLL mode (sect. D.3.1.3).

- **Transfer coefficient** V_{Φ}**:** The steepness of the modulation at the working point defines the transfer coefficient V_{Φ}. The gradient x/y is determined by using the derivation mode of the oscilloscope. V_{period} is the time for one flux

---

[12]Finding an optimized working point: Firstly, optimize 2$^{\mathrm{nd}}$ stage (SQUID array) by looking at the array characteristics:

- Adjust `Ib`: Best value is determined by the steepest positive slope of modulation.

- Adjust `Vb`: Shift modulation so that the point of steepest slope (inflection point) is at zero of x-axis.

Secondly, optimize front-end (single SQUID) by looking at the overall characteristics:

- Increase `I`, until a modulation is seen.

- Adjust `PhiX`: Find characteristic shape with steep positive slope.

- Adjust `I` and `PhiX`: Shift modulation so that the point of steepest slope is at zero of x-axis and is symmetrically in inflection point.

A more sophisticated approach is to optimize the SQUID working point by observing the noise level.

quantum and the `Amp Gain` is set in the `Mode Palette`, which is normally 2000. Thus, the transfer coefficient is:

$$V_\Phi \,[\text{V}/\Phi_0] = \frac{y\,[\text{V}]}{x\,[\text{s}]} \frac{V_{\text{period}}\,[\text{s}/\Phi_0]}{\text{Amp Gain}} \tag{D.2}$$

V_Φ can also be determined in FLL mode (sect. D.3.1.3). Using the transfer coefficient, the 3 dB system bandwidth is estimated.

D.3.1.2. Defluxing and compensating magnetic fields

If the SQUID sensor traps magnetic flux during the process of becoming super-conducting – during a cool-down or definitely after a recharge cycle – the SQUID characteristics is defective by side peaks. The trapped flux can be defluxed if the ambient magnetic field does not exceed a critical field. For the PTB 2-stage SQUIDs, the specific value is given by the datasheet value B_{coolmax}:

- **Defluxing:** An integrated heater of the SQUID chip shortly allows to heat the sensor above T_c before it becomes superconducting again. In the `Heater Palette`, heating time and power can be set.

If the defluxing is not succesful, the ambient magnetic field is probably higher than B_{coolmax}. In this case, an additional magnetic field is applied to compensate the ambient field during defluxing:

- **Compensating magnetic field:** In the `Extension Palette`, the low noise current source (LNCS) activates the bucking coil (sect. C.1). A current between -25 to +25 mA can be applied which provides a magnetic field which is perpendicular to the chip plane. A sufficient compensating field diminishes the ambient fieldto a value less than B_{coolmax} (see above). The required strength and orientation of the compensating field has to be found in a trial-and-error procedure. Afterwards, the compensating field can be switched off.[13] If the ambient field is below the tolerable field value B^* of the superconducting SQUID, the SQUID stays defluxed. In this case, the SQUID as a superconductor expulses the ambient magnetic field.

During defluxing, the stray field of the ADR magnet to regulate the temperature to 80 mK does not affect the SQUID operation. Thus, the regulation can be switched onduring defluxing. Further discussion is found in section 3.3.2.

D.3.1.3. Ready for read-out: FLL mode

If both stages are biased (sect. D.3.1.1), the SQUID is set in FLL mode to use it as a TES current sensor. For this purpose, switch off the `Phib` generator signal and press

---

[13] In this setup, the active bucking coil causes a high power load to the detector bench due to resistive parts of the superconducting coil.

the `Mode` button in the main window or in the `Mode palette`. Now, the SQUID is in FLL mode. In FLL mode, `Phib` bias is adjusted, the FLL output is checked, and V_Φ can be determined:

- **Baseline adjustment and digital output:** In FLL mode, the range of the voltage output is ±10 V. After setting the SQUID in FLL, the output is probably not exactly at 0 V. With the `Phib` bias source in the `Bias Palette`, the output can be calibrated to 0 V. Now, the working point in the modulation also intersects the y-axis.

  In the `Channel Info` of the main window, the digital voltage output of the channel `OUT (V)` is displayed. If the output exceeds the ±10 V range, the SQUID is probably dropped out of the FLL mode. The FLL mode is reset by pressing the `Mode` button twice.

- **Quick output check:** The FLL output can be tested by switching on the generator signal `Phib`. If the triangle signal is displayed at the output signal with a 180°-shift, everything is properly set up.

- **Determine V_Φ:** Set the `Gain Bandw. Prod.` (GPB) in the `Mode Palette` to the lowest value of 0.23 GHz. Apply a squared-wave signal at the `Vb` source with a small peak-to-peak $\mathrm{Vb}_{\text{peak-to-peak}} \sim 20\ \mu\mathrm{V}$. Using the scope in average mode, the peak-to-peak value of the voltage output ΔV_{out} is measured. With M_f^{-1} and the selected feedback resistance R_f in the `Mode Palette`, the transfer coefficient is calculated by:

$$V_\Phi\ [\mu\mathrm{V}/\Phi_0] = \frac{\Delta \mathrm{Vb}_{\text{peak-to-peak}}\ [V]}{\Delta V_{\text{out}}\ [V]}\ R_f\ [\Omega]\ M_f^{-1}\ [\mu A/\Phi_0] \tag{D.3}$$

Now, the TES current is read out and the system bandwidth can be estimated:

- **Calculating the TES current:** With the inverse mutual input inductance M_{in}^{-1}, the inverse mutual feedback inductance M_f^{-1}, and the selected feedback resistance R_f, the TES current is given by:

$$\Delta I_{\text{TES}}\ [\mu A] = \Delta V_{\text{out}}\ [\mathrm{mV}] \cdot \frac{M_{\text{in}}^{-1}\ [\mu A/\Phi_0]}{R_f\ [\mathrm{k}\Omega]\ M_f^{-1}\ [\mu A/\Phi_0]} \tag{D.4}$$

  If the voltage output should be referred to the change of magnetic flux, it is calculated:

$$\Delta \Phi_{\text{SQUID}}\ [\Phi_0] = \Delta V_{\text{out}}\ [\mathrm{mV}] \cdot \frac{1}{R_f\ [\mathrm{k}\Omega]\ M_f^{-1}\ [\mu A/\Phi_0]} \tag{D.5}$$

- **Estimate system bandwidth:** The FLL gain is given by:

$$G_\mathrm{S} = \frac{V_\Phi \, [\mu\mathrm{V}/\Phi_0]}{R_\mathrm{f} \, [\Omega] \, M_\mathrm{f}^{-1} \, [\mu\mathrm{A}/\Phi_0]} \tag{D.6}$$

With the chosen GBP in the `Mode palette`, the system bandwidth given as the 3 dB point is estimated. It describes the dynamic range of the whole electronic system:

$$f_\mathrm{3dB} \, [\mathrm{Hz}] \approx G_\mathrm{S} \, \mathrm{GBP} \, [\mathrm{Hz}] \tag{D.7}$$

D.3.2. TES operation

Now, the TES can be characterized and be set into a working point:

- By applying the TES bias current I_BIAS in the `Extension Palette`, the TES resistance R_TES can be determined (sect. D.3.2.1).
- If the TES is superconducting, the phase transition and the *IV*-curve can be measured by sweeping the bias current (sect. D.3.2.2).
- If a working point is found, TES measurements can be done (sect. D.3.2.3).

D.3.2.1. Current divider test

In principle, the TES circuit is a current divider:

$$\frac{R_\mathrm{TES}}{R_\mathrm{SH}} \approx \frac{I_\mathrm{BIAS}}{I_\mathrm{TES}} - 1 \tag{D.8}$$

By applying a small I_BIAS to avoid a self heating of the sensor, R_TES is directly determined by using the shunt resistor R_SH value from the data sheet and the calculated TES current I_TES from the voltage output (eqn. D.4).

At a bath temperature above T_c, the normal resistance of the TES $R_\mathrm{TES,N}$ including the parasitic resistance in the TES branch is measured. At a bath temperature below T_c, the parasitic resistance R_PAR alone is measured. If the measurement suggests that the TES is not superconducting, probably the local TES temperature is above T_c due to a heat input.

D.3.2.2. TES transition: *IV*-characteristic

If the TES is superconducting, the superconducting phase transition can be measured by applying the proper I_BIAS. To get the *IV*-curve of the TES, I_BIAS has to be modulated in a proper range:

- **Measurement:** By applying a high enough I_BIAS[14], bring the TES into normal resistive condition. Now decrease the I_BIAS either manually step by step or by

---

[14]A current of $I_\mathrm{BIAS} = 500 \, \mu\mathrm{A}$ should be enough. When changing the current with such a high

an external generator till nearly reaching $I_{\text{BIAS}} = 0\,\mu\text{A}$.[15] Simultaneously, the voltage output has to be recorded.

- *IV*-**curve:** To get the *IV*-curve, TES current I_{TES} and voltage V_{TES} is required. I_{TES} (y-axis) is determined via V_{out} with the standard calculation by formula D.4. In voltage-bias condition, V_{TES} (x-axis) is simply:

$$V_{\text{TES}} = I_{\text{BIAS}}\, R_{\text{SH}} \tag{D.9}$$

Because of differential measurement, I_{TES} (y-axis) has to be shifted, so that the linear slope of the normal resistance intersects the zero-point. In figure 3.9, an exemplary *IV*-curve is shown.[16]

- **Fractions of $R_{\text{TES,N}}$ and working point:** The linear slope of the *IV*-curve corresponds to the TES normal resistance:

$$R_{\text{TES,N}} = \left(\frac{I_{\text{TES}}}{V_{\text{TES}}} \right)^{-1} \tag{D.10}$$

Fractions of $R_{\text{TES,N}}$ are within the phase transition and define the working point: The intersections between lines with a gradient of (frac. $\times R_{\text{TES,N}})^{-1}$ and the *IV*-curve indicates which voltage over the TES or I_{BIAS} is required. Thus, the x-axis of the *IV*-curve should stay in units of I_{BIAS}.

D.3.2.3. Ready for measurements

The favored working point is set by applying the corresponding I_{BIAS} in the `Extension Palette`.[17] Before measurements, the SQUID software should be set into `global sleeping mode` to reduce interference with the microcontroller of the SQUID electronics (sect. 3.3.1).[18] Now, the whole TES detector setup is ready for measurements. Basically, two types of measurements were done within this thesis using proper electronics for digitizing the voltage output (app. C.5.2):

- **Noise measurements:** Using a spectrum analyzer, the noise spectrum and the bandwidth is measured (sect. 3.2.2.5). This can be compared with the estimated bandwidth with formula D.7. By calculating the current noise

---

difference at once, the SQUID working point can be shifted by one flux quantum or it will even drop out the FLL. By resetting the FLL, the SQUID should be stable in its initial working point again.

[15] As long as the TES circuit stays in voltage biased condition, the measured values are comparable. Coming to small I_{BIAS}, the TES can become non-voltage-biased.

[16] Here, ~25 data points are recorded by hand.

[17] As above, firstly, a high I_{BIAS} should be set to ensure the voltage-biased condition and then, the bias current can be set for the chosen working point.

[18] A right, left mouse click on the `Sleep Mode` button in the `Hardware Palette` sets the whole system in the `global sleeping mode`.

(eqn. D.4), the sensor temperature or resistance can be estimated with the Johnson-Nyquist formula:

$$S_I = \frac{4\,k\,T}{R} \tag{D.11}$$

Furthermore, noise measurements indicate interferences (sect. 3.3).

- **Photon (signal) measurements:** Using an oscilloscope in time mode, single photons and background can be measured (chap. 4). The SQUID electronics should be set in AC-coupling mode in the `Hardware Palette`, so that the baseline is at zero. To analyze signals, an optical connection by a fiber and a suitable signal photon source are required.

E. Milestones and cool-down history of the ALPS TES detector

E.1. TES development of ALPS

The following list shows the milestones of TES development of ALPS:

- Dec. 2010: Meeting Beyer (PTB)
- Mar. 2011: Learning SQUID operation at PTB
- Apr. 2011: Preparing TES setup in Camerino with Cantatore (INFN) in Trieste and Camerino
- Jun./Nov. 2011: Setting up a TES detector in Camerino with Natali, Kuruza and di Giuseppe
- Aug. 2011: Attending LTD-14 in Heidelberg and meeting with TES community (Miller, Lita, Fukuda, Lolli, ...)
- Nov. 2011: Purchasing ADR system from Entropy
- Feb. 2012: 1st TES day at DESY
- Apr. 2012: Contact to Nam (NIST)
- May 2012: Visit of the Zeilinger group, Vienna
- June 2012: Meeting with Beyer (PTB) and Fukuda (AIST) in Berlin
- Aug./Sept. 2012: First operation of ADR cryostat system and first measurements at PTB-Berlin
- Oct. 2012: Installing the ADR system in Hamburg at the DESY site
- Dec. 2012: First 4 K- and mK-run
- Jan./Feb. 2012: Measurements with magnetometer
- May 2013: Characterization of AIST module at PTB/DESY
- June 2013: Characterization of NIST module at PTB/DESY
- From July 2013: Signal/background measurements with NIST module
- Nov. 2013: 2nd TES day at DESY

E.2. Cool-down history of ADR

Table E.2 shows the cool-down history. Time of cool down is given in days while the precooling system was switched on.

CD	date	Setup & result
	July 2012	**ADR at PTB-Berlin** **Start of commissioning phase**
B1	31.7.- 2.8.	Installation and assembling of HS/pill unit. ⇒ Bad coupling of the pills.
B2	8.8.- 9.8.	Adjustment of HS and moving during cool down. ⇒ Stuck HS.
B3	9.8.- 10.8.	Adjustment of HS unit. ⇒ Bad coupling of the pills.
B4	14.8.- 16.8.	Adjustment of HS unit, installation of 4 K-PCB. ⇒ Bad coupling of the pills.
B5	20.8.- 24.8.	Adjustment of HS unit. ⇒ Short between pills and 4 K-stage because of damaged pills.
B6	31.8.- 6.9.	New pills unit, new HS electronics. ⇒ First recharge touching 30 mK, small hold times.
B7	10.9.- 13.9.	General maintenance. ⇒ HS problems, small hold time.
B8	14.9.- 21.9.	First experiment with Vienna module, no moving of HS during cool down. ⇒ Proof of principle: Sensor module within in ADR.
B9	24.9.- 27.9.	Improvement of the cabling, TES with fiber. ⇒ First single photon pulses (880 nm).
B10	28.9.- 28.9.	Improvement of HS unit, without experiment. ⇒ Good coupling but no total opening of HS.
		ADR in ALPS IIa lab in Hamburg
0	28.11.- 29.11.	Precooling test without HS unit and pills. ⇒ 2.55 K as base temperature of 4 K-stage.

CD	date	Setup & result
1	10.12.- 21.12.	Installation of maintained HS/pills unit, software tests by Entropy. $\Rightarrow$ First mK temperatures in ALPS lab.
	2013	**End of commissioning phase**
2	8.1.- 10.1.	Refill of He. $\Rightarrow$ Fair HS performance.
3	11.1.- 15.1.	Vienna module as experiment. $\Rightarrow$ Slight HS problems, module not working.
		Magnetometer
4	5.2.- 11.2.	Magnetometer, sealing of magnet current feedthrough. $\Rightarrow$ Measurements of magnetic environment, stuck HS.
5	12.2.- 18.2.	Adjustment of HS plate. $\Rightarrow$ Bad coupling of FAA but total opening of HS.
6	21.2.- 26.2.	New adjustments of pills and HS unit. $\Rightarrow$ Good coupling but opening HS needs > 100k steps.
7	1.3.- 13.3.	Adjustment of HS plate. $\Rightarrow$ Reproducible perf. of HS, sufficient hold times (> 24 h).
8	14.3.- 11.4.	Adjustment of HS plate. $\Rightarrow$ Repr. perf. of HS (60-80k steps), hold measurements.
9	29.4.- 5.9.	Heater, new current magnet feedthrough. $\Rightarrow$ Load test.
		AIST module
10	7.5.- 16.5.	AIST module, makeshift Al shield. $\Rightarrow$ Channel A broken bond wire, defluxing tests.
		NIST module
11	17.5.- 23.5.	NIST module, makeshift Al shield, only NIST fiber. $\Rightarrow$ TES did not become superconducting.
12	30.5.- 5.6.	Massive Al shield and plate, adjustment of HS/pill unit. $\Rightarrow$ First functionality test but trapped flux problem.

CD	date	Setup & result
13	7.6.- 18.6.	Al plate with **Cu shield**, adjusmtent of HS plate. ⇒ Functionality test, spectrum measurement, first pulse analysis.
14	19.6.- 21.6.	Removed fiber from ch A. ⇒ No reference for bias point.
15	1.7.- 19.7.	Nothing changed. ⇒ Working point analysis of ch B but no reference for bias point, doubled peak height. Quench and water problems (pump).
16	28.7.- 30.7.	Extended fibers by splicing. ⇒ Ch A not superconducting, ch B at lower bias point.
17	31.7.- 23.8.	Fibers coiled and coupled to mK. Adjust. of HS bars, water filter. ⇒ Working point measurements, signal sample.
18	28.8.- 10.9.	Without fiber, fiber end stored at 70 K-stage. ⇒ First long-term background measurement.
19	11.9.- 16.9.	Completely without fiber. ⇒ Background measurement.
20	17.9.- 4.10.	Fibers attached to TESs, fiber end inside ADR at 70/300 K-stage. ⇒ Background measurement.
21	14.10.- 25.10.	Swapped fiber channels to TESs. ⇒ Background measurement.
22	1.11.- 6.11.	Spliced fiber feed out of ADR. ⇒ Signal reproducibility
23	8.11.- 15.11.	Spliced fiber feed out of ADR. ⇒ Background measurements.
24	21.11.- 13.12.	Spliced fiber feed out of ADR. ⇒ Signal/background measurements.

E.3. Alignment history of heat switch unit

Table E.3 lists alignments of the heat switch unit and results during CD 1-24. Four alignments with subsequent fine tunings (app. D.1.1.3) were done during the ADR operation in Hamburg. Here, an overview is given of the alignments, the points of tightening Vespel pins and a brief comment on the result of the moving performance of the heat switch. The resistance between the stages was measured with a multimeter in the warm with an opened heat switch. This provides a reference of the Vespel pin alignment in the warm.

CD	alignment in the warm and result in the cold
1-4	**1st alignment** by Entropy GmbH: reason: first assembly of new pills unit and heat switch unit pins: first installation and no measurement. ⇒ range with >100k steps, touching during ramping down
5	fine tuning: plate shifted counterclockwise ⇒ range with <100k steps, no touch during ramping down
6	**2nd alignment** with Entropy GmbH: reason: insufficient coupling of FAA and loose Vespel pins of GGG pins: retightening of GGG pins by ~1/2 turn (in mounting position $R_{GGG-FAA}$ = 17-20 kΩ and $R_{GGG/FAA-4K}$ = 900 kΩ, in operating position $R_{GGG-FAA}$ = 27 kΩ and $R_{GGG/FAA-4K}$ = 900 kΩ) ⇒ range with <100k steps, touch during ramping down
7	fine tuning: plate shifted clockwise ⇒ range with ~100k steps, touch during ramping down
8	fine tuning: plate shifted counterclockwise ⇒ reproducible moving with -60/+75k steps, no touch during ramping down
9-11	no tuning ⇒ slow decreasing performance: lower thermal coupling and bigger range

CD	alignment in the warm and result in the cold
12	**3rd alignment**: reason: loose Vespel pins of FAA pins: retightening of upper FAA pins by ~1/2 turn (in mounting position $R_{\text{GGG–FAA}} = 11.5$ kΩ and $R_{\text{GGG/FAA–4K}} > 1$ MΩ, in operating position $R_{\text{GGG–FAA}} = 11.5\text{-}12.7$ kΩ and $R_{\text{GGG/FAA–4K}} > 1$ MΩ. $\Rightarrow$ range with <100k steps, no complete opening at 6 T
13-15	fine tuning: plate shifted counterclockwise and slightly angled $\Rightarrow$ reproducible moving with -60/+75k steps, no complete opening at 6 T
16	fine tuning: plate less angled $\Rightarrow$ range with <100k steps, no complete opening at 6 T
17	**4th alignment**: slightly angled bars and tightened GGG pins reason: no complete opening at 6 T pins: retightening of upper GGG pins by ~1/10 turn (in mounting position $R_{\text{GGG–FAA}} = $ kΩ and $R_{\text{GGG/FAA–4K}}$ MΩ, in operating position $R_{\text{GGG–FAA}} = $ kΩ and $R_{\text{GGG/FAA–4K}} = $ MΩ) $\Rightarrow$ range with <100k steps, complete opening at 6 T, no touch during ramping down
18-24	no tuning $\Rightarrow$ stable and similar to CD 17 but slow decreasing performance

F. Acronyms & Constants

F.1. Acronyms

Lingusitic terms:

app.	appendix
cf.	compare (Latin: *confer*)
e.g.	for example (Latin: *exempli gratia*)
eqn.	equation
fig.	figure
i.e.	that is (Latin: *id est*)
sect.	section
tab.	table

Technical terms:

AC	alternating current
ADR	adiabatic demagnetization refrigerator
AIST	National Institute of Advanced Industrial Science and Technology
ALP	axion-like particle
ALPS	Any Light Particle Search
CCD	charge-coupled device
DC	direct current
DESY	Deutsches Elektronen-Synchrotron
EMI	electro-magnetic interference
ETF	electrothermal feedback
FAA	Ferric Ammonium Alum
FC/PC	ferrule connector with physical contact
FC/APC	ferrule connector with angled physical contact
FLL	flux-locked loop
GGG	Gadolinium Gallium Garnet

HIA	(pulse) height and integral analysis
HS	heat switch
IQOQI	Institute for Quantum Optics and Quantum Information
LTD	Low Temperature Detector (conference)
NA	numerical aperture
NIR	near-infrared
NIST	National Institute of Standards and Technology
PCB	printed circuit board
PHD	pulse height distribution
PID	proportional-integral-derivative
PSA	pulse shape analysis
PTB	Physikalisch-Technische Bundesanstalt
RMS	root mean square
SM	Standard Model of Particle Physics
SMF	single mode fiber
SQUID	superconducting quantum interference device
TES	transition-edge sensor
TFN	thermal fluctuation noise
WIMP	weakly interacting massive particle
WISP	weakly interacting sub-eV/slim/slight particle

F.2. Constants

$$\text{speed of light:} \quad c \;=\; 2.998 \cdot 10^8 \,\text{m/s} \tag{F.1}$$

$$\text{elementary charge:} \quad e \;=\; 1.602 \cdot 10^{-19} \,\text{C} \tag{F.2}$$

$$\text{Planck constant:} \quad h \;=\; 6.626 \cdot 10^{-24} \,\text{Js} \tag{F.3}$$

$$\text{Boltzmann constant:} \quad k_{\text{B}} \;=\; 1.381 \cdot 10^{-23} \,\text{J/K} \tag{F.4}$$

$$\text{magnetic flux quantum:} \quad \Phi_0 \;=\; 2.068 \cdot 10^{-15} \,\text{Wb or J/A or Tm}^2 \tag{F.5}$$

$$\text{magnetic permeability:} \quad \mu_0 \;=\; 1.257 \cdot 10^{-6} \,\text{H/m or Tm/A or Wb/(Am)} \tag{F.6}$$

$$\text{gas constant:} \quad R \;=\; 8.314 \,\text{J/mol/K} \tag{F.7}$$

$$\text{Bohr magneton:} \quad \mu_{\text{B}} \;=\; 9.274 \cdot 10^{-24} \,\text{J/T} \tag{F.8}$$

$$\text{electron g-factor:} \quad g_e \;=\; -2.002 \tag{F.9}$$

$$\text{Avogadro constant:} \quad N_{\text{A}} \;=\; 6.022 \cdot 10^{-23} \,\text{1/mol} \tag{F.10}$$

$$\text{h times c:} \quad hc \;=\; 1.24 \,\text{eV}\,\mu\text{m} \tag{F.11}$$

Bibliography

Abraham, E. R. and Cornell, E. A. (1998). "Teflon Feedthrough for Coupling Optical Fibers Into Ultrahigh Vacuum Systems". *Appl. Opt.*, 37(10):1762–1763. URL: `http://ao.osa.org/abstract.cfm?URI=ao-37-10-1762`.

Afanasev, A.; Baker, O.; Beard, K.; et al. (2008). "New experimental limit on optical photon coupling to neutral, scalar bosons". *Phys.Rev.Lett.*, 101:120401. arXiv: `0806.2631`.

Agnese, R.; Ahmed, Z.; Anderson, A. J.; et al. (2013). "Silicon Detector Dark Matter Results from the Final Exposure of CDMS II". *Phys. Rev. Lett.*, 111:251301. URL: `http://link.aps.org/doi/10.1103/PhysRevLett.111.251301`.

Andriamonge, S. et al. (2005). "First results from the CERN Axion Solar Telescope (CAST)". *Phys. Rev. Lett.*, 94:121301. arXiv: `hep-ex/0411033`.

Angloher, G.; Bauer, M.; Bavykina, I.; et al. (2012). "Results from 730 kg days of the CRESST-II Dark Matter search". *The European Physical Journal C*, 72(4):1–22. URL: `http://dx.doi.org/10.1140/epjc/s10052-012-1971-8`.

Arias, P.; Cadamuro, D.; Goodsell, M.; et al. (2012). "WISPy cold dark matter". *JCAP*, 1206:013. arXiv: `1201.5902`.

Arias, P.; Jaeckel, J.; Redondo, J.; et al. (2010). "Optimizing light-shining-through-a-wall experiments for axion and other WISP searches". *Phys.Rev.*, D82:115018. arXiv: `1009.4875`.

Armengaud, E.; Augier, C.; Benoît, A.; et al. (2011). "Final results of the EDELWEISS-II WIMP search using a 4-kg array of cryogenic germanium detectors with interleaved electrodes". *Physics Letters B*, 702:329–335. arXiv: `1103.4070`.

Armengaud, E.; Avignone, F.; Betz, M.; et al. (2014). "Conceptual Design of the International Axion Observatory (IAXO)". arXiv: `1401.3233`.

Bähre, R. (2013). Internal note. ALPS collaboration.

Bähre, R.; Döbrich, B.; Dreyling-Eschweiler, J.; et al. (2013). "Any light particle search II – Technical Design Report". *Journal of Instrumentation*, 8(09):T09001. arXiv: `1302.5647`.

Barthelmess, H. (2013). Private communication. Magnicon GmbH.

Bastidon, N. and Januschek, F. (2014). Internal note. ALPS collaboration.

Bibliography

Beringer, J. et al. (2012). "Review of Particle Physics". *Physical Review D*, 86:010001. URL: `http://pdg.lbl.gov/`. Particle Data Group.

Betz, M.; Caspers, F.; Gasior, M.; et al. (2013). "First results of the CERN Resonant Weakly Interacting sub-eV Particle Search (CROWS)". *Phys.Rev.*, D88(7):075014. arXiv: `1310.8098`.

Beyer, J. (2011-2013). Private communication. PTB.

van Bibber, K. and Carosi, G. (2013). "Status of the ADMX and ADMX-HF experiments". arXiv: `1304.7803`.

Buckel, W. and Kleiner, R. (2012). *Supraleitung: Grundlagen und Anwendungen*. Lehrbuch Physik. Wiley.

Cabrera, B.; Clarke, R. M.; Colling, P.; et al. (1998). "Detection of single infrared, optical, and ultraviolet photons using superconducting transition edge sensors". *Applied Physics Letters*, 73:735.

Cantatore, G. (2011). "Talk at PATRAS 2011". 7th Patras Workshop on Axions, WIMPs, and WISPs, in Mykonos (Greece).

Cantatore, G. (2013). "Talk at PATRAS 2013". 9th Patras Workshop on Axions, WIMPs, and WISPs, in Mainz (Germany).

Clarke, J. and Braginski, A. I. (2004). *The SQUID Handbook: Fundamentals and Technology of SQUIDs and SQUID Systems*. Wiley-VCH, 1. edition.

Clarke, J. and Braginski, A. I. (2006). *The SQUID Handbook Vol II: Applications of SQUIDs and SQUID Systems*. Wiley-VCH, Weinheim, 2. edition.

Claycomb, J. R. and Miller, J. H. (1999). "Superconducting magnetic shields for SQUID applications". *Review of Scientific Instruments*, 70:4562–4568.

Dreyling-Eschweiler, J.; Horns, D.; Januschek, F.; et al. (2013). "Detecting an infrared Photon within an Hour – Transition-Edge Detector at ALPS-II". DESY 13-167. Proceedings of the 9th Patras Workshop on Axions, WIMPs and WISPs, in Mainz (Germany). arXiv: `1309.5024`.

Drung, D. .; Assmann, C. .; Beyer, J. .; et al. (2007). "Highly Sensitive and Easy-to-Use SQUID Sensors". *IEEE Transactions on Applied Superconductivity*, 17:699–704.

Eckart, C. and Shonka, F. R. (1938). "Accidental Coincidences in Counter Circuits". *Phys. Rev.*, 53:752–756. URL: `http://link.aps.org/doi/10.1103/PhysRev.53.752`.

Ehret, K.; Frede, M.; Ghazaryan, S.; et al. (2009). "Resonant laser power build-up in ALPS – A light shining through a wall experiment". *Nuclear Instruments and Methods in Physics Research Section A: Accelerators, Spectrometers, Detectors and Associated Equipment*, 612(1):83 – 96.

Ehret, K.; Frede, M.; Ghazaryan, S.; et al. (2010). "New ALPS results on hidden-sector lightweights". *Physics Letters B*, 689(4-5):149 – 155.

Eidelman, S. et al. (2004). "Review of Particle Physics". *Physical Letters B*, 592:1. URL: `http://pdg.lbl.gov/`. Particle Data Group.

Enss, C., editor. (2005). *Cryogenic particle detection*. Topics in applied physics. Springer-Verlag Berlin Heidelberg.

Entropy. (2011). *Offer of Entropy ADR system (PRO-A-0278), ANG-2011-10394-1*. Entropy GmbH.

Entropy. (2012). *Handbook ADR M-Series*. Entropy GmbH.

Entropy. (2013). "Website". URL: `http://www.entropy-cryogenics.com`. Entropy GmbH.

Fujii, G.; Fukuda, D.; Numata, T.; et al. (2011). "Effect of black body derived photon emission to superconducting optical detectors". Poster at LTD14, Heidelberg.

Fukuda, D. (2012). Private communication. AIST.

Fukuda, D.; Fujii, G.; Numata, T.; et al. (2011). "Titanium-based transition-edge photon number resolving detector with 98% detection efficiency with index-matched small-gap fiber coupling". *Opt. Express*, 19(2):870–875. URL: `http://www.opticsexpress.org/abstract.cfm?URI=oe-19-2-870`.

Ghazaryan, S. (2013). Private communication. ALPS collaboration, DESY.

Gies, H.; Jaeckel, J.; and Ringwald, A. (2006). "Polarized light propagating in a magnetic field as a probe of millicharged fermions". *Phys.Rev.Lett.*, 97:140402. arXiv: `hep-ph/0607118`.

Giustina, M. (2013). Private communication. IQOQI, Vienna.

Gondolo, P. and Raffelt, G. G. (2009). "Solar neutrino limit on axions and keV-mass bosons". 79(10):107301.

Goodsell, M.; Jaeckel, J.; Redondo, J.; et al. (2009). "Naturally light hidden photons in LARGE volume string compactifications". *JHEP*, 0911:027. arXiv: `0909.0515`.

Hadley, L. N. and Dennison, D. M. (1947). "Reflection and Transmission Interference Filters". *J. Opt. Soc. Am.*, 37(6):451–453. URL: `http://www.opticsinfobase.org/abstract.cfm?URI=josa-37-6-451`.

Hagmann, C.; Sikivie, P.; Sullivan, N. S.; et al. (1990). "Results from a search for cosmic axions". *Phys. Rev. D*, 42:1297–1300. URL: `http://link.aps.org/doi/10.1103/PhysRevD.42.1297`.

Hewett, J.; Weerts, H.; Brock, R.; et al. (2012). "Fundamental physics at the intensity frontier". arXiv: `1205.2671`.

Bibliography

Hodajerdi, R. (2013). Internal note. ALPS collaboration.

Holdom, B. (1986). "Two U(1)'s and epsilon charge shifts". *Phys.Lett.*, B166:196.

Horns, D.; Jaeckel, J.; Lindner, A.; et al. (2013). "Searching for WISPy cold dark matter with a dish antenna". *Journal of Cosmology and Astroparticle Physics*, 2013(04):016. URL: `http://stacks.iop.org/1475-7516/2013/i=04/a=016`. arXiv: `1212.2970`.

Horowitz, P. and Hill, W. (1989). *The Art of Electronics*. Cambridge University Press, New York, NY, USA.

Irwin, K. (1995). "An application of electrothermal feedback for high resolution cryogenic particle detection". *Applied Physics Letters*, 66:1998–2000.

Irwin, K. (2014). Private communication. Stanford University.

Irwin, K. D. and Hilton, G. C. "Transition-Edge Sensors". In: Enss, C., editor, "Cryogenic Particle Detection", pages 63–149. Springer-Verlag Berlin Heidelberg, (2005).

Isern, J.; Althaus, L.; Catalan, S.; et al. (2012). "White dwarfs as physics laboratories: the case of axions". pages 158–162. arXiv: `1204.3565`.

Janssen Precision Engineering. (2013). *Homepage*. Janssen Precision Engineering. www.jpe.nl.

Johnson, J. B. (1928). "Thermal Agitation of Electricity in Conductors". *Phys. Rev.*, 32(1):97.

Khoury, J. (2013). "Chameleon field theories". *Classical and Quantum Gravity*, 30(21):214004. arXiv: `1306.4326`.

Lindeman, M. (2000). *Microcalorimetry and the Transition-Edge Sensor*. Ph.D. thesis, Lawrence Livermore National Laboratory.

Lindeman, M. e. a. (2004). "Impedance measurements and modeling of a transition-edge-sensor". *Review of Scientific Instruments*, 75(5):1283–1289.

Lita, A. (2013). Private communication. NIST.

Lita, A.; Rosenberg, D.; Nam, S.; et al. (2005). "Tuning of Tungsten Thin Film Superconducting Transition Temperature for Fabrication of Photon Number Resolving Detectors". *IEEE Transactions on Applied Superconductiviy*, 25.

Lita, A. E.; Calkins, B.; Pellouchoud, L. A.; et al. (2010). "Superconducting transition-edge sensors optimized for high-efficiency photon-number resolving detectors". volume 7681 of *Society of Photo-Optical Instrumentation Engineers (SPIE) Conference Series*.

Lita, A. E.; Miller, A. J.; and Nam, S. W. (2008). "Counting near-infrared single-photons with 95% efficiency". *Opt. Express*, 16(5):3032–3040. URL: `http:`

`//www.opticsexpress.org/abstract.cfm?URI=oe-16-5-3032`.

Lolli, L. (2012). *Photon-Number Resolving by Superconductive Devices*. Ph.D. thesis, Politecnico di Torino.

Lolli, L. (2013). Private communication. INRIM, Turin.

Lolli, L.; Brida, G.; Degiovanni, I. P.; et al. (2011). "Ti/Au TES as superconducting detector for quantum technologies". *Int. J. Quantum Inf.*, 9:405–413.

Lolli, L.; Taralli, E.; and Rajteri, M. (2012). "Ti/Au TES to Discriminate Single Photons". *Journal of Low Temperature Physics*, 167(5-6):803–808. URL: `http://dx.doi.org/10.1007/s10909-012-0473-2`.

Magnicon. (2010). *Cryocable for SEL-1/XXF-1 SQUID Electronics – CC-1 – Manual*. Magnicon GmbH.

Magnicon. (2011). *High Performance dc SQUID Electronics – XXF-1 – Manual*. Magnicon GmbH., v3.3.7 edition.

McCammon, D. "Thermal Equilibrium Calorimeters – An Introduction". In: Enss, C., editor, "Cryogenic Particle Detection", pages 1–34. Springer-Verlag Berlin Heidelberg, (2005).

Meyer, M.; Horns, D.; and Raue, M. (2013). "First lower limits on the photon-axion-like particle coupling from very high energy gamma-ray observation". *Phys.Rev.*, D87:035027. arXiv: `1302.1208`.

Midwinter, J. and Guo, Y. (1992). *Optoelectronics and lightwave technology*. Wiley.

Miller, A.; Lita, A.; Rosenberg, D.; et al. (2007). "Superconducting photon number resolving detectors: performance and promise". *Proceedings of the 8th International Conference on Quantum Communication, Measurement and Computing*, pages 445–450.

Miller, A. J. (2001). *Development of a broadband optical spectrophotometer using superconducting transition-edge sensors*. Ph.D. thesis, Stanford University.

Miller, A. J. (2011). Private communication. Albion College.

Miller, A. J.; Lita, A. E.; Calkins, B.; et al. (2011). "Compact cryogenic self-aligning fiber-to-detector coupling with losses below one percent". *Opt. Express*, 19(10):9102–9110. URL: `http://www.opticsexpress.org/abstract.cfm?URI=oe-19-10-9102`.

Miller, A. J.; Nam, S. W.; Martinis, J. M.; et al. (2003). "Demonstration of a low-noise near-infrared photon counter with multiphoton discrimination". *Applied Physics Letters*, 83:791–793.

Mueller, G.; Sikivie, P.; Tanner, D. B.; et al. (2010). "Resonantly-enhanced axion-photon regeneration". *AIP Conf.Proc.*, 1274:150–155.

Bibliography

Natali, R. (2011). "Internal note". University of Camerino, Italy.

Nyquist, H. (1928). "Thermal Agitation of Electric Charge in Conductors". *Phys. Rev.*, 32(1):110–113.

Onnes, H. K. (1911). "The resistance of pure mercury at helium temperatures". *Commun. Phys. Lab. Univ. Leiden*, 12:120+.

Peccei, R. and Quinn, H. R. (1977). "CP conservation in the presence of instantons". *Phys.Rev.Lett.*, 38:1440–1443.

Phelan, K. (2012). Private communication. Entropy GmbH.

Pobell, F. (2007). *Matter and Methods at Low Temperatures*. Springer.

Previtali, E. (2006). "20 years of cryogenic particle detectors: past, present and future". *Nuclear Physics B - Proceedings Supplements*, 150(0):3 – 8. URL: `http://www.sciencedirect.com/science/article/pii/S092056320500798X`.

Redondo, J. and Ringwald, A. (2011). "Light shining through walls". *Contemp.Phys.*, 52:211–236. arXiv: `1011.3741`.

Rosenberg, D.; Lita, A. E.; Miller, A. J.; et al. (2005). "Noise-free high-efficiency photon-number-resolving detectors". *Phys. Rev. A*, 71:061803. URL: `http://link.aps.org/doi/10.1103/PhysRevA.71.061803`.

Rosenberg, D.; Nam, S.; Miller, A.; et al. (2004). "Near-unity absorption of near-infrared light in tungsten films". *Nuclear Instruments and Methods in Physics Research Section A: Accelerators, Spectrometers, Detectors and Associated Equipment*, 520(1-3):537 – 540. URL: `http://www.sciencedirect.com/science/article/pii/S0168900203032364`.

Schneider, P. (2006). *Einführung in Die Extragalaktische Astronomie und Kosmologie*. Springer, 1. edition.

Schott, M. et al. (2011). "First Results of the Full-Scale OSQAR Photon Regeneration Experiment". arXiv: `1110.0774`.

Schwabl, F. (2000). *Statistische Mechanik*. Springer-Lehrbuch. Springer, 2. edition.

von Seggern, J. E. (2013). "Overview of Low-flux Detectors". Proceedings of the 9th Patras Workshop on Axions, WIMPs and WISPs, in Mainz (Germany). arXiv: `1310.0660`.

von Seggern, J. E. (2014). *Constraining Weakly Interacting Slim Particles with a Massive Star and in the Laboratory*. Ph.D. thesis, University of Hamburg / DESY.

SHI. (2008). *Technical Instruction – F-50H Compressor Unit*. Sumitomo Heavy Industries, Ltd.

SHI. (2011). *Technical Instruction – 4K Pulse Tube Cryocooler*. Sumitomo Heavy Industries, Ltd.

SHI Cryogenics Group. (2013). *Homepage*. Sumitomo (SHI) Cryogenics Group. URL: `http://www.shicryogenics.com/`.

Srednicki, M. (1985). "Axion Couplings to Matter. 1. CP Conserving Parts". *Nucl.Phys.*, B260:689.

Taralli, E.; Portesi, C.; Lolli, L.; et al. (2012). "Impedance measurements for photon number resolving Transition-Edge Sensors". *Eur. Phys. J. Plus*, 127(13).

Trines, D. (2013). Internal note. ALPS collaboration.

Weinberg, S. (1978). "A new light boson?" *Phys.Rev.Lett.*, 40:223–226.

Wellstood, F.; Urbina, C.; and Clarke, J. (1994). "Hot-electron effects in metals". *Physical review. B, Condensed matter*, 49(9):5942–5955.

Wernicke, D. (2013). Private communication. Entropy GmbH.

White, G. K. and Meeson, P. J. (2002). *Experimental Techniques in Low-Temperature Physics*. Oxford Science Publications, 4. edition.

Wilczek, F. (1978). "Problem of strong P and T invariance in the presence of instantons". *Phys.Rev.Lett.*, 40:279–282.

Young, B. A.; Saab, T.; Cabrera, B.; et al. (2002). "Effect of implanted metal impurities on superconducting tungsten films". *Journal of Applied Physics*, 91(10):6516–6519. URL: `http://scitation.aip.org/content/aip/journal/jap/91/10/10.1063/1.1469690`.

Acknowledgments